FACULTY OF ENGINEERING
AND ARCHITECTURE

The mystery of high-temperature superconductivity: solving effective Hamiltonians of cuprates with tensor networks

Sander De Meyer
Student number: 01809159

Supervisors: Prof. Frank Verstraete, Prof. dr. ir. Veronique Van Speybroeck
Counsellors: Dr. Laurens Vanderstraeten, Lukas Devos, Quinten Mortier

Master's dissertation submitted in order to obtain the academic degree of
Master of Science in Engineering Physics

Academic year 2022-2023

GHENT
UNIVERSITY

CENTER FOR
MOLECULAR MODELING

This work has been performed at the Center for Molecular Modeling.

”Everything must be made as simple as possible, but not simpler.”

- *Mark Scroggins*

Acknowledgements

Before starting this thesis, I would like to express my gratitude to the multitudes that have helped me in the process of writing my thesis. It is a list of promotors, counselors, friends, and family, most of whom have had influences that range far longer than just this year.

I would like to start with the people who made this thesis possible, namely Professor Frank Verstraete and Professor Veronique Van Speybroeck. Thank you for creating this project and for the attendance, attention, and counsel at progress meetings. Those meetings often led to new interesting ideas and new ways of thinking about the subject, and have undoubtedly given more direction to this thesis. In this list, Professor Jutho Haegeman and Dr. Nick Bultinck should also be mentioned.

Thank you to the QuantumGroup in general, for involving me as a thesis student in group activities that are normally not meant for thesis students. These included lunch, the Christmas party, and QIP, and decreased the distance between thesis and non-thesis students, making me feel more part of a research group rather than a burden. The CMM deserves the same credit, for the potluck breakfast and summer event, which have given me a better understanding of what it would be like to do a PhD.

Thank you to Quinten Mortier, for the interesting explanations that mainly at the beginning of the year helped set me off in the right direction. Thank you to Lander Burgelman for fixing a bug in Tensortrack here and there, and for buying the sandwiches at noon. Thank you to Laurens Vanderstraeten for all the explanations on everything that had any connection to my thesis, ranging from fundamental information on tensor networks, to structure factors and superconductivity. And lastly, but anything but least, thank you to Lukas Devos: Thank you for the many, many explanations about all theoretical and practical things. Thank you for the introductory lectures at the beginning and for guiding me throughout the whole year. Thank you for answering the many questions. Thank you for also answering those on Saturday evening, after 11 PM, after I sent you a question thinking you would answer it the next Monday, but answering it about five minutes later. Thank you for the many bug fixes. Sorry for the many bug fixes where I sent examples that took quite a long time to run (especially the one that took 1.5 hours). And thank you for making the frustration regarding these examples not super explicit. This thesis would not be what it is now without your contributions.

Apart from the promotors and counselors, there are many other people who deserve credit too.

Thank you to Daan Verraes, for all the discussions on the project, his thesis, and my thesis. I think those conversations helped us both gain a much more fundamental understanding of everything that is going on in the broader project of which the theses are a part. Talking about physics with friends still is one of the greatest pleasures of life. Thank you to everyone at the VVN, for making it an amazing year, for not voting me down as president, for organizing everything, for going to the pub after meetings, for the trip, and for the friendships. “Let’s vlieg erin” was never more applicable.

Thank you to Brent Nissens for thinking Arsenal would be crowned champions, and thereby making extremely hilarious statements time and time again. Thank you to Thymen Van de Steene for the company during the lectures of the second semester. Thank you to Jan De Neve for showing that you can also write a thesis using colored pencils. Thank you to Dante Van Poucke for thanking me in his preface. Thank you to Zion Thuypens for the tea, the drinking of the tea, for the nice and interesting conversations. Thank you to all the ‘burgies’ I did not yet mention, together with

Roberto Di Bisceglie, Corneel De Vos, and Lucas Hock, for the extra relaxation during the summer. Thank you to ChatGPT for writing this thesis (For everyone on the evaluation committee: this is, to be absolutely clear, a joke) and thank you to all the forums on Matlab and Latex for guiding me through their weird habits.

Lastly, thank you to my parents and sisters, for pretending that what I do is interesting.

Sander De Meyer, July 2023

Declarations

Sander De Meyer, August 2023

The mystery of high-temperature superconductivity: solving effective Hamiltonians of cuprates with tensor networks

by

Sander De Meyer

Master's Dissertation submitted in order to obtain the academic degree of
Master of Science in Engineering Physics
Academic year 2022-2023

Supervisors: prof. dr. ir. Frank Verstraete, prof. dr. ir. Veronique Van Speybroeck
Counsellors: dr. ir. Laurens Vanderstraeten, Lukas Devos, ir. Quinten Mortier
Faculty of Engineering and Architecture
Ghent University

Abstract

The ground states of different Hubbard Hamiltonians are investigated with tensor networks by placing them on cylinders and helices. The way these effective Hamiltonians can be obtained using electronic structure methods is briefly explained, before expanding upon the theory behind tensor networks. The Heisenberg model is used as a benchmark to evaluate the used methods. There is an emphasis on the influence of using finite-size systems like cylinders and helices, together with a discussion on spontaneous symmetry breaking.

The two-dimensional Hubbard model is examined for $U/t > 0$. The competition of stripe order and superconducting order is investigated. The results confirm previous calculations and show the existence of filled stripes on a two-leg cylinder and half-filled stripes on a four-leg cylinder. The density and pair correlation functions are fitted to obtain the Luttinger exponents. It is concluded that bond dimensions $D > 2336$ need to be used to resolve the competition between stripe and superconducting order, which was not feasible within this thesis.

The benchmarked methods are then applied to the cuprates, a class of materials that can exhibit high-temperature superconductivity. The one-band model of $\mathrm{HgBa_2CuO_4}$ is investigated as a case study. The charge density was modulated along the length of the cylinder, whereas pair-forming was found along the circumference. The Luttinger exponents were fitted for a wide range of hole doping levels δ, and showed that the phase is superconducting for $\delta \in [\delta_{min}, \delta_{max}]$, where $4.45\% \lesssim \delta_{min} \lesssim 12.47\%$ and $24.25\% \lesssim \delta_{max} \lesssim 30.36\%$. This is in accordance with the general form of the phase diagram of the cuprates at zero temperature. It is also shown that this superconductivity can coexist with stripe order.

Keywords

Charge density waves, cuprates, Luttinger exponents, superconductivity, tensor networks.

The mystery of high-temperature superconductivity: solving effective Hamiltonians of cuprates with tensor networks

Sander De Meyer

Supervisors: prof. dr. ir. Frank Verstraete, prof. dr. ir. Veronique Van Speybroeck
Counsellors: dr. ir. Laurens Vanderstraeten, Lukas Devos, ir. Quinten Mortier

Abstract— **The ground states of different Hubbard Hamiltonians are investigated with tensor networks by placing them on cylinders and helices. The way these effective Hamiltonians can be obtained using electronic structure methods is briefly explained, before expanding upon the theory behind tensor networks. The Heisenberg model is used as a benchmark to evaluate the used methods, with an emphasis on the influence of using finite-size systems like cylinders and helices.**

The two-dimensional Hubbard model is examined for $U/t > 0$. The competition of stripe order and superconducting order is investigated. The results confirm previous calculations and show the existence of filled stripes on a two-leg cylinder and half-filled stripes on a four-leg cylinder. The density and pair correlation functions are fitted to obtain the Luttinger exponents. It is concluded that bond dimensions $D > 2336$ need to be used to resolve the competition between stripe and superconducting order, which was not feasible within this thesis.

The benchmarked methods are then applied to the cuprates, a class of materials that can exhibit high-temperature superconductivity. The one-band model of $HgBa_2CuO_4$ is investigated as a case study. The charge density was modulated along the length of the cylinder, whereas pair-forming was found along the circumference. The Luttinger exponents were fitted for a wide range of hole doping levels δ, and showed that the phase is superconducting for $\delta \in [\delta_{min}, \delta_{max}]$, where $4.45\% \leq \delta_{min} \leq 12.47\%$ and $24.25\% \leq \delta_{max} \leq 30.36\%$. This is in accordance with the general form of the phase diagram of the cuprates at zero temperature. It is also shown that this superconductivity can coexist with stripe order.

Keywords— **Charge density waves, cuprates, Luttinger exponents, superconductivity, tensor networks.**

I. INTRODUCTION

Superconductors have vanishing electrical resistance under a certain temperature, called the critical temperature T_c. They were first discovered by the Dutch physicist Heike Kamerlingh Onnes in 1911, when he found that mercury exhibits superconductivity with $T_c = 4.2K$ [1]. Thus began the search for materials exhibiting superconductivity at room temperature. A big step in this search was the discovery of high-temperature superconductivity in 1986 [2]. Here, they found a critical temperature of 30K, the highest at the time, for a system consisting of barium, lanthanum, copper, and oxide, specifically $Ba_xLa_{5-x}Cu_5O_{5(3-y)}$ with $x = 1$ and 0.75 and $y > 0$. The original theory to describe superconductivity proposed by Bardeen, Cooper, and Schrieffer, called BCS theory, failed to describe this high-temperature superconductivity [3, 4]. A complete theory of this effect is still missing, more than 40 years after its discovery.

The La-Ba-Cu-O system where high-T_c superconductivity was first found is part of a more general class of materials called the cuprates. They consist of sheets of CuO_2-planes, which are shown in figure 1. Here, the d-orbitals of the copper atoms are shown in red and form a square lattice. The p_x and p_y-orbitals of oxygen are shown in blue and are situated between two copper atoms. These CuO_2-planes are stacked on top of each other and are separated by insulating charge reservoirs, consisting of oxygen and heavier elements. The conduction occurs within these CuO_2-planes, which makes it a 2-dimensional problem [5]. The copper d-orbitals and the oxygen p-orbitals are responsible for the (super)conductivity.

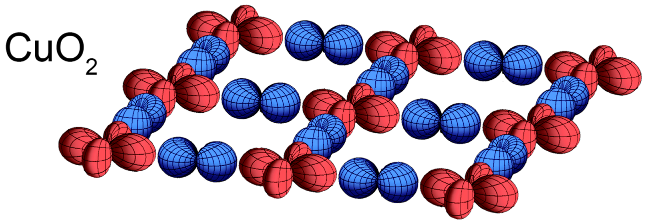

Figure 1: A CuO_2-plane [6].

The Hubbard model was proposed as a simple model that could describe the cuprates. Despite its simplicity, basic questions about the ground state in different parameter regimes of the Hubbard model remain unanswered. Only in 1D, where the Hubbard model can be exactly solved by the Bethe ansatz [7], have those questions been settled. For higher dimensions, the only option is to resort to numerical methods. Many new methods have been developed over the years to obtain the desired accuracy of such quantum many-body problems. These methods include quantum Monte Carlo (QMC), density matrix embedding theory (DMET), density matrix renormalization group (DMRG), dynamical cluster approximation (DCA), unrestricted coupled cluster theory, and tensor networks [8]. These methods allowed us to explore the rich physics inherent to the Hubbard model, and in recent years have reached a consensus on the ground state in many of its parameter regimes [9].

Figure 2 shows the current phase diagram of the non-extended 2D Hubbard model at zero temperature as a function of doping for intermediate interaction strengths [9]. This shows great similarity with the experimental phase diagram of the cuprates, which is the reason why the Hubbard model has been identified as a good model to describe these materials. Many different phases have been identified in both the cuprates and the Hubbard model, such as the antiferromagnetism, stripe order, d-wave superconductivity, and the Fermi liquid [10–13].

Figure 2: The phase diagram of the Hubbard model at zero Kelvin for intermediate interaction strengths [9]

The Hubbard model can be extended by introducing extra terms with new parameters, which will be introduced in the next section. In order to accurately describe the cuprates with an extended Hubbard model, a reliable way to calculate its parameters is needed. This can be done by a procedure called downfolding. First, a calculation based on density functional theory is performed. For strongly correlated systems such as cuprates, this does not yield reliable results on the electronic structure. However, the strong electron correlations which DFT can not describe, occur only for a few electron states in the many-electron system. Methods like the constrained random phase approximation [14–16] and the constrained GW approximation [17, 18] can predict parameters for the (extended) Hubbard model. This Hubbard model is an effective Hamiltonian describing these few states, taking into account the interactions between these states, as well as the interactions with the neglected states [18].

In this thesis, we try to solve these low-energy effective Hamiltonians for the strongly interacting states using tensor networks. For this, the physical Hilbert space of the tensors is based on the occupancy of localized orbitals centered on the atoms, namely the maximally localized Wannier functions (MLWF). Using this basis allows for a lattice description of the system with local, finite-dimensional Hilbert spaces.

Section II will introduce the different models and methods. Section III applies these to the two-dimensional Heisenberg and Hubbard model, together with the one-band model of $HgBa_2CuO_4$. Finally, a conclusion is given in section IV.

II. METHODS

A. The Heisenberg model

The Heisenberg XXX model has only nearest-neighbor interactions with interaction Hamiltonian

$$H_{ij} = \vec{S}_i \cdot \vec{S}_j \tag{1}$$

with S_i the spin operator on site i. In 1D, this can describe a chain of spin-$\frac{1}{2}$ particles [19–21].

B. The Hubbard model

The Hubbard model was proposed in 1963 as a simple model describing interacting fermions on a lattice by Hubbard, Kanamori, and Gutzwiller [9]. It is defined as [9, 22–24]

$$H = -\sum_{i,j\in\Lambda}\sum_{\sigma} t_{ij}\left(c^{\dagger}_{i\sigma}c_{j\sigma} + c^{\dagger}_{j\sigma}c_{i\sigma}\right) + \sum_{i\in\Lambda} U_i n_{i\uparrow}n_{i\downarrow} \tag{2}$$

i and j denote sites on a lattice Λ. $c^{\dagger}_{i\sigma}$ is the creation operator for an electron with spin σ on site i. $n_{i\sigma}$ is the number operator and counts how many electrons of spin σ are present on site i. The sites have an interaction strength U_i and sites i and j interact with a hopping term t_{ij}. For the translationally invariant case, $U_i = U$ and $t_{ij} = t$. This is the simple Hubbard model, which can be extended to include further-reaching hopping terms and off-site repulsive interactions of the form

$$H_V = \sum_{i,j\in\Lambda} V_{ij} n_i n_j \tag{3}$$

The ground states of these Hamiltonians have been calculated using the Variational Uniform Matrix Product State (VUMPS) algorithm [25, 26].

C. Describing the cuprates

The one-band model of the cuprates is a model in which only the d-orbitals of copper are taken into account explicitly. It is a Hubbard model with nearest-neighbor and next-to-nearest neighbor hopping, and nearest-neighbor off-site Coulomb interaction terms. The Hamiltonian is given by

$$\begin{aligned} H = &-t\sum_{\langle ii'\rangle\sigma}\left(c^{\dagger}_{i\sigma}c_{i'\sigma} + h.c.\right) - t'\sum_{\langle\langle ii'\rangle\rangle\sigma}\left(c^{\dagger}_{i\sigma}c_{i'\sigma} + h.c.\right) \\ &+ U\sum_{i} n_{i\sigma}n_{i\bar{\sigma}} + V\sum_{\langle ii'\rangle\sigma\sigma'} n_{i\sigma}n_{i'\sigma'} \end{aligned} \tag{4}$$

Here, $\langle\cdots\rangle$ denotes nearest-neighbor interactions and $\langle\langle\cdots\rangle\rangle$ denotes next-to-neighbour interactions, i.e. interactions along a diagonal. The one-band model is visualized in figure 3. Doping a cuprate changes the electron filling f of the Hubbard model.

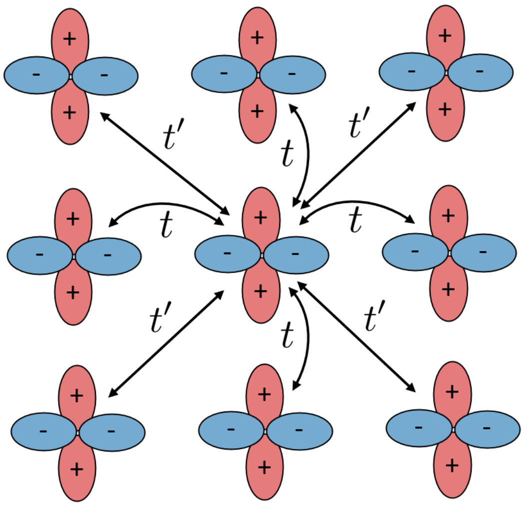

Figure 3: Definition of the hopping terms of the one-band Hubbard model with the appropriate conventions. V-terms act on the same locations as t-terms.

D. Modelling two-dimensional systems

In 1D, tensor networks represent the quantum many-body state as a Matrix Product State (MPS). Even though this MPS description is one-dimensional, it can nevertheless be used to describe two-dimensional systems by wrapping it around a cylinder. The 2D system is made 1D by considering a chain of lattice points looping around the cylinder, thus perfect for the MPS language. Each site in the bulk i is connected to the sites $i+1$,$i-1$, $i+N$, and $i-N$, where N is called the circumference of the cylinder. The system is still infinite in the x-direction, but finite in the y-direction. This is shown in figure 4. Either periodic or spiral boundary conditions can be applied along the y-direction, corresponding to cylinders and helices respectively.

E. Extrapolation to bond dimension $D \to \infty$

An MPS has a certain bond dimension D, which is related to the accuracy of the description. For accurate results, this should be infinite. In numerical calculations, however, D has to be finite, and thus a way of extrapolating the results to $D \to \infty$ is needed.

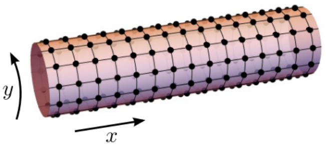

Figure 4: 2D system wrapped around a cylinder [27]

A possible way to do this is by looking at the transfer matrix, which is a tensor that can be calculated based on the ground state MPS [26]. The eigenvalues of this transfer matrix can be written as

$$\lambda_n = e^{-(\epsilon_n + i\theta_n)} \tag{5}$$

where $\epsilon_n, \theta_n \in \mathbb{R}$ and $\epsilon_m \geq \epsilon_n$, if $m > n$. Normalisation fixes $\epsilon_1 = 0$ and $\theta_1 = 0$. ϵ_2 is related to the effective correlation length as $\epsilon_2 = 1/\xi_{\text{eff}}$, and θ_2 captures the leading oscillations of the correlation function. These definitions are visualized in figure 5.

In theory, this spectrum should have a gap to ϵ_2, after that possibly some separate bands, and eventually a continuum. Due to the finite bond dimension used in the calculations, this continuum will be discrete. Deviations from the continuum, and by extension deviations from infinite bond dimension, can thus be characterized in the variable δ

$$\delta = \epsilon_3 - \epsilon_2 \tag{6}$$

If the system is degenerate and $\epsilon_2 = \epsilon_3$, then $\delta_{42} = \epsilon_4 - \epsilon_2$ can be used instead.

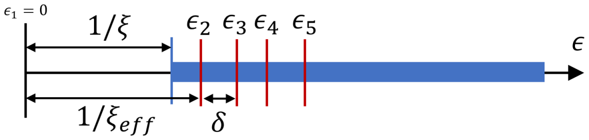

Figure 5: Visualization of the extrapolation measure

The bigger the bond dimension, the closer the spectrum will be to a continuum, and the smaller δ will be. This δ can be used in a scaling hypothesis [28], where it is assumed that an observable g obeys the following function

$$g(\delta) = g_e + a\delta^b \tag{7}$$

where g_e is the extrapolated value. b is usually close to 1, allowing for a linear fit in many cases. Alternatively to δ, the inverse bond dimension $1/D$ can also be used as an error measure [28].

F. Determination of the phase

To determine whether the ground state is superconducting in the 2D model, the Luttinger exponents of the pair and charge correlation functions $N(r)$ and $\Phi_{\alpha\beta}(x)$ are calculated. These correlation functions correspond to the operators

$$\begin{aligned} \Phi_{\alpha\beta}(x) &= \frac{1}{N}\sum_{y=1}^{N} \left\langle \Delta_\alpha^\dagger(x_0, y)\Delta_\beta(x_0 + x, y)\right\rangle \\ N(r) &= \langle \hat{n}_i \hat{n}_{i+r}\rangle - \langle \hat{n}_i\rangle \langle \hat{n}_{i+r}\rangle \end{aligned} \tag{8}$$

$\Delta_\alpha^\dagger(x, y)$ is the spin-singlet pair-field creation operator, defined as [29, 30]

$$\Delta_\alpha^\dagger(x, y) = \frac{1}{\sqrt{2}}\left(c^\dagger_{(x,y),\uparrow} c^\dagger_{(x,y)+\alpha,\downarrow} - c^\dagger_{(x,y),\downarrow} c^\dagger_{(x,y)+\alpha,\uparrow}\right) \tag{9}$$

These correlation functions can be used to determine the charge and pair Luttinger exponents K_ρ and K_{SC} as

$$\begin{aligned} N(r) &\propto r^{-K_\rho} \\ \Phi_{yy}(x) &\propto x^{-K_{SC}} \end{aligned} \tag{10}$$

The ground state is said to be superconducting when $K_{SC} < K_\rho$, whereas it exhibits stripe order and charge density waves (CDW) when $K_{SC} > K_\rho$ [29, 31].

The correlation functions can be fitted by subdividing the logarithm of the distances r in bins, and calculating the maximal value of the correlation function within that bin. These maximal values together with their respective r-values are then used in a linear log-log fit to obtain the Luttinger exponent. The bin widths correspond to the biggest difference between successive local maxima of the correlation function. This procedure is similar to the method used in references [30, 32]. Only the range beyond the short-range effects and before the onset of exponential decay is considered.

G. Filling fraction

The filling fraction FF of a CDW is defined as

$$FF = \delta\lambda_{CDW} \tag{11}$$

$FF = 1$ and $FF = 1/2$ correspond to filled and half-filled stripes, respectively.

III. RESULTS

A. 2D Heisenberg model

The 2D Heisenberg model defined in (1) can be used as a benchmark, since there exists considerably more consensus on this model than the Hubbard model [33–35]. The ground state energy of cylinders and of helices were calculated for various values of the circumference N. Figure 6 shows that the ground state energy indeed approaches the correct value for large circumferences, while the smaller systems can show significant deviations.

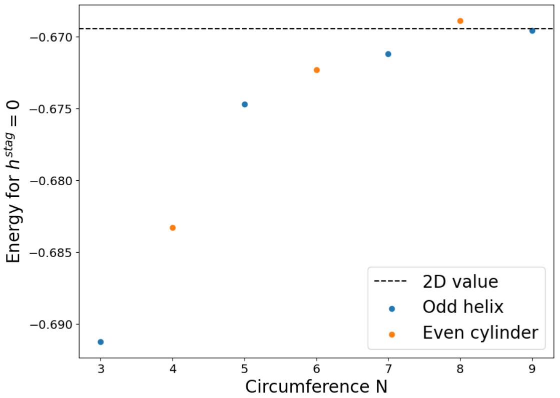

Figure 6: Ground state energy per site of the 2D XXX Heisenberg model for helices and cylinders. The 2D value is taken from [36].

B. 2D simple Hubbard model

The simple Hubbard model only has nearest neighbor interactions and was simulated using the $U(1)\otimes SU(2)\otimes f\mathbb{Z}_2$ symmetry. For $U/t = 8$ and $f = 7/8$, CDWs are seen, which have a charge modulation along the x-direction and are uniform along the y-direction. For $N = 2$ cylinders, a CDW with period $\lambda = 8$ is found, whereas the period is 4 for $N = 4$. These results correspond to filled and half-filled stripes, respectively, and are shown in figure 7. The same conclusions were drawn in references [29, 37–39]. The results are reproduced without imposing the $U(1)$ symmetry for the charge sector, to make sure the number of rungs does not influence the resulting period. The eigenvalues of the transfer matrix are used for this and are shown in figure 8. These confirm that a CDW with period $\lambda = 8$ exists for $N = 2$.

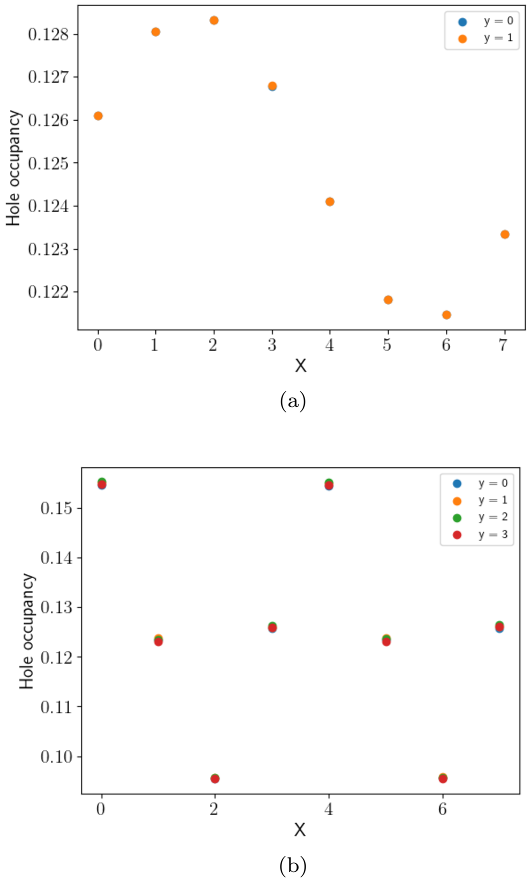

(a)

(b)

Figure 7: Hole occupancies for the simple Hubbard model with $t = 1$, $U = 8$, and $f = 7/8$ on a 8-rung cylinder with (a) $N = 2$, $D = 600$ and (b) $N = 4$, $D = 767$.

To determine the phase of the simple Hubbard model, the density and pair correlation functions were calculated and their Luttinger exponents were fitted. This was done by imposing the $SU(2)\otimes f\mathbb{Z}_2$ symmetry. Figure 9 shows the results.

The Luttinger exponents from these fits can be extracted from calculations at different bond dimensions, and are extrapolated using (7). The results are given in figure 10. For the extrapolation of K_ρ, b was set to 1. Unfortunately, the 95% confidence intervals of the Luttinger exponents overlap, so it can not be determined which correlations are dominant. This is a result of the strong competition of stripe and superconducting order. The heaviest calculations used $D = 2336$, and performing these calculations for even higher bond dimensions was not feasible due to the limited computational resources.

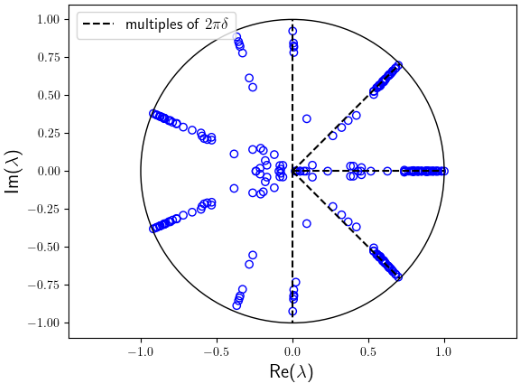

Figure 8: Spectrum of the transfer matrix for the simple Hubbard model with $t = 1$, $U = 8$, and $f \approx 7/8$ on a cylinder with $N = 2$ and 1 rung, using the $SU(2)\otimes f\mathbb{Z}_2$ symmetry and $D = 2336$. The dashed lines correspond to multiples of $\theta = \frac{\pi}{4} = 2\pi\delta$.

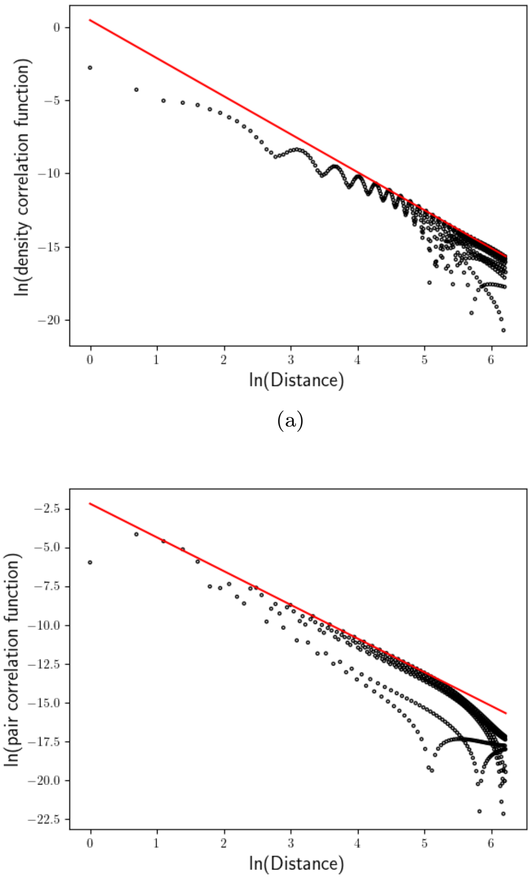

(a)

(b)

Figure 9: Fit of the (a) density and (b) pair correlation function for the simple Hubbard model with $t = 1$, $U = 8$, and $f \approx 7/8$ on a cylinder with $N = 2$ and $D = 2336$

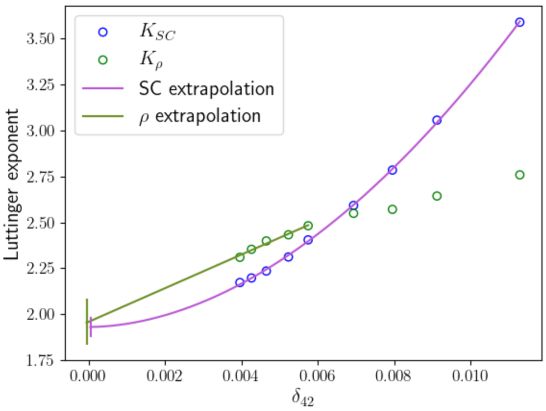

Figure 10: Luttinger exponents of the simple Hubbard model with $t = 1$, $U = 8$, and $f \approx 7/8$ together with their extrapolation and error bars. Only the five most accurate calculations are used to obtain K_ρ for better results.

C. one-band model of $HgBa_2CuO_4$

The one-band model of $\mathrm{HgBa_2CuO_4}$ was investigated as a case study. The parameters of (4) for this cuprate were taken from [40]. The hole occupancies for $N = 4$ are shown in figure 11. This shows that there is charge modulation with a period $\lambda = 4$ along the x-direction, while there is pair-forming along the y-direction.

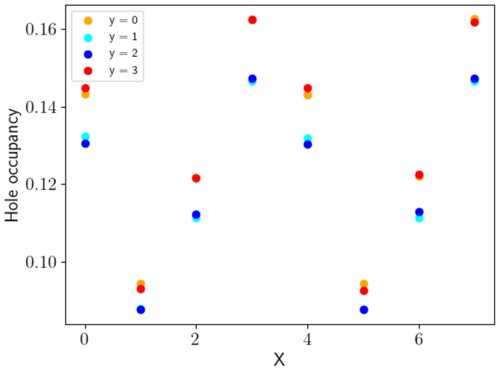

Figure 11: Hole occupancies for the one-band model on a cylinder with $N = 4$ at $f = 7/8$ and $D = 300$

In the same way as for the simple Hubbard model, the density and pair correlation functions are fitted and the corresponding Luttinger exponents are calculated. They are then also extrapolated as a function of δ. Figure 12 shows the result for two values of the electron filling. It is concluded that for $f = 0.8732$, the phase is SC, whereas for $f = 0.9555$ it is a CDW. By varying the electron filling, a phase diagram of the one-band model of $\mathrm{HgBa_2CuO_4}$ can be constructed. This is shown in figure 13.

It is interesting to look at the eigenvalues of the transfer matrix for the various values of the electron filling to see whether there exists a spatial modulation. Figure 14 shows the results. It is seen that these are consistent with filled stripes. This holds for all the values for electron filling that were considered, i.e. $f \in [0.6254, 0.9555]$. These results point to the coexistence of stripe and superconducting order, or to the presence of pair density waves [41].

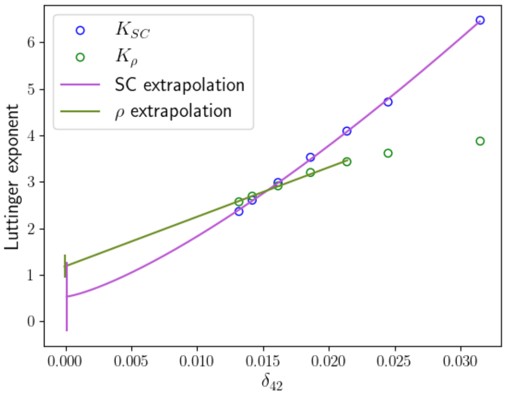

(a) $f = 0.8732$

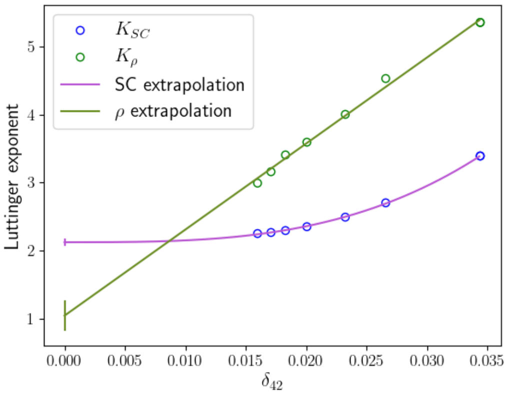

(b) $f = 0.9555$

Figure 12: Luttinger exponents of the one-band model of $\mathrm{HgBa_2CuO_4}$, together with their extrapolation and error bars.

IV. CONCLUSION

Tensor networks were discussed as a reliable way to investigate high-temperature superconductivity in the cuprates. The Hubbard model was introduced, together with possible extensions using further reaching hopping terms and off-site repulsive interactions. The one-band model of the cuprates was presented as a minimal model to investigate high-temperature superconductivity. It was explained how a two-dimensional system can be investigated by placing it around a cylinder, while applying either periodic or spiral boundary conditions. It was described how different calculations at different finite bond dimensions can be used to postulate a scaling hypothesis. This allows us to extrapolate the results to infinite bond dimensions to obtain more accurate results. The pair and charge correlation functions were defined. It was demonstrated that the Luttinger exponents of these correlation functions can be used to determine what the dominant correlations are.

The different methods were benchmarked by looking at the two-dimensional Heisenberg model. It was seen that using large values of the circumference can lead to accurate results on the energy of the two-dimensional system, while smaller systems can show considerable deviations.

The two-dimensional Hubbard model was investigated with an emphasis on the competition between stripe order and superconductivity. For $U/t = 8$ and $f = 7/8$, filled

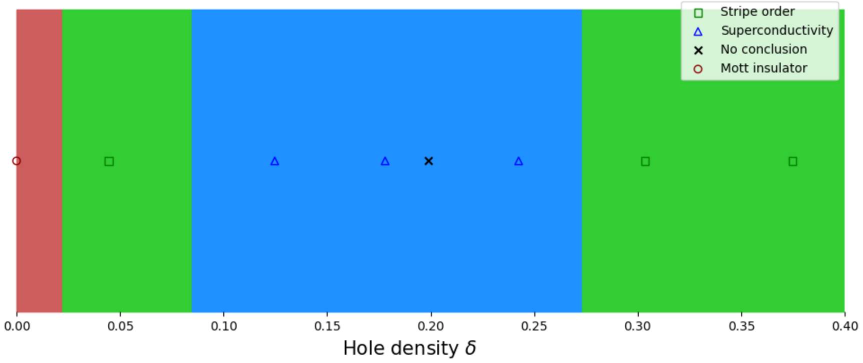

Figure 13: Sketch of the phase diagram of the one-band model of $HgBa_2CuO_4$ in function of the hole density $\delta = 1 - f$. The phase transitions are simply said to occur in the middle between two successive data points.

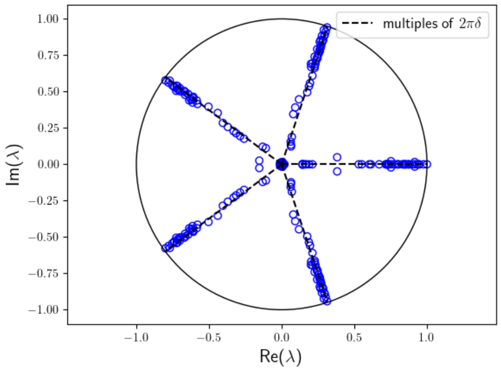

Figure 14: Eigenvalues of the transfer matrix for $f = 0.8010$ for the one-band model of $HgBa_2CuO_4$ and $D = 1460$. The results that are expected for filled stripes are denoted by black dashed lines.

stripes were seen for $N = 2$, whereas half-filled stripes were seen for $N = 4$. The charge and pair correlation functions, together with the corresponding Luttinger exponents, were calculated to determine the ground state phase. It was concluded that bond dimensions $D > 2336$ are needed to resolve their competition.

Lastly, the one-band model of $HgBa_2CuO_4$ was investigated in the same way as the two-dimensional Hubbard model. This showed that the model is superconducting for $\delta \in [\delta_{min}, \delta_{max}]$, where $4.45\% \leq \delta_{min} \leq 12.47\%$ and $24.25\% \leq \delta_{max} \leq 30.36\%$. It was also shown that this superconducting phase can coexist with stripe order. This allowed us to sketch a phase diagram, which shows striking similarities with the experimental phase diagram of the cuprates.

ACKNOWLEDGEMENTS

This work was performed at the Quantum Group and the Center for Molecular Modeling of Ghent University, under the supervision of dr. ir. Laurens Vanderstraeten, Lukas Devos, ir. Quinten Mortier, prof. dr. ir. Frank Verstraete, and prof. dr. ir. Veronique Van Speybroeck. I would like to thank them for their continuing support and guidance throughout the realization of this thesis.

REFERENCES

1. Dirk, v. & Kes, P. *Europhysics News* **63** (2011).
2. Bednorz, J. G. & Muller, K. A. *Z. Phys. B* **64,** 189–193 (1986).
3. Bardeen, J. *et al. Physical Review* **106,** 162–164 (1957).
4. Bardeen, J. *et al. Physical Review* **108,** 1175–1204 (1957).
5. Anderson, P. ISBN: 9780691043654 (Princeton University Press, 1997).
6. Communications, A. Accessed 21 March 2023. 2021.
7. Lieb, E. H. & Wu, F. Y. *Physical Review Letters* **20,** 1445–1448 (1968).
8. LeBlanc, J. P. F. *et al. Physical Review X* **5,** 041041 (2015).
9. Qin, M. *et al. Annual Review of Condensed Matter Physics* **13,** 275–302 (2022).
10. Keimer, B. *et al. Nature (London)* **518** (2015).
11. Greene, R. L. *et al. Annual Review of Condensed Matter Physics* **11,** 213–229 (2020).
12. Proust, C. & Taillefer, L. *Annual Review of Condensed Matter Physics* **10,** 409–429 (2019).
13. Lee, P. A. *et al. Rev. Mod. Phys.* **78,** 17–85 (2006).
14. Aryasetiawan, F. *et al. Physical Review B* **74,** 125106 (2006).
15. Aryasetiawan, F. *et al. Physical Review B* **70** (2004).
16. Pavarini, E. *et al.*, 209–234, Record converted from VDB: 12.11.2012. (Jülich: Forschungszenrum Jülich GmbH Zentralbibliothek, Verlag, 2011).
17. Hirayama, M. *et al. Physical Review B* **87,** 195144 (2013).
18. Imada, M. & Miyake, T. *Journal of the Physical Society of Japan* **79,** 112001 (2010).
19. Faddeev, L. D. 1996.
20. Schmoll, P. *et al. SciPost Physics* **11** (2021).
21. Rakov, M. V. & Weyrauch, M. *Physical Review B* **100** (2019).
22. Arovas, D. P. *et al. Annual Review of Condensed Matter Physics* **13,** 239–274 (2022).
23. Essler, F. *et al. The One-Dimensional Hubbard Model, by Fabian H. L. Essler , Holger Frahm , Frank Göhmann , Andreas Klümper , Vladimir E. Korepin, Cambridge, UK: Cambridge University Press, 2010* (2010).
24. Maier, T. *et al. Rev. Mod. Phys.* **77,** 1027–1080 (2005).
25. Zauner-Stauber, V. *et al. Physical Review B* **97,** 045145 (2018).
26. Vanderstraeten, L. *et al. SciPost Physics Lecture Notes* (2019).
27. Motruk, J. *et al. Physical Review B* **93** (2016).
28. Rams, M. M. *et al. Physical Review X* **8** (2018).
29. Jiang, H.-C. & Devereaux, T. P. *Science* **365,** 1424–1428 (2019).
30. Shen, Y. *et al.* 2023.
31. Dolfi, M. *et al. Physical Review B* **92,** 195139 (2015).
32. Jiang, Y.-F. *et al. Physical Review Research* **2** (2020).
33. Sandvik, A. W. *Physical Review B* **56,** 11678–11690 (1997).
34. Hasik, J. *et al. SciPost Physics* **10** (2021).
35. Vanhecke, B. *et al. Physical Review Letters* **123,** 250604 (2019).
36. Vanhecke, B. *et al. Physical Review Letters* **129** (2022).
37. Xu, H. *et al. Physical Review Research* **4** (2022).
38. Zheng, B.-X. *et al. Science* **358,** 1155–1160 (2017).
39. Xu, H. *et al.* 2023.
40. Hirayama, M. *et al. Physical Review B* **98,** 134501 (2018).
41. Jiang, H.-C. *Physical Review B* **107** (2023).

Table of Contents

List of Figures

List of Tables

List of Algorithms

List of Abbreviations

BCS Bardeen–Cooper–Schrieffer

BO Born-Oppenheimer

CDW Charge Density Wave

DFT Density Functional Theory

(i)DMRG (infinite) Density Matrix Renormalization Group

FF Filling fraction

HF Hartree-Fock

LDA Local Density Approximation

MPO Matrix Product Operator

MPS Matrix Product State(s)

PDW Pair Density Wave

PEPO Projected Entangled Pair Operator

PEPS Projected Entangled Pair State(s)

SDW Spin Density Wave

SVD Singular Value Decomposition

TN Tensor Networks

VUMPS Variational Uniform Matrix Product State

ZRS Zhang-Rice Singlet(s)

List of Symbols

$\boldsymbol{A_C}$ Center site in the mixed gauge

$\boldsymbol{A_L}$ Left-orthonormal form in the mixed gauge

$\boldsymbol{A_R}$ Right-orthonormal form in the mixed gauge

$\boldsymbol{c}$ Annihilation operator

$\boldsymbol{d}$ Hopping parameter of the copper atoms in the one-band or three-band model of the cuprates

$\mathbf{D}$ Bond dimension

$\mathbf{E}$ Energy

$\mathbf{f}$ Electron filling

$\boldsymbol{h^{stag}}$ Staggered magnetic field

$\mathbf{H}$ Hamiltonian

$\mathcal{H}$ Hilbert space

$\mathbf{K}$ Luttinger exponent

$\boldsymbol{m^{stag}}$ Staggered magnetization

$\mathbf{M}$ JordanMpo

$\boldsymbol{n}$ Number operator

$\mathbf{N}$ Circumference of a cylinder of helix OR Size of the system OR Density correlation function

$\boldsymbol{p}$ Hopping parameter of the oxygen atoms in the three-band model of the cuprates

$\mathbf{P}$ Nominator of the filling $f = P/Q$

$\mathbf{q}$ Momentum of the static structure factor

$\mathbf{Q}$ Denominator of the filling $f = P/Q$

$\mathbf{s}$ Structure factor

$\mathbf{S}$ (Von Neumann) Entanglement entropy OR Spin operator

t Parameter of the Hubbard model denoting the hopping term

T Transfer matrix

U Parameter of the Hubbard model denoting the on-site interaction term OR Matrix resulting from SVD

V Parameter of the extended Hubbard model OR Matrix resulting from SVD

w Period of the MPS

$\boldsymbol{\delta}$ Hole density OR error measure for extrapolation OR Kronecker delta

$\boldsymbol{\Delta}$ Parameter of the Heisenberg model OR Parameter of the one-band and three-band model of the cuprates OR Operator in the definition of the superconducting pair-field correlator

$\boldsymbol{\epsilon}$ Related to the modulus of the eigenvalues of the transfer matrix

$\boldsymbol{\lambda}$ Square of a singular value OR Eigenvalues of the transfer matrix OR Wavelength of a CDW

$\boldsymbol{\Lambda}$ Lattice

$\boldsymbol{\mu}$ Chemical potential

$\boldsymbol{\xi}$ Correlation length

$\boldsymbol{\rho}$ Electron density based on the wave function OR density operator

$\boldsymbol{\sigma}$ Pauli sigma matrix OR spin

$\boldsymbol{\Sigma}$ Singular value OR Matrix resulting from SVD

$\boldsymbol{\phi}$ Wave function

$\boldsymbol{\Phi}$ Superconducting correlation function

$\boldsymbol{\psi}$ Wave function OR State vector

1

Introduction

Superconductors are materials that have a vanishing resistance below a certain critical temperature. They can then conduct current without energy loss, a property that would be very useful in modern technology. Furthermore, the lack of energy loss also means that very high currents can be conducted. This technology is being used in certain high-tech applications like CERN and ITER, where high magnetic fields are needed. However, the problem with all these superconductors is that the critical temperature is significantly colder than room temperature, thus needing coolants like liquid nitrogen or helium. The holy grail in the field of superconductivity is hence to find a material that remains superconducting up to room temperature and at ambient pressure. A class of materials that currently shows the highest critical temperature are the cuprates, consisting of layers of copper and oxide. The mechanism behind this high-temperature superconductivity is different from the Bardeen–Cooper–Schrieffer (BCS) theory that applies to other superconductors, however, and is still not fully understood. To get more insight into this mechanism, the (electronic) structure of the cuprates needs to be investigated. This is a quantum many-body problem in which many of the electrons in the cuprate interact strongly with each other, and is thus far from a trivial task.

The quantum many-body problem has been a central problem in physics for a long time. The main problem in solving it is the fact that the Hilbert space associated with it scales exponentially in the system size. Since it is generally infeasible to find the ground state in such a large Hilbert space, the question arises whether the ground state wave function could be approximated or described in a condensed way. This condensed description should have far fewer parameters to be able to find it classically, while still allowing measurable quantities to be calculated accurately and efficiently from it. This ground state can then be found by a variational method, where the full Hilbert space is approximated by a low-dimensional manifold in which the energy is minimized. If the ground state in the full Hilbert space is well approximated by the one in the variational manifold, the problem is solved.

One of the first variational techniques in many-body physics was the Hartree-Fock (HF) method [1, 2]. Here, the Born-Oppenheimer (BO) approximation is assumed, which treats the motions of the nuclei and the electrons separately [2, 3, 4, 5]. Furthermore, HF assumes that the states of the variational manifold are single Slater determinants, which are fully antisymmetric product-like wave functions. Being a product state, the electron correlations are thus neglected. Because of these approximations, the properties derived from the HF formalism are in many cases not accurate enough.

An improvement on HF came with the development of density functional theory (DFT) [5, 6, 7, 8]. DFT tries to solve the problem of the exponentially large electronic Hilbert space by not looking for the wave function, but by looking for the electron density. In a system with N electrons, each electron has three degrees of freedom, and the full wavefunction is thus a function of $3N$ parameters. Since the electron density is only a function of three spatial directions, this serves as a huge simplification of the complexity of the solution. Due to the Hohenberg-Kohn theorems, DFT is formally exact, and the only approximations that need to be made are due to the unknown exchange-correlation functional. This proves that condensed ways of describing many-body wave functions do not necessarily introduce errors [5, 6, 7, 8].

DFT turned out to be a big improvement on HF, mostly because it incorporated electron correlations. However, because of the problem mentioned above, namely the fact that DFT relies on approximations of the exchange-correlation functional, these correlations are still not taken into account accurately. This explains why materials in which electron correlations are amongst the dominant factors, such as cuprates, are not well described by DFT.

The problem with both HF and DFT is that they approximate the true electron-electron interactions with average potentials [1, 2, 5, 8]. Electron entanglement is thus not well described. The problem is the one of locality. Electrons and their interactions are inherently local, whereas average potentials act at a distance and are defined in such a way as to mimic these local interactions. A way to amend this is to introduce objects in a local Hilbert space, which carry additional entanglement degrees of freedom (DOF), which can describe the interactions between these local objects.

That is where tensor networks (TN) come in [9]. Here, the full wave function is described by a network of interconnected tensors. These will have both physical and entanglement DOF, thus connecting the two. They will correspond to a physical and virtual Hilbert space, respectively. The entanglement will be defined between two neighboring tensors, but will nevertheless be able to carry long-range correlations. The set of states that can be described by TN is the variational manifold contained in the much bigger Hilbert space. They will obey an area law for entanglement and can be efficiently represented with TN [10, 11, 12, 13]. Finding the ground state tensor within this manifold relies on efficient variational algorithms developed over the years, such as (infinite) Density Matrix Renormalization Group ((i)DMRG) [14, 15], Corner Transfer Matrix Renormalization Group (CTMRG) [16, 17], and Variational Uniform Matrix Product States (VUMPS) [18, 19]. Both the local and global properties of the ground state of the system can then be calculated based only on this tensor.

TN can not only be useful for materials science, but have also helped the description of more fundamental 1D and 2D systems, where entanglement has prohibited mean field methods to give accurate results. The monogamy property of entanglement is an important notion in this regard [9, 20, 21]. It says that the more entanglement a site has with a second site, the less entanglement it can have with a third site. As a result, the more neighbors a site has, the less entanglement it can have with each neighbor. Entanglement thus has a bigger influence in 1D and 2D systems than in 3D, and mean field methods are especially problematic in 1D and 2D. There, it was discovered that, under the influence of entanglement, many different phases can exist, like superconductivity, Néel order, etc. The classification of these phases can prove useful in the current discussion, since it can give qualitative information on the system under investigation. The emergence and competition of the different phases, together with their phase transitions, can give new insights into the fundamental mechanisms behind e.g. high-temperature superconductivity.

DFT is a very mature theory that can describe 3D materials to sometimes impressive accuracy, while suffering from electron-electron correlations. TN, on the other hand, can handle entanglement well, but most of the research is being done on 1D and 2D toy models and not on 3D systems of real materials, due to the computational complexity. One could ask if these two seemingly very different descriptions of reality can be complemented, and thus whether a framework can be devised that exploits the advantages of each description. That is the goal of the project of which this thesis is a part.

Luckily for us, the strong electron correlations because of which DFT fails, occur only for a few states in a material, not per se for all states. Methods exist that can devise effective Hamiltonians describing these few states, taking into account the interactions between these states, as well as the interactions with the neglected states [8]. This is a procedure called downfolding and this will be a very important part of the project. Downfolding is based on the theory of renormalization group [8, 22], and some of the approaches to make the calculations computationally feasible are constrained local-density approximation (cLDA) [23, 24, 25, 26], linear response approach [27], constrained random phase approximation (cRPA) [23, 28, 29], and constrained GW approximation (cGW) [30, 8].

This thesis, on the other hand, tries to solve these low-energy effective Hamiltonians for the strongly interacting states, which can be done by TN. For this, the physical Hilbert space of the tensors will be based on the occupancy of localized orbitals centered on the atoms, namely the maximally localized Wannier functions (MLWF) [8]. Using this basis allows for a lattice description of the system with local, finite-dimensional Hilbert spaces, which does not have to take the underlying continuous system into account explicitly. The only things that need to be known are the structure of the lattice and the effective Hamiltonian defined on it.

I

Theory

2

From DFT to effective Hamiltonians

> ”The fundamental laws necessary for the mathematical treatment of large parts of physics and the whole of chemistry are thus fully known, and the difficulty lies only in the fact that application of these laws leads to equations that are too complex to be solved.”
>
> *Paul Dirac (Nobel Prize 1933)*

A lot of effort in the 20th and 21st centuries has been devoted to finding an accurate description of the electronic structure of materials. Solving these quantum many-body systems, consisting of nuclei and electrons, has proven to be far from trivial. The time-independent Schrödinger equation for a quantum many-body system can be written down as [31]

$$\hat{H}\psi(\{\vec{R}_I\}_{I=1}^{P}, \{x_i\}_{i=1}^{N}) = E\psi(\{\vec{R}_I\}_{I=1}^{P}, \{x_i\}_{i=1}^{N}) \tag{2.1}$$

Where $\hat{H}$ is the Hamiltonian of the model, $\vec{R}_I$ are the positions of the nuclei, x_i are the quantum numbers of the electrons ($x_i = (\vec{r}_i, s_i)$, with $\vec{r}_i$ the position and s_i the spin of the electron). There are P nuclei and N electrons. ψ is the many-body wave function and the sought-after quantity, since all measurable quantities can be derived from it.

The molecular Hamiltonian $\hat{H}$ in atomic units is given by [8]

$$\hat{H} = -\sum_{i=1}^{N}\frac{1}{2}\vec{\nabla}_i^2 - \sum_{I=1}^{P}\frac{1}{2M_I}\vec{\nabla}_I^2 + \frac{1}{2}\sum_{i=1}^{N}\sum_{\substack{j=1\\ j\neq i}}^{N}\frac{1}{|\vec{r}_i - \vec{r}_j|} - \sum_{i=1}^{N}\sum_{I=1}^{P}\frac{Z_I}{|\vec{r}_i - \vec{R}_I|} + \frac{1}{2}\sum_{I=1}^{P}\sum_{\substack{J=1\\ J\neq I}}^{P}\frac{Z_I Z_J}{|\vec{R}_J - \vec{R}_I|} \tag{2.2}$$

This Hamiltonian includes the kinetic energy of the electrons ($\hat{T}_e$) and the nuclei ($\hat{T}_N$), and the potential energy due to the Coulomb interaction between the electrons ($\hat{V}_{ee}$), the nuclei and electrons ($\hat{V}_{eN}$), and the nuclei ($\hat{V}_{NN}$).

Solving (2.1) has been a long-standing problem in physics. Due to the exponentially large number of degrees of freedom, the only viable way of finding an appropriate solution is by means of approximations. (2.1) itself is already an approximate Hamiltonian, since spin effects are neglected and the nuclei are considered to be point particles. However, even the Schrödinger equation with this simpler Hamiltonian remains too complex to be solved. One of the most famous and widely used approximations in this regard is the BO approximation, which assumes that the wave function of the electrons and the nuclei can be treated separately. This approach consists of first solving the Schrödinger equation of the electrons for a fixed set of nuclear coordinates, yielding electronic wave functions ϕ_n. This assumes the nuclei to be fixed in place, called the clamped nuclei approximation, which can be justified by their higher mass and thus lower speeds [32, 33]. The total wave function ψ_m can then be written as a linear combination of electronic wave functions with expansion coefficients χ_{nm} depending on the nuclear coordinates.

$$\psi_m(\{\vec{R}_I\}_{I=1}^P, \{x_i\}_{i=1}^N) = \sum_n \chi_{nm}(\{\vec{R}_I\}_{I=1}^P)\, \phi_n(\{\vec{R}_I\}_{I=1}^P, \{x_i\}_{i=1}^N) \tag{2.3}$$

In the BO approximation, $\hat{T}_N$ can be neglected since the nuclei are assumed to be fixed in place and $\hat{V}_{NN}$ is a constant depending on the nuclear coordinates. $\hat{V}_{eN}$ can be considered as an external potential for the electrons v representing the electron-nuclei interactions. With these approximations, the Hamiltonian governing the motion of the electrons reduces to

$$\hat{H}_e = -\sum_{i=1}^N \frac{1}{2}\vec{\nabla}_i^2 + \frac{1}{2}\sum_{i=1}^N \sum_{\substack{j=1 \\ j\neq i}}^N \frac{1}{|\vec{r_i} - \vec{r_j}|} + \sum_{i=1}^N v(\vec{r_i}) \tag{2.4}$$

The Schrödinger equation based on this Hamiltonian can be solved for each set of nuclear coordinates. This yields the electronic energies $U_n^{BO}(\{\vec{R}_I\}_{I=1}^P)$ and electronic wave functions $\phi_n(\{\vec{R}_I\}_{I=1}^P, \{x_i\}_{i=1}^N)$. The electronic energies U_n^{BO} for all nuclear configurations form the BO surfaces.

Afterwards, on each BO surface U_n^{BO}, the nuclear eigenvalue equation can be solved, with the nuclear Hamiltonian $\hat{H}_N$.

$$\hat{H}_N = -\sum_{I=1}^P \frac{1}{2M_I}\vec{\nabla}_I^2 + U_n^{BO}(\{\vec{R}_I\}_{I=1}^P) \tag{2.5}$$

This yields a set of nuclear energy levels E_m^{BO} and nuclear wave functions $\chi_{nm}(\{\vec{R}_I\}_{I=1}^P)$. These are the expansion coefficients from (2.3) [32].

The problem is reduced to solving the Schrödinger equation with the electronic Hamiltonian of (2.4). Because of this simplification, many theories try to solve the electronic structure problem starting from the BO approximation. The first of these, and also the most simple, is called the HF formalism [1, 2]. HF assumes a non-interacting system, in which the electrons occupy single-particle orbitals ϕ_m. The electronic wave function will then be a product state. However, electrons are fermions and have to obey the Pauli-exclusion principle [34]. To accommodate for this, the wave function is written down as a Slater determinant, i.e. [35]

$$\psi^{HF}\left(\{x_i\}_{i=1}^N\right) = \frac{1}{\sqrt{N!}}\begin{vmatrix} \phi_1(x_1) & \phi_1(x_2) & \cdots & \phi_1(x_N) \\ \phi_2(x_1) & \phi_2(x_2) & \cdots & \phi_2(x_N) \\ \vdots & \vdots & \ddots & \vdots \\ \phi_N(x_1) & \phi_N(x_2) & \cdots & \phi_N(x_N) \end{vmatrix} = \begin{vmatrix} \phi_1 & \phi_2 & \cdots & \phi_N \end{vmatrix} \tag{2.6}$$

The Slater determinants fully neglect the entanglement present in the system [1].

Another important theory is DFT [5, 6, 7, 8]. Here, instead of looking at the $3N$-dimensional wave function ψ, the total ground state electronic density ρ is searched for, which is only 3-dimensional.

$$\rho(\vec{r}) = N \sum_{s_1,\cdots,s_N} \int \cdots \int \psi^*(\vec{r}, s_1, \vec{r}_2, s_2, \cdots, \vec{r}_N, s_N)\psi(\vec{r}, s_1, \vec{r}_2, s_2, \cdots, \vec{r}_N, s_N) d\vec{r}_2 \cdots d\vec{r}_N \tag{2.7}$$

---

[1] apart from the exchange interaction

Due to the Hohenberg-Kohm theorem, the ground state density ρ of the Hamiltonian $\vec{H}_e$ of (2.4) is completely determined by the external potential v, and vice versa [6, 7].

Inspired by the Hohenberg-Kohm theorems, DFT does not look to the interacting system, but instead considers a non-interacting system with a special effective external potential v_{eff}. This external potential is chosen such that the ground state density of the non-interacting system is equal to the ground state density of the interacting system. To this end, the effective potential needs to be defined as

$$v_{eff}(\vec{r}) = v(\vec{r}) + \int \frac{\rho(\vec{r'})d\vec{r'}}{|\vec{r} - \vec{r'}|} + \frac{\partial E_{XC}}{\partial \rho} \tag{2.8}$$

with E_{XC} the exchange-correlation functional [5]. Since this functional is unknown, one is forced to look for approximations. These range from very simple functionals such as in the local density approximation (LDA), where the functional only depends on the local value of the density, to very complicated functionals that take into account more properties at the expense of a higher computational cost [5].

2.1 Downfolding

DFT has been a success in describing most materials, but fails in describing systems with strongly correlated electrons [36]. Luckily, most electrons in strongly correlated materials are strongly bound to their nuclei and can be approximated fairly well using DFT, as they show little correlation. It thus makes sense to recalculate the properties of the other electrons with methods that can take into account correlation, while keeping the DFT results for the strongly bound electrons. This separates the full Hilbert space in a low-energy and a high-energy subspace, corresponding to the strongly and weakly correlated electrons, respectively. The low-energy subspace typically consists of electrons from partially filled d or f-orbitals. This low-energy subspace can be described by an effective Hamiltonian which takes interactions between multiple low-energy electrons into account completely, but only takes interactions between low-energy and high-energy electrons into account perturbatively. The advantage of this approach is that the low-energy subspace is much smaller, thus making more accurate and more computationally demanding methods feasible.

A possible effective Hamiltonian is the widely studied Hubbard model [37, 38, 39, 40]. This has been proposed as the most simple model that can encapsulate the rich physics of the cuprates. It consists of a Hubbard U term (interaction energy) between electrons on the same site and a hopping t term (kinetic energy) that describes the hopping of electrons to a neighboring site. It is defined as [37, 38, 39, 40]

$$H = -\sum_{i,j\in\Lambda} \sum_{\sigma} t_{ij} \left(c^{\dagger}_{i\sigma} c_{j\sigma} + c^{\dagger}_{j\sigma} c_{i\sigma} \right) + \sum_{i\in\Lambda} U_i c^{\dagger}_{i\uparrow} c^{\dagger}_{i\downarrow} c_{i\downarrow} c_{i\uparrow} \tag{2.9}$$

i and j denote sites on a lattice Λ. The sites have an interaction strength U_i and sites i and j interact with a hopping term t_{ij}. $c^{\dagger}_{i\sigma}$ and $c_{i\sigma}$ are respectively the creation and annihilation operators for the state with quantum numbers i, the site number, and σ, the spin. The basis states of this lattice should be chosen such that the overlap between orbitals that are far away is minimal. This will reduce the number of hopping terms that reach further than nearest neighbors in order to accurately describe the system. The most widely used orbitals for this are the so-called maximally localized Wannier functions [29].

Obtaining such a low-energy model and its parameters from a calculation (e.g. using DFT) using the full Hilbert space is called downfolding. Even though this effective model is only defined for the low-energy subspace, the downfolding procedure can not neglect the presence of the weakly correlated electrons, as they can cause important corrections to the parameters of the model. To this extent, the downfolding of the full Hilbert space to the low-energy subspace is a general approach to capture the screening effects of the high-energy electrons. These screening effects are in fact the renormalization effects (similar to the Wilson renormalization group) and can be derived using different approximations [8].

One of the possible ways to take into account correlation is the LDA + U approach. Here, the Hubbard U term is considered to be a correction term added to the non-interacting Hamiltonian for the strongly correlated electrons, while the other electrons are described within the theory of LDA. This way, the Hamiltonian can be rewritten as [25, 26]

$$\begin{aligned} \hat{H} &= \hat{H}_{LDA} + \Delta\hat{H} \\ &= \hat{H}_{LDA} + \frac{1}{2}U \sum_{i,\mu\neq\nu} n_{i,\mu}n_{i,\nu} - \hat{H}_{DC} \end{aligned} \tag{2.10}$$

where U is the Hubbard U term, $n_{i,\mu}$ is the number operator of orbital μ on site i, $\hat{H}_{LDA}$ is the non-interacting Hamiltonian within the LDA framework, and $\hat{H}_{DC}$ is a term that contains possible double counting of the Coulomb interaction.

Within the LDA + U approach, a way of deriving the Hubbard U parameter is using the constrained LDA approximation (cLDA). cDLA argues that the Hubbard U parameter between two orbitals can be calculated as the energy cost of moving an electron from one orbital to the other [23, 24, 25, 26].

$$U_{ij} = E[n_i + 1, n_j - 1] - E[n_i, n_j] \tag{2.11}$$

which, in the limit of continuous and large variables, reduces to

$$U_{ij} = \frac{\partial^2 E}{\partial n_i \partial n_j}|_{n_i+n_j=constant} \tag{2.12}$$

A more accurate method is the so-called constrained random phase approximation (cRPA). While cLDA only screens the Coulomb interaction between high-energy electrons, cRPA screens the interaction between high-energy and low-energy electrons as well. Constrained RPA can be used to calculate the effective interaction parameters of a Hubbard model and is more advanced than cLDA [23, 28, 29].

Once the parameters of the Hubbard model are known for a certain material, it can be solved by TN. The resulting ground state can be used to recalculate some of the properties that DFT already calculated, where it is expected that the new results will be more accurate. This procedure is shown in figure 2.1. This thesis will assume that a downfolding procedure has been performed and will start from a given effective Hamiltonian. The next chapters will give a detailed description of how the ground state of a Hamiltonian can be found using TN.

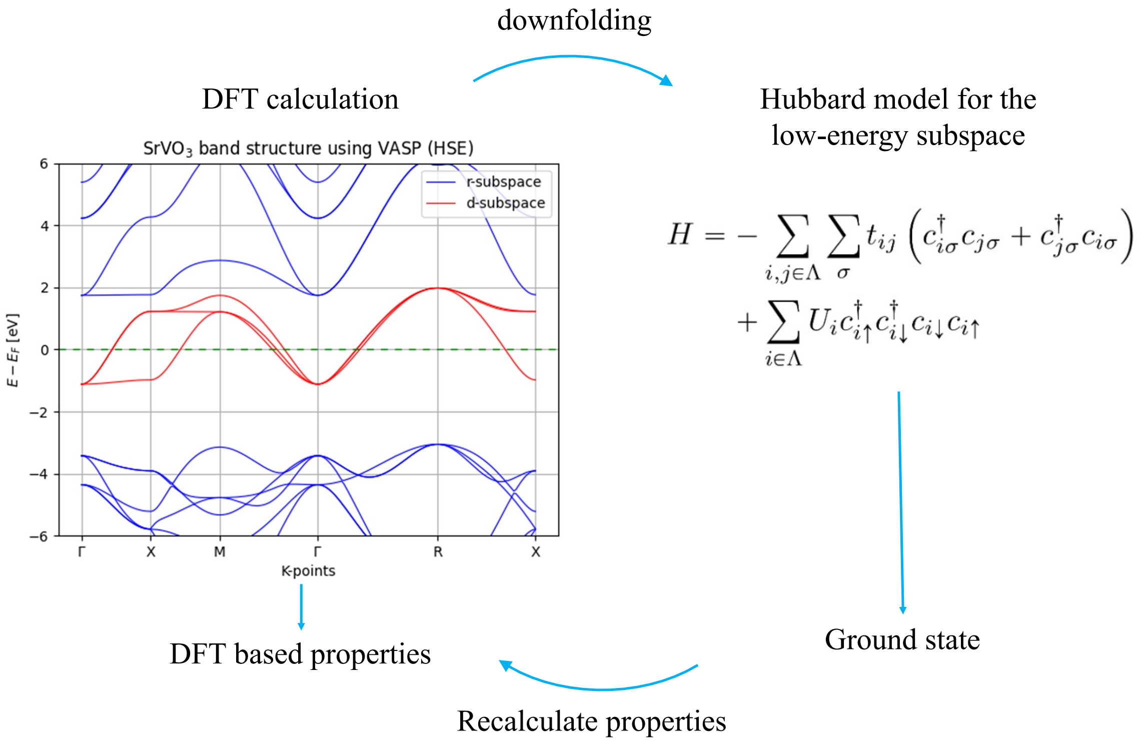

$$H = -\sum_{i,j\in\Lambda}\sum_{\sigma} t_{ij}\left(c^\dagger_{i\sigma}c_{j\sigma} + c^\dagger_{j\sigma}c_{i\sigma}\right) + \sum_{i\in\Lambda} U_i c^\dagger_{i\uparrow}c^\dagger_{i\downarrow}c_{i\downarrow}c_{i\uparrow}$$

Figure 2.1: The general procedure of downfolding to an effective Hamiltonian and solving it with TN. The figure was taken from [41].

3 TN Language

3.1 Introduction

By the discussion of the previous chapter, the problem is reduced to finding the ground and excited states of the effective Hamiltonian acting on a lattice, in which the electron correlations are more pronounced. However, we have not found a way yet to accurately describe these correlations. We will start the discussion by noting that Hamiltonians act on a Hilbert space which has a tensor product structure. If each local Hilbert space has a dimension d, the total Hilbert space for a system of size N has a dimension d^N, thus scaling exponentially in the system size. This is the curse of dimensionality that makes these systems so hard to solve.

The key point to move forward is now to realize that most of the Hamiltonians we are interested in are very special, since they are local. This means that they are the sum of terms that act on at most k bodies that occupy a finite spatially connected region, with k independent of the size of the system. If the system starts in a random initial state and such a local Hamiltonian is used in a time evolution, the many-body states that can be generated in a reasonable timescale [2] occupy only a tiny subset of measure zero of the total exponentially large Hilbert space [42, 43]. This causes these Hamiltonians and their ground states to have special properties. Furthermore, most Hamiltonians are gapped. This means that the energy difference between the ground and first excited states does not vanish in the thermodynamic limit ($N \to \infty$). In 1D, it was proven that the ground states of local, gapped Hamiltonians obey a so-called area law for the entanglement [10, 11, 12], which means that they have very little entanglement with respect to what is possible in the total Hilbert space. Specifically, the entanglement between a certain region and its complement scales with the boundary of that region, not with its volume. It is this area law that will resolve the curse of dimensionality.

This is all the result of the ground states having extremal local properties. They are obtained by minimizing the energy, an inherent local property, and the global properties only emerge to allow for this local optimization. Therefore, an efficient characterization is needed for the states that are allowed by these two-body operators, which for fermions is called the N-representability problem [44]. In that regard, take a look at the following quote from Richard Feynmann.

””

Now in field theory, what’s going on over here and what’s going on over there and all over space is more or less the same. What do we have to keep track in our functional of all things going on over there while we are looking at the things that are going on over here? It’s really quite insane actually: we are trying to find the energy by taking the expectation of an operator which is located here and we present ourselves with a functional which is dependent on everything all over the map. That’s something wrong. Maybe there is some way to surround the object, or the region where we want to calculate things, by a surface and describe what things are coming in across the surface. It tells us everything that’s going on outside. I think it should be possible some day to describe field theory in some other way than with wave functions and amplitudes. It might be something like the density matrices where you concentrate on quantities in a given locality and in order to start to talk about it you don’t immediately have to talk about what’s going on everywhere else. ””

---

[2] A reasonable timescale in this regard is a time scale that scales at most polynomially in the system size.

This is precisely what TN try to do. They try to make smart use of this little entanglement as allowed by the Hamiltonians in a local way, by defining tensors on each local Hilbert space that generate a state that satisfies an area law. A key insight is that they do not try to see the interactions as a perturbation on a non-interacting theory, but as relevant degrees of freedom [45, 14].

Furthermore, the locality of the Hamiltonian forces the low-lying excited states to be local perturbations on the ground state. These perturbations can be interpreted as particles [46], provided the system is gapped and the excitations are isolated. The ground state tensor thus gives information on the low-lying spectrum [47, 48]. This is in sharp contrast with a typical eigenvalue problem, where the knowledge of one eigenvector does not give information on another.

The very explicit way of taking entanglement into account will be explained by the definition, but can already be hinted at by considering the singular value decomposition (SVD) in 1D, a crucial aspect in both theoretical and computational considerations.

In essence, the ground state acts on the total Hilbert space, which is a tensor product over all local Hilbert spaces $\mathcal{H}_i$.

$$\mathcal{H} = \bigotimes_i \mathcal{H}_i \tag{3.1}$$

Now we will consider a bipartition, splitting the total Hilbert space in a left and right Hilbert space, called $\mathcal{H}_L$ and $\mathcal{H}_R$, respectively. Thus, $\mathcal{H} = \mathcal{H}_L \otimes \mathcal{H}_R$. We would like to quantify the amount of entanglement between the left and right part. The ground state can be written as

$$|\psi\rangle = \sum_{kl} C_{kl} \, |k\rangle_L \, |l\rangle_R \tag{3.2}$$

with $\{|k\rangle_L\}$ and $\{|l\rangle_R\}$ orthonormal bases for $\mathcal{H}_L$ and $\mathcal{H}_R$, respectively. The SVD of the matrix C with elements C_{kl} yields the matrices U, Σ, and V, with

$$|\psi\rangle = \sum_{klm} U_{km} \Sigma_{mm} V^\dagger_{ml} \, |k\rangle_L \, |l\rangle_R \tag{3.3}$$

The elements of the diagonal matrix Σ are always real and positive. They are called the singular values of ψ, and are denoted as Σ_{mm} or $\sqrt{\lambda_m}$. The tensors L and R are defined as

$$\begin{aligned} |L\rangle_m &= \sum_k U_{km} \Sigma_{mm} \, |k\rangle_L \\ |R\rangle_m &= \sum_l V^\dagger_{ml} \, |l\rangle_R \end{aligned} \tag{3.4}$$

This corresponds to a change in orthonormal basis, since the matrices U and V are unitary. With χ the number of singular values, (3.3) can be rewritten as

$$|\psi\rangle = \sum_{m=1}^{\chi} |L\rangle_m \, |R\rangle_m \tag{3.5}$$

which is a tensor contraction between the left and the right part. This is diagrammatically shown in figure 3.1.

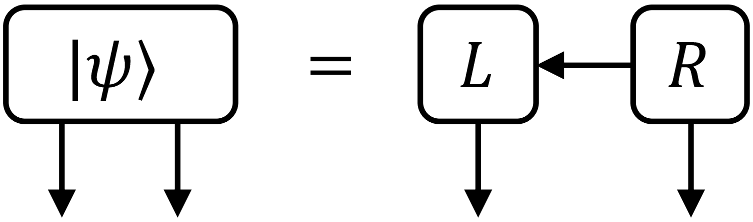

Figure 3.1: Diagrammatic representation of (3.5)

Doing this recursively over the physical Hilbert spaces, the full state $|\psi\rangle$ can be written as the tensor contraction of local tensors, called the Matrix Product State (MPS). Both states and operators can be written in this graphical network of tensor contractions, giving tensor networks (TN) their name.

This construction can be used to quantify the electron entanglement present in the state, by defining an entanglement entropy [49, 50]. Entropy is always positive, and will be 0 for a product state, as explained below.

One such measure is the Von Neumann entropy S, based on the pure density operator ρ

$$\rho = |\psi\rangle\langle\psi| \tag{3.6}$$

and the reduced density operator ρ_i of a subsystem i, obtained by tracing out the relevant degrees of freedom.

$$\begin{aligned} \rho_i &= \mathrm{Tr}_i\left(\rho\right) \\ &= \mathrm{Tr}_i\left(|\psi\rangle\langle\psi|\right) \end{aligned} \tag{3.7}$$

It is defined as [51, 52].

$$S(\rho) = -\mathrm{Tr}\left(\rho_i \log_2 \rho_i\right) \tag{3.8}$$

Other measures of entanglement exist, such as the Renyi entropy R [53] [54]

$$R_\alpha(\rho) = \frac{1}{1-\alpha}\log_2\left(\mathrm{Tr}(\rho_i)\right) \tag{3.9}$$

which reduces to the Von Neumann entropy in the limit $\alpha \to 1$.

The meaning of the entanglement entropy is best illustrated by two examples. The first one is a pure or separable state, the other is a mixed state, in this case a Bell state. They are given for a system comprised of two subsystems, A and B. Each separate subsystem can be in state $|0\rangle$ or $|1\rangle$.

$$\begin{aligned} |\psi\rangle_{pure} &= \left(\frac{|0\rangle_A + |1\rangle_A}{\sqrt{2}}\right)|0\rangle_B \\ |\psi\rangle_{mixed} &= \frac{|0\rangle_A |0\rangle_B + |1\rangle_A |1\rangle_B}{\sqrt{2}} \end{aligned} \tag{3.10}$$

Calculating the Von Neumann entropy for both states, we see that

$$\begin{aligned} S(|\psi\rangle_{pure}) &= 0 \\ S(|\psi\rangle_{mixed}) &= 1 \end{aligned} \tag{3.11}$$

From these examples, it can be seen why the entanglement entropy is considered to be a measure of the uncertainty in the system. For a separable state, the state of subsystem B is completely certain. It is always in the state $|0\rangle_B$, regardless of a measurement on system A [3]. There is thus no entanglement between the subsystems and their entropy is 0. For a mixed state, however, it is not known in which state system B is, unless a measurement on system A is performed. Now there is uncertainty, and the entropy is strictly positive. It can be proven that for the Bell state given in the example, the entropy is maximal.

These measures of entropy can be calculated with the SVD. Namely, if the Hilbert space can be written as $\mathcal{H} = \mathcal{H}_L \otimes \mathcal{H}_R$, then the SVD yields [4]

$$|\psi\rangle = \sum_{m=1}^{\chi} \Sigma_{mm} |L\rangle_m |R\rangle_m \tag{3.12}$$

The reduced density matrix can then be rewritten.

$$\begin{aligned} \rho_R &= \mathrm{Tr}_R(\rho) \\ &= \mathrm{Tr}_R\left(\sum_{m,m'} \Sigma_{mm}\Sigma_{m'm'} |L\rangle_m |R\rangle_m \langle R|_{m'} \langle L|_{m'}\right) \\ &= \sum_m \Sigma_{mm}^2 |L\rangle_m \langle L|_m \end{aligned} \tag{3.13}$$

Now the Von Neumann entropy can be written, with $\Sigma_{mm}^2 = \lambda_m$, as

$$\begin{aligned} S &= -\sum_m \Sigma_{mm}^2 \log_2(\Sigma_{mm}^2) \\ &= -\sum_m \lambda_m \log_2(\lambda_m) \end{aligned} \tag{3.14}$$

---

[3] The same holds for system A

[4] For the clarity of this calculation, Σ_{mm} is here not included in the definition of L, as is the case for (3.4) and (3.5)

Normalisation dictates

$$\sum_m \lambda_m = 1 \tag{3.15}$$

From this, it follows that entropy is always positive and that the maximum is obtained when all λ_m have the same value.

It is this entropy that is bounded in an MPS by an area law [10, 9].

$$S \ \propto \ \partial A \tag{3.16}$$

where ∂A is the area of the boundary between the subsystem i and its complement.

It can be seen that the full spectrum, consisting of the values λ_m, can give much more complete information on the entanglement than the entanglement entropy, which is just a single number [47]. Each λ_m will contribute to the entanglement. They are thus the entanglement degrees of freedom from before. A very important variable will therefore be the number of singular values, χ. This is equal to the dimension of the virtual Hilbert space over which the contraction occurs. Right now, no approximation is yet made, since the SVD is exact, and the total Hilbert space of states obeying an area law can be represented. Since it is expected that the lowest singular values contribute less to the entanglement, they can be neglected, and only the highest D singular values are retained. This D is called the bond dimension and quantifies the maximum amount of entanglement between two regions that can be described. In 1D, the area of the boundary is just a constant. It can be seen from (3.14) that the maximum entropy in this case is

$$\begin{aligned} S_{max} &= -\sum_{m=1}^{D} \frac{1}{D} \log_2(\frac{1}{D}) \\ &= \log_2(D) \end{aligned} \tag{3.17}$$

The area law thus becomes

$$S_{max} \ \propto \ \log(D) \tag{3.18}$$

This is the approximation that gives TN its power, since it incorporates the entanglement as degrees of freedom (the singular values), and can describe the ground state wave function in local tensors with only dD^2 parameters. In general, choosing $D = 1$ means keeping only the highest λ_m. This is equivalent to approximating the ground state as a product state, which is a mean-field method reminiscent of Slater determinants in HF. Choosing $D > 1$ will introduce entanglement properties [45]. In the limit of $D \to \infty$, all states can be described [9, 55].

The MPS with bond dimension D then form the variational manifold in which the optimization occurs. Over the years, many powerful algorithms have been developed, such as DMRG and VUMPS. The reason why these work so well, is because the ground states of gapped Hamiltonians are well approximated by MPS [55], because of their little entanglement. More precisely, the presence of a gap and the resulting little entanglement causes the complexity of finding the ground state to drop from QMA-complete, which is the quantum analog of NP, to P, removing the exponential barrier [56, 57]. The ground state of gapless Hamiltonians can also be well approximated, by the postulation of a scaling regime, which will be explained in section 4.3. Furthermore, the relevant properties, expressed as expectation values, can be efficiently and exactly retrieved from the MPS description. MPS can be generalized to higher dimensions, in which case it is called a Projected Entangled Pair State (PEPS). Here, the calculation of expectation values cannot be done both exactly and efficiently, but efficient approximations exist [58]. Before going into the details of these algorithms and approximations, we will first define PEPS and MPS and give some general properties in the following sections.

3.2 Definitions and general remarks [5]

Consider a lattice consisting of a set of vertices $V = 1, 2, ..., N$ and a set of edges E connecting them. Thus $\forall e \in E : e = (i, j), i, j \in V$. Each vertex v has a local, physical Hilbert space $\mathcal{H}_v = \mathbb{C}^{d_v}$ with dimension d_v. S_v will be defined as the set of vertices that are connected to v, i.e.

$$S_v = \{w \in V : (v, w) \in E\} \tag{3.19}$$

with $z_v = |S_v|$, the coordination number. It is implicitly assumed that $\forall v, w \in V : (v, w) = (w, v)$.

The goal will be to define the total Hilbert space $\mathcal{H}$ of the lattice as $\bigotimes_{v=1}^{N} \mathcal{H}_v$. To achieve this, on each vertex, a number of auxiliary states will be defined, one for each edge connected to the vertex. More explicitly, for each $i \in V$ and $j \in S_i$, the ancilla will be denoted as $a_{i,j}$. It has a Hilbert space $\mathbb{C}^{D_{i,j}}$, where $D_{i,j} = D_{j,i} \in \mathbb{N}$, the local bond dimension. For the auxiliary states, the notation $|*)$ will be used, as opposed to $|*\rangle$ for physical states. Each auxiliary state will be maximally entangled with its neighbor. i.e.

$$|\phi)_{i,j} = \sum_{n=1}^{D_{i,j}} |n)_{a_{i,j}} \otimes |n)_{a_{j,i}} \tag{3.20}$$

where $|\phi)_{i,j}$ denotes the maximally entangled pair state living on the edge (i, j) and where the $\{|n)_{a_{i,j}}\}$ form an orthonormal basis for the ancillae on edge (i, j). This makes the construction basis-dependent. The construction is graphically shown in figure 3.2. The space of all ancillae over the whole lattice is then

$$|\Phi) = \bigotimes_{e \in E} |\phi)_e \tag{3.21}$$

The original reason for this definition couples back to the discussion about the area law. Both the ground states of local, gapped Hamiltonians and entangled pairs of particles distributed among neighbours on a lattice obey an area law for the entanglement entropy. Since they have an equal amount of entanglement, there should exist local operations that transform the one into the other [60]. Therefore, there exists a linear map A_i on each vertex i, mapping the auxiliary spaces into the physical spaces.

$$A_i : \bigotimes_{j \in S_i} \mathbb{C}^{D_{i,j}} \to \mathbb{C}^{d_i} \tag{3.22}$$

The PEPS, a physical state defined on the whole lattice, is then defined as

$$|\psi(A)\rangle = \bigotimes_{i \in V} A_i |\Phi) \tag{3.23}$$

---

[5] This discussion is mostly based on references [9] and [19].

(a) MPS

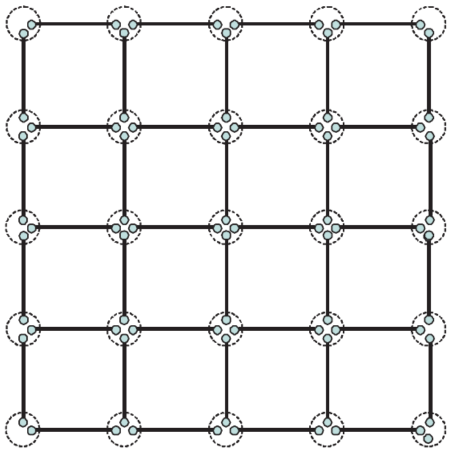

(b) PEPS

Figure 3.2: Visualizations of (a) an MPS and (b) a PEPS. The connected ancillae are maximally entangled. Ancillae belonging to one vertex are encircled. [59]

The PEPS is thus obtained by the direct product over all vertices of the linear map of the local entangled pairs into the physical ones. The name PEPS comes from the fact that the entangled pairs are projected onto the physical ones. This state will be entangled, since the entanglement of the ancillae is transferred by the linear map. Even more so, this final state will be able to carry long-range entanglement, even though the pairs are only entangled to their neighbors.

The map A_i is characterized by its coefficients in a basis.

$$A^s_{\alpha_1,\ldots,\alpha_{z_i}} = \langle s| A_i |\alpha_1, \ldots, \alpha_{z_i}) \tag{3.24}$$

This is an object that has one physical index and z_i virtual indices, and is a tensor. The characterization in terms of its virtual and physical indices allows for a graphical representation of the tensor, shown in figure 3.3a for the 1D case.

Another way of defining a PEPS is to define on each vertex a state $|\phi_i\rangle$ of the physical and virtual system.

$$|\phi_i\rangle \in \mathbb{C}^{d_i} \bigotimes_{j \in S_i} \mathbb{C}^{D_{i,j}} \tag{3.25}$$

The PEPS can then be defined as

$$|\psi\rangle = (\Phi| \left(\bigotimes_{i \in V} |\phi_i\rangle \right) \tag{3.26}$$

This coincides with the first definition if

$$|\phi_i\rangle = \sum_{s,\alpha_1,\ldots,\alpha_{z_i}} A^s_{\alpha_1,\ldots,\alpha_{z_i}} |s\rangle \otimes |\alpha_1,\ldots,\alpha_{z_i}) \tag{3.27}$$

and if the $A^s_{\alpha_1,\ldots,\alpha_{z_i}}$ are chosen as the elements of the map A_i in the physical $\{|s\rangle\}$ and virtual basis $\{|\alpha_j)\}$.

In 1D, the elements of the map A_i can be denoted as $A^{s_i}_{\alpha,\beta}$ and the matrices $A^{s_i} \in \mathbb{C}^{D_{i-1,i}\times D_{i,i+1}}$ can be defined. If periodic boundary conditions are applied, i.e. when A_1 is connected to A_N, then it can be proven that

$$\langle s_1,\ldots,s_N|\psi\rangle = \mathrm{Tr}\left[A_1^{s_1}A_2^{s_2}\ldots A_N^{s_N}\right] \tag{3.28}$$

and thus

$$\begin{aligned} |\psi(A)\rangle &= \mathrm{Tr}\left[A_1A_2\ldots A_N\right] \\ &= \sum_{\alpha,\beta,\ldots,\psi,\omega} (A_1)_{\omega\alpha}(A_2)_{\alpha\beta}\ldots(A_N)_{\psi\omega} \end{aligned} \tag{3.29}$$

which is the trace over the virtual indices of the product of N matrices. The 1D case of a PEPS is therefore called a Matrix Product State (MPS).

A very important case is the case of translational invariance, in which $A_i = A$, which implies $D_{i,j} = D$, the bond dimension. Since in this case, a state is uniquely defined when this single linear map A is known, A is said to generate the corresponding state, which will be denoted as $|\psi(A)\rangle$.

The generalization to Matrix Product Operator (MPO) and Projected Entangled Pair Operator (PEPO) is straightforward. Such an operator now has multiple physical indices, some corresponding to the domain (the bra) and some corresponding to the codomain (the ket). An MPO with p legs in its domain and p in its codomain will be denoted as a (p,p) MPO. This is an operator for which it holds that

$$(p,p)\ \text{MPO}: \bigotimes_{i=1}^{p} \mathbb{C}^{d_i} \to \bigotimes_{i=1}^{p} \mathbb{C}^{d_i} \tag{3.30}$$

The same notations can be used for general tensors. A (p,q) tensor will denote a tensor with p legs in its codomain and q legs in its domain.

Both the PEPS and PEPO will be represented in a graphical way, and thus as a tensor network, as seen in figure 3.3b and 3.3c for the 1D case. This will simplify the notations greatly. Each block denotes a tensor, with the number of edges equal to the number of indices. An open edge denotes an open index. An edge connecting 2 tensors denotes a contraction of the tensors over the index that connects them. This has a rigorous mathematical meaning. For example, the tensor in figure 3.4a is defined as

$$A = A^w_{uv}|u)_1\,|v\rangle_2\,(w|_3 \tag{3.31}$$

where the convention is used that the first, second, and third index are the edges on the left, bottom, and right respectively. Furthermore, the conjugate of the tensor A from (3.31) can be defined as

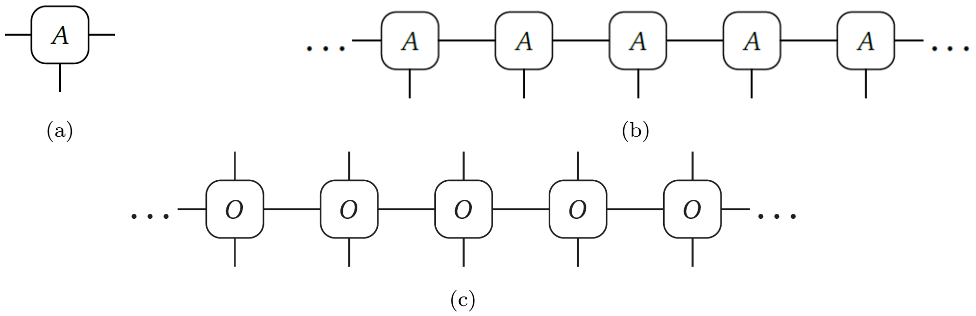

(a)

(b)

(c)

Figure 3.3: Graphical visualizations of (a) a tensor, (b) the MPS $|\psi\rangle$ according to (3.29), and (c) an MPO [19]

$$\overline{A} = \overline{A^{w}_{uv}}|w)_3 \langle v|_2 \, (u|_1 \tag{3.32}$$

The tensor network in figure 3.4b can then be evaluated by calculating the contraction of A with the tensor B.

$$B = B^{k}_{ij}|i)_4 \, |j\rangle_5 \, (k|_6 \tag{3.33}$$

$$\begin{aligned} AB &= A^{w}_{uv}|u)_1 \, |v\rangle_2 \, (w|_3 B^{k}_{ij}|i)_4 \, |j\rangle_5 \, (k|_6 \\ &= A^{w}_{uv}B^{k}_{ij}|u)_1 \, |v\rangle_2 \, (w|_3|i)_4 \, |j\rangle_5 \, (k|_6 \\ &= A^{w}_{uv}B^{k}_{ij}|u)_1 \, |v\rangle_2 \, \delta_{wi} \, |j\rangle_5 \, (k|_6 \\ &= A^{w}_{uv}B^{k}_{wj}|u)_1 \, |v\rangle_2 \, |j\rangle_5 \, (k|_6 \end{aligned} \tag{3.34}$$

with δ the Kronecker delta. This yields, as figure 3.4b already indicated, a tensor with 4 indices.

(a)

(b)

Figure 3.4: (a) a tensor A and (b) a contraction of tensors A and B

Expectation values can also be represented graphically. E.g., the energy of a state $E(\psi)$ is given as the expectation value of the Hamiltonian, which is in this example taken as a (2,2) tensor, visualized in figure 3.5a. The convention is used that the top of the figure denotes the domain, and the bottom of the figure denotes the codomain.

$$E = \langle\psi(A)| \, H \, |\psi(A)\rangle \tag{3.35}$$

Its graphical representation is given in figure 3.5b, where $\bar{A}$ denotes the complex conjugate of A, and its infinite contraction is $\langle\psi(A)|$.

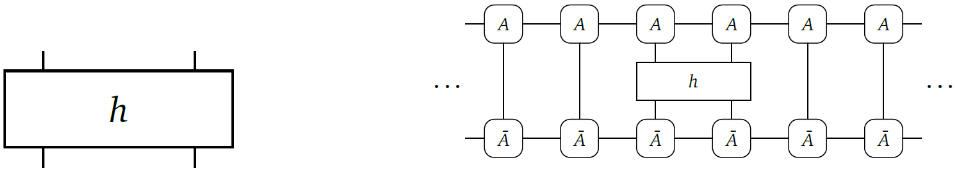

(a) (b)

Figure 3.5: Graphical visualizations of (a) a (2,2) tensor and (b) the energy according to (3.35) [19]

This is not equal to the actual energy of the system, since the expression in figure 3.5b is the expectation value of a local Hamiltonian, acting on only 2 sites. The total Hamiltonian will in most cases be translationally invariant, just as the MPS, which means that in this example

$$H = \sum_{i \in V} H_{i,i+1} \tag{3.36}$$

and the expression of figure 3.5b is equal to

$$E_{i,i+1} = \langle\psi(A)| H_{i,i+1} |\psi(A)\rangle \tag{3.37}$$

which is only one term of the infinite sum of (3.36). To calculate the full energy, this infinite sum has to be carried out.

$$\begin{aligned} E &= \langle\psi(A)| H |\psi(A)\rangle \\ &= \sum_{i \in V} \langle\psi(A)| H_{i,i+1} |\psi(A)\rangle \\ &= N \langle\psi(A)| H_{i,i+1} |\psi(A)\rangle \end{aligned} \tag{3.38}$$

where N is the number of sites. In the thermodynamic limit, this will be $|\mathbb{Z}|$, the cardinal number of $\mathbb{Z}$, which is infinite. A possible interpretation that this expectation value can have, is in terms of energy density per site, i.e.

$$E_i = \frac{E}{|\mathbb{Z}|} = \langle\psi(A)| H_{i,i+1} |\psi(A)\rangle \tag{3.39}$$

which is finite. This can also be interpreted as the interaction energy between sites i and $i+1$, or, because of translational invariance, as the average interaction energy between 2 sites.

3.3 Fermions and graded spaces [6]

A problem arises when trying to describe fermions instead of bosons. Bosons obey commutation relations, whereas fermions obey anticommutation relations. These will yield different rules for the tensor contractions. Specifically, the following identities will have to be fulfilled.

---

[6] This discussion is mostly based on [61].

$$\begin{cases} \text{Bosons:} & |i\rangle_1 |j\rangle_2 = a^\dagger_{i,1} a^\dagger_{j,2} |\Omega\rangle = a^\dagger_{j,2} a^\dagger_{i,1} |\Omega\rangle = |j\rangle_2 |i\rangle_1 \\ \text{Fermions:} & |i\rangle_1 |j\rangle_2 = c^\dagger_{i,1} c^\dagger_{j,2} |\Omega\rangle = (-1)^p c^\dagger_{j,2} c^\dagger_{i,1} |\Omega\rangle = (-1)^{|i||j|} |j\rangle_2 |i\rangle_1 \end{cases} \tag{3.40}$$

$a^\dagger_i$ and $c^\dagger_i$ are the creation operators for bosons and fermions, respectively. p is the parity and is equal to $|i||j|$. $|i|$ and $|j|$ are the parity of sites i and j respectively. Thus, the state vector for fermions can get an extra minus sign if two of them switch places.

It turns out that the introduction of $\mathbb{Z}_2$-graded Hilbert spaces can satisfy the requirements of (3.40). These are Hilbert spaces that can be decomposed into two orthogonal sectors.

$$\mathcal{H} = \mathcal{H}^0 \otimes^\perp \mathcal{H}^1 \tag{3.41}$$

where 0 denotes even and 1 denotes odd parity. If a state $|i\rangle$ has support only in one of the sectors, it is called homogeneous and has a parity that will be denoted by $|i|$. The dual of this Hilbert space is $\mathcal{H}^* = \mathrm{Hom}(\mathcal{H}, \mathbb{C})$. The inner product of $\mathcal{H}$ can now be used to define an isomorphism I

$$I : \mathcal{H} \longrightarrow \mathcal{H}^* : |i\rangle \mapsto \langle i| \quad \text{s.t.}\, \langle i| \left(|j\rangle\right) = \langle i|j\rangle_{\mathcal{H}}, \forall\, |i\rangle, |j\rangle \in \mathcal{H} \tag{3.42}$$

We will need to define tensors on the direct product of these graded Hilbert spaces, e.g. $\mathcal{H}_1 \otimes \mathcal{H}_2$, which is still a Hilbert space by using the inner products defined in $\mathcal{H}_1$ and $\mathcal{H}_2$ separately.

$$\langle |i\rangle \otimes |j\rangle, |k\rangle \otimes |l\rangle \rangle = \langle i|k\rangle_{\mathcal{H}_1} \langle j|l\rangle_{\mathcal{H}_2}, \forall\, |i\rangle, |k\rangle \in \mathcal{H}_1, |j\rangle, |l\rangle \in \mathcal{H}_2 \tag{3.43}$$

A contraction always occurs over a ket and a bra, or equivalently, a Hilbert space and its dual. Because of the anticommutation relations, the contraction defined on $\mathcal{H} \otimes \mathcal{H}^*$ will be different than the one defined on $\mathcal{H}^* \otimes \mathcal{H}$. In a contraction, it is thus important to specify which tensor is associated with the ket, and which tensor with the bra. This can be represented with an arrow, as was already shown in the previous section. The convention used in this thesis is that an outgoing arrow corresponds to a vector and an incoming arrow to a dual vector.

To be able to obey the (anti)commutation relations, we introduce the fermionic reordering operator $\mathcal{F}$, mapping $\mathcal{H}_1 \otimes \mathcal{H}_2$ to $\mathcal{H}_2 \otimes \mathcal{H}_1$.

$$\mathcal{F} : \mathcal{H}_1 \otimes \mathcal{H}_2 \to \mathcal{H}_2 \otimes \mathcal{H}_1 : |i\rangle_1 |j\rangle_2 \mapsto (-1)^{|i||j|} |j\rangle_2 |i\rangle_1 \tag{3.44}$$

With this operator, the definitions of the contractions have to be revisited. This can be done by looking at the example of a contraction of tensors A and B, as shown in figure 3.4b. The contraction over an index where the arrow points from B to A ($\langle i| \ |j\rangle$ case) will be different than when the arrow points from A to B ($|i\rangle\langle j|$ case). Specifically, the contraction operators can then be respectively defined as

$$\mathcal{C} : \mathcal{H}^* \otimes \mathcal{H} \to \mathbb{C} : \mathcal{C}(\langle i| \ |j\rangle) = \langle i|j\rangle = \delta_{ij} \tag{3.45}$$

$$\widetilde{\mathcal{C}} : \mathcal{H} \otimes \mathcal{H}^* \to \widetilde{\mathbb{C}} : \mathcal{C}(|i\rangle\langle j|) = (-1)^{|i||j|} \delta_{ij} \tag{3.46}$$

where both will be denoted by $\mathcal{C}$. $\mathcal{C}_{ij}$ will denote that the contraction occurs over the i-th of the first tensor and the j-th index of the second tensor. $\mathcal{C}(A, a, B, b)$, where a and b are lists of indices of equal size, denotes the successive application of $\mathcal{C}_{a_k b_k}$ on $A \otimes B$, with a_k and b_k the k-th element of a and b respectively. Changing the order of the applications will not change the end result, but will have a big effect on the complexity. This will be explained in section 7.2.1.

These formulas can be illustrated by the inner product of 2 tensors A and B.

$$\begin{aligned} A &= A^w_{uv} \left|u\right\rangle_1 \left|v\right\rangle_2 \left\langle w\right|_3 \\ B &= B^k_{ij} \left|i\right\rangle_1 \left|j\right\rangle_2 \left\langle k\right|_3 \end{aligned} \tag{3.47}$$

This leads to

$$\begin{aligned} \langle A, B\rangle &= \operatorname{Tr}\left(\overline{A}B\right) \\ &= \mathcal{C}(\overline{A}, [1,2,3], B, [1,2,3]) \\ &= \mathcal{C}(\overline{A^w_{uv}} \left|w\right\rangle_3 \left\langle v\right|_2 \left\langle u\right|_1, [1,2,3], B^k_{ij} \left|i\right\rangle_1 \left|j\right\rangle_2 \left\langle k\right|_3, [1,2,3]) \\ &= \overline{A^w_{uv}} B^k_{ij} \mathcal{C}(\left\langle u\right|_1 \left|i\right\rangle_1) \mathcal{C}(\left\langle v\right|_2 \left|j\right\rangle_2) \widetilde{\mathcal{C}}(\left|w\right\rangle_3 \left\langle k\right|_3) \\ &= \overline{A^w_{uv}} B^k_{ij} \delta_{ui} \delta_{vj} (-1)^{|w||k|} \delta_{wk} \\ &= \overline{A^k_{ij}} B^k_{ij} (-1)^{|k|} \end{aligned} \tag{3.48}$$

The known formula for an inner product arises, with the inclusion of a parity factor, yielding possibly an extra minus sign. This is called the supertrace. For fermionic Hilbert spaces, both gradings 0 and 1 will be present, and (3.45) and (3.46) will have to be implemented separately. The latter formula is defined with the inclusion of a 'twist' or an extra parity operator P with respect to the former formula. In fermionic calculations requiring a trace instead of a supertrace, an extra parity operator should be included to cancel out the one in the definition. For bosonic Hilbert spaces, the grading will always be 0, the contractions will yield the same results regardless of the presence of a parity operator.

This discussion justifies the use of graphical notations for tensor contractions as already used in the previous section. Each edge is a tensor index and a connection denotes a contraction over these indices, where either $\widetilde{\mathcal{C}}$ or $\mathcal{C}$ is used depending on the arrow. Sometimes, the arrows in the graphical notations are left out for simplicity. A possible extra twist in the calculation of a trace instead of a supertrace, as explained above, is suppressed in the diagrams unless explicitly mentioned (this will only be the case in chapter 7).

3.4 The transfer matrix [7]

Calculating the energy per site is not possible by evaluating the expression of figure 3.5b, since it is still infinite. It thus needs to be rewritten in a form that can be evaluated using a finite number of tensors and contractions. For this reason, we look at the tensor that occurs an infinite amount of times in this expression, namely the contraction of A and $\bar{A}$, which is called the transfer matrix T, a (2,2) tensor. Its diagrammatic representation is given in figure 3.6 [19].

$$T = \sum_{s=1}^{d} A^s \otimes \overline{A}^s \tag{3.49}$$

---

[7] The discussions from this point to the end of this chapter are mostly based on reference [19]

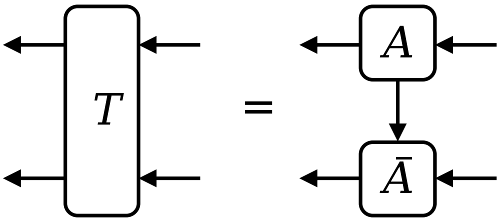

Figure 3.6: Diagrammatic representation of the transfer matrix

The transfer matrix has both left and right eigenvectors, corresponding to the same spectrum. Since it is bounded, its eigenvalues are all finite, and A can always be redefined by $A \to A/\sqrt{\lambda}$, with λ the biggest eigenvalue. With this definition, the biggest eigenvalue is 1. This is how the MPS is normalized.

The transfer matrix of a normalized MPS can be written in its spectral decomposition

$$T = |1\rangle\langle 1| + \sum_{n=2}^{\infty} \lambda_n |n\rangle\langle n| \tag{3.50}$$

and thus

$$T^m = |1\rangle\langle 1| + \sum_{n=2}^{\infty} \lambda_n^m |n\rangle\langle n| \tag{3.51}$$

where $|\lambda_i| < 1$ if $i > 1$ and $|\lambda_i| \leqslant |\lambda_j|$ if $i > j$. In the limit of $m \to \infty$, T^m reduces to

$$\lim_{m\to\infty} T^m = |1\rangle\langle 1| \tag{3.52}$$

Because the system is infinite, we can start from arbitrary left and right boundaries. The left boundary can be written as

$$\langle l'| = \sum_{n=1}^{\infty} a_n \langle n| \tag{3.53}$$

and similar for the right boundary.

$$|r'\rangle = \sum_{n=1}^{\infty} b_n |n\rangle \tag{3.54}$$

The exact expression of this boundary will not matter, since

$$\lim_{m\to\infty} T^m |r'\rangle = b_1 |1\rangle \tag{3.55}$$

and thus only the leading eigenvector will remain. Denoting the left and right eigenvector with eigenvalue 1 as $|l\rangle$ and $|r\rangle$, the expressions of figure 3.7 hold.

The eigenvectors can be normalized to 1, which means that their overlap is equal to 1.

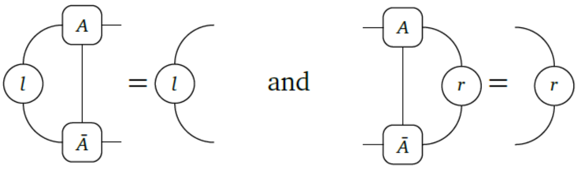

Figure 3.7: Definition of left and right fixed points [19]

$$\langle l|r\rangle = 1 \tag{3.56}$$

Furthermore, the eigenvectors $|l\rangle$ and $|r\rangle$ are isomorphic to density operators l and r, for which the normalisation condition can be rewritten as

$$\mathrm{Tr}(lr) = 1 \tag{3.57}$$

l and r are respectively called the left and right environments. With the definitions of the fixed points, the expectation value of figure 3.5b reduces to figure 3.8, which is a finite contraction and thus calculable.

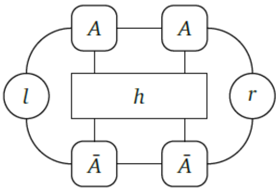

Figure 3.8: Different expression for the expectation value of h, as also given in figure 3.5b [19]

This is the energy functional of h that has to be minimized with respect to A to yield the ground state MPS. Based on this, every other ground state property can be calculated with an expression similar to figure 3.8, where h is substituted with the local operator of which the expectation value is calculated. The algorithms to find the ground state MPS will be explained in section 4.2.

3.4.1 Injectivity

In the discussion above, it has been implicitly assumed that the leading eigenvector is non-degenerate, and thus that the vectors $|l\rangle$ and $|r\rangle$ are unique. If this were not the case, (3.50) would not hold, and the environments l and r would not be well defined. The requirement of injectivity will play a part when defining the symmetry of the system, as will be explained in section 4.4.2.

3.5 Correlation functions

An important concept in the analysis of the ground state MPS is the correlation function. The connected 2-body correlation function with respect to the operators O and O' is defined as [19]

$$C(r) = \left\langle O_i O^{'}_{i+r} \right\rangle - \langle O_i \rangle \langle O'_{i+r} \rangle \tag{3.58}$$

where O is a local operator. The expectation value is taken with respect to the (ground state) wave function, and the expression thus needs to be contracted with the leading eigenvectors on the left and the right, as explained above. The exact value of i does not matter because of translational invariance. The definition can thus be rewritten as

$$C(r) = \langle 1| O_i O^{'}_{i+r} |1\rangle - \langle 1| O |1\rangle \langle 1| O' |1\rangle \tag{3.59}$$

The transfer matrix occurs now only between the 2 operators in the first term of the expression. For large values of r, this can be written as [42]

$$\begin{aligned} C(r) &= \langle 1| O (T^{r-1}) O^{'} |1\rangle - \langle 1| O |1\rangle \langle 1| O' |1\rangle \\ &= \langle 1| O \left(|1\rangle\langle 1| + \sum_{n=2}^{\infty} \lambda_n^{r-1} |n\rangle\langle n| \right) O^{'} |1\rangle - \langle 1| O |1\rangle \langle 1| O' |1\rangle \\ &= \sum_{n=2}^{\infty} \lambda_n^{r-1} \langle 1| O |n\rangle \langle n| O^{'} |1\rangle \\ &\approx \lambda_2^{r-1} \langle 1| O |2\rangle \langle 2| O^{'} |1\rangle \\ &= a(O, O') e^{r \ln |\lambda_2|} \end{aligned} \tag{3.60}$$

where $a(O, O')$ is a constant. In going from line 2 to 3, the second term in (3.58) drops out. This is the disconnected part, and subtracting it gives the connected correlation function its name.

So, for large distances, the correlation has an exponential decay, with

$$\begin{aligned} C(r) &\sim e^{-r/\xi} \\ \xi &= -\frac{1}{\ln |\lambda_2|} > 0 \end{aligned} \tag{3.61}$$

where ξ is called the correlation length, representing a characteristic length scale of the system. In MPS, this will always be finite, and the correlations have an exponential decay. This means that critical systems will not be exactly described, as they have an infinite correlation length and a power law decay for the correlations [62, 48, 63]. States with a finite correlation length were originally called Finitely Correlated States (FCS). It was proven that all these FCS are the unique ground state of local, gapped Hamiltonians (called the parent Hamiltonian), and are thus injective MPS [64, 65, 9].

3.6 Static structure factor

The static structure factor s can be defined as the Fourier transform of the correlation function. Based on two operators O^α and O^β, it can be defined as [19]

$$s^{\alpha\beta}(q) = \frac{1}{|\mathbb{Z}|} \sum_{m,n \in \mathbb{Z}} e^{iq(m-n)} \left\langle \Psi(\bar{A}) \right| (O_n^\beta)^\dagger O_m^\alpha \left| \Psi(A) \right\rangle_c \tag{3.62}$$

where $\langle \cdots \rangle_c$ denotes that the connected correlation function is used. This expression can immediately be rewritten as

$$
\begin{aligned}
s^{\alpha\beta}(q) &= \sum_{n\in\mathbb{Z}} e^{-iqn} \left\langle \Psi(\bar{A})\right| (O_n^{\beta})^{\dagger} O_0^{\alpha} \left|\Psi(A)\right\rangle_c \\
&= \sum_{n\in\mathbb{Z}} e^{-iqn} C(n)
\end{aligned}
\tag{3.63}
$$

which is thus the discrete Fourier transform of the connected correlation function. $C(n)$ is of the form

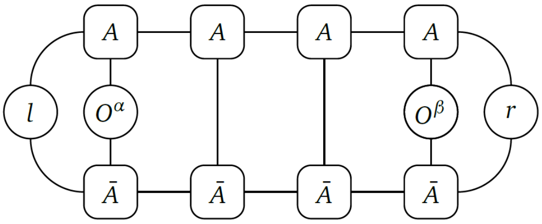

Figure 3.9: C(3) used in (3.63) [19]

This is useful since the static structure factor is experimentally accessible, and can thus be used as experimental validation of the numerical results [19]. Furthermore, it can be used to determine periodic structures in the MPS.

3.6.1 Leading oscillations

Looking at the third line of (3.60), the connected correlation function can be rewritten as

$$
C(r) = \sum_{n=2}^{\infty} |\lambda_n|^{r-1} e^{i(r-1)\theta_n} \langle 1| O |n\rangle \langle n| O^{'} |1\rangle \tag{3.64}
$$

where the eigenvalues of the transfer matrix were rewritten as $\lambda_n = |\lambda_n| e^{i\theta_n}$. In the limit where $|\lambda_2| \gg |\lambda_m|, \forall m > 2$, this reduces to

$$
C(r) = |\lambda_2|^{r-1} e^{i(r-1)\theta_2} \langle 1| O |2\rangle \langle 2| O^{'} |1\rangle \tag{3.65}
$$

The exponential will give rise to a modulation of the correlation function with a period equal to $\frac{2\pi}{\theta_2}$. More generally, each eigenvector will give rise to an oscillation with period $\frac{2\pi}{\theta_n}$.

Substituting (3.64) into (3.63) gives

$$
\begin{aligned}
s^{\alpha\beta}(q) &= \sum_{n\in\mathbb{Z}} e^{-iqn} C(n) \\
&= \sum_{n\in\mathbb{Z}} e^{-iqn} \sum_{m=2}^{\infty} |\lambda_m|^{n-1} e^{i(n-1)\theta_m} \langle 1| O^{\alpha} |m\rangle \langle m| O^{\beta} |1\rangle \\
&= \sum_{n\in\mathbb{Z}} \sum_{m=2}^{\infty} |\lambda_m|^{n-1} e^{-i\theta_m} e^{-in(q-\theta_m)} \langle 1| O^{\alpha} |m\rangle \langle m| O^{\beta} |1\rangle
\end{aligned}
\tag{3.66}
$$

This causes the structure factor to have peaks at $q = \theta_m = \frac{2\pi}{\text{period}}$.

3.7 Gauge freedom

An important thing to note about the definitions given above is that the MPS or PEPS representation of a state is not unique, two tensors may give rise to the same state. In the case of a translationally invariant MPS $|\psi(A)\rangle$, if there exists a B that is related to A via [9]

$$B^i = XA^iX^{-1}, \forall i \tag{3.67}$$

then, by the definition (3.28), these gives rise to the same state, i.e. $|\psi(B)\rangle = |\psi(A)\rangle$. A and B are then said to generate the same state. This is a special case of the fundamental theorem of MPS. Since only the state $|\psi\rangle$ is physical, the gauge freedom can be used at will to make the expressions easier.

3.7.1 Mixed gauge

A particularly interesting and useful gauge is the so-called mixed gauge. For this, the left-orthonormal form A_L is defined, shown in figure 3.10.

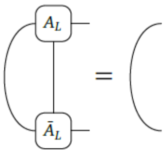

Figure 3.10: Definition of A_L [19]

This is always possible by a good choice of X in (3.67). When the left fixed point l is decomposed as $l = L^\dagger L$, X should be chosen as $X = L$. Then it holds that $A_L = LAL^{-1}$ or $A = L^{-1}A_LL$. This is shown in figure 3.11, which uses the definition above and the equation of figure 3.7.

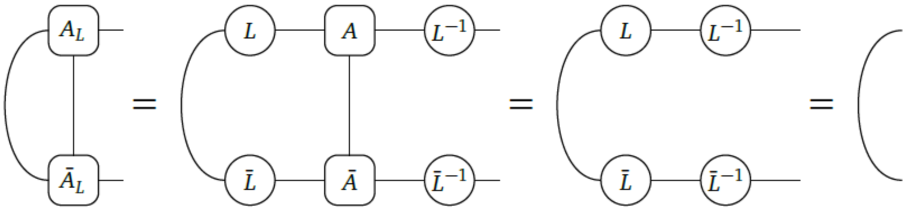

Figure 3.11: Construction of A_L [19]

This choice still leaves room for unitary gauge transformations.

$$A_L \rightarrow UA_LU^\dagger \tag{3.68}$$

Similarly, a right-orthonormal form A_R can be defined, for which $r = R^\dagger R$, $A_R = R^{-1}AR$. The idea of the mixed gauge is to choose a center site, to bring all the tensors to the left in the left-orthonormal form and all the tensors to the right in the right-orthonormal form. The center site will be surrounded by a L and a R tensor, which will be redefined as A_C, i.e.

$$A_C = LAR \tag{3.69}$$

Yet another tensor, C, can be defined as $C = LR$. It holds that

$$A_L C = C A_R = A_C \tag{3.70}$$

With these definitions, there are different possibilities of writing the MPS generated by A, given in figure 3.12.

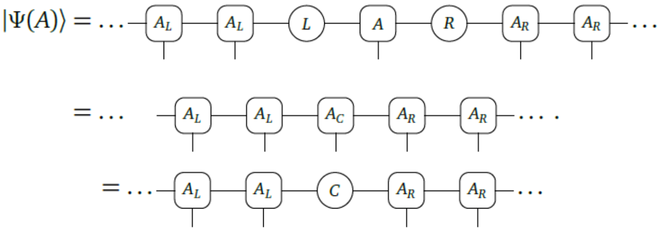

Figure 3.12: Graphical visualizations of different ways of calculating $|\psi(A)\rangle$ for the mixed gauge [19]

The usefulness of this construction is that the expectation value of the Hamiltonian, or any other MPO, as given in figure 3.5b or 3.8, can now be rewritten as in figure 3.13.

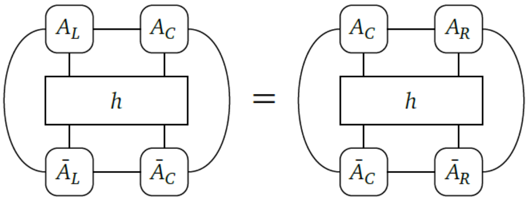

Figure 3.13: Expectation value of h in the mixed gauge [19]

The problem of the boundary conditions is thus reduced to finding the leading eigenvectors, decomposing them, and calculating the tensors A_L, A_C, and A_R, which will completely specify the state [19].

II

Methods

4

Optimization Schemes

For a system based on a certain Hamiltonian, much of the interesting physics can be found from the ground state, or equivalently, from the state at zero temperature. It is therefore imperative to know how the energy functional of figure 3.8 can be optimized with respect to A. Finding the ground state amounts to finding the minimum of this energy functional, i.e.

$$\begin{aligned} A_{gs} &= \underset{A}{\operatorname{argmin}} \frac{\big\langle \Psi(\bar{A}) \big| \, h \, |\Psi(A)\big\rangle}{\big\langle \Psi(\bar{A}) \big| \Psi(A) \big\rangle} = \underset{A}{\operatorname{argmin}} f(A, \bar{A}) \\ E_{gs} &= f(A_{gs}, \bar{A_{gs}}) \end{aligned} \tag{4.1}$$

where f is the energy functional. The denominator is 1 if the MPS is properly normalized. In the thermodynamic limit, this expression will diverge, so instead the energy density will be minimized. This is a variational formulation, which is often more stable than other numerical techniques. Furthermore, the optimized energy will always be higher than the true ground state energy, thus giving an upper bound on the energy.

Another way of looking at this problem is in terms of an eigenvalue problem

$$H \, |\psi\rangle = \lambda \, |\psi\rangle \tag{4.2}$$

The minimization procedure is equivalent to finding the eigenvector with the lowest eigenvalue, which is then called the ground state energy.

4.1 The use of JordanMPO

Since the MPS is defined as an infinite contraction of local tensors, which are the same on all sites, it will turn out to be useful to redefine local operators, especially the Hamiltonian, in the same way. If a local operator O could be rewritten as a infinite contraction of tensors M_i, then the left and right environments of figure 3.7 can be redefined with the inclusion of this M_i, as shown in figure 4.1.

For this, we first need to redefine each local operator acting on multiple sites as a contraction of operators acting on only one site. This can be done by applying the SVD. Assume the Hamiltonian acts on the Hilbert space $\mathcal{H}_{i,j} = \mathcal{H}_i \otimes \mathcal{H}_j$ and can be written as

$$H_{ij} = \sum_{k,l,m,n} C_{kl}^{mn} \, |k\rangle_i \, |l\rangle_j \, \langle m|_j \, \langle n|_i \tag{4.3}$$

where $\{|k\rangle_i\}$ and $\{|l\rangle_j\}$ are the orthonormal bases for $\mathcal{H}_i$ and $\mathcal{H}_j$ respectively. The SVD of the matrix C with elements C_{kl}^{mn} will then yield the matrices U, Σ and V, with

$$H_{ij} = \sum_{k,l,m,n,a} U_{kna} \Sigma_{aa} V_{alm}^{\dagger} \, |k\rangle_i \, \langle n|_i \, |l\rangle_j \, \langle m|_j \tag{4.4}$$

If the tensors L_i and R_j are defined as

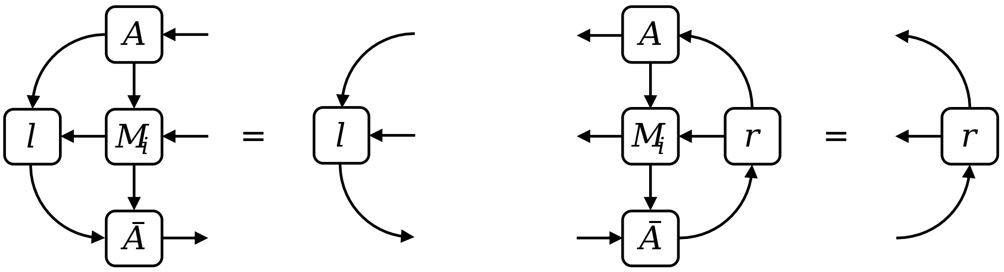

Figure 4.1: New definition of the left and right environment with the inclusion of M_i

$$\begin{aligned}(L_i)^a &= \sum_k U_{kna}\Sigma_{aa} \left|k\right\rangle_i \left\langle n\right|_i \\ (R_j)^a &= \sum_l V^\dagger_{alm} \left|l\right\rangle_j \left\langle m\right|_j\end{aligned} \tag{4.5}$$

then

$$\begin{aligned}H_{ij} &= \sum_{a=1}^{r} (L_i)^a (R_j)^a \\ &= L_i R_j\end{aligned} \tag{4.6}$$

which is indeed a contraction of tensors acting only on one site, over a virtual space of dimension r, determined by the number of non-zero singular values of H_{ij}. For an operator acting on more than two sites, this procedure can be applied iteratively. Thus, an operator acting on multiple sites can always be rewritten as a contraction of operators acting on only one site, as seen in figure 4.2.

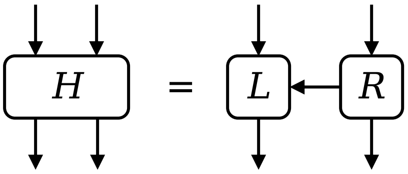

Figure 4.2: Two-site operator H as a contraction of two one-site operators L and R

With this construction, every operator can now be rewritten as a contraction of an infinite number of operators, each one acting on one site. This is shown in figure 4.3. The operators acting on the sites that were not included in the original Hilbert space are just $\mathbb{1}$, and the tensors are contracted over the virtual Hilbert space of dimension 1.

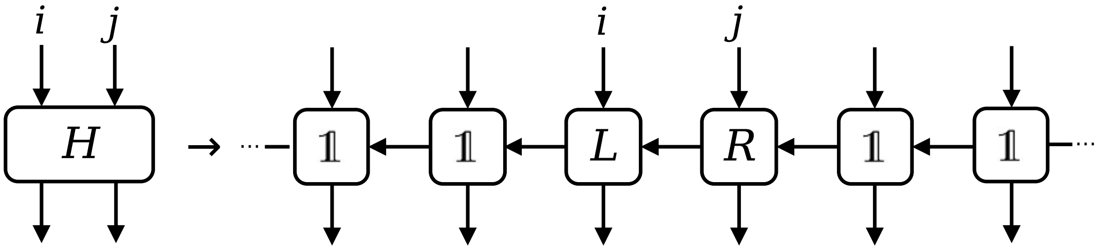

Figure 4.3: Two-site operator as the infinite contraction of local MPOs

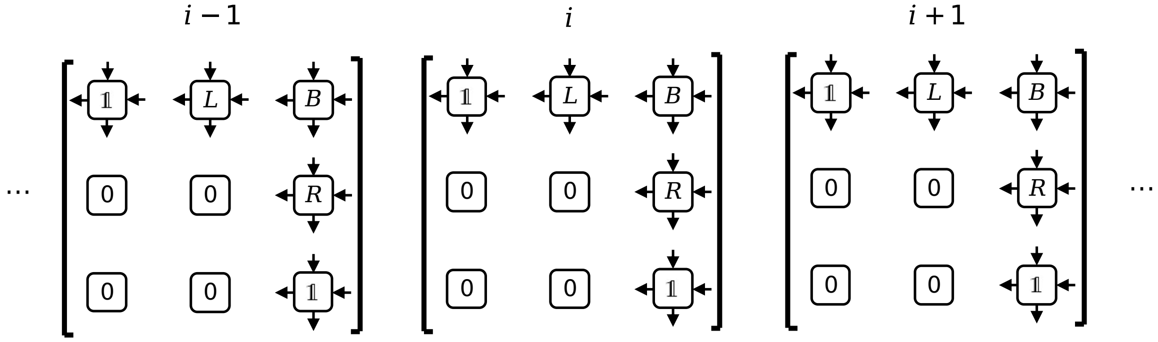

Figure 4.4: Diagrammatic representation of the infinite contraction of JordanMPOs

The operator in figure 4.2 should be placed on all sites, since the system is translationally invariant. Thus, the objects that will be contracted to get the Hamiltonian should be the same on all sites. Or more generally, they should be periodic with the same period as the MPS. This object will be the JordanMPO, a matrix containing multiple one-site operators, acting on the physical space, the dual of the physical space, and possibly multiple virtual spaces [66, 67]. It is implicitly assumed that in the matrix multiplication, the tensors are contracted over the virtual space connecting them.

To make this more concrete, consider a Hamiltonian consisting of a one-site and a two-site interaction

$$H = \sum_i B_i + L_i R_{i+1} \tag{4.7}$$

The JordanMPO M_i will be defined as

$$M_i = \begin{bmatrix} \mathbb{1} & L_i & B_i \\ 0 & 0 & R_i \\ 0 & 0 & \mathbb{1} \end{bmatrix} \tag{4.8}$$

The infinite contraction of tensors M_i can then be diagrammatically represented as in figure 4.4.

The boundary conditions for a JordanMPO are $[1, 0, 0, ...]$ for the left boundary and $[0, ..., 0, 1]^T$ for the right boundary. This means that in the matrix product from left to right, the first index of the first matrix (on site $-\infty$) would be 1. The possible 'choices' for the first matrix would then be

$\mathbb{1}, L_i$, and B_i. For a number of times, $\mathbb{1}$ will be chosen, and the first index of the next matrix would remain 1. On a certain site i, for the first time a different operator will be chosen. There are now two possibilities

1. B_i is chosen, this means the first index of the next matrix will be 3, and for all the matrices to the right, the operator $\mathbb{1}$ has to be chosen.
2. L_i is chosen, this means the first index of the next matrix will be 2, whereby the next matrix has to choose R_i, and for all matrices to the right of R_i, $\mathbb{1}$ has to be chosen.

The first possibility corresponds to the operator B_i, the second to the operator $L_i R_{i+1} = H_{i,i+1}$. By defining the Hamiltonian H as the matrix product of local JordanMPOs, all possible choices will be included, and the operators will automatically be placed on all sites, making the total operator translationally invariant. The set of possible choices at each step can be visualized in a finite-state machine, as shown in figure 4.5. Here, the red circles correspond to the possible 'levels' the system can be in, which are equivalent to the rows and columns of the JordanMPO. The blue arrows denote which transitions are possible, and the black tensors corresponding to them are the operators that are applied in the transition.

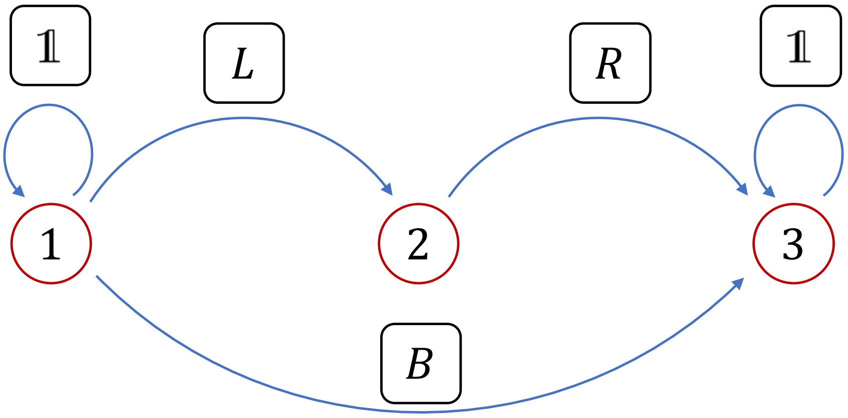

Figure 4.5: Finite-state machine corresponding to the JordanMPO of figure 4.4

This construction can be generalized to a system where the Hamiltonian can be written as the sum of local operators. i.e. if there exists a range r, such that, with $S = \{i, i+1, ..., i+r\}$

$$\begin{aligned} H &= \sum_i \sum_{s_i \in 2^{S_i}} H(s_i) \\ &= \sum_i \sum_{k=0}^{r} H_{i,i+k} \end{aligned} \tag{4.9}$$

where 2^{S_i} is the power set of the set S_i and the sum runs over all subsets of S. H_s denotes an operator acting only on the subset s. $H_{i,j}$ denotes an operator acting between sites i and j. Again, each local operator of a certain range can be used to define a JordanMPO M_i^r. The JordanMPO of the whole operator M_i can then be constructed by placing each M_i^r in a separate matrix block, where the first row and last column of M_i^r have to be placed in the first row and last column of M_i. This construction is visualized in figure 4.6. In almost all cases, however, the construction of the total JordanMPO can be done more efficiently.

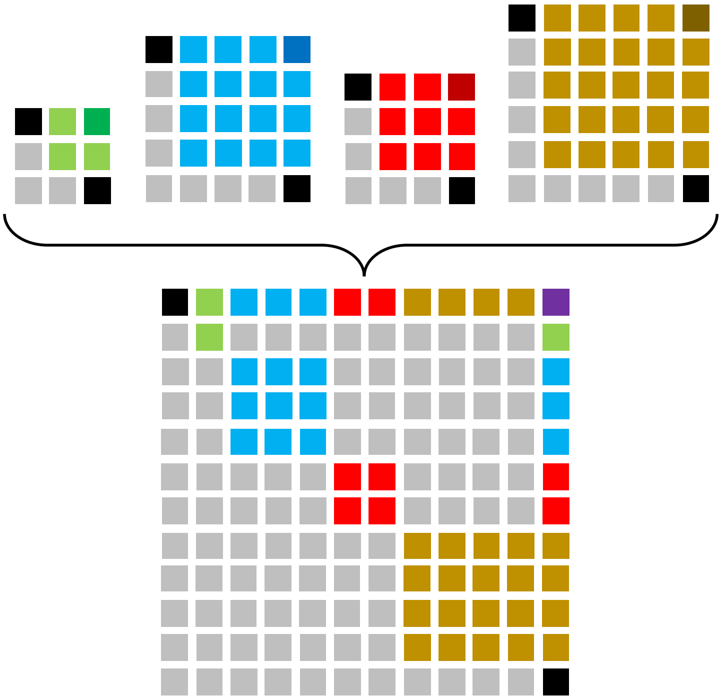

Figure 4.6: Visualization of the construction of a JordanMPO based on smaller JordanMPOs. Grey blocks denote 0. Black blocks denote $\mathbb{1}$. The light colors denote the relevant matrix blocks from the JordanMPO of interactions like those in (4.9). The darker colors denote their on-site interactions and are summed into the purple block in the final JordanMPO.

The general form of a JordanMPO is given in (4.10). A JordanMPO has to be block upper triangular, since elements below the diagonal would correspond to operators 'going back to the left' [66, 67].

$$M_i = \begin{bmatrix} \mathbb{1} & L_i & B_i \\ 0 & D_i & R_i \\ 0 & 0 & \mathbb{1} \end{bmatrix} \tag{4.10}$$

It is interesting to look at the operators contained in the JordanMPO and their meanings. Assume the JordanMPO has dimensions $L \times L$.

Elements (1,1) and (L,L): These have to be $\mathbb{1}$, otherwise the resulting operator would not be correctly normalised.
Operators of the form $H_{i,i+N}$: The general scheme to implement these in the JordanMPO is by applying the SVD of (4.6) and defining

$$\left(M_i^{(N)}\right)_{(p,q)} = \begin{cases} \mathbb{1}, & (p,q) \in \{(1,1),(L,L),(i,i+1), i \in [k, k+N-2]\} \\ R_i, & (p,q) = (1,k) \\ L_i, & (p,q) = (k+N-1, L) \\ 0, & \text{else} \end{cases} \tag{4.11}$$

Elements on the diagonal: These correspond to long-range interactions of possibly infinite length.

The definitions of the JordanMPOs for different systems can be found in appendix A.

4.2 Optimization algorithms

4.2.1 DMRG and iDMRG

The first algorithm based on (4.1) was developed by White in 1992 and is called Density Matrix Renormalization Group (DMRG) [14, 15]. It was originally introduced in a different context, whereas only later it was realized that this is an optimization scheme over the manifold of MPS. The infinite-size variant of DMRG is also called iDMRG and can be used when working directly in the thermodynamic limit, like in this thesis.

The energy functional f of (4.1) is shown in figure 4.7.

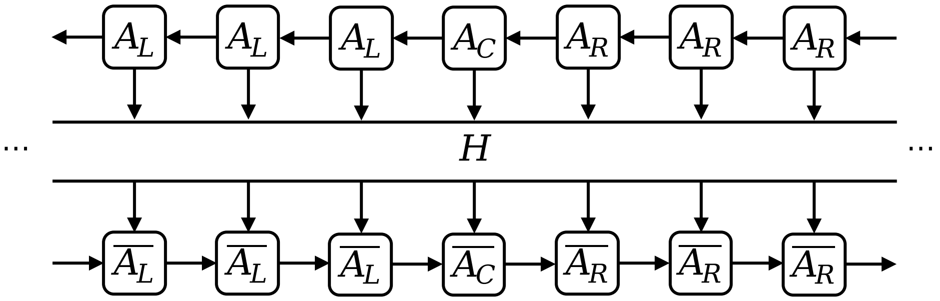

Figure 4.7: Energy functional f in the mixed gauge

This functional has to be optimized with respect to A_C, A_R, and A_L. Let us only focus on the center site A_C. In the spirit of (4.2), this optimization boils down to finding the leading eigenvalues of an operator called H_{A_C}, which is shown in figure 4.8

This can be solved with an eigensolver that yields the leading eigenvector of H_{A_C}. The solution, A'_C, can be both left and right orthonormalized, yielding new values of A_L, A_R, and C. In the most general case, the period of the MPS is greater than one, and effective Hamiltonians $H_{A_C(i)}, i \in [1, w]$, can be defined, with w the period of the MPS. Each $A_C(i)$ has to be updated with $H_{A_C(i)}$, yielding $A'_C(i)$. Since these new values will also redefine the effective Hamiltonians $H_{A_C(j)}$, the order in which this is done is important.

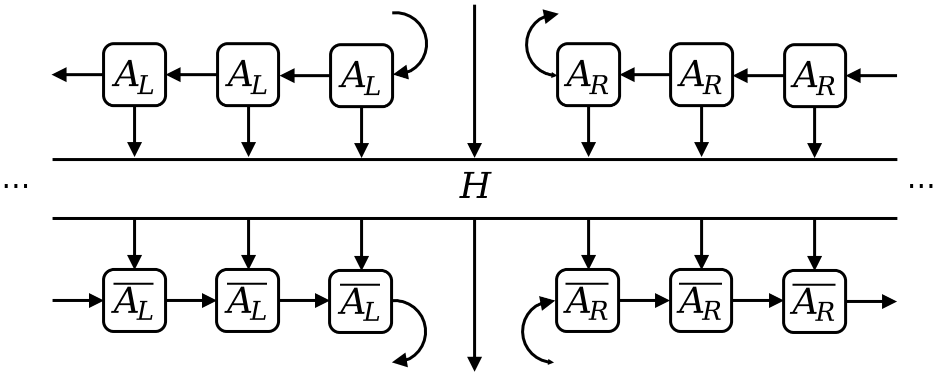

Figure 4.8: Visualization of the effective Hamiltonian H_{A_C}

The algorithm consists of sweeping through the unit cell from left to right. In each step, $A_C(i)$ is updated with $H_{A_C(i)}$, yielding $A'_C(i)$. This tensor will be used to redefine the environments and define the new effective Hamiltonian in the next step. After all sites in the unit cell are updated, a similar sweep occurs. Now, the algorithm sweeps from right to left [57].

The infinite-size variant of this algorithm starts from an MPS with only two sites. In the next step, the MPS is appended with two sites in the center, and its parameters are optimized such that the four-site MPS has minimal energy. The MPS is iteratively grown, until the tensors that are added in successive iterations are sufficiently similar. These converged tensors are then used to construct a translationally invariant, infinite-size MPS [68].

The fact that (i)DMRG always yields wave functions with exponentially decaying correlations, i.e. finite correlation lengths, was the reason they were called FCS, before the link with MPS was made. (i)DMRG is therefore much harder for critical systems [69].

Increasing the bond dimension increases the size of the variational manifold in which the optimization occurs, thus yielding possibly more accurate results with lower energy. In theory, the bond dimension should be infinite, since only then the manifold encompasses all finitely correlated states. This is computationally impossible, so instead the calculation will be done at various bond dimension, and the end result will be extrapolated to $D \to \infty$. This will be explained in section 4.3.

4.2.2 VUMPS [8]

The set of injective MPS forms a complex manifold [9]. Making smart use of the tangent space to this manifold, an algorithm resembling gradient descent can be devised. The combination of DMRG with the ideas of tangent spaces for MPS led to the development of another variational optimization algorithm, called Variational Uniform Matrix Product State (VUMPS) [18, 19].

Finding the ground state again amounts to finding the minimum of the energy functional, i.e.

---

[8] This discussion is mostly based on reference [19].

[9] More specifically, it forms a Kähler manifold [70].

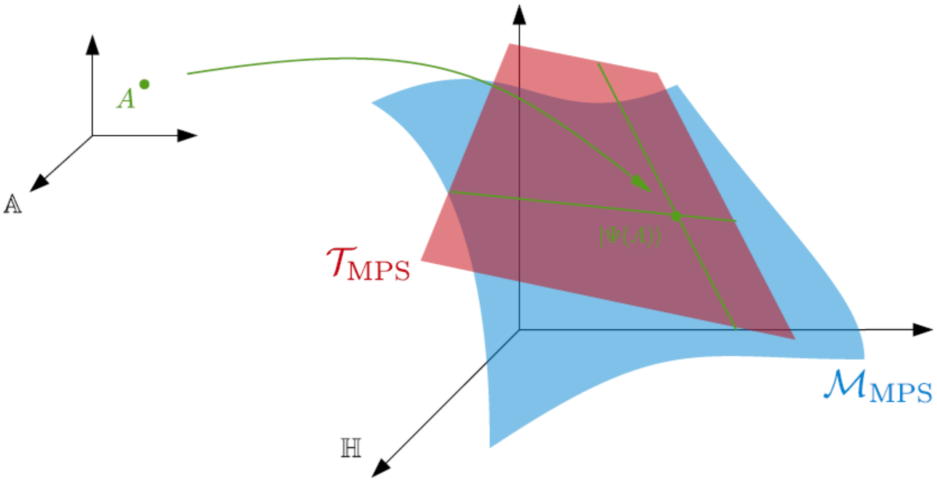

Figure 4.9: MPS manifold and its tangent space [19]

$$E_{gs} = \min_{A} \frac{\left\langle \Psi(\bar{A}) \right| h \left| \Psi(A) \right\rangle}{\left\langle \Psi(\bar{A}) \middle| \Psi(A) \right\rangle} = \min_{A} f(A, \bar{A}) \tag{4.12}$$

In optimizing the energy, the current MPS will be nudged in a certain direction, i.e.

$$A \rightarrow A + \epsilon B \tag{4.13}$$

which yields a certain nudge in the energy functional

$$f\left(A, \bar{A}\right) \rightarrow f\left(A, \bar{A}\right) + \epsilon g^{\dagger} B + O(\epsilon^2) \tag{4.14}$$

with g the gradient. It is now useful to interpret the set of uniform MPS with the same bond dimension as a manifold within the total Hilbert space of the system in which the energy will be minimized. The sum of two MPS will not necessarily remain in this manifold. Therefore, the tangent space to every MPS will be defined, together with a tangent-space projector. This is shown in figure 4.9.

Projecting the gradient g to the tangent-space gradient G yields

$$G = A'_C - A_L C' \tag{4.15}$$

with

$$\begin{aligned} A'_C &= H_{A_C}(A_C) \\ C' &= H_C(C) \end{aligned} \tag{4.16}$$

where H_{A_C} is visualized in figure 4.8 and H_C is a similar effective Hamiltonian. Together with the condition that the gradient should be zero in the minimum, these yield the VUMPS set of equations.

$$
\begin{aligned}
H_{A_C}(A_C) &\propto A_C \\
H_C(C) &\propto C \\
A_C &= A_L C = C A_R
\end{aligned}
\tag{4.17}
$$

The VUMPS algorithm consists of first solving the two eigenvalue equations, which yield new values of A_C and C. The updates for A_L and A_R are calculated by minimizing the error in the third equation. More details on this optimization procedure and tangent spaces can be found in appendix B.

4.2.3 iDMRG2 and VUMPS2

Both iDMRG and VUMPS try to optimize the MPS with a fixed bond dimension D. A simple extension to these algorithms can be obtained by first grouping the tensors in pairs of two, which can be done by contracting the tensors over their shared index. The algorithm then updates this newly joined tensor, instead of the individual ones. After the optimization step, the original tensors are obtained by performing an SVD on the updated joined tensor. This process is illustrated in figure 4.10. These algorithms are called iDMRG2 and VUMPS2. The huge advantage of this technique is that, while performing the SVD, the bond dimension can be chosen, by only keeping the D highest Schmidt-values. This allows for the dynamic growing or shrinking of the bond dimension during the optimization. This procedure is most natural for MPS with a period of at least 2, but can also be done for MPS with a single-site unit cell, by artificially doubling the period and allowing the left and right tensors in the unit cell to have different values and bond dimensions.

One way of choosing the bond dimension is to put a maximum on the bond dimension in each sector, or all sectors in total. Another way is by defining a truncation, below which value the singular values are neglected. The first can be used to put a maximum on the computational effort, whereas the latter corresponds to defining the accuracy of the calculation. This accuracy can be quantified by the truncated singular values [57].

Other factorizations than the SVD can also be used. The SVD is preferred, however, since truncating the SVD is the ideal approximation in going from a higher to a lower rank. More explicitly, if

$$X = U\Sigma V^\dagger \tag{4.18}$$

is the exact tensor, then its low-rank approximation is

$$X^{(D)} = U\Sigma^{(D)} V^\dagger \tag{4.19}$$

where $\Sigma^{(D)}$ contains the D highest singular values of Σ. The Eckart-Young theorem then states that [71]

$$\|X - X^{(D)}\|_F \leqslant \|X - Y\|_F \tag{4.20}$$

For all Y of matrix-rank D. This theorem was later generalized by Mirsky to norms other than the Frobenius norm [72, 57].

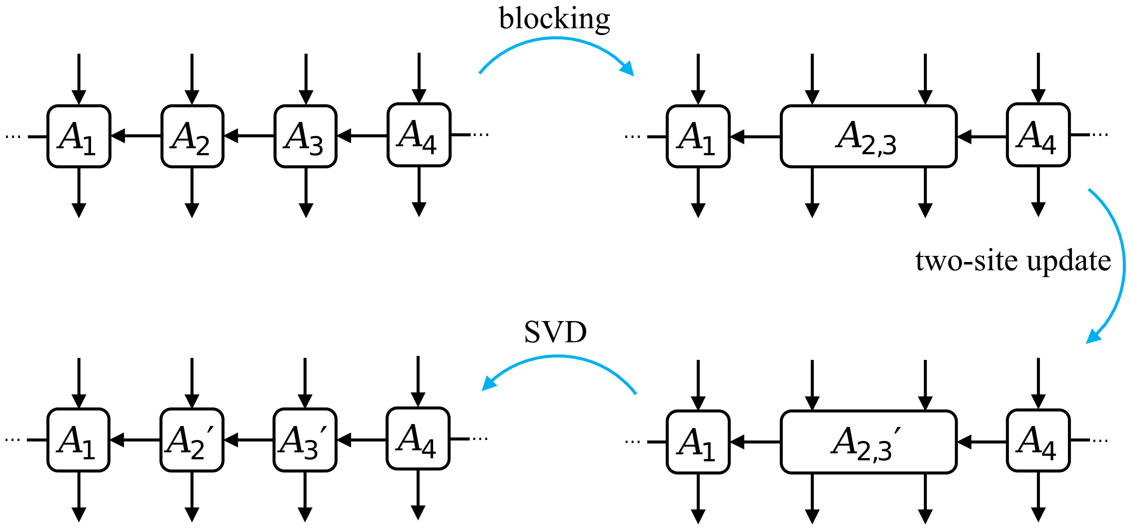

Figure 4.10: Illustration of a two-site update using e.g. VUMPS2 or iDMRG2. An arbitrary gauge is used.

4.2.4 Expand steps

VUMPS2 is not always stable, since the charges and bond dimensions of the tensors are updated locally in each iteration. This can result in large differences in the dimension of the left and right virtual Hilbert space of certain tensors in the unit cell. A more stable algorithm can be found by updating the charges and bonds for the whole unit cell at the same time. This is called an Expand step. The two-site version of this algorithm proceeds in the same way as VUMPS2, in which two adjacent tensors are blocked and updated, after which an SVD is performed. Now, the result of this SVD is not immediately used to update the MPS. Rather, the charges and bond dimensions are saved, and the algorithm proceeds to the next two adjacent tensors. After going through the whole unit cell, the charges and bond dimensions of the whole unit cell are updated. If a bond dimension is smaller than its previous value, the extra charges are just thrown away. If a bond dimension is bigger than its previous value, the charges are added, and some random noise is added to these sectors to ensure numerical stability.

4.3 Entanglement scaling

An intrinsic problem in the optimization of MPS is that the bond dimension has to be finite, whereas the exact solution would only be obtained in the limit of $D \to \infty$. The error resulting from choosing a finite bond dimension vanishes exponentially with the bond dimension for local, gapped Hamiltonians [55]. A possible strategy to amend this, is to plot the observables in function of an error measure, postulate a scaling hypothesis, and extrapolate the results towards error measure zero. Especially for observables like the correlation length this is necessary, since these suffer more from finite bond dimension effects than e.g. the ground state energy.

A first possible error measure is the inverse bond dimension, $\frac{1}{D}$, but it turns out that a much more effective and physical error measure is obtained by looking at the eigenvalues of the transfer matrix, defined in (3.49) and (3.50).

$$T = |1\rangle\langle 1| + \sum_{n=1}^{\infty} \lambda_n |n\rangle\langle n| \tag{4.21}$$

These eigenvalues can be rewritten as

$$\lambda_n = e^{-(\epsilon_n + i\theta_n)} \tag{4.22}$$

where $\epsilon_n, \theta_n \in \mathbb{R}$ and $\epsilon_m \geqslant \epsilon_n$, if $m > n$. Normalisation fixes $\epsilon_1 = 0$ and $\theta_1 = 0$. ϵ_2 is related to the effective correlation length as $\epsilon_2 = 1/\xi_{\text{eff}}$, and θ_2 captures the leading oscillations of the correlation function. In the limit of infinite bond dimension, $\xi_{\text{eff}} = \xi$, the correct correlation length of the system. These definitions are visualized in figure 4.11.

In theory, this spectrum should have a gap to ϵ_2, after that possibly some separate bands, and eventually a continuum. Due to the finite bond dimension used in the calculations, this continuum will be discrete. Deviations from the continuum, and by extension deviations from infinite bond dimension, can thus be characterized in the variable δ

$$\delta = \epsilon_3 - \epsilon_2 \tag{4.23}$$

The bigger the bond dimension, the closer the spectrum will be to a continuum, and the smaller δ will be.

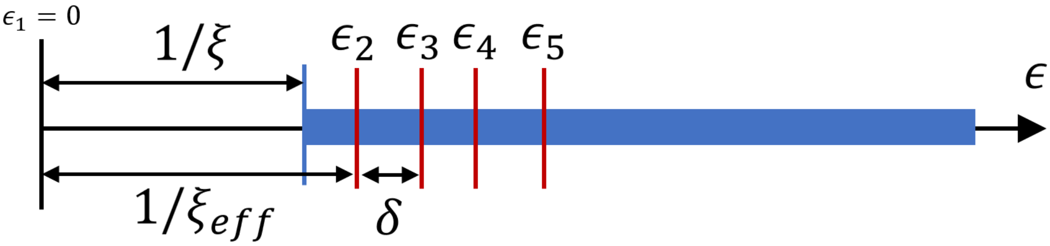

Figure 4.11: Visualization of the extrapolation measure

The observables can then be extrapolated to $D = \infty$ by considering them as a function of the error measure $1/D$ or δ and extrapolating those functions to zero [73, 74]. This can be done by postulating a scaling hypothesis, where it is assumed that for large enough values of D, an observable g obeys the following function

$$g(\delta) = g_e + a\delta^b \tag{4.24}$$

where g_e is the extrapolated value. The fitted value b is usually close to 1, allowing for a simple linear fit in many cases [74]. An example of this extrapolation will be given in figure 8.3, where it is also seen that extrapolation with δ yields more accurate results for the correlation length than extrapolation in $1/D$. This is more generally true [74]. This approach can even be extended beyond the scaling regime, if it is possible to postulate a scaling ansatz for $g(\delta)$ [73].

There are some cases where an alternative to (4.23) should be used. An example is when one is only interested in the correlation functions of a certain sector. Only the eigenvectors corresponding to that sector are then computed, with corresponding eigenvalues ϵ_n^s. The error measure of that specific sector can then be calculated in an analogous way

$$\delta^s = \epsilon_2^s - \epsilon_1^s \tag{4.25}$$

Also, when the eigenvalues are degenerate or become close to degenerate for increasing bond dimension, the error measure should be changed to

$$\delta = \epsilon_n - \epsilon_1 \tag{4.26}$$

if the eigenvalues $\{\epsilon_2, \ldots, \epsilon_{n-1}\}$ are (near) degenerate [74].

Other error measures can be defined, such as the truncation error of the SVD [75, 76]

$$\epsilon_{trunc} = \sum_{m=D+1}^{\infty} \lambda_m = 1 \tag{4.27}$$

which is the sum of the squares of all singular values that are thrown away, and the (approximated or exact) energy variance [77, 78, 79, 80, 81].

$$\epsilon_{var} = \langle\psi| \left(\hat{H} - E\right)^2 |\psi\rangle \tag{4.28}$$

Yet another error measure can be used for critical systems. Here, it is known that the correlation length should be infinite, and the inverse effective correlation length $1/\xi$ of the calculation at finite bond dimension can be used as an error measure. [82, 83, 84, 85, 86, 87]. These approaches do not work outside the critical regimes, however, since there they would require knowledge of a nontrivial scaling function [74].

For finite systems, one can look at the observables in the thermodynamic limit by extrapolating in $1/L$, with L the size of the system [88, 89, 90]. This is called finite-length scaling. Since the MPS used in this thesis are defined directly in the thermodynamic limit, there is no need to do this in this approach.

4.4 Symmetries

4.4.1 Symmetric Tensors

An important way to reduce the computational cost of the algorithms is to take into account the symmetry of the system. When there is a symmetry, not all of the parameters of the MPS will be free and independent. Rather, the MPS can then be fully characterized by a reduced number of free parameters and its symmetry. The symmetry of the MPS will be denoted as one or multiple charges of the corresponding symmetry group, living on each leg of each tensor. This charge will be a conserved quantity, and the way it moves between tensor legs will be denoted with so-called fusion trees [91]. Examples of fusion trees are given in figure 4.12. Each leg of the fusion trees carries a charge, and the total charge should be conserved in each vertex point. The fusion tree of a symmetric two-site operator will look like figure 4.12c.

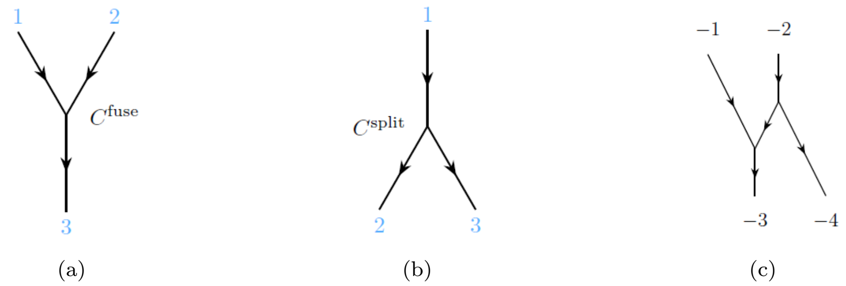

(a) (b) (c)

Figure 4.12: Graphical representation of fusion trees [91]

The mathematics are as follows. For a general fusion tree with k external charges (=legs), there are $l = k - 3$ internal charges. This gives $k + l$ charges in total.

$$\begin{aligned} j_e &= (j_1, \cdots, j_k) \\ j_i &= (j_1, \cdots, j_l) \\ j &= (j_e, j_i) \end{aligned} \tag{4.29}$$

Fixing a certain value of the internal and external charges j gives a block of components of the tensor, or equivalently, a matrix block of its matrix representation. The Wigner-Eckart theorem states that this block can be decomposed in a degeneracy tensor P_j and a structural tensor Q_j. The latter is completely fixed by the symmetry, whereas the former contains only the free (or variational) parameters of the tensor T_j [92, 93, 94, 95]. A three-index structural tensor is also called a Clebsch-Gordan tensor.

$$T_j = P_j \otimes Q_j \tag{4.30}$$

The total tensor T can then be written as

$$T = \bigoplus_j (P_j)_{t_j} \otimes (Q_j)_{m_j} \tag{4.31}$$

where t_j and m_j are the dimensions of the tensors P_j and Q_j, respectively. The structural tensor of an incompatible set of charges is zero, so the direct sum runs only over compatible sets of charges.

Considering a tensor with only one set of external charges, or equivalently, considering a block of a tensor by fixing the external charges, this reduces to

$$T = \bigoplus_{j_i} (P_{j_i})_{t_{j_i}} \otimes (Q_{j_i})_{m_{j_i}} \tag{4.32}$$

Consider a case where the Hamiltonian is a four-leg tensor with fixed spins and degeneracies of one, which implies only one internal leg, as also shown in figure 4.12c. P_{j_i} is now a tensor with only one element, or just a scalar. This means that the expression reduces to

$$T = \sum_{j_i} P_{j_i}(Q_{j_i})_{m_{j_i}} \tag{4.33}$$

This gives a very practical way to implement the Hamiltonian into a numerical simulation. First, the external charges are given, then the fusion trees will be calculated. Finally, the coefficients of each fusion tree are given and the results are summed into the full tensor. Only the coefficients corresponding to fusion trees of an allowed set of external and internal charges, i.e. charges that can conserve the symmetry of the tensor, will be non-zero [91].

4.4.2 The need for a bigger unit cell

Each tensor in a symmetric system will be defined in terms of its symmetry, which means that the Hilbert space on which every space (or leg) of the tensor acts, can be separated into different charge sectors. These charge sectors will be represented by a combination of charges of the total symmetry group of the system.

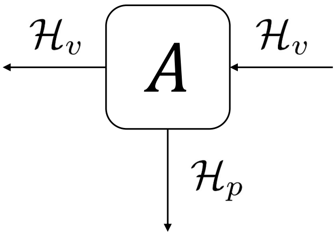

Figure 4.13: Example of a tensor A with its Hilbert spaces

In the case of the tensor of figure 4.13, the Hilbert space is

$$\mathcal{H} = \mathcal{H}_v \otimes \mathcal{H}_p \otimes \mathcal{H}_v^* \tag{4.34}$$

with $\mathcal{H}_v$ and $\mathcal{H}_p$ are respectively the virtual and physical Hilbert spaces. The $*$ denotes the Hermitian conjugate and is represented as an incoming arrow instead of an outgoing one.

A case of non-injectivity is when the Hilbert spaces have a grading and when the physical Hilbert space has odd grading.

$$\begin{cases} \mathcal{H}_v = \mathcal{H}_{v+} \oplus \mathcal{H}_{v-} \\ \mathcal{H}_{v+} \otimes \mathcal{H}_{p-} \cong \mathcal{H}_{v-} \\ \mathcal{H}_{v-} \otimes \mathcal{H}_{p-} \cong \mathcal{H}_{v+} \end{cases} \quad \Rightarrow \text{MPO non-injective} \tag{4.35}$$

The matrix representing the tensor will decompose into separate blocks. The leading eigenvalue will then not be unique anymore, causing problems in the optimization scheme, as mentioned in section 3.4.1.

An example of this will be the Heisenberg XXZ model (see section 5.1), with symmetry $U(1)$. The physical Hilbert space is 2-dimensional and has charges ± 1. The virtual Hilbert space (in theory consisting of all integers) will decompose in the Hilbert space of odd charges and the Hilbert space of even charges. This can be easily seen by realizing that $U(1)$ is abelian and thus that fusing $U(1)$-charges corresponds to simple addition and subtraction. The solution to this is defining a bigger unit cell, consisting of two tensors. $\mathcal{H}_{v1}$ and $\mathcal{H}_{v2}$ will respectively be the left and right virtual spaces of the first site of the unit cell, and the other way around for the second site. This is shown in figure 4.14. In this way, there will be unique left and right environments for each of the tensors in the unit cell, and all problems regarding non-injectivity are solved.

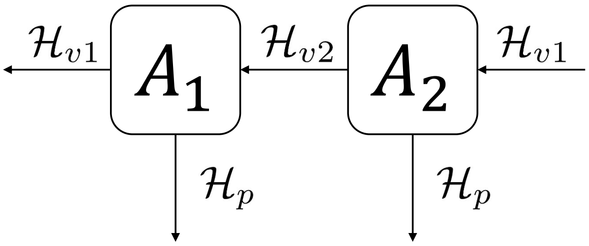

Figure 4.14: Redefinition of the unit cell of a non-injective MPS

4.5 Cylinders

4.5.1 Modelling 2D systems

MPS are inherently 1D objects, but can nevertheless be used to model 2D systems. This can be done by considering the 2D lattice wrapped around a cylinder, as shown in figure 4.15a. Although this new system is quasi-1D, it can still yield accurate results for the 2D system in various cases [96, 97, 98]. Note that the 2D system in this example is defined on the square lattice, which will be used throughout this thesis. This method holds more generally for other lattices, but their mapping to a 1D chain may be more difficult.

The 2D system is made 1D by considering a chain of lattice points looping around the cylinder, thus perfect for the MPS language. Each site in the bulk i is connected to the sites $i+1$,$i-1$, $i+N$, and $i-N$, where N is called the circumference of the cylinder. The system is still infinite in the x-direction, but finite in the y-direction. There are essentially two ways of implementing boundary conditions in the y-direction.

The first option is implementing periodic boundary conditions, as in figure 4.15b. In a certain rung of the cylinder, the first and last site of the rung are connected. The second option is implementing spiral boundary conditions, where the last site of a certain rung is connected to the first site of the next rung, as shown in figure 4.15c. The former quasi-1D system is called a cylinder, the latter a helix.

The Hamiltonian of the 2D system is

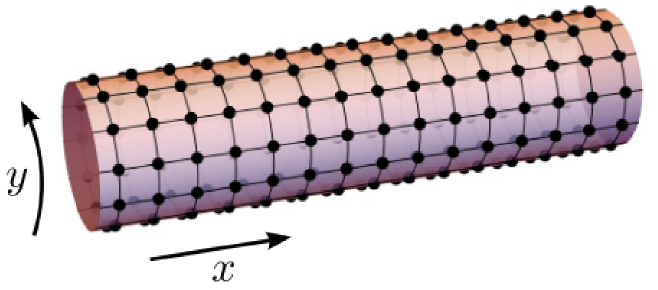

(a) 2D system wrapped around a cylinder [98]

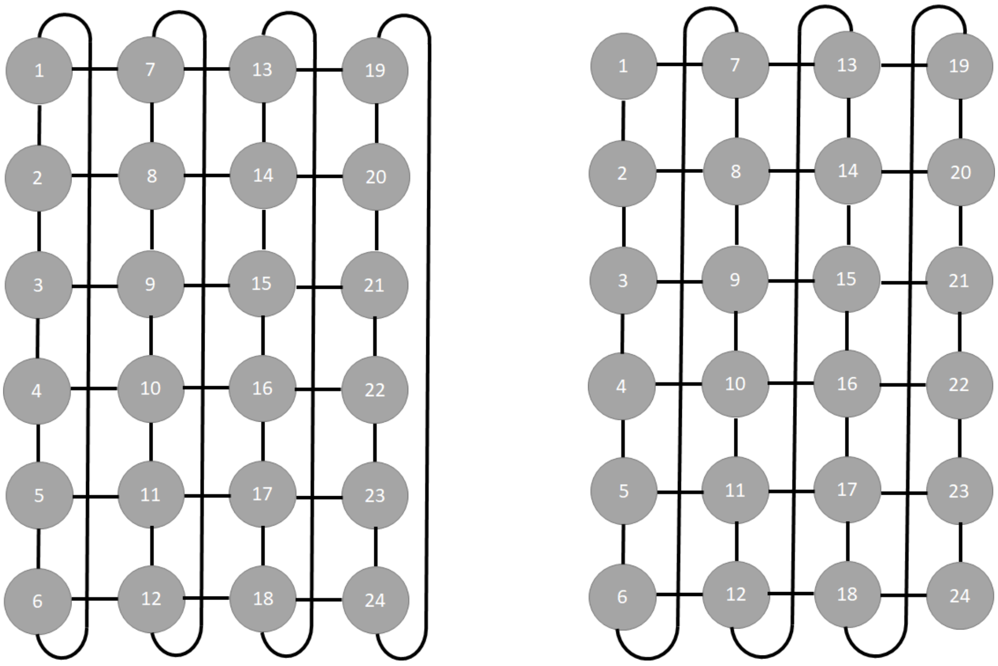

(b) Cylinder

(c) Helix

Figure 4.15: (a) Modelling a 2D system as a quasi-1D system by placing it on a cylinder. Either (b) periodic boundary conditions, corresponding to the cylinder, or (c) spiral boundary conditions, corresponding to the helix, can be imposed. The example shows the $N = 6$ case.

$$H = \sum_{(i,j)\in V} B_{(i,j)} + H_{(i,j),(i+1,j)} + H_{(i,j),(i,j+1)} \tag{4.36}$$

and is approximated in quasi-1D as

$$H = \sum_{i\in V} B_i + H_{i,i+1} + H_{i,i+N} \tag{4.37}$$

where the boundary effects are neglected. $H_{i,j}$ is the interaction Hamiltonian between two sites and B_i the self-interaction. For the limit of N going to infinity, the 2D lattice is successively better approximated.

The JordanMPOs for the 1D Hamiltonian of the cylinder and the helix are given in appendix A. The advantage of the cylinder is that it is the most natural boundary condition for describing 2D systems that preserve a clear distinction between the x and y-direction. The big advantage of the helix however, is the fact that it is translationally invariant in the period of the unit cell, since the Hamiltonian in (4.37) is exact in this case, and the boundary conditions do not need to be taken into account explicitly. For the cylinder, there is only translational invariance over N sites, which means the unit cell has to be an integer multiple of N, which can result in a higher complexity. For a given unit cell, however, the parameter that determines the complexity is the total bond dimension. Since adjacent sites in the x-direction are not adjacent in the 1D system, the information on the entanglement between those two sites now has to pass through $N-1$ other sites. For a given accuracy, this causes an exponential increase in the needed bond dimension. This problem is the same for helices and cylinders.

4.5.2 Staggered magnetization and geometric frustration

To further evaluate whether cylinders and helices can be accurate descriptions of the 2D systems, the staggered magnetization will be investigated. A staggered magnetic field can be applied on the 2D system, i.e.

$$B_{(i,j)} = (-1)^{i+j} h^{stag} \sigma^z_{(i,j)} \tag{4.38}$$

where $B_{(i,j)}$ is the magnetic field on site (i,j). h^{stag} is the staggered magnetic field strength and $\sigma^z_{(i,j)}$ is the Pauli sigma z matrix acting on site (i,j). This can result in a staggered magnetization per site, calculated as the expectation value of

$$m^{stag}_{(i,j)} = (-1)^{i+j} \sigma^z_{(i,j)} \tag{4.39}$$

where thus $-1 < m^{stag} < 1$. The results will be vastly different depending on whether a cylinder or a helix is used.

Figures 4.16a and 4.16b show a cylinder with a staggered magnetic field. For even cylinders, there is no frustration and an external staggered magnetic field can be applied, resulting in a non-zero staggered magnetization. For odd cylinders, there is frustration on the boundary conditions, and the staggered magnetic field will have to be strong enough to overcome the antiferromagnetic two-site interactions. These figures also show that a unit cell of $2N$ is needed in this case, resulting in a higher complexity.

Figures 4.16c and 4.16d show a helix with a staggered magnetic field. For odd helices, there is no frustration, leading to a non-zero staggered magnetization. However, for even helices, applying a staggered magnetic field in two directions (which correspond to the 2D case) is not possible if a unit cell of two is chosen (corresponding to the period of the MPS). A unit cell of $2N$ would have to be chosen, losing the advantage of complexity. Furthermore, there would be frustration on the boundary conditions. Again, the applied staggered magnetic field will have to be strong enough to overcome the antiferromagnetic interactions.

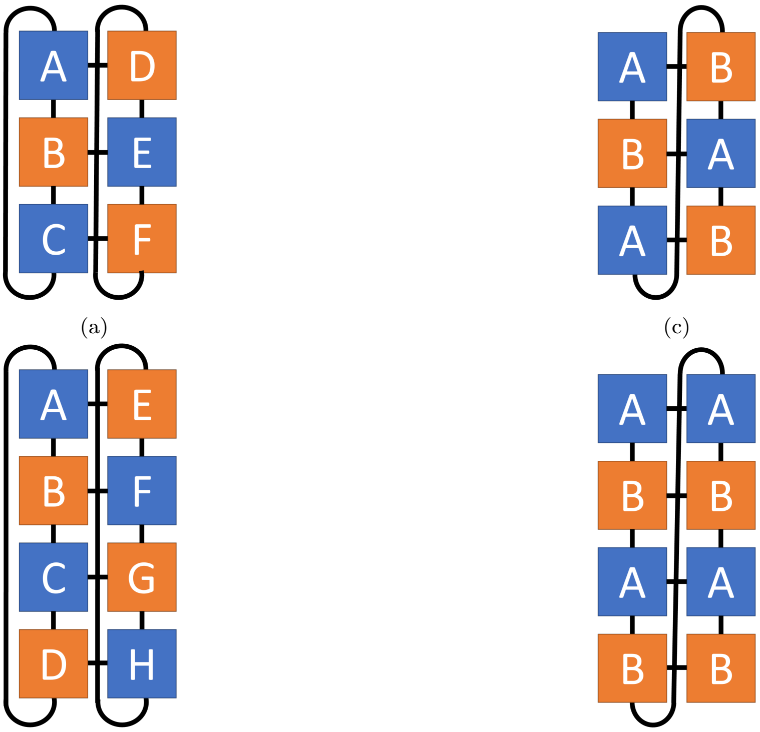

(a) (c) (b) (d)

Figure 4.16: Modelling a 2D system with a staggered magnetic field on a cylinder for (a) N = odd and (b) N = even, and on a helix for (c) N = odd and (d) N = even. Blue and orange denote a positive and negative magnetic field respectively.

A nonzero staggered magnetization breaks the translational invariance of the system. This occurs in the 2D system even without an external field and is called spontaneous symmetry breaking [10]. This can not occur in the 1D system due to Coleman's theorem, which states that continuous symmetries corresponding to an order parameter that does not commute with the Hamiltonian cannot be broken at zero temperature in one-dimensional quantum systems [11] [101]. However, the MPS representation of quasi-1D systems can show spontaneous symmetry breaking because the bond dimension has to be finite. It is thus expected that even though the quasi-1D systems can give accurate results on the 2D system for large N, things like spontaneous symmetry breaking will still not be well described. Results on staggered magnetization will be given in section 8.2.2.

---

[10] Spontaneous symmetry breaking occurs when the ground state of a model does not obey the same symmetry as the underlying system

[11] This is the quantum analog of the Mermin-Wagner theorem [99, 100]

5

Models for Hamiltonians

In this chapter, two important models for Hamiltonians will be described, each with a few of its properties.

5.1 1D Heisenberg Model

The 1D Heisenberg model describes a chain of spin 1/2 particles, with in the most general case the Hamiltonian

$$H_{ij} = J_x \sigma_i^x \sigma_j^x + J_y \sigma_i^y \sigma_j^y + J_z \sigma_i^z \sigma_j^z \tag{5.1}$$

acting between nearest neighbors, where σ_i^a is the Pauli sigma matrix a (x, y or z) on site i. J_x, J_y and J_z are external parameters [82, 102].

5.1.1 1D Heisenberg XXZ Model: U(1) symmetry

If $J_x = J_y \neq J_z$, the model is called the XXZ-model and has U(1) symmetry due to rotational invariance around the z-axis. It corresponds to the conservation of spin projection along the z-axis. In this case, the Hamiltonian is redefined as

$$H_{ij} = \sigma_i^x \sigma_j^x + \sigma_i^y \sigma_j^y + \Delta \sigma_i^z \sigma_j^z \tag{5.2}$$

with Δ a parameter. As a representation of the symmetry, U(1) charges $+1$ and -1 are chosen, which correspond to spin up $|\uparrow\rangle$ and spin down $|\downarrow\rangle$. $\sigma_i \otimes \sigma_i$ corresponds to a 4×4 matrix. In the basis $\{|\uparrow\rangle_i |\uparrow\rangle_j, |\uparrow\rangle_i |\downarrow\rangle_j, |\downarrow\rangle_i |\uparrow\rangle_j, |\downarrow\rangle_i |\downarrow\rangle_j\}$, they can be written down as

$$\sigma_x \otimes \sigma_x = \begin{bmatrix} 0 & 0 & 0 & 1 \\ 0 & 0 & 1 & 0 \\ 0 & 1 & 0 & 0 \\ 1 & 0 & 0 & 0 \end{bmatrix} \tag{5.3}$$

$$\sigma_y \otimes \sigma_y = \begin{bmatrix} 0 & 0 & 0 & -1 \\ 0 & 0 & 1 & 0 \\ 0 & 1 & 0 & 0 \\ -1 & 0 & 0 & 0 \end{bmatrix} \tag{5.4}$$

$$\sigma_z \otimes \sigma_z = \begin{bmatrix} 1 & 0 & 0 & 0 \\ 0 & -1 & 0 & 0 \\ 0 & 0 & -1 & 0 \\ 0 & 0 & 0 & 1 \end{bmatrix} \tag{5.5}$$

$\sigma_x \otimes \sigma_x$ and $\sigma_y \otimes \sigma_y$ break the U(1) symmetry explicitly, but the combination $\sigma_x \otimes \sigma_x + \sigma_y \otimes \sigma_y$ does not, as this corresponds to

$$\sigma_x \otimes \sigma_x + \sigma_y \otimes \sigma_y = \begin{bmatrix} 0 & 0 & 0 & 0 \\ 0 & 0 & 2 & 0 \\ 0 & 2 & 0 & 0 \\ 0 & 0 & 0 & 0 \end{bmatrix} \tag{5.6}$$

This corresponds to flipping the spin of site i and site j. Together with $\sigma_z \otimes \sigma_z$, the full Hamiltonian is given by

$$H_{ij}^{(XXZHeisenberg)} = \begin{bmatrix} \Delta & 0 & 0 & 0 \\ 0 & -\Delta & 2 & 0 \\ 0 & 2 & -\Delta & 0 \\ 0 & 0 & 0 & \Delta \end{bmatrix} \tag{5.7}$$

This Hamiltonian can be exactly diagonalized. The eigenfunctions and their corresponding energy are given by

$$\begin{cases} \left|\uparrow\right\rangle_i \left|\uparrow\right\rangle_j & \sim \Delta \\ \left|\downarrow\right\rangle_i \left|\downarrow\right\rangle_j & \sim \Delta \\ \frac{1}{\sqrt{2}} \Big(\left|\uparrow\right\rangle_i \left|\downarrow\right\rangle_j + \left|\downarrow\right\rangle_i \left|\uparrow\right\rangle_j \Big) & \sim -\Delta + 2 \\ \frac{1}{\sqrt{2}} \Big(\left|\uparrow\right\rangle_i \left|\downarrow\right\rangle_j - \left|\downarrow\right\rangle_i \left|\uparrow\right\rangle_j \Big) & \sim -\Delta - 2 \end{cases} \tag{5.8}$$

Depending on the parameter Δ, different regimes will exist. $\Delta > 1$ is called the antiferromagnetic region. From (5.8), it can be seen that the antisymmetric combination has the lowest energy, yielding an antiferromagnetic ground state (also called Néel order [103, 104]). $\Delta < -1$ is called the ferromagnetic region due to similar arguments. $-1 < \Delta < 1$ is called the XY region. $\Delta = 1$ is a critical point of the system and is called the Heisenberg XXX model. This will be further discussed below.

There are 6 allowed fusion channels. The fusion trees and their values (see (4.33)), are given in table 5.1.

Table 5.1: Fusion trees and their values of the 1D Heisenberg XXZ-model

number	incoming charges	internal charge	outgoing charges	value
(1)	-1 & -1	-2	-1 & -1	Δ
(2)	+1 & -1	0	-1 & +1	2
(3)	-1 & +1	0	-1 & +1	-Δ
(4)	+1 & -1	0	+1 & -1	-Δ
(5)	-1 & +1	0	+1 & -1	2
(6)	+1 & +1	+2	+1 & +1	Δ

5.1.2 1D Heisenberg XXX Model: SU(2) symmetry

If $J_x = J_y = J_z$, or $\Delta = 1$ in the XXZ-model, the model is called the XXX-model and has SU(2) symmetry due to full rotational invariance [82, 102].

H_{ij} can be rewritten as

$$\begin{aligned}H_{ij} =& \sigma_i^x\sigma_j^x + \sigma_i^y\sigma_j^y + \sigma_i^z\sigma_j^z \\ \propto& \, \vec{S}_i \cdot \vec{S}_j \\ =& \frac{1}{2}\left((\vec{S}_i + \vec{S}_j)^2 - S_i^2 - S_j^2\right) \\ =& \begin{cases} \frac{1}{4}, & S_{tot} = 1 \\ -\frac{3}{4}, & S_{tot} = 0 \end{cases}\end{aligned} \tag{5.9}$$

with S the spin operator. The lowest corresponds to total spin 0, which means antiferromagnetic order.

Choosing the two-dimensional representation of SU(2) (with internal charges 0 and 1) leads to the fusion trees and their values given in table 5.2. The difference in sign with respect to (5.9) is due to different conventions in the definition of the Clebsch-Gordan coefficients.

Table 5.2: Fusion trees and their values of the 1D Heisenberg XXZ-model

number	incoming charges	internal charges	outgoing charges	value
(1)	1/2 & 1/2	0	1/2 & 1/2	-3/4
(2)	1/2 & 1/2	1	1/2 & 1/2	-1/4

5.2 Hubbard Model

The Hubbard model was proposed in 1963 as a simple model describing interacting fermions on a lattice by Hubbard, Kanamori, and Gutzwiller [38, 105, 106, 107]. It is defined as [37, 38, 39, 40]

$$\begin{aligned}H &= -\sum_{i,j\in\Lambda}\sum_{\sigma} t_{ij}\left(c_{i\sigma}^\dagger c_{j\sigma} + c_{j\sigma}^\dagger c_{i\sigma}\right) + \sum_{i\in\Lambda} U_i c_{i\uparrow}^\dagger c_{i\downarrow}^\dagger c_{i\downarrow} c_{i\uparrow} \\ &= -\sum_{i,j\in\Lambda}\sum_{\sigma} t_{ij}\left(c_{i\sigma}^\dagger c_{j\sigma} + c_{j\sigma}^\dagger c_{i\sigma}\right) + \sum_{i\in\Lambda} U_i n_{i\uparrow} n_{i\downarrow}\end{aligned} \tag{5.10}$$

i and j denote sites on a lattice Λ. The sites have an interaction strength U_i and sites i and j interact with a hopping term t_{ij}. $c_{i\sigma}^\dagger$ and $c_{i\sigma}$ are respectively the creation and annihilation operators for the state with quantum numbers i, the site number, and σ, the spin. $n_{i\sigma}$ is the number operator and counts the number of fermions with spin σ on site i.

For the translationally invariant case, $U_i = U$ and $t_{ij} = t$ when i and j are neighboring sites. It can be rewritten as

$$H_{ij} = -\sum_{\sigma} t\left(c_{i\sigma}^\dagger c_{j\sigma} + c_{j\sigma}^\dagger c_{i\sigma}\right) \tag{5.11}$$

$$B_i = U c_{i\uparrow}^\dagger c_{i\downarrow}^\dagger c_{i\downarrow} c_{i\uparrow} \tag{5.12}$$

$$H = \sum_{\langle ij \rangle \in \Lambda} H_{ij} + \sum_{i \in \Lambda} B_i \tag{5.13}$$

with H_{ij} the two-site interaction or hopping term and B_i the self-interaction. $\langle \cdots \rangle$ denotes nearest neighbors. The Hilbert space at one site is

$$\mathcal{H} = \{|0\rangle, |\uparrow\rangle, |\downarrow\rangle, |\uparrow\downarrow\rangle\} \tag{5.14}$$

H_{ij} is thus a (2,2) tensor operator with dimension $4^{2+2} = 256$.

In the 1D case, with only neighbor hopping, this reduces to

$$H = -\sum_{i \in \Lambda} \sum_{\sigma} t_{i,i+1} \left(c^{\dagger}_{i\sigma} c_{i+1,\sigma} + c^{\dagger}_{i+1,\sigma} c_{i\sigma} \right) + U \sum_{i \in \Lambda} c^{\dagger}_{i\uparrow} c^{\dagger}_{i\downarrow} c_{i\downarrow} c_{i\uparrow} \tag{5.15}$$

The Hubbard model has the symmetry $U(2) \cong U(1) \otimes SU(2)$. The U(1) symmetry denotes global charge conservation and makes the number operator $\hat{n} = \sum_{i,\sigma} c^{\dagger}_{i\sigma} c_{i\sigma}$ a good quantum number. The SU(2) symmetry denotes spin isotropy and makes the total spin and the spin projection on the z-axis, $\hat{\vec{S}}^2$ and $\hat{S}^z$, good quantum numbers [37].

Due to spin isotropy, there will be no distinction between spin up and spin down states. Their Hilbert space is thus 4-dimensional and corresponds to representations of $U(1) \otimes SU(2) \otimes f\mathbb{Z}_2$, where $f\mathbb{Z}_2$ is the $\mathbb{Z}_2$ symmetry of fermions, denoting that they have anticommutation relations. The quantum numbers for this case are given in table 5.3.

Table 5.3: Quantum number for U(1) $\otimes$ $SU(2) \otimes f\mathbb{Z}_2$

state	U(1)	SU(2)	$f\mathbb{Z}_2$
$\|0\rangle$	0	0	1
$\|\uparrow\rangle$ or $\|\downarrow\rangle$	1	1/2	-1
$\|\uparrow\downarrow\rangle$	2	0	1

If a distinction between spin up and spin down is made, the Hilbert space will correspond to representations of $U(1) \otimes U(1) \otimes f\mathbb{Z}_2$, leading to the quantum numbers of table 5.4

Table 5.4: Quantum number for U(1) $\otimes$ $U(1) \otimes f\mathbb{Z}_2$

state	U(1)	U(1)	$f\mathbb{Z}_2$
$\|0\rangle$	0	0	1
$\|\uparrow\rangle$	1	1	-1
$\|\downarrow\rangle$	1	-1	-1
$\|\uparrow\downarrow\rangle$	2	0	1

5.2.1 Filling

The electron filling f is defined as

$$f = \frac{N_e}{N} \tag{5.16}$$

where N_e is the number of electrons in the system and N is the number of sites. Consequently, $0 \leqslant f \leqslant 2$. The corresponding hole density δ can be defined as

$$\delta = \frac{N_h}{N} = 1 - f \tag{5.17}$$

with N_h the number of holes in the system, and thus $N_e + N_h = N$. Half-filling is obtained for $N_e = N$ or $\delta = 0$. For half-filling, it can be interesting to redefine the Hubbard Hamiltonian as

$$H_{ph} = -\sum_{i,j\in\Lambda}\sum_{\sigma} t_{ij}\left(c^{\dagger}_{i\sigma}c_{j\sigma} + c^{\dagger}_{j\sigma}c_{i\sigma}\right) + \sum_{i\in\Lambda} U_i(n_{i\uparrow}-1)(n_{i\downarrow}-1) \tag{5.18}$$

The difference with the Hamiltonian defined in (5.10), is

$$\begin{aligned} H_{ph} &= H + \sum_{i\in\Lambda} U_i(1 - n_{i\uparrow} - n_{i\downarrow}) \\ &= H + \sum_{i\in\Lambda} U_i(1 - n_i) \end{aligned} \tag{5.19}$$

If $U_i \equiv U$, this just corresponds to an energy shift of $U(1-f)$ per site. This will not influence the ground state for a given filling. What is interesting about this, is that the Hamiltonian of (5.18) is particle-hole symmetric around half-filling. This means that the same result is obtained for fillings $f = 1+g$ as for $f = 1-g$. This particle-hole symmetry is an extra $SU(2)$ symmetry, giving the whole system the symmetry $SO(4)$ [37]. The Hubbard model as defined in (5.10) will be used throughout this thesis unless mentioned otherwise.

If the $U(1)$ symmetry is not imposed for the charge sector, the filling can be optimized as well. Using Hamiltonian H, the system will be optimized towards zero filling. Using Hamiltonian H_{ph}, the system will be optimized towards half-filling. If a certain filling f is desired, it has to be specified somehow, for which there are two main possibilities. One uses the chemical potential, where a higher chemical potential means fewer electrons in the system. In this case, it is not a priori known in all cases which value for the chemical potential is needed for a given filling. Another possibility is to impose the filling exactly, using the charges of the symmetries in the physical Hilbert space. Here, it is a priori known which charges are needed for a given filling. Both will be explained below.

Exact implementation Supplying the quantum numbers of table 5.3 or 5.4 to the VUMPS algorithm will give zero filling everywhere, since the optimized MPS will transform trivially under each symmetry group, and will thus have charge zero in each sector. The way to amend this is to impose a certain filling f. In the case of a rational filling $f = P/Q$ [12], this leads to table 5.5 for the case of $U(1) \otimes SU(2) \otimes f\mathbb{Z}_2$.

This reduces to the case above if $P = 0$ and $Q = 1$. Half-filling is obtained by $P = Q = 1$. The virtual spaces can be found in appendix C. This approach has the downside that the minimal size of the unit cell has to be

---

[12] The code required integer values of the $U(1)$ charges, whereby only rational fillings can be implemented. This is theoretically sufficient, however, since $\mathbb{Q}$ is dense in $\mathbb{R}$. Practically, however, the value of Q influences the complexity.

Table 5.5: Quantum number for $U(1) \otimes\ SU(2) \otimes f\mathbb{Z}_2$ in case of filling P/Q

state	U(1)	SU(2)	$f\mathbb{Z}_2$
$\vert 0\rangle$	$-P$	0	1
$\vert \uparrow\rangle$	$Q-P$	1/2	-1
$\vert \downarrow\rangle$	$Q-P$	1/2	-1
$\vert \uparrow\downarrow\rangle$	$2Q-P$	0	1

$$\begin{cases} Q, \text{if } P \text{ is even} \\ 2Q, \text{if } P \text{ is odd} \end{cases} \tag{5.20}$$

The size of the unit cell always has to be an integer multiple of this minimal size.

Implementation using the chemical potential An alternative to the exact implementation of the previous section is the implementation of a chemical potential μ. Here, the Hubbard Hamiltonian is changed to [108]

$$H \rightarrow H' = H - \mu \sum_{i \in \Lambda} n_i \tag{5.21}$$

The introduction of a positive (negative) chemical potential makes it more favorable for the system to have a higher (lower) electron filling. In order for this extra term to have an effect on the ground state electron filling, the $U(1)$ symmetry can not be imposed for the charge sector. Furthermore, it is not a priori known what value of the chemical potential needs to be imposed in order to have a given filling (unless the analytical result is known, which only exists in 1D). Both methods will be looked at, as they both have advantages and disadvantages.

5.2.2 Implementation

The implementation of the above model can most easily be done by defining the creation and annihilation operators separately. Specifically, only the creation operators $c_\uparrow^\dagger$ and $c_\downarrow^\dagger$ have to be defined, since the annihilation operators follow by hermitian conjugation.

These operators do not satisfy the symmetries, since they create or annihilate an electron and its corresponding $U(1)$-charge. They can nevertheless still be defined by adding an auxiliary leg that carries this additional charge. The tensor can then be defined as acting on the physical space and the auxiliary space. Explicitly, if an operator creates a charge c, a corresponding Hilbert space $\mathcal{H}_c$ can be defined, and the operator $\hat{O}$ can be defined as

$$\hat{O} : \mathcal{H}_p \otimes \mathcal{H}_c \longrightarrow \mathcal{H}_p \tag{5.22}$$

The conjugate of this operator has the conjugate charge going into the tensor, or equivalently, the same charge coming out of the tensor. The operator $\hat{O}\hat{O}^*$ can then be written down as a tensor contraction of the 2 individual operators and will satisfy all symmetries. This is shown in figure 5.1.

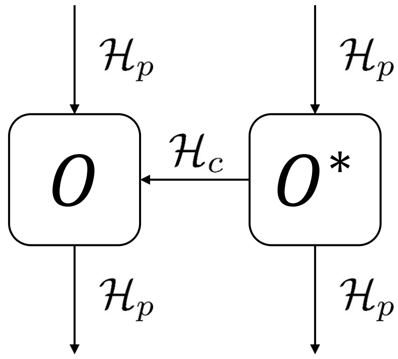

Figure 5.1: Diagrammatic representation of the operator $\hat{O}\hat{O}^*$

In the case of imposing $U(1) \otimes U(1) \otimes f\mathbb{Z}_2$, $\mathcal{H}_c$ has dimension 1, and the operators are $4 \times 1 \times 4$ operators. They are given in (5.23)-(5.26) in the basis defined by $\{|0\rangle, |{\downarrow}\rangle, |{\uparrow}\rangle, |{\uparrow\downarrow}\rangle\}$.

$$c_\uparrow^\dagger = \begin{bmatrix} 0 & 0 & 0 & 0 \\ 0 & 0 & 0 & 0 \\ 1 & 0 & 0 & 0 \\ 0 & 1 & 0 & 0 \end{bmatrix} \tag{5.23}$$

$$c_\downarrow^\dagger = \begin{bmatrix} 0 & 0 & 0 & 0 \\ 1 & 0 & 0 & 0 \\ 0 & 0 & 0 & 0 \\ 0 & 0 & -1 & 0 \end{bmatrix} \tag{5.25}$$

$$c_\uparrow = \begin{bmatrix} 0 & 0 & 1 & 0 \\ 0 & 0 & 0 & 1 \\ 0 & 0 & 0 & 0 \\ 0 & 0 & 0 & 0 \end{bmatrix} \tag{5.24}$$

$$c_\downarrow = \begin{bmatrix} 0 & 1 & 0 & 0 \\ 0 & 0 & 0 & 0 \\ 0 & 0 & 0 & -1 \\ 0 & 0 & 0 & 0 \end{bmatrix} \tag{5.26}$$

where matrix element $O_{kl} = \langle\psi_k| \hat{O} |\psi_l\rangle$ and where the convention $|{\uparrow\downarrow}\rangle = c_\uparrow^\dagger c_\downarrow^\dagger |0\rangle$ is used.

In the case of imposing $U(1) \otimes SU(2) \otimes f\mathbb{Z}_2$, operators like $c_{i\uparrow}$ can not be defined and the operator $c_{i\uparrow}^\dagger c_{j\uparrow} + c_{j\downarrow}^\dagger c_{i\downarrow}$ has to be redefined as $c_i^\dagger c_j$, where c and $c^\dagger$ are operators of the form of (5.22). Here, $\mathcal{H}_c$ has dimension 2, one for $|{\uparrow}\rangle$ and one for $|{\downarrow}\rangle$, and the operators are $4 \times 2 \times 4$ operators. They are given in (5.27)-(5.30) [13].

$$c_1^\dagger = \begin{bmatrix} 0 & 0 & 0 & 0 \\ 1 & 0 & 0 & 0 \\ 0 & 0 & 0 & 0 \\ 0 & 0 & -1 & 0 \end{bmatrix} \tag{5.27}$$

$$c_2^\dagger = \begin{bmatrix} 0 & 0 & 0 & 0 \\ 0 & 0 & 0 & 0 \\ 1 & 0 & 0 & 0 \\ 0 & 1 & 0 & 0 \end{bmatrix} \tag{5.29}$$

$$c_1 = \begin{bmatrix} 0 & 1 & 0 & 0 \\ 0 & 0 & 0 & 0 \\ 0 & 0 & 0 & 1 \\ 0 & 0 & 0 & 0 \end{bmatrix} \tag{5.28}$$

$$c_2 = \begin{bmatrix} 0 & 0 & 1 & 0 \\ 0 & 0 & 0 & -1 \\ 0 & 0 & 0 & 0 \\ 0 & 0 & 0 & 0 \end{bmatrix} \tag{5.30}$$

The same operators when the $U(1)$ symmetry is dropped, are

---

[13] The subindex denotes the second index of the operators

$$c_1^\dagger = \begin{bmatrix} 0 & 0 & 0 & 0 \\ 0 & 0 & 0 & -1 \\ 1 & 0 & 0 & 0 \\ 0 & 0 & 0 & 0 \end{bmatrix} \tag{5.31}$$

$$c_1 = \begin{bmatrix} 0 & 0 & 1 & 0 \\ 0 & 0 & 0 & 0 \\ 0 & 0 & 0 & 0 \\ 0 & 1 & 0 & 0 \end{bmatrix} \tag{5.32}$$

$$c_2^\dagger = \begin{bmatrix} 0 & 0 & 0 & 0 \\ 0 & 0 & 1 & 0 \\ 0 & 0 & 0 & 0 \\ 1 & 0 & 0 & 0 \end{bmatrix} \tag{5.33}$$

$$c_2 = \begin{bmatrix} 0 & 0 & 0 & 1 \\ 0 & 0 & 0 & 0 \\ 0 & -1 & 0 & 0 \\ 0 & 0 & 0 & 0 \end{bmatrix} \tag{5.34}$$

The basis used is $\{\{|0\rangle, |\uparrow\downarrow\rangle\}, |\downarrow\rangle, |\uparrow\rangle\}$.

5.2.3 The extended Hubbard model

The Hubbard model defined in (5.10) is called the simple or pure Hubbard model, with only nearest-neighbor interactions. In the extended Hubbard model, there are further-reaching hopping terms and off-site repulsive interactions. The latter correspond to extra terms in the Hamiltonian

$$H_V = \sum_{i,j\in\Lambda} V_{ij} n_i n_j \tag{5.35}$$

Example Hamiltonians of extended Hubbard models are the one-band and three-band models defined in the next chapter.

6 The cuprates

> ”It doesn’t matter whether you can or cannot achieve high-temperature superconductivity or fuel cells, they will always be on the list because if you could achieve them they would be extremely valuable.”
>
> *Martin Fleischmann*

6.1 Introduction

Superconductors have vanishing electrical resistance under a certain temperature, called the critical temperature T_c. They were first discovered by the Dutch physicist Heike Kamerlingh Onnes in 1911, when he found that mercury exhibits superconductivity with $T_c = 4.2K$ [109]. Thus began the search for materials exhibiting superconductivity at room temperature. A big step in this search was the discovery of high-temperature superconductivity in 1986 [110]. Here, they found a critical temperature of 30K, the highest at the time, for a system consisting of barium, lanthanum, copper, and oxide, specifically $\mathrm{Ba}_x\mathrm{La}_{5-x}\mathrm{Cu}_5\mathrm{O}_{5(3-y)}$ with $x = 1$ and 0.75 and $y > 0$. The original theory to describe superconductivity proposed by Bardeen, Cooper, and Schrieffer, called BCS theory, failed to describe this high-temperature superconductivity [111, 112]. A complete theory of this effect is still missing, more than 40 years after its discovery. A historical overview of different types of superconductors is shown in figure 6.1.

The La-Ba-Cu-O system where high-T_c superconductivity was first found is part of a more general class of materials called the cuprates. They consist of sheets of CuO_2-planes, which are shown in figure 6.2. Here, the d-orbitals of the copper atoms are shown in red and form a square lattice. The p_x and p_y-orbitals of oxygen are shown in blue and are situated between two copper atoms. These CuO_2-planes are stacked on top of each other and are separated by insulating charge reservoirs, consisting of oxygen and heavier elements. The conduction occurs within these CuO_2-planes, which makes it a 2-dimensional problem [114]. The copper d-orbitals and the oxygen p-orbitals are responsible for the (super)conductivity. The atomic structures of two important cuprates are shown in figure 6.3.

In the basis compound, e.g. in $\mathrm{La}_2\mathrm{CuO}_4$, the insulating layers consist only of lanthanum and oxygen. The corresponding electron filling in the CuO_2-planes is $f = 5/3$, where the p-orbitals of oxygen are completely filled and one electron resides on the d-orbitals of copper [118]. By changing a fraction x of the lanthanum atoms to e.g. barium or strontium, thus creating the compound $\mathrm{La}_{2-x}\mathrm{Ba}_x\mathrm{CuO}_4$ or $\mathrm{La}_{2-x}\mathrm{Sr}_x\mathrm{CuO}_4$, the CuO_2-planes are doped with holes, decreasing the filling to $f = (5 - x)/3$.

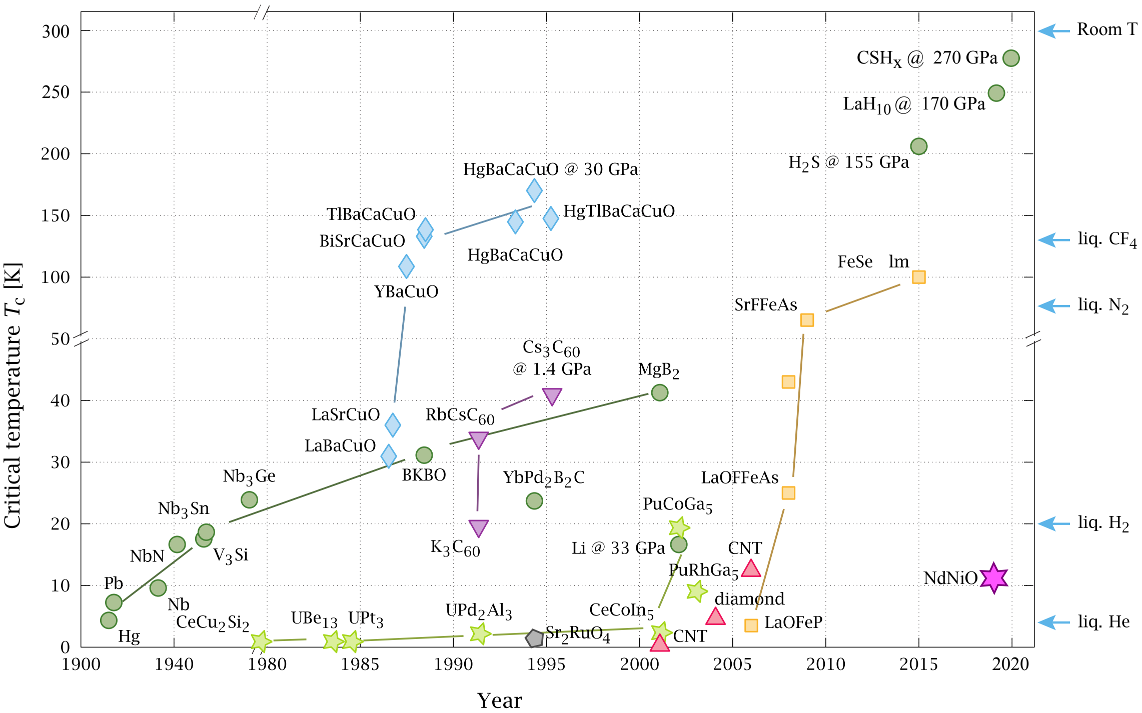

Figure 6.1: Historical evolution of confirmed superconductors [113]

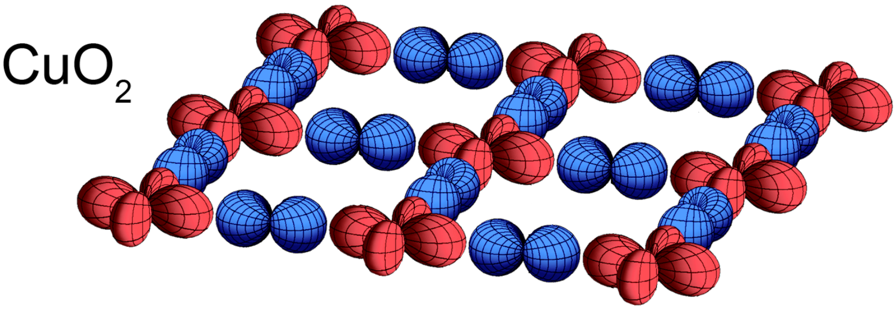

Figure 6.2: A CuO_2-plane [115].

6.2 Three-band versus one-band

6.2.1 Definitions and Hamiltonians

To describe these systems with TN, a 2D lattice has to be defined. One possibility is to define a tensor for each copper d-orbital and oxygen p-orbital atom separately. This is the three-band model and is shown in figure 6.4. The minimal unit cell then consists of a square containing a copper d-orbital, an oxygen p_x-orbital, and an oxygen p_y-orbital. Since the MPS are wrapped around cylinders, which are 1D, this unit cell will have to be flattened out. In this thesis, the order copper

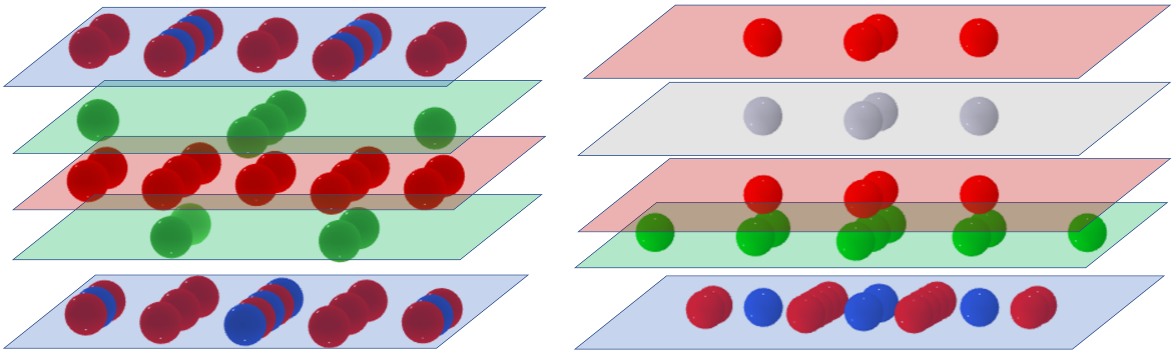

(a) La_2CuO_4. Figure adapted from [116]

(b) Ba_2HgCuO_4. Figure adapted from [117]

Figure 6.3: Atomic structure for cuprates (a) La_2CuO_4 and (b) Ba_2HgCuO_4 showing high-T_c superconductivity. Oxygen is red, copper is blue. For (a), lanthanum is green. For (b), barium is green and mercury is grey. The blue planes are the CuO_2-plane showing superconductivity. The other planes are insulating and act as charge reservoirs.

d, oxygen p_x, oxygen p_y from top to bottom was chosen [14]. The filling of the undoped compound in the three-band model is 5/3, by the discussion of section 6.1. The Hamiltonian that corresponds to this model is written down in (6.1) in the electron picture.

$$\begin{aligned} H = &- \sum_{\langle ij\rangle\sigma} (-1)^{P_{ij}} t_{pd} \left(d^\dagger_{i\sigma} p_{j\sigma} + p^\dagger_{j\sigma} d_{i\sigma} \right) - \sum_{\langle jj'\rangle\sigma} (-1)^{P_{ij}} t_{pp} \left(p^\dagger_{j\sigma} p_{j\sigma} + p^\dagger_{j'\sigma} p_{j\sigma} \right) - \Delta_{dp} \sum_{i\sigma} n_{i\sigma} \\ &+ U_d \sum_i n_{i\uparrow} n_{i\downarrow} + U_p \sum_i n_{j\uparrow} n_{j\downarrow} + V_{pd} \sum_{\langle ij\rangle\sigma\sigma'} n_{i\sigma} n_{j\sigma'} + V_{dd} \sum_{\langle ii'\rangle\sigma\sigma'} n_{i\sigma} n_{i'\sigma'} + V_{pp} \sum_{\langle jj'\rangle\sigma\sigma'} n_{j\sigma} n_{j'\sigma'} \end{aligned} \tag{6.1}$$

$d^\dagger_{i\sigma}$ ($d_{i\sigma}$) and $p^\dagger_{j\sigma}$ ($p_{j\sigma}$) are the creation (annihilation) operators for an electron on a copper atom on site i and an oxygen atom on site j, respectively. $t_{pd} > 0$ is the hopping between neighbouring copper and oxygen atoms. $t_{pp} > 0$ is the hopping between neighbouring oxygen atoms. Δ_{dp} is the energy difference between the occupation of an electron between the copper d and oxygen p-orbital and is equal to $\epsilon_p - \epsilon_d > 0$. U_d and U_p are the on-site screened Coulomb repulsion terms (also called self-interaction) for the copper and oxygen atoms respectively [15]. V_{pd} is the off-site Coulomb repulsion between neighbouring copper and oxygen atoms. $\langle \cdots \rangle$ denotes neighbouring sites. $\overline{\sigma}$ denotes the opposite spin of σ. $n_{i\sigma}$ denotes the number operator on site i of spin σ.

It can still be chosen how the orbitals are oriented, i.e. what their phase is. The relative phases between orbitals will determine the sign of the interaction. The definition of the phases is chosen such that hopping between copper and oxygen within a unit cell has a positive sign. The resulting sign conventions are shown in figure 6.4. This determines whether P_{ij} is even or odd for a given interaction. The interactions V_{pd} are placed on the same sites as the terms t_{pd}, but always have a positive sign [120].

---

[14] The order of the orbitals must be chosen such that strongly entangled sites are as close to each other as possible along the 1D chain [119].

[15] When using cRPA as downfolding procedure, these are the partially screened Coulomb repulsion terms [28].

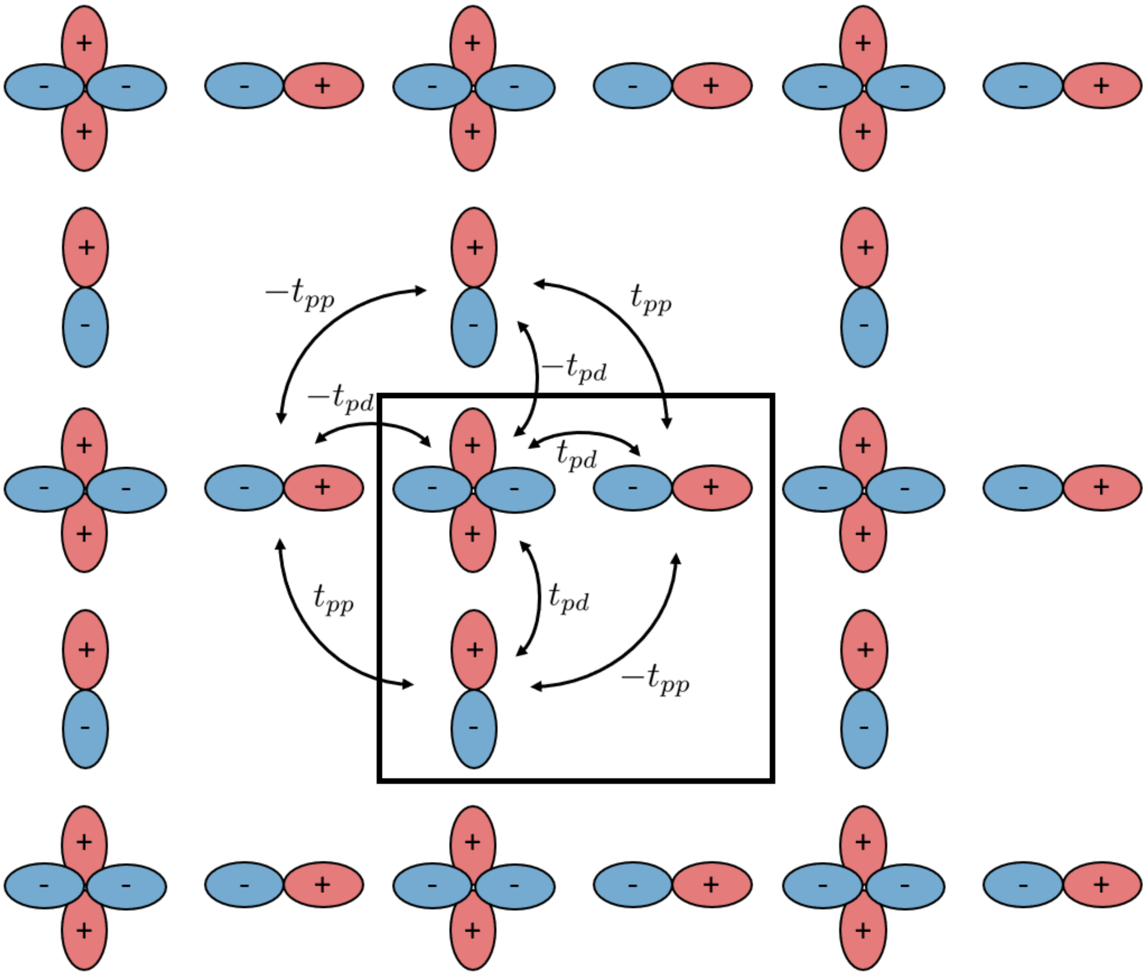

Figure 6.4: Definition of the hopping terms of the three-band Hubbard model with the appropriate conventions. The p_x and p_y-orbitals correspond to oxygen atoms, the d-orbitals correspond to copper atoms. The V_{pd} and V_{pp} terms act on the same locations as t_{pd} and t_{pp}, respectively, but are always positive. The V_{dd} terms act between nearest-neighbor copper atoms and are not shown for clarity.

Anderson [121, 122] showed that the rich physics of the cuprates might even be captured in full by considering only the copper d-orbitals. An effective Hamiltonian for this can be obtained by downfolding the three-band effective Hamiltonian further to this one-band model. (6.2) shows this Hamiltonian. Figure 6.5 shows the one-band model with the definitions for this equation. In the one-band model, the p-orbitals of oxygen are assumed to be completely filled and are not taken into account explicitly. This one-band model is thus half-filled in the case of no doping. This reasoning will be refined in the next section.

$$H = -t \sum_{\langle ii'\rangle\sigma} \left(d^\dagger_{i\sigma} d_{i'\sigma} + d^\dagger_{i'\sigma} d_{i\sigma}\right) - t' \sum_{\langle\langle ii'\rangle\rangle\sigma} \left(d^\dagger_{i\sigma} d_{i'\sigma} + d^\dagger_{i'\sigma} d_{i\sigma}\right) + U \sum_i n_{i\sigma} n_{i\bar{\sigma}} + V \sum_{\langle ii'\rangle\sigma\sigma'} n_{i\sigma} n_{i'\sigma'} \tag{6.2}$$

Here, $\langle\langle\cdots\rangle\rangle$ denotes next-to-neighbour interactions, i.e. interactions along a diagonal. From the sign conventions in figure 6.5 it is immediately clear that $t > 0$ and $t' < 0$.

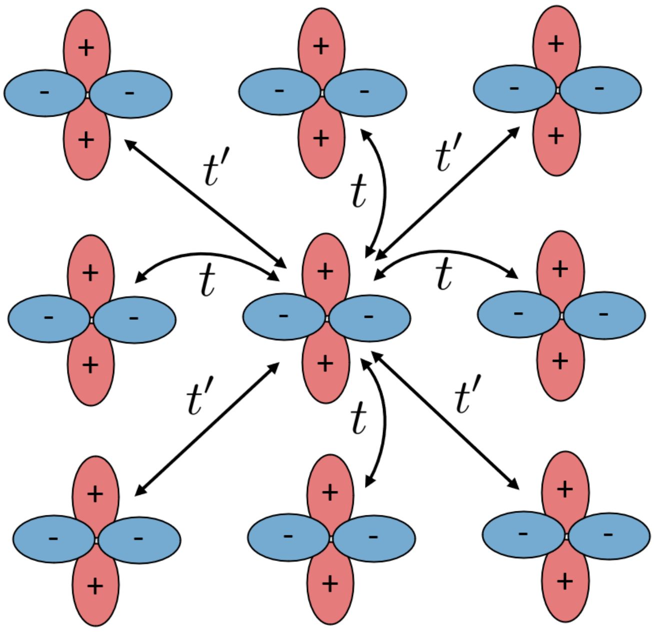

Figure 6.5: Definition of the hopping terms of the one-band Hubbard model with the appropriate conventions

Hirayama et al. derived the relevant Hubbard parameters for the description of cuprates $HgBa_2CuO_4$ and La_2CuO_4 [123] [124]. The values of the former, as used in this thesis, are given in appendix D.

6.2.2 Downfolding from three-band to one-band model

When doping the three-band model, most holes reside on oxygen atoms. The idea behind the downfolding from the three-band to the one-band model is that the hybridization of the orbitals strongly binds a hole on each square consisting of a copper atom and its four surrounding oxygen atoms. Together with the hole present at half-filling, this creates a singlet, called a Zhang-Rice Singlet (ZRS). This singlet can then act as a hole in an effective model describing only the hybridized copper atoms [118, 125, 126, 127, 128]. The Coulomb interactions of the one-band model thus do not describe the interaction between holes located on the different copper atoms, but rather the interactions between these ZRS [129] located on hybridized orbitals. The existence and importance of the ZRS have been verified, and it has been noticed that its weight in the ground state varies surprisingly little across different compounds despite the variation in the three-band parameters. The same holds for the U/t ratio [129]. Although these references state that such a one-band model might be sufficient to describe the cuprates, there are important differences between the one-band and the three-band model. The three-band model is also far less investigated, and a consensus on its properties is still missing [128, 130].

6.3 Ground state

The Hubbard model has turned out to describe the physics of high-temperature superconductivity, sparking extra interest in the numerical simulation of the model. Despite being proposed over 60 years ago and despite its simplicity, basic questions about the ground state in different parameter regimes of the Hubbard model remain unanswered. Only in 1D, where the Hubbard model can be exactly solved by the Bethe ansatz [131], have those questions been settled. For higher dimensions, the only option is to resort to numerical methods. It became clear very early on that the standard methods in condensed matter theory were insufficiently accurate to simulate the Hubbard model, and new methods have been developed in the subsequent years to obtain the desired accuracy. These methods include quantum Monte Carlo (QMC) [132, 133, 134], density matrix embedding theory (DMET) [135, 136], density matrix renormalization group (DMRG) [14, 15], dynamical cluster approximation (DCA) [137], unrestricted coupled cluster theory [138, 139, 140], and TN [9, 42, 48, 141] [142]. These methods allowed us to explore the rich physics inherent to the Hubbard model, and in recent years have reached a consensus in many of the parameter regimes [38].

Figure 6.6a shows the phase diagram of the cuprates in function of the temperature and hole doping. Various phases exist, such as the antiferromagnetic phase, *d*-wave superconductivity, stripe order, the pseudogap phase, the strange metal phase, and the Fermi liquid [143, 144, 145, 146]. The critical temperature exhibits a dome-like shape, with optimal doping around $\delta \approx 0.16$ [147, 148, 149]. The region of superconducting order below and above this value are called the underdoped and overdoped regimes, respectively. This thesis will try to numerically investigate this phase diagram at zero temperature.

On the other hand, figure 6.6b shows the current phase diagram of the 2D Hubbard model at zero temperature in function of doping [38], at intermediate interaction strength. This shows great similarity with the phase diagram of the cuprates, which is the reason why the Hubbard model has been identified as a good model to describe these materials. At half-filling, the Hubbard model is a Mott insulator with antiferromagnetic order [150]. The value $U/t \approx 8$ has been identified as being realistic for the cuprates. Extensive studies have looked at the ground state in this parameter regime, and concluded that stripe states, where the charge density is spatially modulated, exist in a wide range of doping levels. The stripe states are also called charge density waves (CDW).

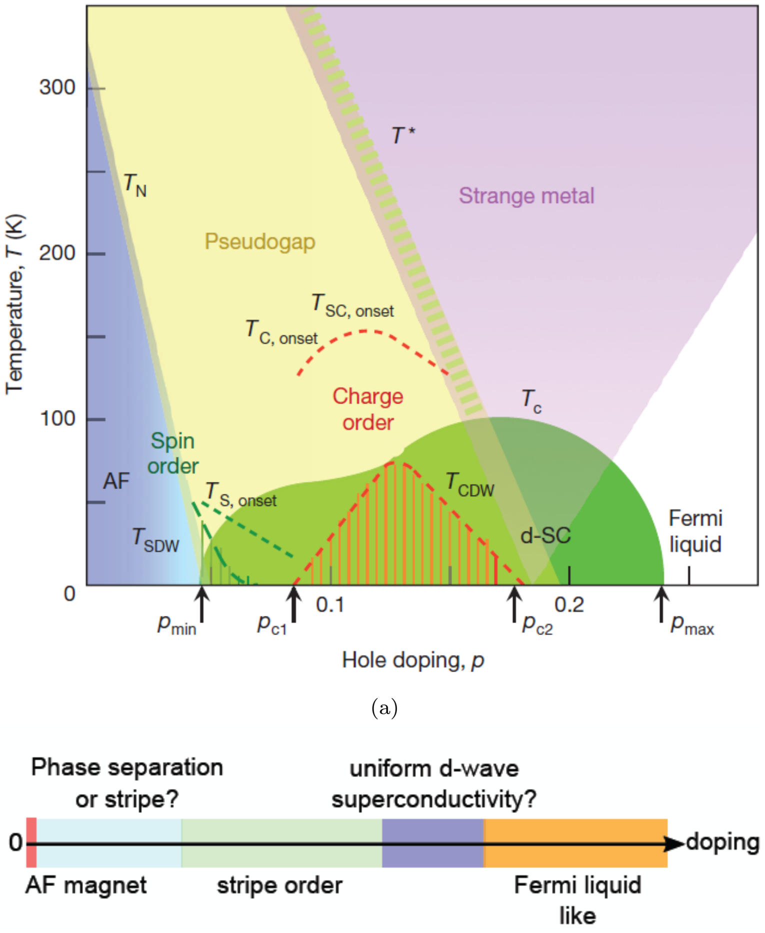

(a)

(b)

Figure 6.6: (a) Phases of the cuprates in function of hole doping and temperature [143] and (b) the phase diagram of the Hubbard model at zero Kelvin for intermediate interaction strengths [38]

7

Computational Details

In this chapter, some of the concepts defined above are explained in more detail, focussing on their efficient implementation. The code that was used for these calculations is Tensortrack [16], developed at the Quantum Group at the University of Ghent, together with code written by myself in Matlab. The diagrams shown in this chapter have explicit extra twists in the calculation of traces to be consistent with their implementation in Tensortrack.

7.1 Generation of the data

The basic structure of the code used to generate data is given in the algorithm below. The parameters that need to be specified are

- the system (e.g. cylinder one-band model)
- necessary parameters (such as N, t, U, number of rungs, filling or chemical potential)
- truncation or Schmidt-cut, this makes sure that all the singular values of C (see (3.70)) are above this value
- number of iterations as used in algorithm 7.1
- the name of the data file where the initial MPS is stored if the calculation is based on a previous MPS

Algorithm 7.1 Generation of data - Basic structure

```
operators ← create all necessary operators based on the parameters $t$, $U$, $V$, ...
MPO ← put these operators in an MPO
JMpo ← create a JMpo from this MPO
if the calculation is based on a previous MPS then
    MPS ← load the previous MPS
else
    create the necessary spaces
    MPS ← create an initial MPS based on the spaces and the system
end if
iterations ← $[20, 20, 20, 20, 20, 20, 500]$                    ▻ This is an example
for $i \in [1, \text{length(iterations)}]$ do
    MPS ← Do 1 Expand step on MPS using JMpo
    MPS ← Do iterations[$i$] VUMPS steps on MPS using JMpo
end for
```

To obtain results of high accuracy, it is best to incrementally decrease the Schmidt-cut. This means that first, a calculation with a Schmidt-cut of e.g. 10^{-4} is performed, after which this result is used as a starting point for a calculation with a Schmidt-cut of e.g. $10^{-4.2}$. Decreasing the Schmidt-cut between successive calculations too quickly can result in non-convergence.

---

[16] https://github.com/quantumghent/TensorTrack

7.2 A note on complexity

7.2.1 Bubbling - The importance of the order of contraction

In a tensor contraction, the order in which the contractions are carried out, called bubbling, has no influence on the end result [57]. However, it will have an influence on the needed memory and computation time. In this regard, consider a tensor T with indices $\{i_1, \dots i_n\}$, which is defined as

$$T : \bigotimes_i \mathbb{C}^{d_i} \to \mathbb{C} \tag{7.1}$$

Since these tensors must be stored as matrices, this is a $d_1 \times d_2 \times \cdots \times d_n$ matrix. The number of parameters thus scales exponentially in the number of indices, or equivalently, open edges. In tensor contractions, these matrices need to be multiplied which each other, resulting in a complexity that again scales with the number of open edges [57]. The order in which contractions are carried out thus needs to be planned carefully. Let us illustrate this by considering the connected correlation function as defined in (3.58). A very inefficient way to carry out this calculation would be to first contract all the MPS tensors in the ket vector up to a certain distance r, then contract all the MPS tensors in the bra vector up to the same distance, then contract the operators on the correct indices, and finally contract all the relevant indices from the ket and the bra. The first and second calculations would result in tensors with $r + 1$ physical and 2 virtual indices, effectively needing to store intermediary tensors with $D^2 d^{r+1}$ parameters. This is not a feasible approach for long distances. A much better approach is to first contract one MPS tensor of the ket and bra with the left operator, yielding a tensor with two virtual indices. One can go to high distances by contracting this tensor with the transfer matrix, and finally closing it all by contracting this with the right operator. This approach will be visualized in section 7.4. The biggest tensor that needs to be stored only has dD^2 parameters. This does not scale with the distance r and the resulting computation time scales linearly with r. Another advantage is that the contractions with the transfer matrix only have to be carried out once for all distances [17]. If the contractions with the transfer matrix up to a certain distance are calculated and yield a tensor T, this tensor can be contracted on the right with the operator, yielding the scalar value $C(r)$, and can be used to contract another transfer matrix for bigger values of r.

This approach also works when the correlation function is calculated with respect to a two-site operator. The two extra indices that are not contracted on the left are just carried along as two extra open indices, yielding a marginally longer computation time. In this regard, it can be useful to perform an SVD on this two-site operator, since then there is only one extra index that needs to be carried along, again decreasing the complexity.

7.2.2 The choice of a bigger unit cell

Some materials have multiple relevant orbitals located on the same atom after the downfolding procedure. When defining a lattice for those systems, there are essentially two options. Take ν to be the number of orbitals on each atom and d the dimension of the local Hilbert space of one orbital ($d = 4$ in the Hubbard model).

---

[17] However, the calculation of this four-leg tensor is in many cases very time-consuming, losing the advantage of only having to calculate it once.

The first option is to define a tensor for each atom with a physical Hilbert space of dimension d^ν, thus combining the ν orbitals on each site. The second option is to define a tensor for each orbital, thus defining a unit cell that is ν times larger, while keeping the dimension of the local physical Hilbert spaces equal to d. Since both the used memory and the complexity of the contractions scale in the number of open indices and their dimension (see section 7.2.1), the first option would yield an exponential dependence on ν. In the second option, the memory use and complexity of contractions remain the same. However, since the size of the unit cell and thus the number of iterations is multiplied with ν, the dependence on ν is linear. Because of this reduction in complexity, the second option was chosen in this thesis.

7.3 Expectation values

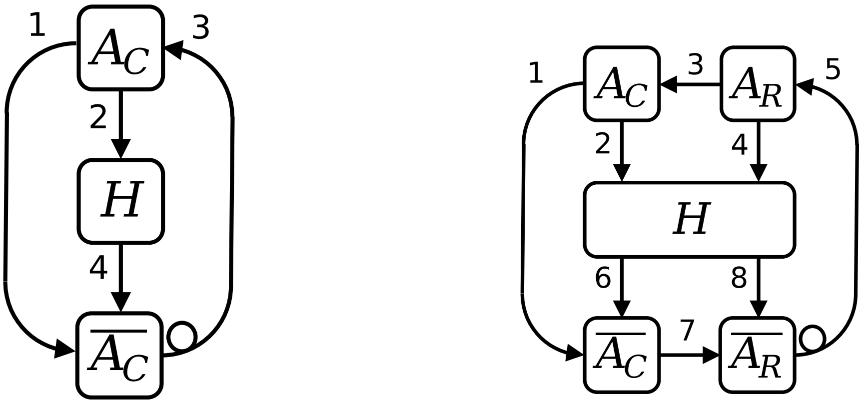

(a)

(b)

Figure 7.1: Diagrammatic notation and contraction order of (a) a one-site and (b) a two-site operator

The contractions that need to be carried out to calculate the expectation value of a one-site or two-site operator H are shown in figures 7.1a and 7.1b respectively. The numbers on the contraction lines denote the order in which the contractions need to be carried out in one of the most efficient implementations for high bond dimensions.

When the period of the MPS is $w > 1$, figure 7.1 needs to be refined. A_C and A_R are then an arrays consisting of w elements, and the tensors A_C and A_R in e.g. figure 7.1b must be replaced with $A_C(\widetilde{b})$ and $A_C(\widetilde{b+1})$, respectively, with $\widetilde{b} = b \bmod w$ and $1 \leqslant b \leqslant w$. For a translationally invariant MPS, the result is independent of b. The only thing that needs to be taken into account is the fact that tensors in a contraction should be placed such that their virtual Hilbert spaces match. Since the right virtual Hilbert space of tensor $A(\widetilde{b})$ is equal to the left virtual Hilbert space of tensor $A(\widetilde{b+1})$ (using the conventions of section 3.2), this means that in contractions like in figure 7.1b, a tensor placed on the right of a tensor with index $\widetilde{b}$ should have index $\widetilde{b+1}$. The choice of index of one tensor thus fixes the indices of all others, and this freedom results in w possible results. The final result can be obtained by taking the average of these w results.

For fermions, taking the trace like in figure 7.1b is implemented to be a supertrace. To take a trace, an extra twist should be present on the right leg of the most right tensor of the bra. If the contracted

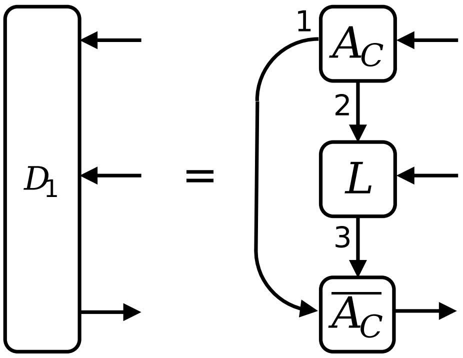

Figure 7.2: Initiation step to calculate the correlation function

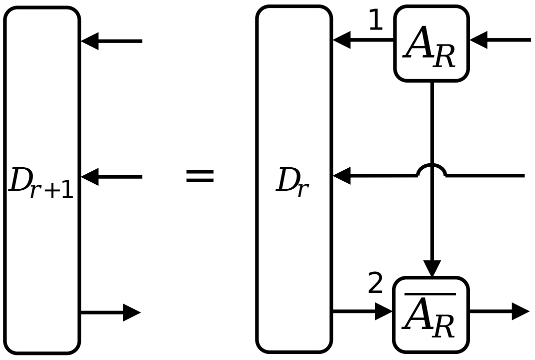

Figure 7.3: Propagation step to calculate the correlation function

tensors are bosonic, this twist does nothing.

7.4 The correlation function

This section will explain how the correlation function of section 3.5 of a two-site operator H can be most efficiently implemented. H can be rewritten as a contraction of one-site operators L and R, as shown in figure 4.2. The first step in the calculation is to contract L with A_C and its conjugate, as shown in figure 7.2. The next step is to take this result and iteratively contract the transfer matrix to go to higher distances, as shown in figure 7.3. Lastly, the contraction of this result with the operator R and tensors A_R and its conjugate (with the appropriate twist) gives the correlation function for a certain distance $C(r)$, as shown in figure 7.4. The algorithm is summarized in algorithm 7.2.

7.5 Structure factor

The structure factor is the discrete Fourier transform of the connected correlation function, as explained and defined in section 3.6. Formula (3.63) only holds in the 1D chain, however, or when the 2D system is only interpreted as its 1D chain. To correctly calculate the structure factor of a

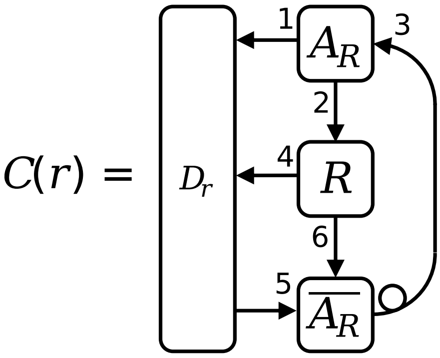

Figure 7.4: Termination step to calculate the correlation function

Algorithm 7.2 Obtaining the correlation function

```
$w \leftarrow$ period(MPS)
$[L, R] \leftarrow$ SVD(H)        ▷ Obtain the operators $L$ and $R$ from $H$ with the SVD.
C $\leftarrow$ zeros(max distance)        ▷ initialize correlation function as a list of size 'max distance'
$x \leftarrow$ cell(w)        ▷ Initialize cell
for $b \in [1, w]$ do
    $x\{b\} \leftarrow D_1(b)$        ▷ Initialization using figure 7.2
end for
for $r \in [1, \text{max dist}]$ do
    $x_{final} \leftarrow$ cell(w)        ▷ Initialize cell
    for $b \in [1, w]$ do
        $x_{final}\{b\} \leftarrow$ C(r,b)        ▷ Final contractions using figure 7.4
    end for
    C(r) $\leftarrow mean(x_{final})$
    if $r \neq$ max distance then
        $x \leftarrow D_{r+1}(x)$        ▷ Increase the distance using figure 7.3
    end if
end for
```

2D cylinder or helix with circumference N, the following formulas should be used.

$$s(q_x, i) \equiv s(q_x, q_y(i)) = \sum_n e^{q_x n_x + q_y n_y} C(n) \tag{7.2}$$

With q_x and q_y the momentum in the x-direction and y-direction, respectively. n_x and n_y are the distances in the x-direction and y-direction, respectively, and can be found based on the distance n in the MPS chain by

$$\begin{aligned} n_x &= \left\lfloor \frac{n}{N} \right\rfloor \\ n_y &= n \bmod N \end{aligned} \tag{7.3}$$

The momentum in the y-direction, i.e. the direction along the circumference of the cylinder or helix, is discrete, and can only obtain values equal to

$$\begin{cases} \text{Cylinder :} & q_y(i) = \frac{2\pi}{N} i \\ \text{Helix :} & q_y(i) = \frac{2\pi}{N}(i + \frac{q_x}{2\pi}) \end{cases} \tag{7.4}$$

with $i \in [0, N-1]$. This is visualized in figure 7.5.

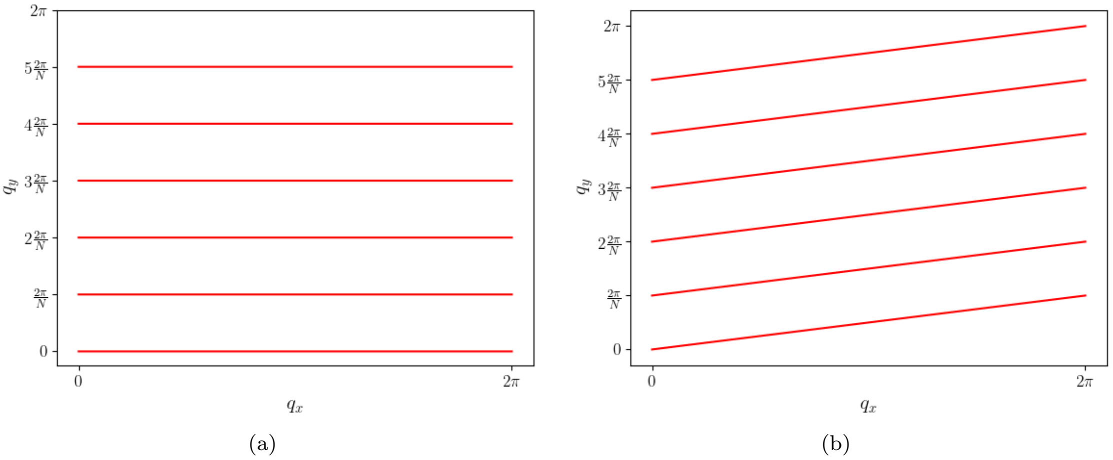

(a) (b)

Figure 7.5: Sampling of the Brillouin zone for (a) a cylinder and (b) a helix of $N = 6$, based on (7.4)

7.6 Superconductivity

To assess whether a certain model shows superconductivity, the pair-field correlator or pair correlation function $\Phi_{\alpha\beta}(x)$ is defined. It is given by

$$\Phi_{\alpha\beta}(x) = \frac{1}{N} \sum_{y=1}^{N} \langle \Delta^{\dagger}_{\alpha}(x_0, y) \Delta_{\beta}(x_0 + x, y) \rangle \tag{7.5}$$

x is the distance along the x-direction. $\Delta^{\dagger}_{\alpha}(x, y)$ is the spin-singlet pair-field creation operator, defined as [151, 152]

$$\Delta^{\dagger}_{\alpha}(x, y) = \frac{1}{\sqrt{2}} \left(c^{\dagger}_{(x,y),\uparrow} c^{\dagger}_{(x,y)+\alpha,\downarrow} - c^{\dagger}_{(x,y),\downarrow} c^{\dagger}_{(x,y)+\alpha,\uparrow} \right) \tag{7.6}$$

Some references define the superconducting pair-pair correlation function $P_{\alpha\beta}(x)$ as [125]

$$P_{\alpha\beta}(x) = \frac{1}{2} \left(\Phi_{\alpha\beta}(x) + \Phi^{\dagger}_{\alpha\beta}(x) \right) \tag{7.7}$$

This order parameter was implemented for both $U(1) \otimes SU(2) \times f\mathbb{Z}_2$ and $SU(2) \otimes f\mathbb{Z}_2$. The way this was implemented is by defining the operator $\Delta^{\dagger}_{d}(\vec{r})\Delta_{d}(\vec{r} + \vec{r}_i)$, which is a (4,4) operator, and then summing it with its conjugate. Since the individual operators are wanted for computational efficiency, the SVD of this sum is taken to yield four one-site operators. It is important to note that this is not equivalent to taking the sum of the operators and their respective conjugates. It is thus needed to construct the full operator, having dimension $4^8 = 65\,536$. It is best to save these four one-site operators separately to make sure they do not have to be recalculated every time.

7.6.1 Luttinger exponents

The density correlation function is defined as

$$N(r) = \langle \hat{n}_i \hat{n}_{i+r} \rangle - \langle \hat{n}_i \rangle \langle \hat{n}_{i+r} \rangle \tag{7.8}$$

r is the distance along the chain of the cylinder, and thus corresponds to $Nx + y$. For a system in the Luther-Emery phase, both $N(r)$ and $\Phi_{yy}(x)$ decay with a power law. It is also possible to average $N(r)$ over the rung of the cylinder, thus obtaining $N(x)$. This will have no influence on the fitted power law exponent.

$$\begin{aligned} N(r) &\propto r^{-K_\rho} \\ \Phi_{yy}(x) &\propto x^{-K_{SC}} \end{aligned} \tag{7.9}$$

K_ρ and K_{SC} are called the Luttinger exponents of the charge and superconducting sector, respectively. The superconducting correlations are dominant when $K_{SC} < K_\rho$, whereas the CDW correlations are dominant when $K_{SC} > K_\rho$ [153, 151]. The reason why $\Phi_{yy}(r)$ is considered instead of $\Phi_{xy}(r)$ or $\Phi_{xx}(r)$ is because it has been identified as the strongest of the three possibilities, which is consistent with plaquette *d*-wave superconductivity [18] on cylinders [155, 156, 157]. For a wide parameter regime, the Hubbard ladders are found to fall into the Luther-Emery universality class, in which the system has a gapped spin mode and a gapless charge mode [158, 159, 153]. For these states, it holds that $K_\rho K_{SC} = 1$. This phase is possibly a precursor phase to two phases in the 2D limit, namely superconductivity and stripe order.

7.7 Finding the value of the chemical potential for a certain filling

In the case of imposing the $SU(2) \otimes f\mathbb{Z}_2$ symmetry, the chemical potential μ has to be found that gives a certain filling, as already explained in section 5.2.1. This can be done simply by gradient descent, as shown in algorithm 7.3. For fillings close to half-filling, the optimization algorithm can get stuck in a half-filled MPS, This can be solved by either using a much higher bond dimension, or using the previous MPS (with lower filling) as starting point for the new calculation with the new μ.

---

[18] A plaquette, consisting of a square of four sites, is the smallest system that can exhibit *d*-wave superconductivity [154].

Algorithm 7.3 Using gradient descent to obtain the chemical potential

```
$f_{goal} \leftarrow$ specify the desired filling
$\epsilon \leftarrow$ specify how close the final filling has to be to $f_{goal}$
$\mu_1 \leftarrow$ starting value 1 of the chemical potential
$\mu_2 \leftarrow$ starting value 2 of the chemical potential
$\mathrm{MPS}_1 \leftarrow$ create and optimize MPS based on $\mu_1$
$\mathrm{MPS}_2 \leftarrow$ create and optimize MPS based on $\mu_2$
$f_1 \leftarrow$ calculate the filling of $\mathrm{MPS}_1$
$f_2 \leftarrow$ calculate the filling of $\mathrm{MPS}_2$
$\mu$-values $\leftarrow [\mu_1, \mu_2]$                         ▷ make a list of $\mu$-values
$f$-values $\leftarrow [f_1, f_2]$                               ▷ make a list of $f$-values
$f \leftarrow f_2$                                               ▷ Initialize $f$ for while loop
while $|f - f_{goal}| > \epsilon$ do
    $(a, b) \leftarrow$ fit a function $f = a\mu + b$ using the 2 most recent values of $\mu$ and $f$
    $\mu \leftarrow (f_{goal} - b)/a$                            ▷ new value of the chemical potential
    MPS $\leftarrow$ create and optimize MPS based on $\mu$
    $f \leftarrow$ calculate the filling of MPS
    add $\mu$ and $f$ to their respective lists
end while
```

III

Numerical results

8 Benchmarking results

> ”Unless you have confidence in the ruler’s reliability, if you use a ruler to measure a table you may also be using the table to measure the ruler.”
>
> *Nassim Nicholas Taleb*

Both the one-dimensional Heisenberg and Hubbard models are investigated in this chapter, since an exact solution has been obtained using the Bethe ansatz [131, 160]. The two-dimensional Heisenberg XXX model is investigated as well, owing to the existing consensus on its ground state energy [161, 162, 73]. [19]

8.1 1D Heisenberg model

The ground state energies and spin correlations $\langle S_z^i S_z^{i+1} \rangle$ of the XXZ Heisenberg model of section 5.1 were calculated using VUMPS. Figure 8.1 shows the results. They are in very good agreement with those found in [102].

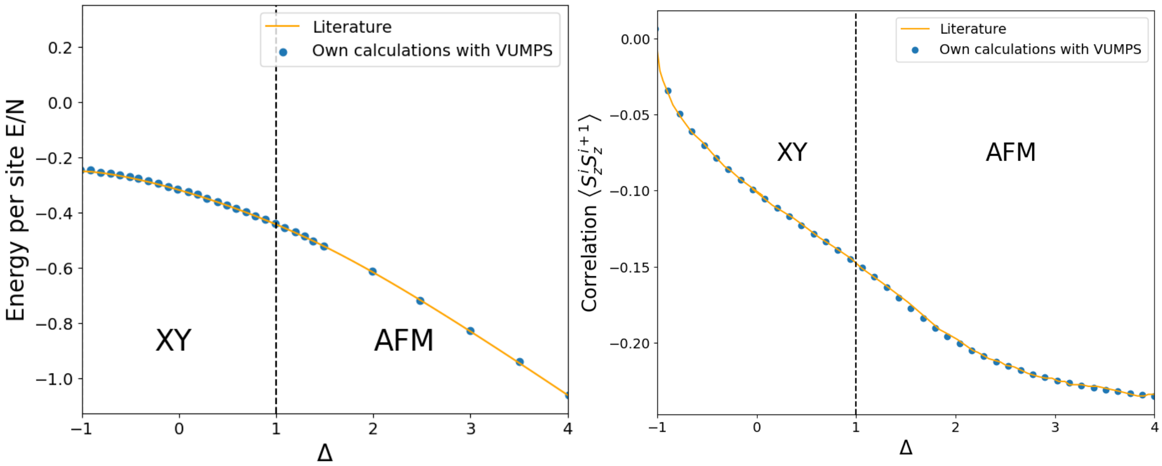

(a)

(b)

Figure 8.1: (a) Ground state energy and (b) spin correlation $\langle S_z^i S_z^{i+1} \rangle$ of the 1D Heisenberg XXZ model in function of Δ. The results are compared with results from [102].

Figure 8.2 shows the correlation length for the XXZ Heisenberg model for different values of Δ. It is seen that it diverges for Δ → 1, as expected since this is a critical point. Doing these calculations

---

[19] The results in this chapter, apart from figures 8.3 and 8.6b, were not extrapolated in bond dimension.

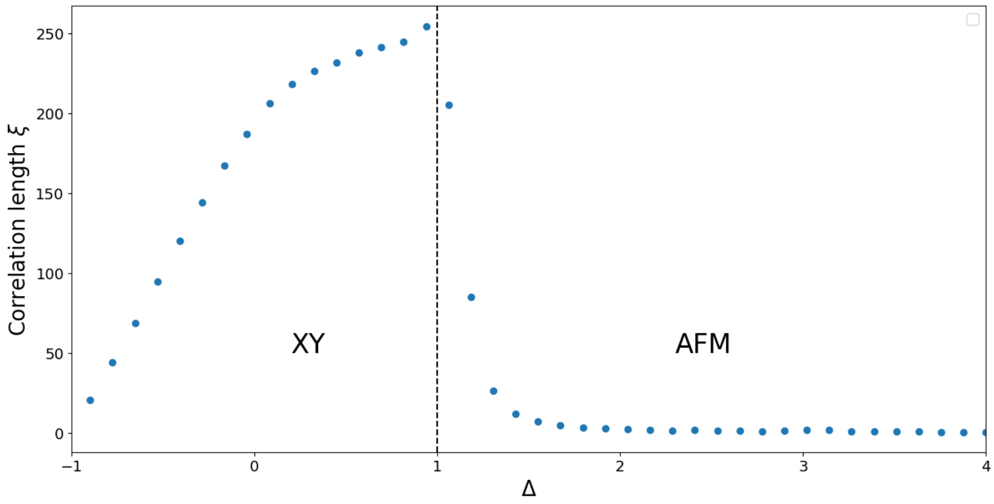

Figure 8.2: Correlation length of the 1D XXZ Heisenberg model

for higher bond dimensions confirms this. Extrapolating the inverse correlation length to $D \to \infty$ using the error measure δ, a 95% confidence interval of $[-4.195 \cdot 10^{-4}, 8.122 \cdot 10^{-5}]$ was obtained. The exact inverse correlation length of 0 is thus within these bounds. The extrapolation is shown in figure 8.3. Using $1/D$ as error measure, a 95% confidence interval of $[-8.297 \cdot 10^{-5}, 1.231 \cdot 10^{-3}]$ was obtained, showing the superiority of the error measure δ in this case.

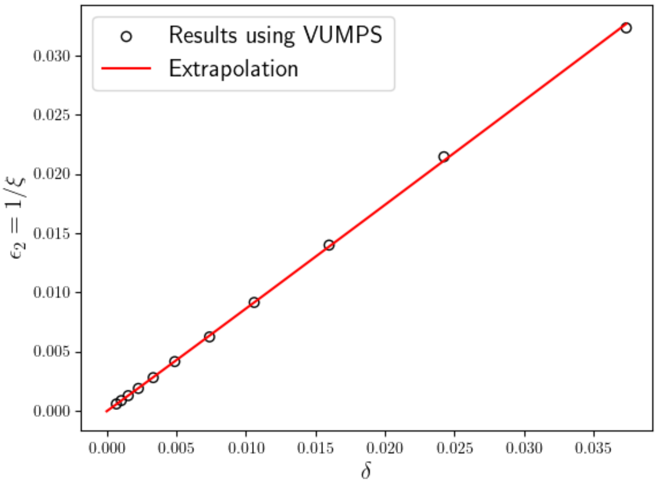

Figure 8.3: Extrapolation of the inverse correlation length of the XXX Heisenberg model

For non-critical systems, the correlation functions are exponentially decreasing, whereas for critical systems they obey power laws [163]. This is shown in figure 8.4, where the correlation function on a log-log plot indeed approaches a linear curve for $\Delta \rightarrow 1$. Even at the critical point, the correlation function would be exponential functions, since MPS are used to represent them, which always have finite correlation lengths.

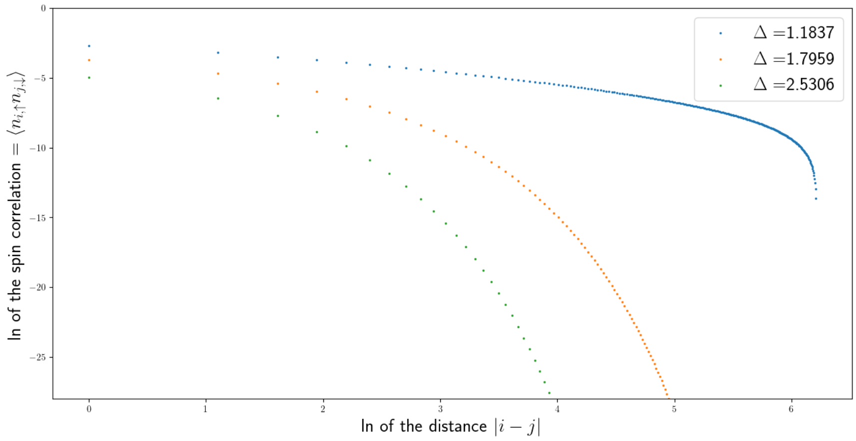

Figure 8.4: Correlation function for the operator $n_{i,\uparrow} n_{j,\downarrow}$ of the 1D XXZ Heisenberg model

8.2 2D XXX Heisenberg model [20]

8.2.1 The energy

As explained in section 4.5.1, the 2D square lattice will be modeled by wrapping the lattice around a cylinder and making it effectively 1D. The first question one should ask is whether this is allowed. There is a priori not a certainty that the correct full 2D values are obtained in the limit of $N \rightarrow \infty$. The first check can be done by looking at the energies of the Heisenberg XXX model on both a helix and a cylinder and comparing them with the correct 2D value. Systems without geometric frustration are chosen, since the 2D square lattice is also not frustrated. The cylinders thus have even circumferences and the helices have odd circumferences, as explained in section 4.5.2. The results are shown in figure 8.5 and show that indeed the correct 2D limit is obtained for $N \rightarrow \infty$.

8.2.2 The staggered magnetization

The staggered magnetization can be spontaneously broken in 2D [104, 164]. It can thus be expected that in this case, the quasi-1D system will not be a good representation of the 2D system, since spontaneous symmetries cannot be broken in 1D, due to the Mermin-Wagner theorem. Figure 8.6a shows the result for when a staggered magnetic field is applied to a cylinder. Indeed, for no external staggered magnetic field, the resulting staggered magnetization is zero, conforming with the

---

[20] The results from this section were obtained using iDMRG2

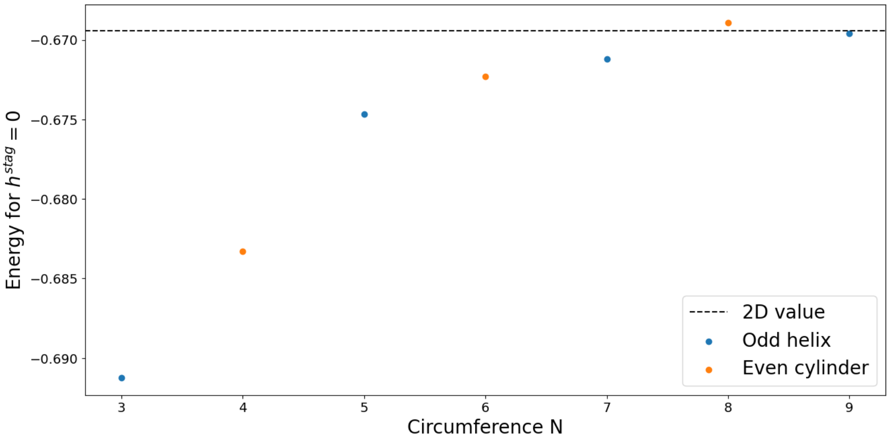

Figure 8.5: Ground state energy per site of the 2D XXX Heisenberg model for helices and cylinders. The 2D value is taken from [87].

Mermin-Wagner theorem.

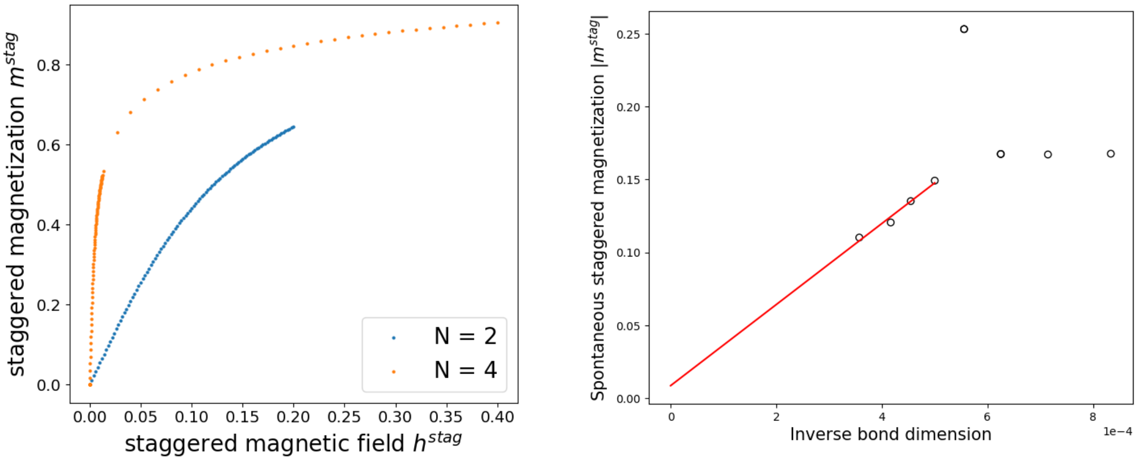

(a)

(b)

Figure 8.6: Results for the Heisenberg XXX model on (a) the staggered magnetization m^{stag} in function of a staggered magnetic field h^{stag} for cylinders with even circumference and (b) the spontaneous staggered magnetization $m^{stag}(m^{stag} = 0)$ on a helix with $N = 3$ as finite bond dimension effect. The four most accurate calculations are used for extrapolation.

For helices, a non-zero spontaneous staggered magnetization is found. The reason for this difference with cylinders can be sought by considering Haldane's conjecture [165]. This states that the excitation spectrum is gapped for integer spin chains and gapless for half-integer spin chains [166] [167]. The cylinder can be seen as a 1D integer spin chain by blocking the sites of one rung together, since they have an even circumference. Helices have odd circumferences and thus have a gapless excitation spectrum according to Haldane's conjecture. Representing the states with MPS introduces a gap in the spectrum, however, and the resulting states can spontaneously break the symmetry. This gap vanishes in the limit $D \to \infty$, and thus the spontaneous staggered magnetization should vanish in this limit. This is indeed seen in figure 8.6b. Using the inverse bond dimension as an error measure, the extrapolated value of the spontaneous staggered magnetization $|m^{stag}|$ is 8.49305×10^{-3}. The 95% confidence interval is given by $[-0.06924, 0.05226]$, where it is indeed seen that 0 is included in this interval. Using higher bond dimensions will increase the accuracy of this extrapolation and will push this value closer to zero.

8.3 1D Hubbard model

8.3.1 The energy

The energy of the 1D Hubbard model was calculated for a range of values for U. The results are shown in figure 8.7, together with the comparison with reference [168]. This again shows good agreement with the literature.

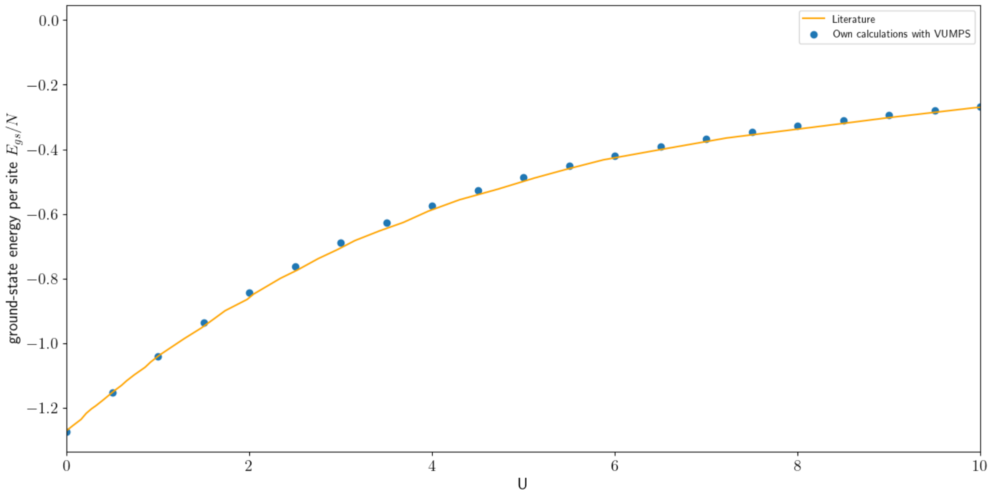

Figure 8.7: Ground state energy per site of the 1D Hubbard model at half-filling for $t = 1$. The energy is compared with results from [168].

8.3.2 Correlation functions and correlation length of different sectors

In the 1D Hubbard model in the region where $U > 0$, the charge sector is gapped and the spin sector is gapless [38, 39]. This can be seen in the correlation functions of the different sectors. In figure 8.8, the correlation functions of the charge and spin sector are shown, corresponding to the operators

$c^\dagger_{\sigma,i}c_{\sigma,j}$ and $O_{\sigma,i}O_{-\sigma,j}$ respectively. O_σ flips the spin of the electron when it has spin σ, and yields 0 when there is no electron with spin σ. The charge correlation function is approximately linear on the log plot, showing that it is an exponentially decreasing function, and thus corresponds to a gapped sector. The spin correlation function, on the other hand, is linear on the log-log plot, thus obeying a power law corresponding to a gapless sector. This is in accordance with the literature cited above.

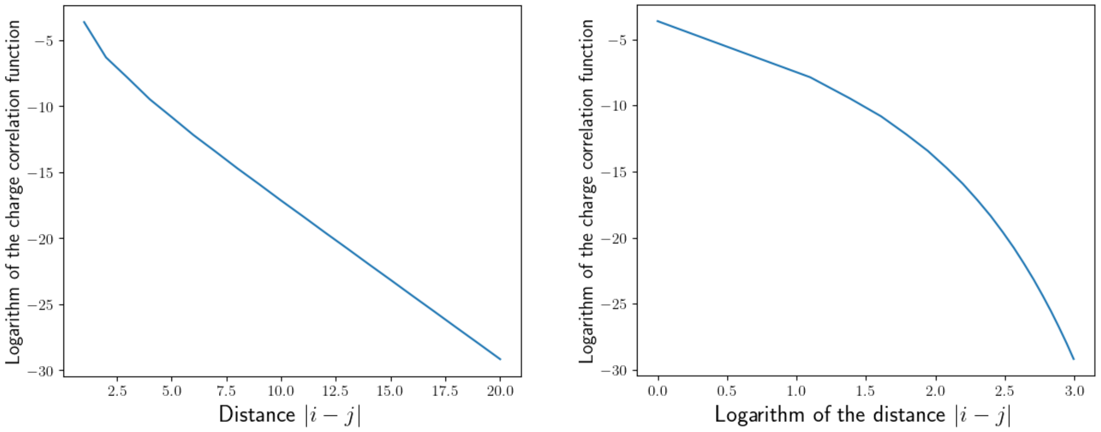

(a) Charge sector - log plot

(b) Charge sector - log-log plot

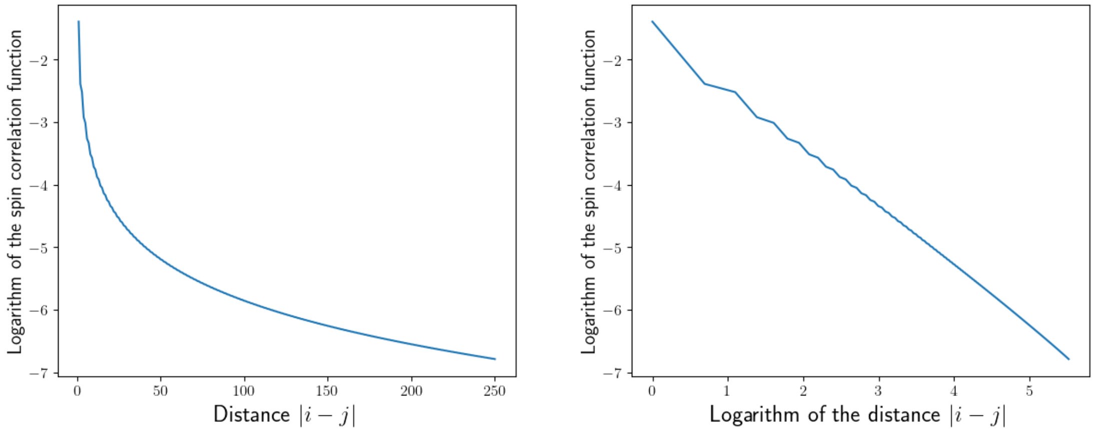

(c) Spin sector - log plot

(d) Spin sector - log-log plot

Figure 8.8: The correlation function of the charge sector on a (a) log plot and (b) log-log plot. The correlation function of the spin sector on a (c) log plot and (d) log-log plot. The calculations were done for the 1D Hubbard model with $t=1, U=6$.

8.3.3 Doping

Changing the doping of the Hubbard model will influence its ground state energy. The total energy in function of the doping for $U/t = 8$ is shown in figure 8.9.

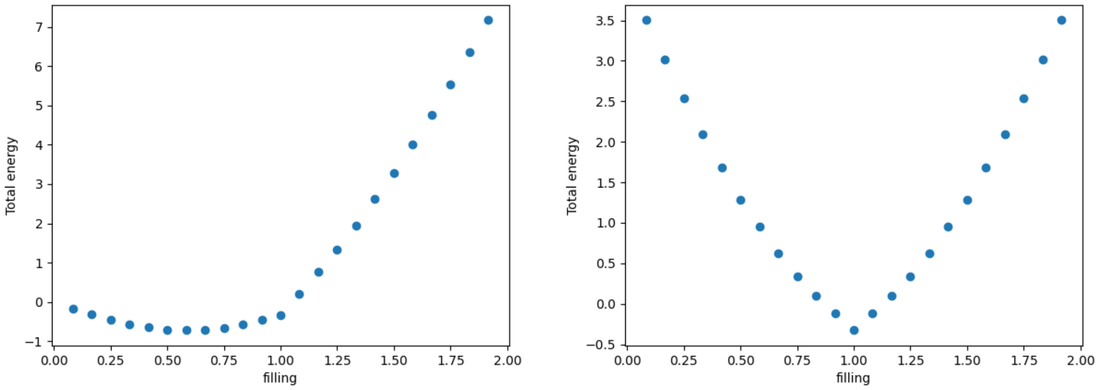

(a) (b)

Figure 8.9: Ground state energy per site in function of the doping for the Hubbard model $t = 1$, $U = 8$ for (a) the 1D Hubbard model based on (5.10) and (b) the 1D particle-hole symmetric Hubbard model based on (5.18)

The trend seen in the figure can be explained better by decomposing it in its kinetic energy, resulting from the hopping term in the Hamiltonian, and the self-interaction energy. The result is shown in figure 8.10. From figure 8.10a, it is clear that the self-interaction energy increases for increasing electron filling. This is logical from its definition. Figure 8.10b is more interesting, however, as it shows that the kinetic energy is particle-hole symmetry around half-filling. The self-interaction energy is also particle-hole symmetric around half-filling if the particle-hole symmetric Hubbard model of (5.18) is used instead.

8.3.4 Results about the static structure factors

The charge and spin structure factors for the 1D Hubbard model with $t = 1$, $U = 8$ are shown in figure 8.11. The sharp peak at $q_x = \pi$ of the spin structure factor signifies a spin order with period $\lambda = 2$. This is a signature of a Mott insulator with antiferromagnetic order, which indeed should be present at half-filling [150, 39].

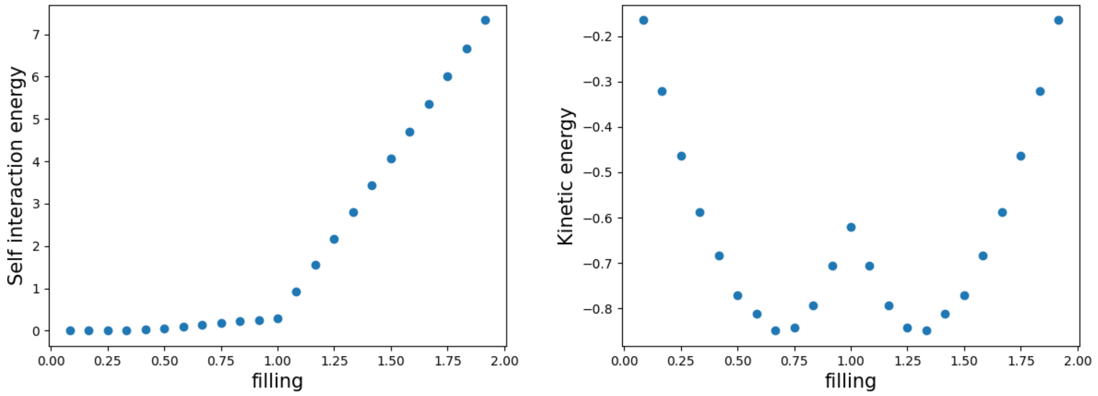

(a) (b)

Figure 8.10: (a) Self-interaction energy per site and (b) kinetic energy per site of the 1D Hubbard model for $U/t = 8$

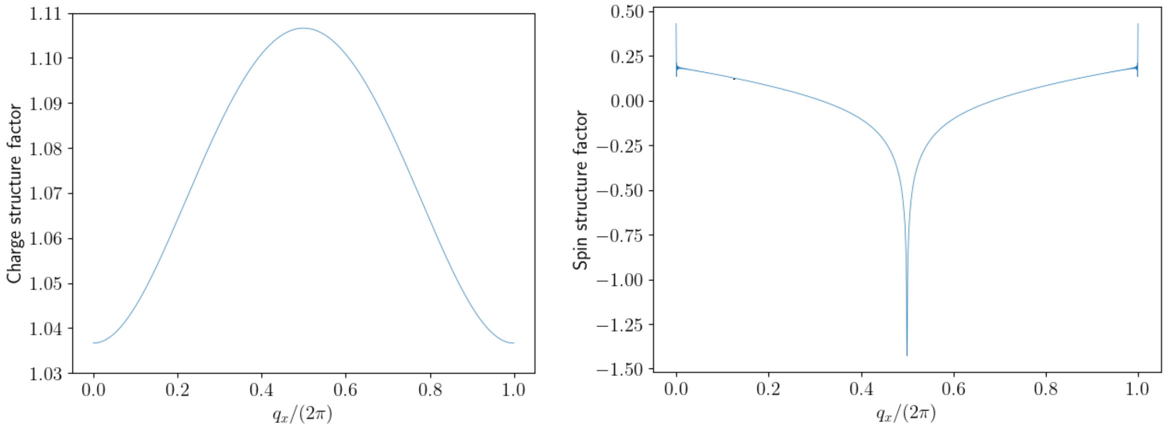

(a) (b)

Figure 8.11: (a) Charge and (b) spin structure factors for the 1D Hubbard model with $t = 1, U = 8$.

9 2D Hubbard model

In this chapter, the results on the simple Hubbard model in 2D are discussed and compared with the existing literature.

9.1 Convergence of the energy - Cylinder vs Helix

It is interesting to see how quickly the ground state energy of a cylinder or a helix converges to the 2D value. The result is shown in figure 9.1, which shows the energy convergence for the Hubbard model with $t = 1$, $U = 8$, both at half-filling and $\delta = \frac{1}{8}$. One sees that the $N = 2$ result does not yield an accurate value [21]. At $N = 4$, the energy is already much closer to the correct value. This result indicates that we need to be careful when using the result of the ladder to make conclusions about the 2D system. On the other hand, it is not a priori known that an inaccurate estimate of the ground state energy is accompanied by an inaccurate evaluation of the phase of the system, even though the stripe order and the superconducting state are close in energy [169, 170]. It could be the case that the boundary effect induces only an energy shift, while the phase is robust, or that the boundary effect can determine the phase. Later results will show that the $N = 2$ gives accurate results in some, but not all, regards.

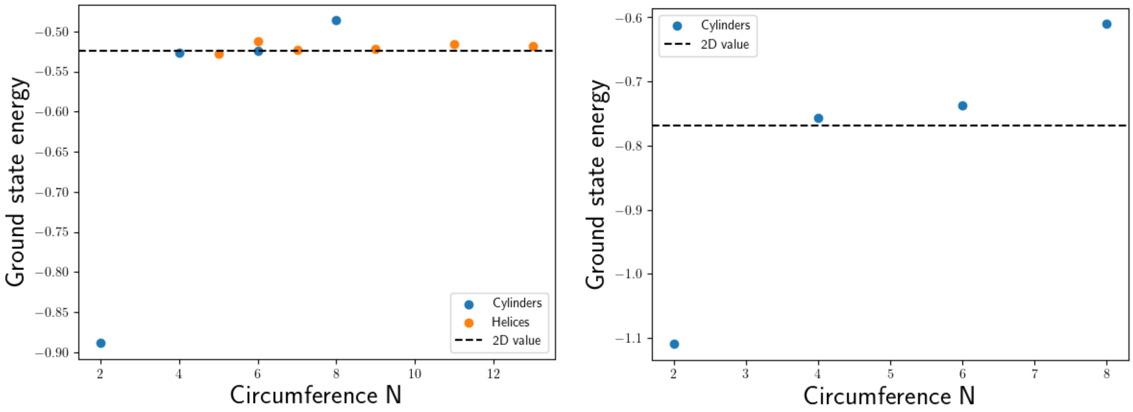

(a) half-filling

(b) $\delta = 1/8$

Figure 9.1: Convergence of the ground state energy of helices and cylinders in function of the circumference for the 2D Hubbard model with $t = 1$, $U = 8$. 2D values are taken from [170]. The $N = 6$ for $\delta = 1/8$ and the $N = 8$ results were not extrapolated in bond dimension. The result for $N = 8$ was performed at a relatively low bond dimension. This results in the fact that for $\delta = 1/8$, the ground state energy of the $N = 6$ and $N = 8$ cylinders can be further away from the exact 2D result than the $N = 4$ result, and that for half-filling, the $N = 8$ result deviates from the exact result more than e.g. the $N = 7$ and $N = 9$ results.

---

[21] A cylinder with $N = 2$ is also called a ladder.

9.2 $N = 2$ - $U(1) \otimes SU(2) \otimes f\mathbb{Z}_2$

In this section, the Hubbard model with $t = 1$, $U = 8$ is investigated on a ladder, with symmetries $U(1) \otimes SU(2) \otimes f\mathbb{Z}_2$. This means that the number of rungs had to be an integer multiple of 8 to match the period of the unit cell.

9.2.1 Charge distribution

To know whether the system exhibits stripe order, we look at the expectation value of the hole density $\langle 1 - \hat{n}_e \rangle$ for each site of the unit cell.

For half-filling, all sites have an expectation value of 0 for the hole doping, with deviations smaller than 10^{-7}. The hole occupancies for $\delta = 1/8$ hole doping are shown in figure 9.2. A CDW with period $\lambda = 8 = \frac{1}{\delta}$ is seen. There is uniformity along the y-direction (along which the cylinder is closed), with differences smaller than 10^{-5}. To further verify that the $\lambda = 8$ CDW is lowest in energy, the same calculation was done with 16 rungs instead of 8, albeit at a lower bond dimension. Both calculations confirm a $\lambda = 8$ CDW, in accordance with the literature [171, 170].

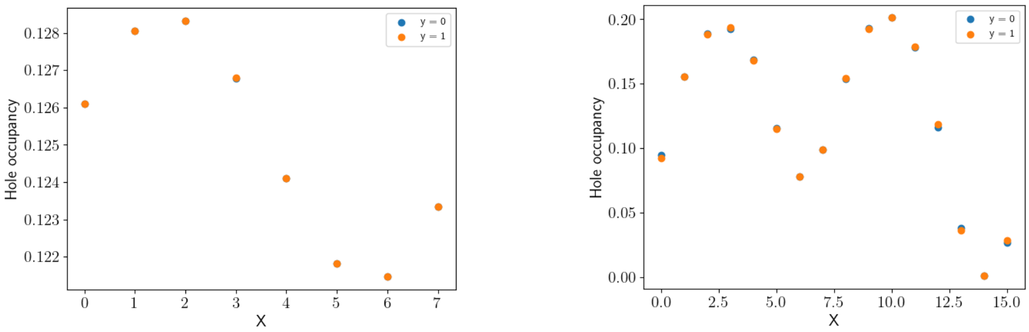

(a) (b)

Figure 9.2: Hole occupancies for the simple Hubbard model with $t = 1$, $U = 8$, and $\delta = 1/8$ on a cylinder with $N = 2$ and (a) 8 rungs, $D = 600$ and (b) 16 rungs, $D = 40$

In this regard, the filling fraction (FF) can be defined [22] [170].

$$FF = \delta \lambda_{CDW} \tag{9.1}$$

This quantifies how many holes are present in one period of the CDW. $FF = 1$ and $FF = 1/2$ correspond to filled and half-filled stripes, respectively.

The stripes here are thus filled, in accordance with results from the literature [170].

---

[22] Reference [172] defined the filling fraction as $FF = \frac{\delta \lambda_{SDW}}{2}$, where λ_{SDW} stands for the period of the spin density wave (SDW). These are consistent, as it has been stated that the characteristic length of the charge correlation is half that of the spin correlation [173, 171]. We will work exclusively with the definition presented in (9.1), as imposing $SU(2)$ symmetry for the spin sector does not allow us to calculate the magnetic moment of a given site.

If the amplitudes of the CDW are calculated, it is noticed that the amplitude decreases for increasing bond dimension. Extrapolation of the amplitude in terms of the error measure δ results in figure 9.3. If the four most accurate calculations are used for the extrapolation, the 95% confidence interval on the extrapolated amplitude is $[-7.898 \cdot 10^{-3}, 3.932 \cdot 10^{-3}]$. The extrapolated value is thus within bounds of zero. The CDW breaks the translational invariance and it is possible that this prohibits the existence of CDWs in the $D \to \infty$ limit in quasi-1D systems within the Luther-Emery liquid theory [153, 174, 175, 176].

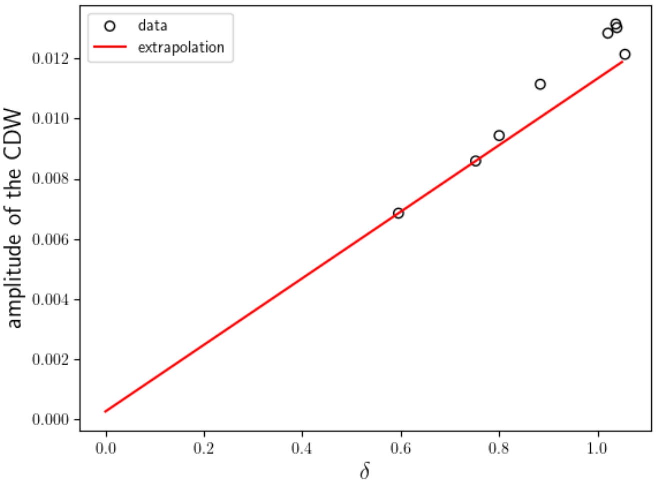

Figure 9.3: Amplitudes of the hole occupancies for the simple Hubbard model with $t = 1$, $U = 8$, and $\delta = 1/8$ on a cylinder with $N = 2$ and 8 rungs for different bond dimensions. The two highest bond dimensions are used for the shown extrapolation, which yields an extrapolated amplitude of $2.700 \cdot 10^{-4}$.

9.2.2 Correlation functions and structure factors

The correlation function and the corresponding static structure factors of both the charge and the spin sectors were calculated and are shown in the appendix in figure E.1. These confirm the conclusions of the previous section, indicating that a period 8 CDW exists. The correlation functions in figure E.1 are given in function of the distance along the chain of the cylinder, i.e. as in figure 4.15. The period of the oscillation of the correlation function thus has to be divided by N to obtain the period of the CDW along the x-direction. The corresponding structure factors have a small peak for $q_x = \frac{2\pi}{\lambda} = \frac{2\pi}{8}$.

9.3 $N = 4$ - $U(1) \otimes SU(2) \otimes f\mathbb{Z}_2$

9.3.1 Charge and spin distributions

The hole occupancies for $\delta = 1/8$ hole doping are shown in figure 9.4. Again, there is uniformity along the y-direction (along which the cylinder is closed), with differences smaller than 10^{-3}. A

CDW with period $\lambda = 4 = \frac{1}{2\delta}$ is now seen, or half-filled stripes. This is also consistent with previous results [172, 151].

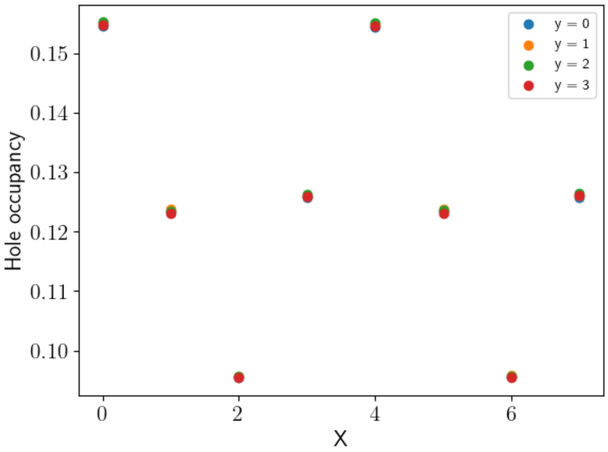

Figure 9.4: Hole occupancies for the simple Hubbard model with $t = 1$, $U = 8$, and $\delta = 1/8$ on a cylinder with $N = 4$ and 8 rungs. $D = 767$.

9.3.2 Correlation functions and structure factors

The correlation function and the corresponding static structure factors of both the charge and the spin sectors are given in the appendix in figure E.2. These confirm the conclusions of the previous paragraph, indicating that a period 4 CDW exists. The corresponding structure factors have a peak for $q_x = \frac{2\pi}{\lambda} = \frac{2\pi}{4}$.

9.4 $N = 2$ - $SU(2) \otimes f\mathbb{Z}_2$

The drawback of imposing $U(1) \otimes SU(2) \otimes f\mathbb{Z}_2$ is the need for a minimal number of rungs, as explained in section 5.2.1. This implicitly favors stripe order with a period $\lambda = \frac{rungs}{k}$, $k \in \mathbb{N}$. CDWs with other periods get a positive energy shift due to the boundary effects, and this might influence the ground state. For example, a $\lambda = 5$ CDW might be the lowest in energy in the 2D system, but because the simulation has 8 rungs, it might not be the ground state anymore. This example is sketched in figure 9.5.

A calculation for the 2D Hubbard model with $t = 1$, $U = 8$, and $\delta \approx 1/8$ was done without imposing the $U(1)$ symmetry for the charge sector and for only one rung [23]. This allows us to again verify the earlier statements regarding the periods of the CDWs. This can be done by looking at the spectrum of eigenvalues of the transfer matrix based on the ground state MPS. The spectrum is shown in

---

[23] This calculation corresponds to a chemical potential of $\mu = -1.6428$, which corresponds to $\delta = 1/8$ with deviations smaller than 5×10^{-5}.

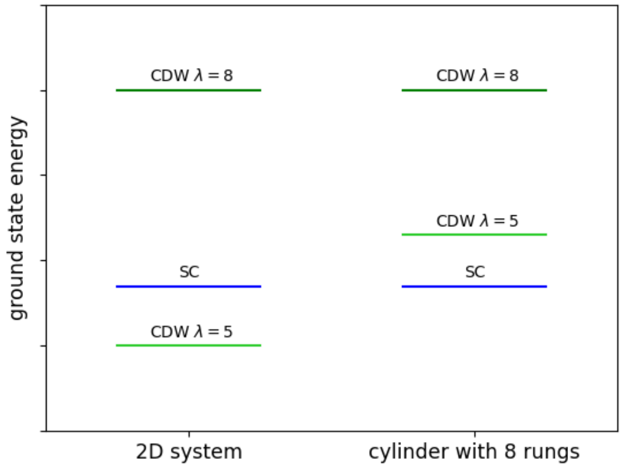

Figure 9.5: Example of how introducing a cylinder with a certain number of rungs can influence the ground state. No numerical results correspond to this example.

figure 9.6. The smallest angles of the eigenvalues that occur are at $\theta = 0$ and $\theta = \pm\frac{\pi}{4} = \pm\frac{2\pi}{\lambda}$. The latter again signifies a CDW with $\lambda = 8$, since this period still has to be multiplied by the period of the unit cell, which in this case is 2. This yields a period along the chain of 16, or a period of 8 along the x-direction after dividing by N.

9.4.1 Superconductivity

Using the $SU(2) \otimes f\mathbb{Z}_2$ symmetry, and thus only needing to simulate one rung of the cylinder, decreases the needed computational complexity, whereby much higher bond dimensions can be simulated. These higher bond dimensions are needed to resolve the energy differences between the highly competitive stripe order and superconductivity. To determine whether a model exhibits superconductivity or stripe order, the Luttinger exponents from (7.9) were fitted to the connected pair and density correlation functions in order to calculate K_{SC} and K_ρ respectively. The fitting is done by subdividing the logarithm of the distances r in bins with a certain bin width, and calculating the maximal value of the correlation function within that bin. These maximal values together with their respective r-values are then used in a linear log-log fit to obtain the Luttinger exponent. The bin widths correspond to the biggest difference between successive local maxima of the correlation function. This procedure is similar to the method used in references [177, 152]. Only the range beyond the short-range effects and before the onset of exponential decay is considered. Figure 9.7 shows the results.

A possible alternative would be to fit the full correlation function, i.e.

$$C(r) = A\cos(\theta_2 r)\, r^{-K} \tag{9.2}$$

Due to the fact that the overlap between the range where the correlation functions exhibit a power

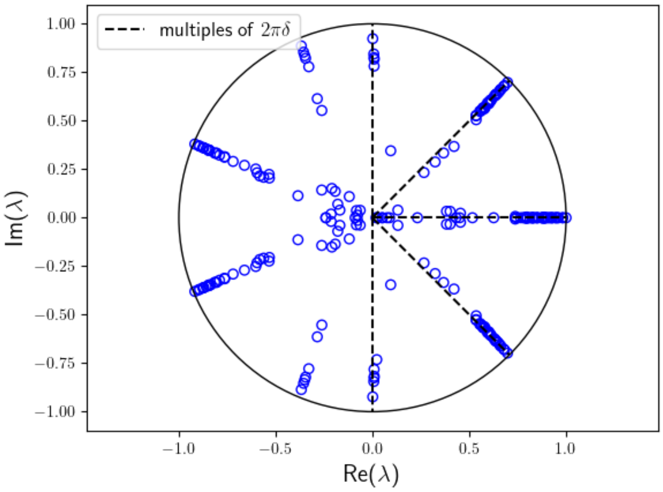

Figure 9.6: Spectrum of the transfer matrix for the simple Hubbard model with $t = 1$, $U = 8$, and $\delta \approx 1/8$ on a cylinder with $N = 2$ and 1 rung, using the $SU(2) \otimes f\mathbb{Z}_2$ symmetry and $D = 2336$. The dashed lines correspond to multiples of $\theta = \frac{\pi}{4} = 2\pi\delta$.

law decay and the range where all but one oscillation has died out is sometimes rather small, the first strategy was chosen.

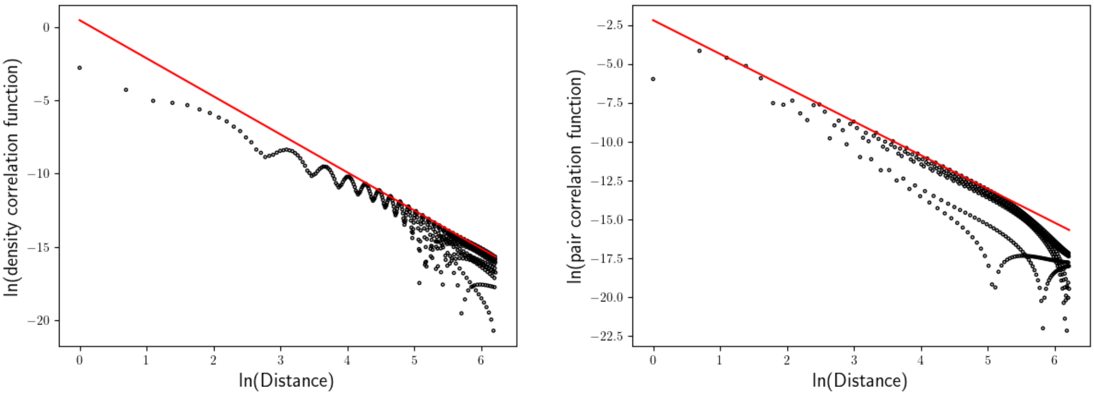

(a) (b)

Figure 9.7: Fit of the (a) density and (b) pair correlation function for the simple Hubbard model with $t = 1$, $U = 8$, and $\delta \approx 1/8$ on a cylinder with $N = 2$ and $D = 2336$

The Luttinger exponents in function of the bond dimension can now be used to determine whether the ground state exhibits stripe order or superconductivity. Figure 9.8 shows the results. For the

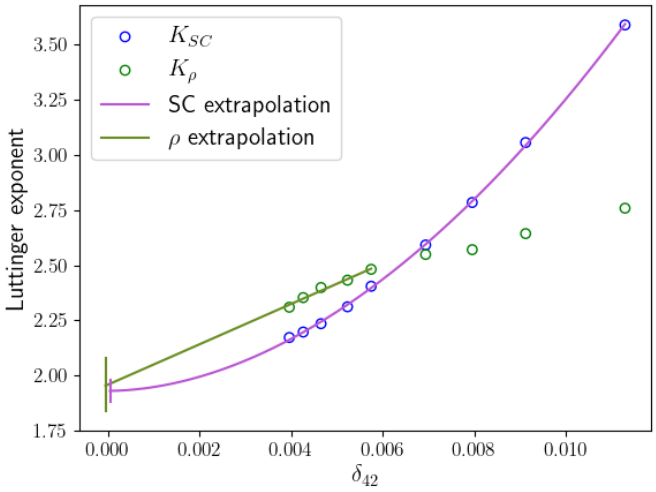

Figure 9.8: Luttinger exponents of the simple Hubbard model with $t = 1$, $U = 8$, and $\delta \approx 1/8$ together with their extrapolation and error bars

extrapolation of K_ρ, b was set to 1. Unfortunately, the 95% confidence intervals of the Luttinger exponents overlap, so it can not be determined which correlations are dominant. The heaviest calculations already used $D = 2336$ and took several days to compute. To determine the dominant order, the calculations should be carried out for even higher bond dimensions, which was not possible within the timeframe of this thesis. The conclusion $K_\rho < K_{SC}$ was drawn in reference [151] for $N = 4$, although $K_{SC} < K_\rho$ has been reported in reference [152] for $N = 2$. It is believed that the 2D Hubbard model is nonsuperconducting in the moderate to strong coupling regime around optimal doping [178], but a consensus is still missing. These results also seem to violate the relation $K_\rho K_{SC} = 1$ of the Luther-Emery liquid phase. Both the observation and the violation of this relation have been found in literature [152, 179, 153].

It was noticed that it was difficult to obtain the Luttinger exponents, with K_ρ being especially hard. Reference [153] found the same difficulties for finite-size calculations and stated that high bond dimensions and system sizes are needed to reliably obtain the Luttinger exponents. They had more difficulty in fitting K_{SC}, however, since a finite-size calculation can use Friedel oscillations to obtain K_ρ, which is possibly more reliable than fitting the spatial decay of the correlation functions [153].

9.5 Extended Hubbard model - influence of t'

The presence of stripe order in the simple Hubbard model yields the question of how stable this order is, and when the ground state is superconducting instead. We can heuristically investigate this by considering next-to-nearest interactions. The hole occupancies for $t = 1$, $U = 8$, and $t' = -0.25$ are shown in figure 9.9. Again, a stripe order exists with $\lambda = 8$. The presence of a stripe order is consistent with the literature, which finds stripe order and suppression of superconductivity [180, 181]. Superconductivity might thus not be present in the Hubbard model with only nearest-neighbor and next-to-nearest neighbor interactions [24]. However, reference [157] found superconductivity in the 2D Hubbard model with next-to-nearest neighbor interactions on cylinders with $N = 6$ for smaller doping levels. It will be seen in chapter 10 that introducing more terms, such as V-interactions, can result in superconducting ground states.

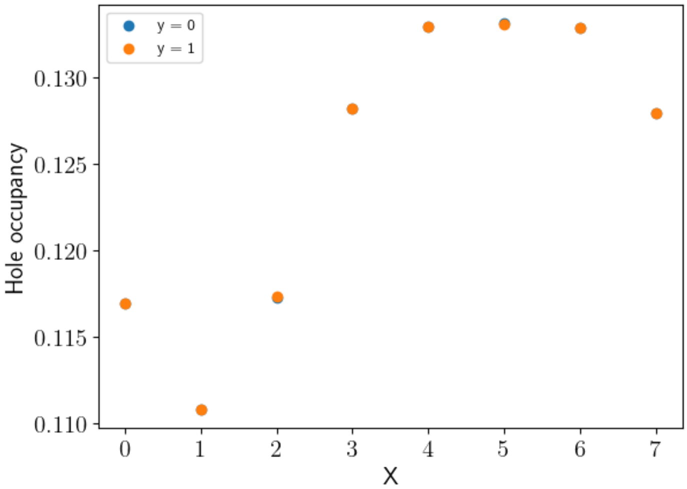

Figure 9.9: Hole occupancies for the extended Hubbard model with $t = 1$, $U = 8$, and $t' = -0.25$ for $\delta = 1/8$ on a cylinder with $N = 2$ and 8 rungs. $D = 200$.

---

[24] It is important to note that the presence of stripe order does not automatically prohibit superconductivity, as will be seen in section 10.4.2

10 Case study: $HgBa_2CuO_4$

As a case study, we will look at the cuprate $HgBa_2CuO_4$. Parameters for both the one-band and the three-band model of this cuprate were taken from [123] and are listed in appendix D. More details on how these parameters were calculated and parameters for other cuprates can be found in references [124, 182]. We will try to investigate the stripe orders and superconductivity for half-filling at the hole-doped side ($\delta \geqslant 0$), since the hole-doped side is said to have stronger superconductivity than the electron-doped side and has been more widely investigated [145].

10.1 three-band model - $U(1) \otimes SU(2) \otimes f\mathbb{Z}_2$

The half-filled three-band model corresponds to a filling $f = \frac{5}{3}$, or doubly occupied oxygen atoms and half-filled copper atoms [118]. The electron occupancies of the half-filled three-band model are shown in figure 10.1a. It is indeed seen that the electrons mostly reside on the oxygen atoms. This is quantified in table 10.1, which shows the mean occupancy and relative difference in the occupancy for both atom types, for four different filling levels. The relative difference is here defined as

$$\Delta_O = \frac{max(O) - min(O)}{mean(O)} \tag{10.1}$$

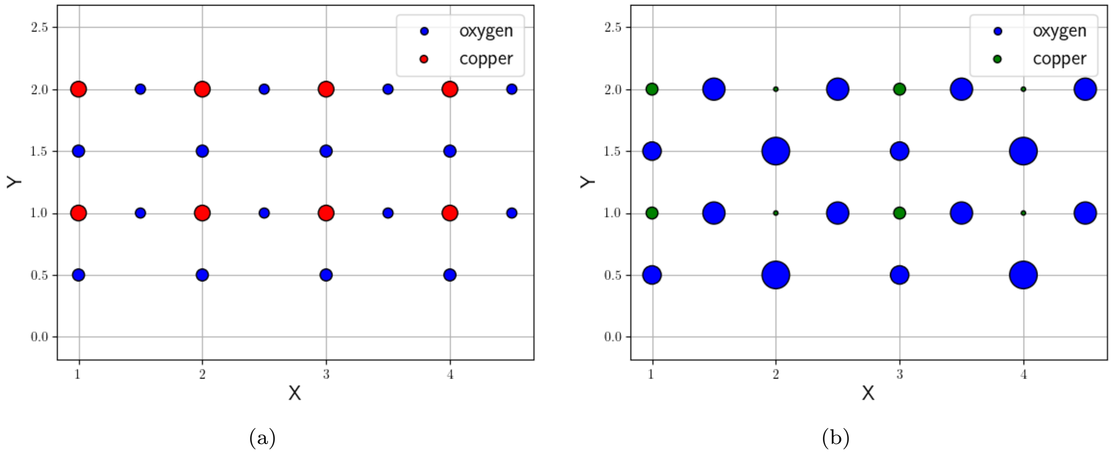

(a)

(b)

Figure 10.1: Hole occupancies for the three-band model of $HgBa_2CuO_4$ for $N = 6$, (a) $f = 5/3$ (half-filling), $D = 124$ and (b) $f = 5/4$, $D = 549$. Oxygen atoms are blue, electron-doped copper atoms are red, hole-doped copper atoms are green. The area of each circle is proportional to the doping away from half filling, i.e. $|1 - \hat{n}|$ and $2 - \hat{n}$ for copper and oxygen respectively

Due to the fact that the oxygen atoms are not completely double-filled for $f = 5/3$, the copper atoms are doped with electrons. When the compound is hole-doped, the filling of the oxygen atoms decreases and the copper atoms become doped with holes. It is seen that upon doping, the

Table 10.1: Mean occupancies of the oxygen and copper sites, together with their relative difference for the thee-band model of $HgBa_2CuO_4$. Bond dimensions from top to bottom are $D = 124, 261, 274, 549$.

f	$\overline{f_{Cu}}$	$\overline{f_{O_x}}$	$\overline{f_{O_y}}$	$\Delta(f_{Cu})$	$\Delta(f_{O_x})$	$\Delta(f_{O_y})$
5/3	1.2716	1.8886	1.8397	$7.3786 \cdot 10^{-5}$	$5.8327 \cdot 10^{-5}$	$3.2448 \cdot 10^{-5}$
19/12	1.1822	1.7927	1.7751	$9.6813 \cdot 10^{-3}$	$9.7228 \cdot 10^{-3}$	$5.1118 \cdot 10^{-3}$
3/2	1.0807	1.7115	1.7079	$1.8773 \cdot 10^{-4}$	$1.3547 \cdot 10^{-2}$	$5.3079 \cdot 10^{-5}$
5/4	0.9115	1.4529	1.3856	$1.4846 \cdot 10^{-1}$	$7.4165 \cdot 10^{-4}$	$3.3934 \cdot 10^{-1}$

added holes mainly reside on the oxygen atoms, as expected from the discussion of section 6.2.2. Interestingly, from table 10.1, it is seen that the hole density stays uniform upon doping until the copper atoms are hole-doped. The charge modulation for $f = 5/4$ is visualised in figure 10.1b. While the hole density of the oxygen p_x-orbitals is uniform, CDWs with $\lambda = 2$ exist on the copper and oxygen p_y-orbitals. These CDWs are in antiphase with respect to each other. If the hole densities on the 'squares' of the one-band model are calculated, i.e.

$$f_{\text{square},(i,j)} = f_{Cu,(i,j)} + \frac{f_{O_x,(i-1,j)} + f_{O_x,(i+1,j)} + f_{O_y,(i,j-1)} + f_{O_y,(i,j+1)}}{2} \tag{10.2}$$

then again CDWs with $\lambda = 2$ are seen, as shown in figure 10.2.

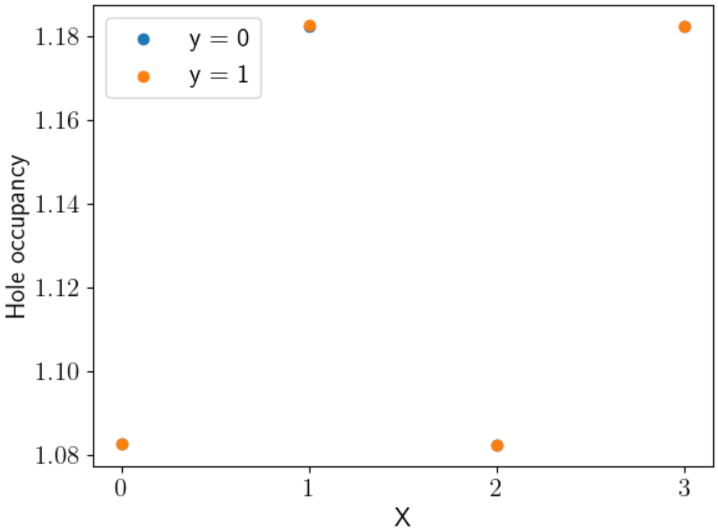

Figure 10.2: Hole occupancies of the ZRS of the three-band model of $HgBa_2CuO_4$ for $N = 6$, $f = 5/4$, $D = 549$

10.2 one-band model - $U(1) \otimes SU(2) \otimes f\mathbb{Z}_2$

10.2.1 Charge occupancies

The charge distributions for the one-band model with $N = 2$ and $N = 4$ is shown in figure 10.3. There is still some debate as to whether the cuprates exhibit stripe order or a checkerboard pattern [183]. This result seems to point to neither of those, but rather to the existence of pair-forming. The result for $N = 2$ shows a CDW with $\lambda = 4$. For $N = 4$, the same general trend as the $N = 2$ case can be seen along the x-direction. However, there is now clear pair-forming along the y-direction. This might be a consequence of the stronger pair-pair correlations and the presence of superconducting order for this model, as will also be shown in section 10.4 for $N = 2$.

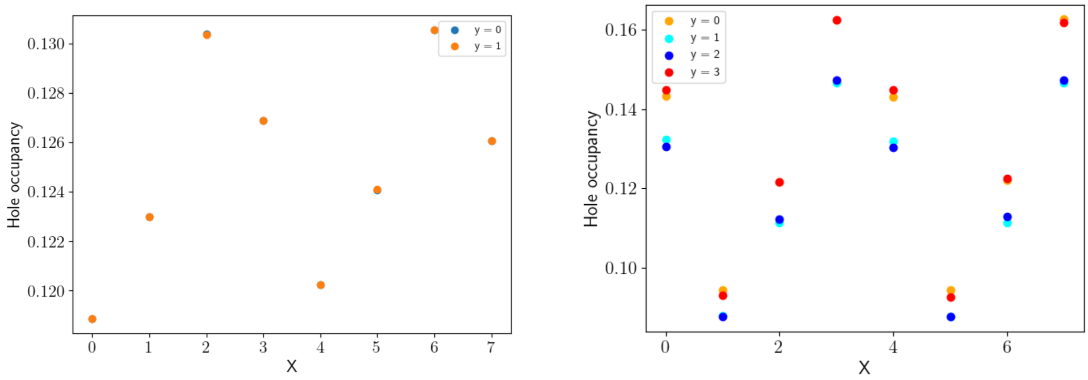

(a) (b)

Figure 10.3: Hole occupancies for the one-band model at $\delta = 1/8$ on a cylinder with (a) $N = 2$, $D = 650$ and (b) $N = 4$, $D = 300$

10.3 Comparison of the three-band and one-band model

A very interesting question is how the one-band and three-band model relate to each other. It was seen that upon slight doping of the three-band model, the charge density remained uniform. This is in sharp contrast with the one-band model. CDWs with $\lambda = 2$ emerged upon heavier doping, whereas $\lambda = 4$ was seen in the one-band model. When comparing these results, it is important to note that they should be compared at the same doping level. However, it is not clear whether the doping level of the copper atoms ($\overline{f_{Cu}}$) or the compound as a whole (f) should be used for the three-band model. The sharp contrast between hole-doped and electron-doped copper atoms seems to point to the use of $\overline{f_{Cu}}$. The three-band model should be investigated more to form a conclusion on this matter.

10.4 one-band superconductivity - $SU(2) \otimes f\mathbb{Z}_2$

10.4.1 Luttinger exponents

The Luttinger exponents of the one-band model of $HgBa_2CuO_4$ are shown in figures 10.4 and 10.5, together with their extrapolation and 95% confidence error bars. The extrapolation function that was used, is

$$K(\delta) = K_0 + a\delta^b \tag{10.3}$$

For the evaluation of K_{SC} for $\delta = 37.46\%$ and the evaluation of K_ρ for $\delta = 12.68\%$ and $\delta = 4.45\%$, b was set to 1 for a better extrapolation. Data for which the error bars of the extrapolation were unphysically large are not shown. It is concluded that for $\delta = 37.46\%$, 30.36%, and 4.45% the phase is a CDW, whereas for $\delta = 24.25\%$, 17.80%, and 12.68% it is SC. For $\delta = 19.90\%$, no conclusion could be drawn, and the calculations should be carried out for even higher bond dimensions in order to determine the phase. The error bars for $\delta = 37.46\%$ are quite large, because only the three most accurate results are used in the extrapolation. For $\delta = 12.68\%$, there is an overlap between the bounds on K_ρ and K_{SC}. It is nevertheless concluded that the phase is superconducting in this case. This is because the expected value of the extrapolation is lower for K_{SC} and because the extrapolation for K_ρ was done using a linear function, which does not take into account the flattening of the curve towards $\delta \to 0$ and is thus probably an underestimation. For $\delta = 30.36\%$, 24.25%, and 17.80%, the error bars were too large. With slight hesitation, the phase can nevertheless be concluded to be SC, due to the general trend of the Luttinger exponents in function of the error measure δ_{42}. Most extrapolations also seem to violate the relation $K_\rho K_{SC} = 1$ of the Luther-Emery class.

These results can be summarized in a sketch of the phase diagram, shown in figure 10.6. The experimental phase diagram of figure 6.6a shows that the superconducting order exists in the regime $\delta \in [\delta_{min}, \delta_{max}]$, where $\delta_{min} \approx 0.05$ and $\delta_{max} \approx 0.24$ [143], whereas the phase diagram based on our results claims $0.0445 \lesssim \delta_{min} \lesssim 0.1247$ and $0.2425 \lesssim \delta_{max} \lesssim 0.3036$. Different experiments and numerical calculations differ in these numbers, however [184, 145, 157].

10.4.2 coexistence of stripe order and superconductivity - Pair density waves

As seen in figure 6.6a, there is a range of hole dopings where stripe order and d-wave superconductivity coexist. This coexistence has been experimentally verified in various cuprates [172, 185, 186]. The eigenvalues of the transfer matrix will again be used to determine whether a CDW wave exists. In the range of dopings considered, i.e. $\delta \in [4.45\%, 37.46\%]$, all systems exhibit fully-filled stripes. Some also exhibit CDWs with a filling fraction $FF > 1$. More details and the corresponding figures can be found in appendix F. These results seem to indicate that stripe order exists in the one-band ladder for a wide range of dopings, and together with the results from the previous section, will coexist with d-wave superconductivity for $\delta \in [\delta_{min}, \delta_{max}]$. This coexistence was also found in literature [187, 157, 188]. Reference [188] found a uniform superconducting phase for $0.17 \lesssim \delta \lesssim 0.22$ and the coexistence of stripe order and d-wave superconductivity for $0.07 \lesssim \delta \lesssim 0.17$.

The coexistence of stripe order and superconductivity can also point towards a new quantum phase of matter, the pair density wave (PDW), which has recently generated interest due to its experimental observations in cuprates. This phase has been proposed as a candidate for the ground state

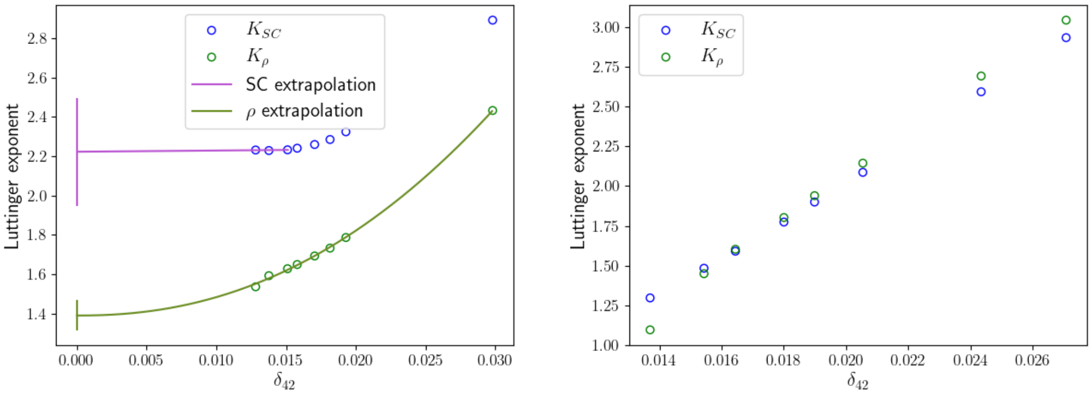

(a) $\mu = -6.5$, $\delta \approx 0.3746$ (b) $\mu = -7.5$, $\delta \approx 0.3036$

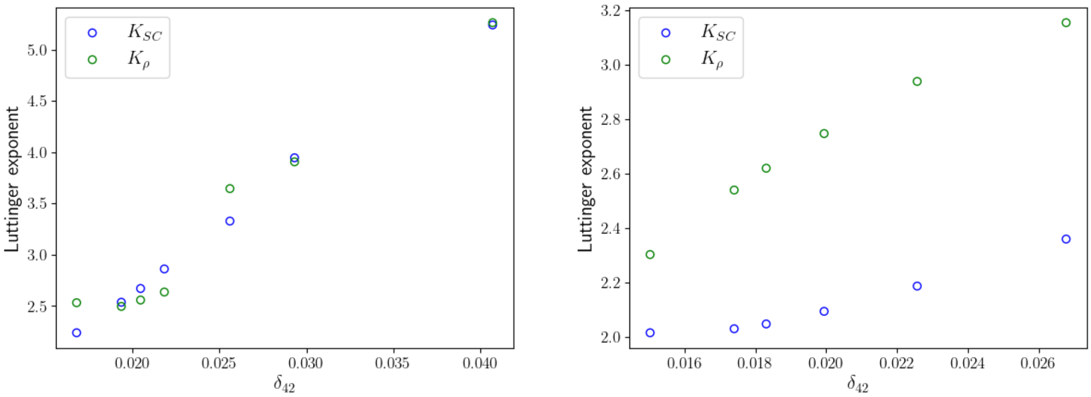

(c) $\mu = -8.5$, $\delta \approx 0.2425$ (d) $\mu = -9.2$, $\delta \approx 0.1990$

Figure 10.4: Luttinger exponents of the one-band model of $HgBa_2CuO_4$, together with their extrapolation and error bars. Data for which the error bars of the extrapolation were too large are not shown. It is concluded that for $\mu = -6.5$ and -7.5, the phase is a CDW, whereas for $\mu = -8.5$ it is SC. For $\mu = -9.2$, no conclusion could be drawn.

of cuprates as an intertwined form of CDWs, SDWs, and superconducting order, rather than severe competition between these phases [189, 190, 185, 191]. It has also been found as the ground state in the three-band model [192]. The definition of a PDW is a phase in which the superconducting order parameter varies spatially with an average of zero, but where the amplitude of the oscillations can be strong [193]. Since the superconducting order parameter is zero in these quasi-1D systems due to the Mermin-Wagner theorem, there is as of yet no way to verify their existence in these systems.

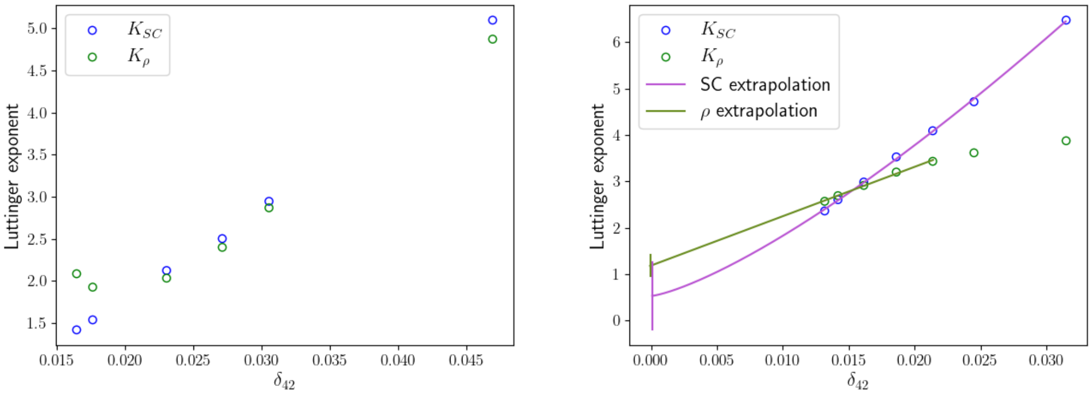

(a) $\mu = -9.5$, $\delta \approx 0.1780$ (b) $\mu = -10.1$, $\delta \approx 0.1268$

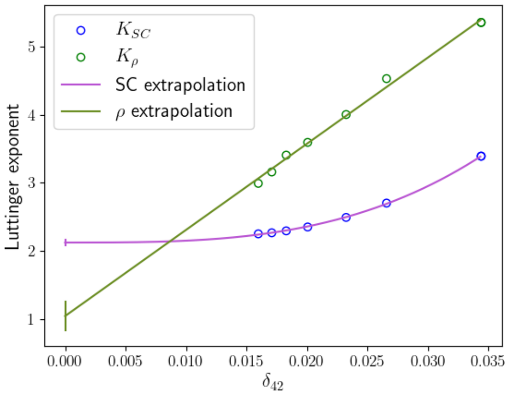

(c) $\mu = -10.607$, $\delta \approx 0.0445$

Figure 10.5: Luttinger exponents of the one-band model of $HgBa_2CuO_4$, together with their extrapolation and error bars. Data for which the error bars of the extrapolation were too large are not shown. It is concluded that for $\mu = -9.5$ and -10.1, the phase is SC, whereas for $\mu = -10.607$ it is a CDW.

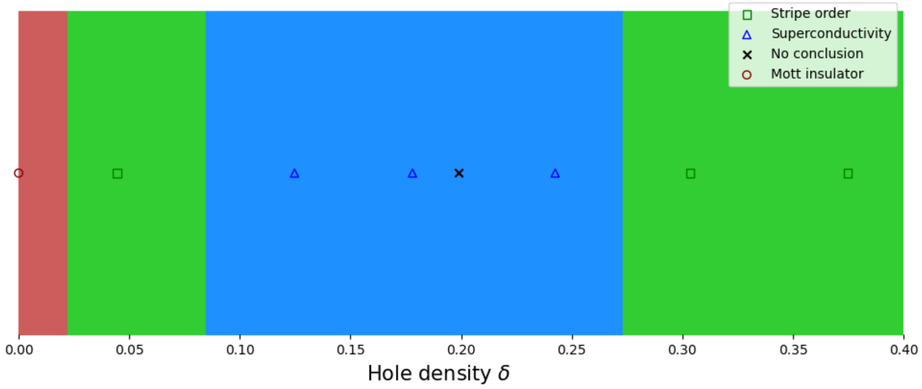

Figure 10.6: Sketch of the phase diagram of the one-band model of $HgBa_2CuO_4$ based on the results from figures 10.4 and 10.5. The phase transitions are simply said to occur in the middle between two successive data points. More data points should be calculated to narrow the range in which the phase transitions occur.

IV

Conclusion and discussion

11

Conclusion

In this thesis, we have investigated the simple Hubbard model in 1D and 2D, together with the one-band and three-band models of the cuprates.

This thesis started with an explanation of the framework of trying to reconcile DFT and TN. After a brief explanation of DFT and the construction of effective Hamiltonians using a downfolding procedure, the theory of solving these effective Hamiltonians was explained more thoroughly. This started with the main ideas behind TN. Afterward, some useful concepts and definitions were introduced, like the mixed gauge and correlation functions, which would prove to be useful in evaluating the properties of the ground state MPS. In part II, more technical details were given. This started with an explanation of the different variational techniques of obtaining the ground state MPS. Both the Heisenberg model and the Hubbard model were introduced, as those are the Hamiltonians used throughout the thesis. Afterward, the properties of the cuprates and the models describing them were expanded upon, prior to explaining the algorithms to evaluate the expressions introduced in chapters before, together with some additional computational details.

Part III listed and interpreted the numerical results. First, the different Hamiltonians and used methods were benchmarked. Both the Heisenberg model and the 1D Hubbard model were benchmarked in terms of energy and correlation functions. For the Heisenberg model, there was additional benchmarking of the used extrapolation in bond dimension, the staggered magnetization, and the influence of using cylinders and helices of various circumferences. This showed that the used Hamiltonians and methods used in this thesis are correct.

Next, The 2D Hubbard model was investigated. It was found that the energy of the cylinders and helices converged to the exact 2D value for $N \to \infty$, although there was a significant deviation from the 2D values for cylinders with $N = 2$. Afterward, the local hole densities were investigated for cylinders with $N = 2$ and $N = 4$ using the $U(1) \otimes SU(2) \otimes f\mathbb{Z}_2$ symmetry. At half-filling, a uniform phase was found, whereas for $\delta = 1/8$, a CDW with $\lambda = 8$ was found for $N = 2$ and a CDW with $\lambda = 4$ for $N = 4$. These results signify filled and half-filled stripes, respectively, and are consistent with the available literature. After that, the same systems were investigated using the $SU(2) \otimes f\mathbb{Z}_2$ symmetry, decreasing the computational complexity and losing the disadvantage of having to look at cylinders with a given number of rungs. Evaluation of the transfer matrix spectrum gave results consistent with the sections before. Finally, power laws with Luttinger exponents were fitted to the density and pair correlation functions. These were given in function of an error measure and extrapolated. Due to the extreme competition between charge order and superconductivity, the 95% confidence intervals of K_ρ and K_{SC} overlapped, even when using very high bond dimensions. As a result, no conclusion could be drawn on the ground state phase of the Hubbard ladder with $t = 1$, $U = 8$, and $\delta = 1/8$.

Lastly, the one-band and three-band models of cuprate $\mathrm{HgBa_2CuO_4}$ were investigated as a case study. The three-band model was investigated and confirmed the hypothesis that the holes at half-filling reside mainly on the oxygen atoms. For small doping levels, the relative differences in the hole occupancies were small, indicating a uniform phase. When the hole doping was strong enough and the copper atoms became hole-doped, a CDW with $\lambda = 2$ was seen. Afterward, the one-band model was investigated. First, the $U(1) \otimes SU(2) \otimes f\mathbb{Z}_2$ symmetry was used and the hole occupancies were calculated. These seemed to point to a CDW with $\lambda = 4$ and the existence of pair forming. Then, the $SU(2) \otimes f\mathbb{Z}_2$ symmetry was imposed to try to determine the phase diagram. The Luttinger exponents were calculated and were extrapolated for the cases where high enough bond dimensions were used. Based on the extrapolated values of these cases, and the general trend in function of the bond dimension for the other cases, the ground state phase could be determined in all but one case. This allowed us to construct the ground state phase diagram of the one-band model of $\mathrm{HgBa_2CuO_4}$ on a cylinder with $N = 2$. This phase diagram was similar to the experimental phase diagram of the cuprates. Additionally, the transfer matrix eigenvalues were calculated for all doping levels. Fully-filled stripes were found in all cases, with sometimes the coexistence with CDWs with larger periods. These results can also point toward the existence of PDWs.

12 Discussion

The investigation of the Hubbard model and the cuprates is a very broad research field, and many roads could have been taken in this thesis. This chapter will explain why some aspects were investigated while others were not, together with a discussion on some of the used approximations. Further work on this topic could include examining some aspects more thoroughly, taking some of the roads that were not taken, or analyzing to what extent the approximations hold.

In the discussion on the 2D Hubbard model and the case study on $HgBa_2CuO_4$, mainly cylinders with $N = 2$ and $N = 4$ were investigated. To make accurate and reliable conclusions for the 2D system, a finite-size scaling in $1/N$ should be performed. This is not feasible using current classical computers, however, since the calculations are restricted to low values of N. Going to higher values of N increases the complexity of the calculation in two ways. First, the bigger circumference results in the fact that the entanglement between neighboring sites in the x-direction has to pass through more sites than e.g. in the $N = 2$ case, thus needing a bigger bond dimension to describe it. Second, the unit cell has to be an integer multiple of N. This causes the complexity of the algorithms to have a linear dependence on N for a given bond dimension. This is also the reason why the phase diagram of the one-band model of $HgBa_2CuO_4$ was not investigated for $N = 4$. The $N = 2$ case already needed very high bond dimensions, sometimes prohibiting the precise extrapolation of the Luttinger exponents. In the cases where the error bounds on K_ρ and K_{SC} overlapped or where no extrapolation could be performed, the conclusion of the phase is much less reliable than in the other cases. These conclusions could be improved by going to even higher bond dimensions. Obtaining the same results for the $N = 4$ case would not have been feasible with the amount of computer power and time given for this thesis. With more time and computer power, it would also have been interesting to plot the Luttinger exponents in function of doping for $N = 2$. T_c has a dome shape in function of doping, as seen in figure 6.6a. This could be related to the robustness of the superconducting order, and we might be able to see a similar dome shape for K_{SC}.

Helices are not discussed thoroughly for the 2D Hubbard model. The reason for this, apart from the limited time available in a year, is that cylinders seem a more natural system to describe the 2D Hubbard model than helices. The presence of stripe order makes a clear distinction between the y-direction, along which there is uniformity, and the x-direction, along which there is charge modulation. A helix is effectively a one-dimensional chain along a direction that is a linear combination of x and y, and one can not really speak about the rungs of a helix. The resulting calculations of the 2D simple Hubbard model on a helix gave non-uniformity along the 'y'-direction, and thus no stripe order exists. Due to both the experimental and numerical verification of the presence of stripe order, the helix was abandoned as a realistic model to describe the cuprates. Helices are also far less investigated for the 2D Hubbard model than cylinders [194]. Moreover, the plaquette symmetry is likely to be violated on helices, begging the question of whether plaquette d-wave superconductivity can even exist on a helix. This last argument, together with the discussion on spontaneous symmetry breaking of the Heisenberg model of section 8.2.2, does make the helix interesting to investigate from a theoretical point of view.

A possible alternative to both cylinders and helices is to work directly in 2D using iPEPS. Here, spontaneous symmetry breaking can occur, and the determination of the ground state phase might be easier than for the cylinder systems. Although it has been found that for cylindrical systems with small to intermediate circumferences, like the ones investigated in this thesis, the MPS description gives more accurate results than the iPEPS description [195], this is likely not the case for the full 2D systems.

In this thesis, both $U(1) \otimes SU(2) \otimes f\mathbb{Z}_2$ and $SU(2) \otimes f\mathbb{Z}_2$ have been imposed and investigated. There are two main reasons why dropping the $U(1)$ symmetry is advantageous for looking for superconductivity. First, the fact that the total number of rungs must be a multiple of a certain value for a given circumference and filling, intrinsically favors stripe order with a wavelength that fits on the cylinder, i.e. for which the number of rungs is an integer multiple of the wavelength. The superconducting order could be lower in energy than this CDW, but higher in energy than a CDW with another wavelength. Second, the need for a cylinder with multiple rungs increases the complexity of the calculation, making only smaller bond dimensions possible. This yields results that are possibly not accurate enough to resolve the highly competitive orders. This is the reason why the Luttinger exponents were calculated while imposing $SU(2) \otimes f\mathbb{Z}_2$. However, the $U(1) \otimes SU(2) \otimes f\mathbb{Z}_2$ symmetry allows for the easy and straightforward calculation and visualization of the local charge densities, whereas without $U(1)$ these have to be found in the transfer matrix eigenvalues. Another downside of dropping the $U(1)$ symmetry is the fact that the filling is not exact and that the chemical potential must be found numerically for a given desired filling. Both symmetries thus have advantages and disadvantages, and it might be interesting to look at both. Using $SU(2)$ instead of $U(1)$ for the spin sector is almost always preferred to its decrease in complexity and its exactness. The only reason to use $U(1)$ for the spin sector is when the local magnetic moments would be needed.

One of the most important questions in the numerical investigation of cuprates is what the most simple model is that captures all their physical properties. In this thesis, hopping terms acting further than nearest neighbors, together with repulsive on-site and off-site interactions have been considered. These already yielded a phase diagram that matches the one of the cuprates to some extent, but might still not be the full story. It is not because the interactions here give rise to d-wave superconductivity, that this is the full mechanism behind the emergence of d-wave superconductivity in the cuprates. Other sets of interactions, with possibly different signs and strengths, might give rise to it as well. For example, Hamiltonians taking into account phonon-electron coupling or attractive on-site or off-site interactions have been found to give rise to superconducting states too [196, 197, 198]. It would be very interesting, though computationally very expensive and time-consuming, to consider all these extra interactions in all parameter regimes, and to systematically switch some of the parameters to zero. This would tell us which interactions are necessary for superconductivity, and which only increase or decrease its stability. Together with a downfolding procedure that can accurately determine the parameters of the various interactions, this could settle the question of what the responsible mechanism behind high-temperature superconductivity is once and for all, and what the correct Hamiltonian is to describe it. This Hamiltonian should be made as simple as possible, but not simpler.

13

References

[1] Errol Lewars. *Computational Chemistry: Introduction to the Theory and Applications of Molecular and Quantum Mechanics.* Jan. 2011, pp. 1–664. ISBN: 978-90-481-3860-9. DOI: `10.1007/978-90-481-3862-3`.

[2] Pablo Echenique and J. L. Alonso. “A mathematical and computational review of Hartree–Fock SCF methods in quantum chemistry”. In: *Molecular Physics* 105.23-24 (2007), pp. 3057–3098. DOI: `10.1080/00268970701757875`. eprint: `https://doi.org/10.1080/00268970701757875`. URL: `https://doi.org/10.1080/00268970701757875`.

[3] Panati, Gianluca, Spohn, Herbert, and Teufel, Stefan. “The time-dependent Born-Oppenheimer approximation”. In: *ESAIM: M2AN* 41.2 (2007), pp. 297–314. DOI: `10.1051/m2an:2007023`. URL: `https://doi.org/10.1051/m2an:2007023`.

[4] I.N. Levine. *Computational Chemistry (Pearson advanced chemistry series). 7th Edition.* Pearson Education, New York, 2014. ISBN: 97803218906031.

[5] Axel D. Becke. “Perspective: Fifty years of density-functional theory in chemical physics”. In: *The Journal of Chemical Physics* 140.18 (Apr. 2014). 18A301. ISSN: 0021-9606. DOI: `10.1063/1.4869598`. eprint: `https://pubs.aip.org/aip/jcp/article-pdf/doi/10.1063/1.4869598/15480507/18a301\_1\_online.pdf`. URL: `https://doi.org/10.1063/1.4869598`.

[6] P. Hohenberg and W. Kohn. “Inhomogeneous Electron Gas”. In: *Physical Review* 136 (3B Nov. 1964), B864–B871. DOI: `10.1103/PhysRev.136.B864`. URL: `https://link.aps.org/doi/10.1103/PhysRev.136.B864`.

[7] W. Kohn and L. J. Sham. “Self-Consistent Equations Including Exchange and Correlation Effects”. In: *Physical Review* 140 (4A Nov. 1965), A1133–A1138. DOI: `10.1103/PhysRev.140.A1133`. URL: `https://link.aps.org/doi/10.1103/PhysRev.140.A1133`.

[8] Masatoshi Imada and Takashi Miyake. “Electronic Structure Calculation by First Principles for Strongly Correlated Electron Systems”. In: *Journal of the Physical Society of Japan* 79.11 (Nov. 2010), p. 112001. DOI: `10.1143/jpsj.79.112001`. URL: `https://doi.org/10.1143%2Fjpsj.79.112001`.

[9] J. Ignacio Cirac, David Pé rez-Garcıa, Norbert Schuch, and Frank Verstraete. “Matrix product states and projected entangled pair states: Concepts, symmetries, theorems”. In: *Reviews of Modern Physics* 93.4 (Dec. 2021). DOI: `10.1103/revmodphys.93.045003`. URL: `https://doi.org/10.1103%2Frevmodphys.93.045003`.

[10] M B Hastings. “An area law for one-dimensional quantum systems”. In: *Journal of Statistical Mechanics: Theory and Experiment* 2007.08 (Aug. 2007), P08024–P08024. DOI: `10.1088/1742-5468/2007/08/p08024`. URL: `https://doi.org/10.1088%2F1742-5468%2F2007%2F08%2Fp08024`.

[11] J. Eisert, M. Cramer, and M. B. Plenio. “Colloquium: Area laws for the entanglement entropy”. In: *Rev. Mod. Phys.* 82 (1 Feb. 2010), pp. 277–306. DOI: `10.1103/RevModPhys.82.277`. URL: `https://link.aps.org/doi/10.1103/RevModPhys.82.277`.

[12] Itai Arad, Zeph Landau, and Umesh Vazirani. “Improved one-dimensional area law for frustration-free systems”. In: *Physical Review B* 85 (19 May 2012), p. 195145. DOI: `10.1103/PhysRevB.85.195145`. URL: `https://link.aps.org/doi/10.1103/PhysRevB.85.195145`.

[13] Michael M. Wolf, Frank Verstraete, Matthew B. Hastings, and J. Ignacio Cirac. "Area Laws in Quantum Systems: Mutual Information and Correlations". In: *Physical Review Letters* 100.7 (Feb. 2008). DOI: `10.1103/physrevlett.100.070502`. URL: `https://doi.org/10.1103%2Fphysrevlett.100.070502`.

[14] Steven R. White. "Density matrix formulation for quantum renormalization groups". In: *Physical Review Letters* 69 (19 Nov. 1992), pp. 2863–2866. DOI: `10.1103/PhysRevLett.69.2863`. URL: `https://link.aps.org/doi/10.1103/PhysRevLett.69.2863`.

[15] Steven R. White. "Density-matrix algorithms for quantum renormalization groups". In: *Physical Review B* 48 (14 Oct. 1993), pp. 10345–10356. DOI: `10.1103/PhysRevB.48.10345`. URL: `https://link.aps.org/doi/10.1103/PhysRevB.48.10345`.

[16] Tomotoshi Nishino and Kouichi Okunishi. "Corner Transfer Matrix Renormalization Group Method". In: *Journal of the Physical Society of Japan* 65.4 (Apr. 1996), pp. 891–894. DOI: `10.1143/jpsj.65.891`. URL: `https://doi.org/10.1143%2Fjpsj.65.891`.

[17] Tomotoshi Nishino and Kouichi Okunishi. "Corner Transfer Matrix Algorithm for Classical Renormalization Group". In: *Journal of the Physical Society of Japan* 66.10 (1997), pp. 3040–3047. DOI: `10.1143/JPSJ.66.3040`. eprint: `https://doi.org/10.1143/JPSJ.66.3040`. URL: `https://doi.org/10.1143/JPSJ.66.3040`.

[18] V. Zauner-Stauber, L. Vanderstraeten, M. T. Fishman, F. Verstraete, and J. Haegeman. "Variational optimization algorithms for uniform matrix product states". In: *Physical Review B* 97 (4 Jan. 2018), p. 045145. DOI: `10.1103/PhysRevB.97.045145`. URL: `https://link.aps.org/doi/10.1103/PhysRevB.97.045145`.

[19] Laurens Vanderstraeten, Jutho Haegeman, and Frank Verstraete. "Tangent-space methods for uniform matrix product states". In: *SciPost Physics Lecture Notes* (Jan. 2019). DOI: `10.21468/scipostphyslectnotes.7`. URL: `https://doi.org/10.21468%2Fscipostphyslectnotes.7`.

[20] B. M. Terhal. "Is entanglement monogamous?" In: *IBM Journal of Research and Development* 48.1 (Jan. 2004), pp. 71–78. DOI: `10.1147/rd.481.0071`. URL: `https://doi.org/10.1147%2Frd.481.0071`.

[21] Xiao-Lan Zong, Hao-Hao Yin, Wei Song, and Zhuo-Liang Cao. "Monogamy of Quantum Entanglement". In: *Frontiers in Physics* 10 (June 2022). DOI: `10.3389/fphy.2022.880560`. URL: `https://doi.org/10.3389%2Ffphy.2022.880560`.

[22] Johannes Bauer, Jong E. Han, and Olle Gunnarsson. "Retardation effects and the Coulomb pseudopotential in the theory of superconductivity". In: *Physical Review B* 87 (5 Feb. 2013), p. 054507. DOI: `10.1103/PhysRevB.87.054507`. URL: `https://link.aps.org/doi/10.1103/PhysRevB.87.054507`.

[23] F. Aryasetiawan, K. Karlsson, O. Jepsen, and U. Schönberger. "Calculations of Hubbard U from first-principles". In: *Physical Review B* 74 (12 Sept. 2006), p. 125106. DOI: `10.1103/PhysRevB.74.125106`. URL: `https://link.aps.org/doi/10.1103/PhysRevB.74.125106`.

[24] P. H. Dederichs, S. Blügel, R. Zeller, and H. Akai. "Ground States of Constrained Systems: Application to Cerium Impurities". In: *Physical Review Letters* 53 (26 Dec. 1984), pp. 2512–2515. DOI: `10.1103/PhysRevLett.53.2512`. URL: `https://link.aps.org/doi/10.1103/PhysRevLett.53.2512`.

[25] Vladimir I. Anisimov, Jan Zaanen, and Ole K. Andersen. "Band theory and Mott insulators: Hubbard U instead of Stoner I". In: *Physical Review B* 44 (3 July 1991), pp. 943–954. DOI: `10.1103/PhysRevB.44.943`. URL: `https://link.aps.org/doi/10.1103/PhysRevB.44.943`.

[26] I. V. Solovyev and M. Imada. "Screening of Coulomb interactions in transition metals". In: *Physical Review B* 71 (4 Jan. 2005), p. 045103. DOI: `10.1103/PhysRevB.71.045103`. URL: `https://link.aps.org/doi/10.1103/PhysRevB.71.045103`.

[27] Matteo Cococcioni and Stefano de Gironcoli. "Linear response approach to the calculation of the effective interaction parameters in the LDA + U method". In: *Physical Review B* 71 (3 Jan. 2005), p. 035105. DOI: `10.1103/PhysRevB.71.035105`. URL: `https://link.aps.org/doi/10.1103/PhysRevB.71.035105`.

[28] F. Aryasetiawan, M. Imada, A. Georges, G. Kotliar, S. Biermann, and A. I. Lichtenstein. "Frequency-dependent local interactions and low-energy effective models from electronic structure calculations". In: *Physical Review B* 70.19 (Nov. 2004). DOI: `10.1103/physrevb.70.195104`. URL: `https://doi.org/10.1103%2Fphysrevb.70.195104`.

[29] E. Pavarini, E. Koch, A. Lichtenstein, and D. Vollhardt. *The LDA+DMFT approach to strongly correlated materials (Schriften des Forschungszentrums Jülich. Reihe modeling and simulation).* Vol. 91. Jülich: Forschungszenrum Jülich GmbH Zentralbibliothek, Verlag, 2011, 209–234, Record converted from VDB: 12.11.2012.

[30] Motoaki Hirayama, Takashi Miyake, and Masatoshi Imada. "Derivation of static low-energy effective models by an ab initio downfolding method without double counting of Coulomb correlations: Application to $SrVO_3$, FeSe, and FeTe". In: *Physical Review B* 87 (19 May 2013), p. 195144. DOI: `10.1103/PhysRevB.87.195144`. URL: `https://link.aps.org/doi/10.1103/PhysRevB.87.195144`.

[31] E. Schrödinger. "An Undulatory Theory of the Mechanics of Atoms and Molecules". In: *Physical Review* 28 (6 Dec. 1926), pp. 1049–1070. DOI: `10.1103/PhysRev.28.1049`. URL: `https://link.aps.org/doi/10.1103/PhysRev.28.1049`.

[32] M. Born and R. Oppenheimer. "Zur Quantentheorie der Molekeln". In: *Annalen der Physik* 389.20 (1927), pp. 457–484. DOI: `https://doi.org/10.1002/andp.19273892002`. eprint: `https://onlinelibrary.wiley.com/doi/pdf/10.1002/andp.19273892002`. URL: `https://onlinelibrary.wiley.com/doi/abs/10.1002/andp.19273892002`.

[33] Ira N. Levine. *Quantum chemistry (Pearson advanced chemistry series).* Pearson, 2014. ISBN: 9780321890603. URL: `https://search.library.wisc.edu/catalog/9910167862202121`.

[34] Wolfgang Pauli. "Exclusion Principle and Quantum Mechanics". In: *Writings on Physics and Philosophy.* Ed. by Charles P. Enz and Karl von Meyenn. Berlin, Heidelberg: Springer Berlin Heidelberg, 1994, pp. 165–181. ISBN: 978-3-662-02994-7. DOI: `10.1007/978-3-662-02994-7_20`. URL: `https://doi.org/10.1007/978-3-662-02994-7_20`.

[35] D. R. Hartree and W. Hartree. "Self-consistent field, with exchange, for beryllium". In: *Proceedings of the Royal Society of London. Series A, Mathematical and Physical Sciences* 150.869 (1935), pp. 9–33.

[36] Paul R. C. Kent and Gabriel Kotliar. "Toward a predictive theory of correlated materials". In: *Science* 361.6400 (2018), pp. 348–354. DOI: `10.1126/science.aat5975`. eprint: `https://www.science.org/doi/pdf/10.1126/science.aat5975`. URL: `https://www.science.org/doi/abs/10.1126/science.aat5975`.

[37] Daniel P. Arovas, Erez Berg, Steven A. Kivelson, and Srinivas Raghu. "The Hubbard Model". In: *Annual Review of Condensed Matter Physics* 13.1 (Mar. 2022), pp. 239–274. DOI: `10.1146/annurev-conmatphys-031620-102024`. URL: `https://doi.org/10.1146%2Fannurev-conmatphys-031620-102024`.

[38] Mingpu Qin, Thomas Schäfer, Sabine Andergassen, Philippe Corboz, and Emanuel Gull. "The Hubbard Model: A Computational Perspective". In: *Annual Review of Condensed Matter Physics* 13.1 (Mar. 2022), pp. 275–302. DOI: `10.1146/annurev-conmatphys-090921-033948`. URL: `https://doi.org/10.1146%2Fannurev-conmatphys-090921-033948`.

[39] Fabian Essler, Holger Frahm, Frank Göhmann, Andreas Klümper, and Vladimir Korepin. "The One-Dimensional Hubbard Model". In: *The One-Dimensional Hubbard Model, by Fabian H. L. Essler , Holger Frahm , Frank Göhmann , Andreas Klümper , Vladimir E. Korepin, Cambridge, UK: Cambridge University Press, 2010* (Aug. 2010). DOI: `10.1142/9789812798268_others01`.

[40] Thomas Maier, Mark Jarrell, Thomas Pruschke, and Matthias H. Hettler. "Quantum cluster theories". In: *Rev. Mod. Phys.* 77 (3 Oct. 2005), pp. 1027–1080. DOI: `10.1103/RevModPhys.77.1027`. URL: `https://link.aps.org/doi/10.1103/RevModPhys.77.1027`.

[41] Daan Verraes. "Increasing the accuracy of quantum-mechanical simulations for strongly correlated functional materials by designing effective Hamiltonians". In: *Not published* (2023).

[42] Román Orús. "A practical introduction to tensor networks: Matrix product states and projected entangled pair states". In: *Annals of Physics* 349 (Oct. 2014), pp. 117–158. DOI: `10.1016/j.aop.2014.06.013`. URL: `https://doi.org/10.1016%2Fj.aop.2014.06.013`.

[43] David Poulin, Angie Qarry, Rolando Somma, and Frank Verstraete. "Quantum Simulation of Time-Dependent Hamiltonians and the Convenient Illusion of Hilbert Space". In: *Physical Review Letters* 106.17 (Apr. 2011). DOI: `10.1103/physrevlett.106.170501`. URL: `https://doi.org/10.1103%2Fphysrevlett.106.170501`.

[44] Yi-Kai Liu, Matthias Christandl, and F. Verstraete. "Quantum Computational Complexity of the N-Representability Problem: QMA Complete". In: *Physical Review Letters* 98 (11 Mar. 2007), p. 110503. DOI: `10.1103/PhysRevLett.98.110503`. URL: `https://link.aps.org/doi/10.1103/PhysRevLett.98.110503`.

[45] Román Orús. "Tensor networks for complex quantum systems". In: *Nature Reviews Physics* 1.9 (Aug. 2019), pp. 538–550. DOI: `10.1038/s42254-019-0086-7`. URL: `https://doi.org/10.1038%2Fs42254-019-0086-7`.

[46] Jutho Haegeman, Bogdan Pirvu, David J. Weir, J. Ignacio Cirac, Tobias J. Osborne, Henri Verschelde, and Frank Verstraete. "Variational matrix product ansatz for dispersion relations". In: *Physical Review B* 85.10 (Mar. 2012). DOI: `10.1103/physrevb.85.100408`. URL: `https://doi.org/10.1103%2Fphysrevb.85.100408`.

[47] Hui Li and F. D. M. Haldane. "Entanglement Spectrum as a Generalization of Entanglement Entropy: Identification of Topological Order in Non-Abelian Fractional Quantum Hall Effect States". In: *Physical Review Letters* 101.1 (July 2008). DOI: `10.1103/physrevlett.101.010504`. URL: `https://doi.org/10.1103%2Fphysrevlett.101.010504`.

[48] Ulrich Schollwöck. "The density-matrix renormalization group in the age of matrix product states". In: *Annals of Physics* 326.1 (Jan. 2011), pp. 96–192. DOI: `10.1016/j.aop.2010.09.012`. URL: `https://doi.org/10.1016%2Fj.aop.2010.09.012`.

[49] R. van Meer and O. V. Gritsenko. "Correlation-coupling entropy as a measure of strong electron correlation and fragment-conditional density spin polarization as a measure of electron entanglement". In: *Physical Review A* 100 (3 Sept. 2019), p. 032335. DOI: `10.1103/PhysRevA.100.032335`. URL: `https://link.aps.org/doi/10.1103/PhysRevA.100.032335`.

[50] Zhen Huang and Sabre Kais. "Entanglement as measure of electron–electron correlation in quantum chemistry calculations". In: *Chemical Physics Letters* 413.1-3 (Sept. 2005), pp. 1–5. DOI: `10.1016/j.cplett.2005.07.045`. URL: `https://doi.org/10.1016%2Fj.cplett.2005.07.045`.

[51] John von Neumann. *Mathematische Grundlagen der Quantenmechanik. (German) [Mathematical Foundations of Quantum Mechanics]*. German. 1932.

[52] Michael A. Nielsen and Isaac L. Chuang. *Quantum Computation and Quantum Information: 10th Anniversary Edition*. Cambridge University Press, 2010. DOI: `10.1017/CBO9780511976667`.

[53] Yu-Xin Wang, Liang-Zhu Mu, Vlatko Vedral, and Heng Fan. "Entanglement Rényi α entropy". In: *Physical Review A* 93.2 (Feb. 2016). DOI: `10.1103/physreva.93.022324`. URL: `https://doi.org/10.1103%2Fphysreva.93.022324`.

[54] Alfréd Rényi. *On Measures of Entropy and Information*. The Regents of the University of California, 1961, pp. 547–562.

[55] F. Verstraete and J. I. Cirac. "Matrix product states represent ground states faithfully". In: *Physical Review B* 73.9 (Mar. 2006). DOI: `10.1103/physrevb.73.094423`. URL: `https://doi.org/10.1103%2Fphysrevb.73.094423`.

[56] Julia Kempe, Alexei Kitaev, and Oded Regev. "The Complexity of the Local Hamiltonian Problem". In: *SIAM Journal on Computing* 35.5 (2006), pp. 1070–1097. DOI: `10.1137/S0097539704445226`. eprint: `https://doi.org/10.1137/S0097539704445226`. URL: `https://doi.org/10.1137/S0097539704445226`.

[57] Jacob C Bridgeman and Christopher T Chubb. "Hand-waving and interpretive dance: an introductory course on tensor networks". In: *Journal of Physics A: Mathematical and Theoretical* 50.22 (May 2017), p. 223001. DOI: `10.1088/1751-8121/aa6dc3`. URL: `https://doi.org/10.1088%2F1751-8121%2Faa6dc3`.

[58] Laurens Vanderstraeten, Lander Burgelman, Boris Ponsioen, Maarten Van Damme, Bram Vanhecke, Philippe Corboz, Jutho Haegeman, and Frank Verstraete. "Variational methods for contracting projected entangled-pair states". In: *Physical Review B* 105 (19 May 2022), p. 195140. DOI: `10.1103/PhysRevB.105.195140`. URL: `https://link.aps.org/doi/10.1103/PhysRevB.105.195140`.

[59] F. Verstraete and J. I. Cirac. *Renormalization algorithms for Quantum-Many Body Systems in two and higher dimensions*. 2004. DOI: `10.48550/ARXIV.COND-MAT/0407066`. URL: `https://arxiv.org/abs/cond-mat/0407066`.

[60] Charles H. Bennett, Herbert J. Bernstein, Sandu Popescu, and Benjamin Schumacher. "Concentrating partial entanglement by local operations". In: *Physical Review A* 53 (4 Apr. 1996), pp. 2046–2052. DOI: `10.1103/PhysRevA.53.2046`. URL: `https://link.aps.org/doi/10.1103/PhysRevA.53.2046`.

[61] Quinten Mortier, Lukas Devos, Lander Burgelman, Bram Vanhecke, Laurens Vanderstraeten, Nick Bultinck, Frank Verstraete, and Jutho Haegeman. "Fermionic tensor network methods". To be published. 2023.

[62] U. Schollwöck. "The density-matrix renormalization group". In: *Rev. Mod. Phys.* 77 (1 Apr. 2005), pp. 259–315. DOI: `10.1103/RevModPhys.77.259`. URL: `https://link.aps.org/doi/10.1103/RevModPhys.77.259`.

[63] Martin Andersson, Magnus Boman, and Stellan Östlund. “Density-matrix renormalization group for a gapless system of free Tfermions”. In: *Physical Review B* 59 (16 Apr. 1999), pp. 10493–10503. DOI: `10.1103/PhysRevB.59.10493`. URL: `https://link.aps.org/doi/10.1103/PhysRevB.59.10493`.

[64] M Fannes, B Nachtergaele, and R F Werner. “Valence bond states on quantum spin chains as ground states with spectral gap”. In: *Journal of Physics A: Mathematical and General* 24.4 (Feb. 1991), p. L185. DOI: `10.1088/0305-4470/24/4/005`. URL: `https://dx.doi.org/10.1088/0305-4470/24/4/005`.

[65] M. Fannes, B. Nachtergaele, and R. F. Werner. “Finitely correlated states on quantum spin chains”. In: *Communications in Mathematical Physics* 144.3 (Mar. 1992), pp. 443–490. DOI: `10.1007/BF02099178`.

[66] Daniel E. Parker, Xiangyu Cao, and Michael P. Zaletel. “Local matrix product operators: Canonical form, compression, and control theory”. In: *Physical Review B* 102 (3 July 2020), p. 035147. DOI: `10.1103/PhysRevB.102.035147`. URL: `https://link.aps.org/doi/10.1103/PhysRevB.102.035147`.

[67] Maarten Van Damme, Jutho Haegeman, Ian McCulloch, and Laurens Vanderstraeten. *Efficient higher-order matrix product operators for time evolution.* 2023. arXiv: `2302.14181 [cond-mat.str-el]`.

[68] Thomas G. Kiely and Erich J. Mueller. “Superfluidity in the one-dimensional Bose-Hubbard model”. In: *Physical Review B* 105.13 (Apr. 2022). DOI: `10.1103/physrevb.105.134502`. URL: `https://doi.org/10.1103%2Fphysrevb.105.134502`.

[69] I. P. McCulloch. *Infinite size density matrix renormalization group, revisited.* 2008. DOI: `10.48550/ARXIV.0804.2509`. URL: `https://arxiv.org/abs/0804.2509`.

[70] Jutho Haegeman, Michaël Mariën, Tobias J. Osborne, and Frank Verstraete. “Geometry of matrix product states: Metric, parallel transport, and curvature”. In: *Journal of Mathematical Physics* 55.2 (Feb. 2014), p. 021902. DOI: `10.1063/1.4862851`. URL: `https://doi.org/10.1063%2F1.4862851`.

[71] Carl Eckart and G. Marion Young. “The approximation of one matrix by another of lower rank”. In: *Psychometrika* 1 (1936), pp. 211–218.

[72] L. MIRSKY. “Symmetric gauge functions and unitarily invariant norms”. In: *The Quarterly Journal of Mathematics* 11.1 (Jan. 1960), pp. 50–59. ISSN: 0033-5606. DOI: `10.1093/qmath/11.1.50`. eprint: `https://academic.oup.com/qjmath/article-pdf/11/1/50/7295335/11-1-50.pdf`. URL: `https://doi.org/10.1093/qmath/11.1.50`.

[73] Bram Vanhecke, Jutho Haegeman, Karel Van Acoleyen, Laurens Vanderstraeten, and Frank Verstraete. “Scaling Hypothesis for Matrix Product States”. In: *Physical Review Letters* 123 (25 Dec. 2019), p. 250604. DOI: `10.1103/PhysRevLett.123.250604`. URL: `https://link.aps.org/doi/10.1103/PhysRevLett.123.250604`.

[74] Marek M. Rams, Piotr Czarnik, and Lukasz Cincio. “Precise Extrapolation of the Correlation Function Asymptotics in Uniform Tensor Network States with Application to the Bose-Hubbard and XXZ Models”. In: *Physical Review X* 8.4 (Nov. 2018). DOI: `10.1103/physrevx.8.041033`. URL: `https://doi.org/10.1103%2Fphysrevx.8.041033`.

[75] Steven R. White. “Density matrix renormalization group algorithms with a single center site”. In: *Physical Review B* 72 (18 Nov. 2005), p. 180403. DOI: `10.1103/PhysRevB.72.180403`. URL: `https://link.aps.org/doi/10.1103/PhysRevB.72.180403`.

[76] G. Ehlers, S. R. White, and R. M. Noack. “Hybrid-space density matrix renormalization group study of the doped two-dimensional Hubbard model”. In: *Physical Review B* 95 (12 Mar. 2017), p. 125125. DOI: `10.1103/PhysRevB.95.125125`. URL: `https://link.aps.org/doi/10.1103/PhysRevB.95.125125`.

[77] C. Hubig, J. Haegeman, and U. Schollwöck. “Error estimates for extrapolations with matrix-product states”. In: *Physical Review B* 97 (4 Jan. 2018), p. 045125. DOI: `10.1103/PhysRevB.97.045125`. URL: `https://link.aps.org/doi/10.1103/PhysRevB.97.045125`.

[78] Hui-Hai Zhao, Kota Ido, Satoshi Morita, and Masatoshi Imada. “Variational Monte Carlo method for fermionic models combined with tensor networks and applications to the hole-doped two-dimensional Hubbard model”. In: *Physical Review B* 96 (8 Aug. 2017), p. 085103. DOI: `10.1103/PhysRevB.96.085103`. URL: `https://link.aps.org/doi/10.1103/PhysRevB.96.085103`.

[79] Sandro Sorella. “Generalized Lanczos algorithm for variational quantum Monte Carlo”. In: *Physical Review B* 64 (2 June 2001), p. 024512. DOI: `10.1103/PhysRevB.64.024512`. URL: `https://link.aps.org/doi/10.1103/PhysRevB.64.024512`.

[80] Masatoshi Imada and Tsuyoshi Kashima. “Path-Integral Renormalization Group Method for Numerical Study of Strongly Correlated Electron Systems”. In: *Journal of the Physical Society of Japan* 69.9 (2000), pp. 2723–2726. DOI: `10.1143/JPSJ.69.2723`. eprint: `https://doi.org/10.1143/JPSJ.69.2723`. URL: `https://doi.org/10.1143/JPSJ.69.2723`.

[81] Yongkyung Kwon, D. M. Ceperley, and Richard M. Martin. “Effects of three-body and backflow correlations in the two-dimensional electron gas”. In: *Physical Review B* 48 (16 Oct. 1993), pp. 12037–12046. DOI: `10.1103/PhysRevB.48.12037`. URL: `https://link.aps.org/doi/10.1103/PhysRevB.48.12037`.

[82] Philipp Schmoll, Augustine Kshetrimayum, Jens Eisert, Román Orús, and Matteo Rizzi. “The classical two-dimensional Heisenberg model revisited: An $SU(2)$-symmetric tensor network study”. In: *SciPost Physics* 11.5 (Nov. 2021). DOI: `10.21468/scipostphys.11.5.098`. URL: `https://doi.org/10.21468%2Fscipostphys.11.5.098`.

[83] L. Tagliacozzo, Thiago. R. de Oliveira, S. Iblisdir, and J. I. Latorre. “Scaling of entanglement support for matrix product states”. In: *Physical Review B* 78 (2 July 2008), p. 024410. DOI: `10.1103/PhysRevB.78.024410`. URL: `https://link.aps.org/doi/10.1103/PhysRevB.78.024410`.

[84] Philippe Corboz, Piotr Czarnik, Geert Kapteijns, and Luca Tagliacozzo. “Finite Correlation Length Scaling with Infinite Projected Entangled-Pair States”. In: *Physical Review X* 8 (3 July 2018), p. 031031. DOI: `10.1103/PhysRevX.8.031031`. URL: `https://link.aps.org/doi/10.1103/PhysRevX.8.031031`.

[85] B. Pirvu, G. Vidal, F. Verstraete, and L. Tagliacozzo. “Matrix product states for critical spin chains: Finite-size versus finite-entanglement scaling”. In: *Physical Review B* 86 (7 Aug. 2012), p. 075117. DOI: `10.1103/PhysRevB.86.075117`. URL: `https://link.aps.org/doi/10.1103/PhysRevB.86.075117`.

[86] Frank Pollmann, Subroto Mukerjee, Ari M. Turner, and Joel E. Moore. “Theory of Finite-Entanglement Scaling at One-Dimensional Quantum Critical Points”. In: *Physical Review Letters* 102 (25 June 2009), p. 255701. DOI: `10.1103/PhysRevLett.102.255701`. URL: `https://link.aps.org/doi/10.1103/PhysRevLett.102.255701`.

[87] Bram Vanhecke, Juraj Hasik, Frank Verstraete, and Laurens Vanderstraeten. “Scaling Hypothesis for Projected Entangled-Pair States”. In: *Physical Review Letters* 129.20 (Nov. 2022). DOI: `10.1103/physrevlett.129.200601`. URL: `https://doi.org/10.1103%2Fphysrevlett.129.200601`.

[88] E. Brézin. “An Investigation of Finite Size Scaling”. In: *Finite-Size Scaling*. Ed. by John L. CARDY. Vol. 2. Current Physics–Sources and Comments. Elsevier, 1988, pp. 12–19. DOI: `https://doi.org/10.1016/B978-0-444-87109-1.50008-X`. URL: `https://www.sciencedirect.com/science/article/pii/B978044487109150008X`.

[89] Michael E. Fisher and Michael N. Barber. “Scaling Theory for Finite-Size Effects in the Critical Region”. In: *Physical Review Letters* 28 (23 June 1972), pp. 1516–1519. DOI: `10.1103/PhysRevLett.28.1516`. URL: `https://link.aps.org/doi/10.1103/PhysRevLett.28.1516`.

[90] Philipp T. Dumitrescu, Romain Vasseur, and Andrew C. Potter. “Scaling Theory of Entanglement at the Many-Body Localization Transition”. In: *Physical Review Letters* 119.11 (Sept. 2017). DOI: `10.1103/physrevlett.119.110604`. URL: `https://doi.org/10.1103%2Fphysrevlett.119.110604`.

[91] Philipp Schmoll, Sukhbinder Singh, Matteo Rizzi, and Román Orús. “A programming guide for tensor networks with global $SU(2)$ symmetry”. In: *Annals of Physics* 419 (Aug. 2020), p. 168232. DOI: `10.1016/j.aop.2020.168232`. URL: `https://doi.org/10.1016%2Fj.aop.2020.168232`.

[92] J.F. Cornwell. “Chapter 4 - Representations of Groups – Principal Ideas”. In: *Group Theory in Physics*. Ed. by J.F. Cornwell. Vol. 1. Techniques of Physics. San Diego: Academic Press, 1997, pp. 47–63. DOI: `https://doi.org/10.1016/B978-012189800-7/50004-2`. URL: `https://www.sciencedirect.com/science/article/pii/B9780121898007500042`.

[93] Sukhwinder Singh, Robert N. C. Pfeifer, and Guifré Vidal. “Tensor network decompositions in the presence of a global symmetry”. In: *Physical Review A* 82.5 (Nov. 2010). DOI: `10.1103/physreva.82.050301`. URL: `https://doi.org/10.1103%2Fphysreva.82.050301`.

[94] Sukhwinder Singh, Robert N. C. Pfeifer, and Guifre Vidal. “Tensor network states and algorithms in the presence of a global U(1) symmetry”. In: *Physical Review B* 83 (11 Mar. 2011), p. 115125. DOI: `10.1103/PhysRevB.83.115125`. URL: `https://link.aps.org/doi/10.1103/PhysRevB.83.115125`.

[95] Sukhwinder Singh and Guifre Vidal. “Tensor network states and algorithms in the presence of a global SU(2) symmetry”. In: *Physical Review B* 86.19 (Nov. 2012). DOI: `10.1103/physrevb.86.195114`. URL: `https://doi.org/10.1103%2Fphysrevb.86.195114`.

[96] Shoudan Liang and Hanbin Pang. “Approximate diagonalization using the density matrix renormalization-group method: A two-dimensional-systems perspective”. In: *Physical Review B* 49 (13 Apr. 1994), pp. 9214–9217. DOI: `10.1103/PhysRevB.49.9214`. URL: `https://link.aps.org/doi/10.1103/PhysRevB.49.9214`.

[97] E.M. Stoudenmire and Steven R. White. “Studying Two-Dimensional Systems with the Density Matrix Renormalization Group”. In: *Annual Review of Condensed Matter Physics* 3.1 (2012), pp. 111–128. DOI: `10.1146/annurev-conmatphys-020911-125018`. eprint: `https://doi.org/10.1146/annurev-conmatphys-020911-125018`. URL: `https://doi.org/10.1146/annurev-conmatphys-020911-125018`.

[98] Johannes Motruk, Michael P. Zaletel, Roger S. K. Mong, and Frank Pollmann. “Density matrix renormalization group on a cylinder in mixed real and momentum space”. In: *Physical Review B* 93.15 (Apr. 2016). DOI: `10.1103/physrevb.93.155139`. URL: `https://doi.org/10.1103%2Fphysrevb.93.155139`.

[99] N. D. Mermin and H. Wagner. “Absence of Ferromagnetism or Antiferromagnetism in One- or Two-Dimensional Isotropic Heisenberg Models”. In: *Physical Review Letters* 17 (22 Nov. 1966), pp. 1133–1136. DOI: `10.1103/PhysRevLett.17.1133`. URL: `https://link.aps.org/doi/10.1103/PhysRevLett.17.1133`.

[100] P. C. Hohenberg. “Existence of Long-Range Order in One and Two Dimensions”. In: *Physical Review* 158 (2 June 1967), pp. 383–386. DOI: `10.1103/PhysRev.158.383`. URL: `https://link.aps.org/doi/10.1103/PhysRev.158.383`.

[101] Sidney Coleman. “There are no Goldstone bosons in two dimensions”. In: *Communications in Mathematical Physics* 31.4 (Dec. 1973), pp. 259–264. DOI: `10.1007/BF01646487`.

[102] Mykhailo V. Rakov and Michael Weyrauch. “Spin-1/2 XXZ Heisenberg chain in a longitudinal magnetic field”. In: *Physical Review B* 100.13 (Oct. 2019). DOI: `10.1103/physrevb.100.134434`. URL: `https://doi.org/10.1103%2Fphysrevb.100.134434`.

[103] Tom Kennedy, Elliott H. Lieb, and B. Sriram Shastry. “Existence of Néel order in some spin-1/2 Heisenberg antiferromagnets”. In: *Journal of Statistical Physics* 53 (1988), pp. 1019–1030. URL: `https://api.semanticscholar.org/CorpusID:8991724`.

[104] Steven R. White and A. L. Chernyshev. “Neél Order in Square and Triangular Lattice Heisenberg Models”. In: *Physical Review Letters* 99.12 (Sept. 2007). DOI: `10.1103/physrevlett.99.127004`. URL: `https://doi.org/10.1103%2Fphysrevlett.99.127004`.

[105] J. Hubbard and Brian Hilton Flowers. “Electron correlations in narrow energy bands”. In: *Proceedings of the Royal Society of London. Series A. Mathematical and Physical Sciences* 276.1365 (1963), pp. 238–257. DOI: `10.1098/rspa.1963.0204`. eprint: `https://royalsocietypublishing.org/doi/pdf/10.1098/rspa.1963.0204`. URL: `https://royalsocietypublishing.org/doi/abs/10.1098/rspa.1963.0204`.

[106] Junjiro Kanamori. “Electron Correlation and Ferromagnetism of Transition Metals”. In: *Progress of Theoretical Physics* 30.3 (Sept. 1963), pp. 275–289. ISSN: 0033-068X. DOI: `10.1143/PTP.30.275`. eprint: `https://academic.oup.com/ptp/article-pdf/30/3/275/5278869/30-3-275.pdf`. URL: `https://doi.org/10.1143/PTP.30.275`.

[107] Martin C. Gutzwiller. “Effect of Correlation on the Ferromagnetism of Transition Metals”. In: *Physical Review Letters* 10 (5 Mar. 1963), pp. 159–162. DOI: `10.1103/PhysRevLett.10.159`. URL: `https://link.aps.org/doi/10.1103/PhysRevLett.10.159`.

[108] Tommaso Roscilde. “Exploring the grand-canonical phase diagram of interacting bosons in optical lattices by trap squeezing”. In: *Physical Review A* 82 (2 Aug. 2010), p. 023601. DOI: `10.1103/PhysRevA.82.023601`. URL: `https://link.aps.org/doi/10.1103/PhysRevA.82.023601`.

[109] van Dirk and Peter Kes. “The discovery of superconductivity”. In: *Europhysics News* 63 (Jan. 2011). DOI: `10.1051/epn/2011104`.

[110] J. G. Bednorz and K. A. Muller. “Possible high Tc superconductivity in the Ba-La-Cu-O system”. In: *Z. Phys. B* 64 (1986), pp. 189–193. DOI: `10.1007/BF01303701`.

[111] J. Bardeen, L. N. Cooper, and J. R. Schrieffer. “Microscopic Theory of Superconductivity”. In: *Physical Review* 106.1 (Apr. 1957), pp. 162–164. DOI: `10.1103/PhysRev.106.162`.

[112] J. Bardeen, L. N. Cooper, and J. R. Schrieffer. “Theory of Superconductivity”. In: *Physical Review* 108.5 (Dec. 1957), pp. 1175–1204. DOI: `10.1103/PhysRev.108.1175`.

[113] B. Jankuloski. *Timeline of Superconductivity from 1990 to 2015.* Accessed 5 March 2023. Aug. 2016. URL: `https://commons.wikimedia.org/wiki/File:Timeline_of_Superconductivity_from_1900_to_2015.svg/`.

[114] P.W. Anderson. *The Theory of Superconductivity in the High-Tc Cuprates.* Princeton series in physics. Princeton University Press, 1997. ISBN: 9780691043654. URL: `https://books.google.be/books?id=dDViQgAACAAJ`.

[115] ALS Communications. *The electronic structure of a two-dimensional pure copper oxide lattice.* Accessed 21 March 2023. Oct. 2021. URL: `https://als.lbl.gov/the-electronic-structure-of-a-two-dimensional-pure-copper-oxide-lattice/`.

[116] The Materials Project. *Materials explorer - La_2CuO_4.* Accessed 21 March 2023. URL: `https://materialsproject.org/materials/mp-1077929?chemsys=Cu-La-O%5C%5C`.

[117] The Materials Project. *Materials explorer - Ba_2CuHgO_4.* Accessed 21 March 2023. URL: `https://materialsproject.org/materials/mp-6562?chemsys=Cu-O-Ba-Hg%5C%5C`.

[118] F. C. Zhang and T. M. Rice. “Effective Hamiltonian for the superconducting Cu oxides”. In: *Physical Review B* 37 (7 Mar. 1988), pp. 3759–3761. DOI: `10.1103/PhysRevB.37.3759`. URL: `https://link.aps.org/doi/10.1103/PhysRevB.37.3759`.

[119] Benedikt Graswald and Gero Friesecke. “Electronic wavefunction with maximally entangled MPS representation”. In: *The European Physical Journal D* 75 (June 2021). DOI: `10.1140/epjd/s10053-021-00189-2`.

[120] Huihuo Zheng, Hitesh J. Changlani, Kiel T. Williams, Brian Busemeyer, and Lucas K. Wagner. “From Real Materials to Model Hamiltonians With Density Matrix Downfolding”. In: *Frontiers in Physics* 6 (May 2018). DOI: `10.3389/fphy.2018.00043`. URL: `https://doi.org/10.3389%2Ffphy.2018.00043`.

[121] P. W. Anderson. “The Resonating Valence Bond State in La¡sub¿2¡/sub¿CuO¡sub¿4¡/sub¿ and Superconductivity”. In: *Science* 235.4793 (1987), pp. 1196–1198. DOI: `10.1126/science.235.4793.1196`. eprint: `https://www.science.org/doi/pdf/10.1126/science.235.4793.1196`. URL: `https://www.science.org/doi/abs/10.1126/science.235.4793.1196`.

[122] Ricardo A. Broglia, J. Robert Schrieffer, and Società Italiana di Fisica. “Frontiers and borderlines in many-particle physics : Varenna on Lake Como, Villa Monastero, 7-17 July 1987”. In: 1988.

[123] Motoaki Hirayama, Youhei Yamaji, Takahiro Misawa, and Masatoshi Imada. “Ab initio effective Hamiltonians for cuprate superconductors”. In: *Physical Review B* 98 (13 Oct. 2018), p. 134501. DOI: `10.1103/PhysRevB.98.134501`. URL: `https://link.aps.org/doi/10.1103/PhysRevB.98.134501`.

[124] Motoaki Hirayama, Takahiro Misawa, Takahiro Ohgoe, Youhei Yamaji, and Masatoshi Imada. “Effective Hamiltonian for cuprate superconductors derived from multiscale ab initio scheme with level renormalization”. In: *Physical Review B* 99 (24 June 2019), p. 245155. DOI: `10.1103/PhysRevB.99.245155`. URL: `https://link.aps.org/doi/10.1103/PhysRevB.99.245155`.

[125] Jeong-Pil Song, Sumit Mazumdar, and R. Torsten Clay. *Doping asymmetry in the three-band Hamiltonian for cuprate ladders: failure of the standard model of superconductivity in cuprates.* 2023. arXiv: `2302.08356 [cond-mat.str-el]`.

[126] Adrian E. Feiguin, Christian Helman, and Armando A. Aligia. *Effective one-band models for the 1D cuprate* $Ba_{2-x}Sr_xCuO_{3+\delta}$. 2023. arXiv: `2303.11905 [cond-mat.str-el]`.

[127] Shengtao Jiang, Douglas J. Scalapino, and Steven R. White. *A single-band model with enhanced pairing from DMRG-based downfolding of the three-band Hubbard model.* 2023. arXiv: `2303.00756 [cond-mat.str-el]`.

[128] Zhi-Hao Cui, Chong Sun, Ushnish Ray, Bo-Xiao Zheng, Qiming Sun, and Garnet Kin-Lic Chan. “Ground-state phase diagram of the three-band Hubbard model from density matrix embedding theory”. In: *Physical Review Res.* 2 (4 Nov. 2020), p. 043259. DOI: `10.1103/PhysRevResearch.2.043259`. URL: `https://link.aps.org/doi/10.1103/PhysRevResearch.2.043259`.

[129] K. Sheshadri, D. Malterre, A. Fujimori, and A. Chainani. “Connecting the one-band and three-band Hubbard models of cuprates via spectroscopy and scattering experiments”. In: *Physical Review B* 107 (8 Feb. 2023), p. 085125. DOI: `10.1103/PhysRevB.107.085125`. URL: `https://link.aps.org/doi/10.1103/PhysRevB.107.085125`.

[130] W. Hanke, M.L. Kiesel, M. Aichhorn, S. Brehm, and E. Arrigoni. “The 3-band Hubbard-model versus the 1-band model for the high-T c cuprates: Pairing dynamics, superconductivity and the ground-state phase diagram”. In: *The European Physical Journal Special Topics* 188.1 (Oct. 2010), pp. 15–32. DOI: `10.1140/epjst/e2010-01294-y`. URL: `https://doi.org/10.1140%2Fepjst%2Fe2010-01294-y`.

[131] Elliott H. Lieb and F. Y. Wu. “Absence of Mott Transition in an Exact Solution of the Short-Range, One-Band Model in One Dimension”. In: *Physical Review Letters* 20 (25 June 1968), pp. 1445–1448. DOI: `10.1103/PhysRevLett.20.1445`. URL: `https://link.aps.org/doi/10.1103/PhysRevLett.20.1445`.

[132] Shiwei Zhang. “Ab Initio Electronic Structure Calculations by Auxiliary-Field Quantum Monte Carlo”. In: *Handbook of Materials Modeling : Methods: Theory and Modeling.* Ed. by Wanda Andreoni and Sidney Yip. Cham: Springer International Publishing, 2018, pp. 1–27. ISBN: 978-3-319-42913-7. DOI: `10.1007/978-3-319-42913-7_47-1`. URL: `https://doi.org/10.1007/978-3-319-42913-7_47-1`.

[133] Hao Shi and Shiwei Zhang. “Infinite variance in fermion quantum Monte Carlo calculations”. In: *Physical Review E* 93.3 (Mar. 2016). DOI: `10.1103/physreve.93.033303`. URL: `https://doi.org/10.1103%2Fphysreve.93.033303`.

[134] Hao Shi and Shiwei Zhang. “Symmetry in auxiliary-field quantum Monte Carlo calculations”. In: *Physical Review B* 88 (12 Sept. 2013), p. 125132. DOI: `10.1103/PhysRevB.88.125132`. URL: `https://link.aps.org/doi/10.1103/PhysRevB.88.125132`.

[135] Gerald Knizia and Garnet Kin-Lic Chan. “Density Matrix Embedding: A Simple Alternative to Dynamical Mean-Field Theory”. In: *Physical Review Letters* 109 (18 Nov. 2012), p. 186404. DOI: `10.1103/PhysRevLett.109.186404`. URL: `https://link.aps.org/doi/10.1103/PhysRevLett.109.186404`.

[136] Gerald Knizia and Garnet Kin-Lic Chan. “Density Matrix Embedding: A Strong-Coupling Quantum Embedding Theory”. In: *Journal of Chemical Theory and Computation* 9.3 (2013). PMID: 26587604, pp. 1428–1432. DOI: `10.1021/ct301044e`. eprint: `https://doi.org/10.1021/ct301044e`. URL: `https://doi.org/10.1021/ct301044e`.

[137] Thomas Maier, Mark Jarrell, Thomas Pruschke, and Matthias H. Hettler. “Quantum cluster theories”. In: *Rev. Mod. Phys.* 77 (3 Oct. 2005), pp. 1027–1080. DOI: `10.1103/RevModPhys.77.1027`. URL: `https://link.aps.org/doi/10.1103/RevModPhys.77.1027`.

[138] Josef Paldus and Xiangzhu Li. “A Critical Assessment of Coupled Cluster Method in Quantum Chemistry”. In: *Advances in Chemical Physics.* John Wiley Sons, Ltd, 1999, pp. 1–175. ISBN: 9780470141694. DOI: `https://doi.org/10.1002/9780470141694.ch1`. eprint: `https://onlinelibrary.wiley.com/doi/pdf/10.1002/9780470141694.ch1`. URL: `https://onlinelibrary.wiley.com/doi/abs/10.1002/9780470141694.ch1`.

[139] Rodney J. Bartlett and Monika Musiał. “Coupled-cluster theory in quantum chemistry”. In: *Rev. Mod. Phys.* 79 (1 Feb. 2007), pp. 291–352. DOI: `10.1103/RevModPhys.79.291`. URL: `https://link.aps.org/doi/10.1103/RevModPhys.79.291`.

[140] Isaiah Shavitt and Rodney Bartlett. *Many-Body Methods in Chemistry and Physics: MBPT and Coupled-Cluster Theory.* Jan. 2009. ISBN: 9780521818322. DOI: `10.1017/CBO9780511596834`.

[141] F. Verstraete, V. Murg, and J.I. Cirac. “Matrix product states, projected entangled pair states, and variational renormalization group methods for quantum spin systems”. In: *Advances in Physics* 57.2 (2008), pp. 143–224. DOI: `10.1080/14789940801912366`. eprint: `https://doi.org/10.1080/14789940801912366`. URL: `https://doi.org/10.1080/14789940801912366`.

[142] J. P. F. LeBlanc et al. “Solutions of the Two-Dimensional Hubbard Model: Benchmarks and Results from a Wide Range of Numerical Algorithms”. In: *Physical Review X* 5 (4 Dec. 2015), p. 041041. DOI: `10.1103/PhysRevX.5.041041`. URL: `https://link.aps.org/doi/10.1103/PhysRevX.5.041041`.

[143] B. Keimer, S. A. Kivelson, M. R. Norman, S. Uchida, and J. Zaanen. “From quantum matter to high-temperature superconductivity in copper oxides”. In: *Nature (London)* 518.7538 (Feb. 2015). ISSN: 0028-0836. DOI: `10.1038/nature14165`. URL: `https://www.osti.gov/biblio/1357580`.

[144] Richard L. Greene, Pampa R. Mandal, Nicholas R. Poniatowski, and Tarapada Sarkar. “The Strange Metal State of the Electron-Doped Cuprates”. In: *Annual Review of Condensed Matter Physics* 11.1 (Mar. 2020), pp. 213–229. DOI: `10.1146/annurev-conmatphys-031119-050558`. URL: `https://doi.org/10.1146%2Fannurev-conmatphys-031119-050558`.

[145] Cyril Proust and Louis Taillefer. “The Remarkable Underlying Ground States of Cuprate Superconductors”. In: *Annual Review of Condensed Matter Physics* 10.1 (Mar. 2019), pp. 409–429. DOI: `10.1146/annurev-conmatphys-031218-013210`. URL: `https://doi.org/10.1146%2Fannurev-conmatphys-031218-013210`.

[146] Patrick A. Lee, Naoto Nagaosa, and Xiao-Gang Wen. “Doping a Mott insulator: Physics of high-temperature superconductivity”. In: *Rev. Mod. Phys.* 78 (1 Jan. 2006), pp. 17–85. DOI: `10.1103/RevModPhys.78.17`. URL: `https://link.aps.org/doi/10.1103/RevModPhys.78.17`.

[147] Kyle Shen and Jc Davis. “Cuprate high-T superconductors”. In: *Materials Today* 11 (Sept. 2008), pp. 14–21. DOI: `10.1016/S1369-7021(08)70175-5`.

[148] Peayush Choubey et al. “Atomic-scale electronic structure of the cuprate pair density wave state coexisting with superconductivity”. In: *Proceedings of the National Academy of Sciences* 117.26 (2020), pp. 14805–14811. DOI: `10.1073/pnas.2002429117`. eprint: `https://www.pnas.org/doi/pdf/10.1073/pnas.2002429117`. URL: `https://www.pnas.org/doi/abs/10.1073/pnas.2002429117`.

[149] Shin-ichi Uchida Shin-ichi Uchida. “Recent Progress in High-Tc Superconductor Research: Unique and Novel Metallic State in Doped CuO2 Plane”. In: *Japanese Journal of Applied Physics* 32.9R (Sept. 1993), p. 3784. DOI: `10.1143/JJAP.32.3784`. URL: `https://dx.doi.org/10.1143/JJAP.32.3784`.

[150] N F Mott. “The Basis of the Electron Theory of Metals, with Special Reference to the Transition Metals”. In: *Proceedings of the Physical Society. Section A* 62.7 (July 1949), p. 416. DOI: `10.1088/0370-1298/62/7/303`. URL: `https://dx.doi.org/10.1088/0370-1298/62/7/303`.

[151] Hong-Chen Jiang and Thomas P. Devereaux. “Superconductivity in the doped Hubbard model and its interplay with next-nearest hopping it/i ′”. In: *Science* 365.6460 (Sept. 2019), pp. 1424–1428. DOI: `10.1126/science.aal5304`. URL: `https://doi.org/10.1126%2Fscience.aal5304`.

[152] Yang Shen, Guang-Ming Zhang, and Mingpu Qin. *Reexamining the doped two-legged Hubbard ladders.* 2023. arXiv: `2303.16487 [cond-mat.str-el]`.

[153] Michele Dolfi, Bela Bauer, Sebastian Keller, and Matthias Troyer. “Pair correlations in doped Hubbard ladders”. In: *Physical Review B* 92 (19 Nov. 2015), p. 195139. DOI: `10.1103/PhysRevB.92.195139`. URL: `https://link.aps.org/doi/10.1103/PhysRevB.92.195139`.

[154] A. M. Rey, R. Sensarma, S. Fölling, M. Greiner, E. Demler, and M. D. Lukin. “Controlled preparation and detection of d-wave superfluidity in two-dimensional optical superlattices”. In: *EPL (Europhysics Letters)* 87.6 (Sept. 2009), p. 60001. DOI: `10.1209/0295-5075/87/60001`. URL: `https://doi.org/10.1209%2F0295-5075%2F87%2F60001`.

[155] Chia-Min Chung, Mingpu Qin, Shiwei Zhang, Ulrich Schollwöck, and Steven R. White. “Plaquette versus ordinary d-wave pairing in the t'-Hubbard model on a width-4 cylinder”. In: *Physical Review B* 102 (4 July 2020), p. 041106. DOI: `10.1103/PhysRevB.102.041106`. URL: `https://link.aps.org/doi/10.1103/PhysRevB.102.041106`.

[156] John F. Dodaro, Hong-Chen Jiang, and Steven A. Kivelson. “Intertwined order in a frustrated four-leg $t - J$ cylinder”. In: *Physical Review B* 95 (15 Apr. 2017), p. 155116. DOI: `10.1103/PhysRevB.95.155116`. URL: `https://link.aps.org/doi/10.1103/PhysRevB.95.155116`.

[157] Yi-Fan Jiang, Thomas P. Devereaux, and Hong-Chen Jiang. *Ground state phase diagram and superconductivity of the doped Hubbard model on six-leg square cylinders.* 2023. arXiv: `2303.15541 [cond-mat.str-el]`.

[158] A. Luther and V. J. Emery. “Backward Scattering in the One-Dimensional Electron Gas”. In: *Physical Review Letters* 33 (10 Sept. 1974), pp. 589–592. DOI: `10.1103/PhysRevLett.33.589`. URL: `https://link.aps.org/doi/10.1103/PhysRevLett.33.589`.

[159] F. D. M. Haldane. “General Relation of Correlation Exponents and Spectral Properties of One-Dimensional Fermi Systems: Application to the Anisotropic $S = \frac{1}{2}$ Heisenberg Chain”. In: *Physical Review Letters* 45 (16 Oct. 1980), pp. 1358–1362. DOI: `10.1103/PhysRevLett.45.1358`. URL: `https://link.aps.org/doi/10.1103/PhysRevLett.45.1358`.

[160] Fedor Levkovich-Maslyuk. “The Bethe ansatz”. In: *Journal of Physics A: Mathematical and Theoretical* 49.32 (July 2016), p. 323004. DOI: `10.1088/1751-8113/49/32/323004`. URL: `https://doi.org/10.1088%2F1751-8113%2F49%2F32%2F323004`.

[161] Anders W. Sandvik. “Finite-size scaling of the ground-state parameters of the two-dimensional Heisenberg model”. In: *Physical Review B* 56 (18 Nov. 1997), pp. 11678–11690. DOI: `10.1103/PhysRevB.56.11678`. URL: `https://link.aps.org/doi/10.1103/PhysRevB.56.11678`.

[162] Juraj Hasik, Didier Poilblanc, and Federico Becca. “Investigation of the Néel phase of the frustrated Heisenberg antiferromagnet by differentiable symmetric tensor networks”. In: *SciPost Physics* 10.1 (Jan. 2021). DOI: `10.21468/scipostphys.10.1.012`. URL: `https://doi.org/10.21468%2Fscipostphys.10.1.012`.

[163] Matthew B. Hastings and Tohru Koma. “Spectral Gap and Exponential Decay of Correlations”. In: *Communications in Mathematical Physics* 265.3 (Apr. 2006), pp. 781–804. DOI: `10.1007/s00220-006-0030-4`. URL: `https://doi.org/10.1007%2Fs00220-006-0030-4`.

[164] Masahiro Kadosawa, Masaaki Nakamura, Yukinori Ohta, and Satoshi Nishimoto. “Study of Staggered Magnetization in the Spin-iS/i Square-Lattice Heisenberg Model Using Spiral Boundary Conditions”. In: *Journal of the Physical Society of Japan* 92.2 (Feb. 2023). DOI: `10.7566/jpsj.92.023701`. URL: `https://doi.org/10.7566%2Fjpsj.92.023701`.

[165] F. D. M. Haldane. “Nonlinear Field Theory of Large-Spin Heisenberg Antiferromagnets: Semiclassically Quantized Solitons of the One-Dimensional Easy-Axis Néel State”. In: *Physical Review Letters* 50 (15 Apr. 1983), pp. 1153–1156. DOI: `10.1103/PhysRevLett.50.1153`. URL: `https://link.aps.org/doi/10.1103/PhysRevLett.50.1153`.

[166] Li-Hua Pan and Chang-De Gong. “A note on Haldane’s conjecture”. In: *Journal of Physics: Condensed Matter* 20.21 (Apr. 2008), p. 215232. DOI: `10.1088/0953-8984/20/21/215232`. URL: `https://dx.doi.org/10.1088/0953-8984/20/21/215232`.

[167] Hsiang-Hsuan Hung and Chang-De Gong. “Numerical evidence of a spin-12 chain approaching a spin-1 chain”. In: *Physical Review B* 71 (5 Feb. 2005), p. 054413. DOI: `10.1103/PhysRevB.71.054413`. URL: `https://link.aps.org/doi/10.1103/PhysRevB.71.054413`.

[168] Roman Lopez-Sandoval and G. Pastor. “Interaction energy functional for lattice density functional theory: Applications to one-, two- and three-dimensional Hubbard models”. In: *Physical Review B* 69 (Feb. 2004), pp. 1–10. DOI: `10.1103/PhysRevB.69.085101`.

[169] Masatoshi Imada. “Charge Order and Superconductivity as Competing Brothers in Cuprate High-iT/isubc/sub Superconductors”. In: *Journal of the Physical Society of Japan* 90.11 (Nov. 2021), p. 111009. DOI: `10.7566/jpsj.90.111009`. URL: `https://doi.org/10.7566%2Fjpsj.90.111009`.

[170] Bo-Xiao Zheng et al. “Stripe order in the underdoped region of the two-dimensional Hubbard model”. In: *Science* 358.6367 (Dec. 2017), pp. 1155–1160. DOI: `10.1126/science.aam7127`. URL: `https://doi.org/10.1126%2Fscience.aam7127`.

[171] Hao Xu, Hao Shi, Ettore Vitali, Mingpu Qin, and Shiwei Zhang. “Stripes and spin-density waves in the doped two-dimensional Hubbard model: Ground state phase diagram”. In: *Physical Review Research* 4.1 (Mar. 2022). DOI: `10.1103/physrevresearch.4.013239`. URL: `https://doi.org/10.1103%2Fphysrevresearch.4.013239`.

[172] Hao Xu, Chia-Min Chung, Mingpu Qin, Ulrich Schollwöck, Steven R. White, and Shiwei Zhang. *Coexistence of superconductivity with partially filled stripes in the Hubbard model.* 2023. arXiv: `2303.08376 [cond-mat.supr-con]`.

[173] Chia-Chen Chang and Shiwei Zhang. “Spin and Charge Order in the Doped Hubbard Model: Long-Wavelength Collective Modes”. In: *Physical Review Letters* 104 (11 Mar. 2010), p. 116402. DOI: `10.1103/PhysRevLett.104.116402`. URL: `https://link.aps.org/doi/10.1103/PhysRevLett.104.116402`.

[174] Alexander Seidel and Dung-Hai Lee. “The Luther-Emery liquid: Spin gap and anomalous flux period”. In: *Physical Review B* 71.4 (Jan. 2005). DOI: `10.1103/physrevb.71.045113`. URL: `https://doi.org/10.1103%2Fphysrevb.71.045113`.

[175] J. Greitemann, S. Hesselmann, S. Wessel, F. F. Assaad, and M. Hohenadler. “Finite-size effects in Luther-Emery phases of Holstein and Hubbard models”. In: *Physical Review B* 92.24 (Dec. 2015). DOI: `10.1103/physrevb.92.245132`. URL: `https://doi.org/10.1103%2Fphysrevb.92.245132`.

[176] Luca Fausto Tocchio, Federico Becca, and Arianna Montorsi. “Superconductivity in the Hubbard model: a hidden-order diagnostics from the Luther-Emery phase on ladders”. In: *SciPost Physics* 6.2 (Feb. 2019). DOI: `10.21468/scipostphys.6.2.018`. URL: `https://doi.org/10.21468%2Fscipostphys.6.2.018`.

[177] Yi-Fan Jiang, Jan Zaanen, Thomas P. Devereaux, and Hong-Chen Jiang. “Ground state phase diagram of the doped Hubbard model on the four-leg cylinder”. In: *Physical Review Research* 2.3 (July 2020). DOI: `10.1103/physrevresearch.2.033073`. URL: `https://doi.org/10.1103%2Fphysrevresearch.2.033073`.

[178] Mingpu Qin, Chia-Min Chung, Hao Shi, Ettore Vitali, Claudius Hubig, Ulrich Schollwöck, Steven R. White, and Shiwei Zhang and. “Absence of Superconductivity in the Pure Two-Dimensional Hubbard Model”. In: *Physical Review X* 10.3 (July 2020). DOI: `10.1103/physrevx.10.031016`. URL: `https://doi.org/10.1103%2Fphysrevx.10.031016`.

[179] R.M. Noack, S.R. White, and D.J. Scalapino. “The ground state of the two-leg Hubbard ladder a density-matrix renormalization group study”. In: *Physica C: Superconductivity* 270.3 (1996), pp. 281–296. ISSN: 0921-4534. DOI: `https://doi.org/10.1016/S0921-4534(96)00515-1`. URL: `https://www.sciencedirect.com/science/article/pii/S0921453496005151`.

[180] Boris Ponsioen, Sangwoo S. Chung, and Philippe Corboz. “Period 4 stripe in the extended two-dimensional Hubbard model”. In: *Physical Review B* 100.19 (Nov. 2019). DOI: `10.1103/physrevb.100.195141`. URL: `https://doi.org/10.1103%2Fphysrevb.100.195141`.

[181] Kota Ido, Takahiro Ohgoe, and Masatoshi Imada. “Competition among various charge-inhomogeneous states and *d*-wave superconducting state in Hubbard models on square lattices”. In: *Physical Review B* 97 (4 Jan. 2018), p. 045138. DOI: `10.1103/PhysRevB.97.045138`. URL: `https://link.aps.org/doi/10.1103/PhysRevB.97.045138`.

[182] Jean-Baptiste Morée, Motoaki Hirayama, Michael Thobias Schmid, Youhei Yamaji, and Masatoshi Imada. “low-energy effective Hamiltonians for the high-temperature superconducting cuprates $Bi_2Sr_2CuO_6$, $Bi_2Sr_2CaCu_2O_8$ and $CaCuO_2$”. In: *Physical Review B* 106.23 (Dec. 2022). DOI: `10.1103/physrevb.106.235150`. URL: `https://doi.org/10.1103%2Fphysrevb.106.235150`.

[183] Jaewon Choi et al. *Stripe Symmetry of Short-range Charge Density Waves in Cuprate Superconductors.* 2023. arXiv: `2301.07637 [cond-mat.str-el]`.

[184] Takahiro Ohgoe, Motoaki Hirayama, Takahiro Misawa, Kota Ido, Youhei Yamaji, and Masatoshi Imada. “Ab initio study of superconductivity and inhomogeneity in a Hg-based cuprate superconductor”. In: *Physical Review B* 101 (4 Jan. 2020), p. 045124. DOI: `10.1103/PhysRevB.101.045124`. URL: `https://link.aps.org/doi/10.1103/PhysRevB.101.045124`.

[185] Q. Li, M. Hücker, G. D. Gu, A. M. Tsvelik, and J. M. Tranquada. “Two-Dimensional Superconducting Fluctuations in Stripe-Ordered $\mathrm{La}_{1.875}\mathrm{Ba}_{0.125}\mathrm{CuO}_4$”. In: *Physical Review Letters* 99 (6 Aug. 2007), p. 067001. DOI: `10.1103/PhysRevLett.99.067001`. URL: `https://link.aps.org/doi/10.1103/PhysRevLett.99.067001`.

[186] A. Gabovich, Alexander Voitenko, J. Annett, and Marcel Ausloos. “Topical Review: Charge and spin-density-wave superconductors”. In: *Superconductor Science & Technology* 14 (Apr. 2001). DOI: `10.1088/0953-2048/14/4/201`.

[187] Boris Ponsioen, Sangwoo S. Chung, and Philippe Corboz. *Superconducting stripes in the hole-doped three-band Hubbard model.* 2023. arXiv: `2306.12910 [cond-mat.str-el]`.

[188] Andrew S. Darmawan, Yusuke Nomura, Youhei Yamaji, and Masatoshi Imada. "Stripe and superconducting order competing in the Hubbard model on a square lattice studied by a combined variational Monte Carlo and tensor network method". In: *Physical Review B* 98.20 (Nov. 2018). DOI: `10.1103/physrevb.98.205132`. URL: `https://doi.org/10.1103%2Fphysrevb.98.205132`.

[189] P. M. Lozano, Tianhao Ren, G. D. Gu, A. M. Tsvelik, J. M. Tranquada, and Qiang Li. "Testing for pair density wave order in $La_{1.875}Ba_{0.125}CuO_4$". In: *Physical Review B* 106.17 (Nov. 2022). DOI: `10.1103/physrevb.106.174510`. URL: `https://doi.org/10.1103%2Fphysrevb.106.174510`.

[190] Wei Ruan, Xintong Li, Cheng Hu, Zhenqi Hao, Haiwei Li, Peng Cai, Xingjiang Zhou, Dung-Hai Lee, and Yayu Wang. "Visualization of the periodic modulation of Cooper pairing in a cuprate superconductor". In: *Nature Physics* 14.12 (Sept. 2018), pp. 1178–1182. DOI: `10.1038/s41567-018-0276-8`. arXiv: `1905.02425 [cond-mat.supr-con]`.

[191] S. D. Edkins et al. "Magnetic-field induced pair density wave state in the cuprate vortex halo". In: *Science* 364.6444 (2019), pp. 976–980. DOI: `10.1126/science.aat1773`. eprint: `https://www.science.org/doi/pdf/10.1126/science.aat1773`. URL: `https://www.science.org/doi/abs/10.1126/science.aat1773`.

[192] Hong-Chen Jiang. "Pair density wave in the doped three-band Hubbard model on two-leg square cylinders". In: *Physical Review B* 107.21 (June 2023). DOI: `10.1103/physrevb.107.214504`. URL: `https://doi.org/10.1103%2Fphysrevb.107.214504`.

[193] Eduardo Fradkin, Steven A. Kivelson, and John M. Tranquada. "Colloquium: Theory of intertwined orders in high temperature superconductors". In: *Rev. Mod. Phys.* 87 (2 May 2015), pp. 457–482. DOI: `10.1103/RevModPhys.87.457`. URL: `https://link.aps.org/doi/10.1103/RevModPhys.87.457`.

[194] Masahiro Kadosawa, Masaaki Nakamura, Yukinori Ohta, and Satoshi Nishimoto. "One-dimensional projection of two-dimensional systems using spiral boundary conditions". In: *Physical Review B* 107 (8 Feb. 2023), p. L081104. DOI: `10.1103/PhysRevB.107.L081104`. URL: `https://link.aps.org/doi/10.1103/PhysRevB.107.L081104`.

[195] Juan Osorio Iregui, Matthias Troyer, and Philippe Corboz. "Infinite matrix product states versus infinite projected entangled-pair states on the cylinder: A comparative study". In: *Physical Review B* 96.11 (Sept. 2017). DOI: `10.1103/physrevb.96.115113`. URL: `https://doi.org/10.1103%2Fphysrevb.96.115113`.

[196] Hao-Xin Wang, Yi-Fan Jiang, and Hong Yao. *Robust d-wave superconductivity from the Su-Schrieffer-Heeger-Hubbard model: possible route to high-temperature superconductivity.* 2022. arXiv: `2211.09143 [cond-mat.str-el]`.

[197] E. Linnér, C. Dutreix, S. Biermann, and E. A. Stepanov. *Coexistence of s-wave superconductivity and phase separation in the half-filled extended Hubbard model with attractive interactions.* 2023. arXiv: `2301.10755 [cond-mat.str-el]`.

[198] Joel Hutchinson and Frank Marsiglio. "Mixed temperature-dependent order parameters in the extended Hubbard model". In: *Journal of Physics: Condensed Matter* 33.6 (Nov. 2020), p. 065603. DOI: `10.1088/1361-648X/abc801`. URL: `https://dx.doi.org/10.1088/1361-648X/abc801`.

V

Appendices

A Hamiltonian and JordanMPO for different cases

A.1 Linear Chain

The Hamiltonian of a chain can be written as

$$\begin{aligned} H_{chain} &= \sum_i H_{i,i+1} + B_i \\ &= \sum_i L_i R_{i+1} + B_i \end{aligned} \tag{A.1}$$

where $H_{i,j}$ is the two-site Hamiltonian acting between nearest-neighbors and B_i is the on-site Hamiltonian. For this Hamiltonian, a 3×3 matrix is needed. The elements are then

$$(M_i)_{(p,q)} = \begin{cases} \mathbb{1}, & (p,q) \in \{(1,1),(3,3)\} \\ L_i, & (p,q) = (1,2) \\ R_i, & (p,q) = (2,3) \\ B_i, & (p,q) = (1,3) \\ 0, & else \end{cases} \tag{A.2}$$

or equivalently,

$$M_i = \begin{bmatrix} \mathbb{1} & L_i & B_i \\ 0 & 0 & R_i \\ 0 & 0 & \mathbb{1} \end{bmatrix} \tag{A.3}$$

A.2 Cylinder

The Hamiltonian of a normal cylinder can be written as

$$\begin{aligned} H_{cyl} &= \sum_r \left(\sum_{i=r_0}^{r_0+N-1} H_{i,i+N} + \sum_{i=r_0}^{r_0+N-2} H_{i,i+1} + H_{r_0+N-1,r_0} + \sum_{i=r_0}^{r_0+N-1} B_i \right) \\ &= \sum_r \left(\sum_{i=r_0}^{r_0+N-1} L_i R_{i+N} + \sum_{i=r_0}^{r_0+N-2} L_i R_{i+1} + L_{r_0+N-1} R_{r_0} + \sum_{i=r_0}^{r_0+N-1} B_i \right) \end{aligned} \tag{A.4}$$

with the same definitions for $H_{i,j}$ and B_i as before. Here, the sum over r denotes the sum over the different rungs of the cylinder, and r_0 denotes the first site of that rung in the 1D representation. It can easily be seen that $r_0 = Nr$ if $r \in \mathbb{Z}$. The JordanMPO will not be the same on all sites. Rather, there will be a distinction between the first ($M_i^{(F)}$), the middle ($M_i^{(M)}$), and the last ($M_i^{(L)}$) sites of one rung.

For this Hamiltonian, a $(N+4) \times (N+4)$ matrix is needed. The elements are then

$$\left(M_i^{(F)}\right)_{(p,q)} = \begin{cases} \mathbb{1}, & (p,q) \in \{(1,1),(N+4,N+4),(i,i+1), i \in [4,N+2]\} \\ L_i, & (p,q) \in \{(1,2),(1,4)\} \\ R_i^*, & (p,q) = (1,3) \\ R_i, & (p,q) = (N+3,N+4) \\ B_i, & (p,q) = (1,N+4) \\ 0, & else \end{cases}$$

$$\left(M_i^{(M)}\right)_{(p,q)} = \begin{cases} \mathbb{1}, & (p,q) \in \{(1,1),(N+4,N+4),(3,3),(i,i+1), i \in [4,N+2]\} \\ L_i, & (p,q) \in \{(1,2),(1,4)\} \\ R_i, & (p,q) \in \{(N+3,N+4),(2,N+4)\} \\ B_i, & (p,q) = (1,N+4) \\ 0, & else \end{cases} \tag{A.5}$$

$$\left(M_i^{(L)}\right)_{(p,q)} = \begin{cases} \mathbb{1}, & (p,q) \in \{(1,1),(N+4,N+4),(i,i+1), i \in [4,N+2]\} \\ L_i, & (p,q) = (1,4) \\ L_i^* & (p,q) = (3,N+4) \\ R_i, & (p,q) \in \{(2,L),(N+3,N+4)\} \\ B_i, & (p,q) = (1,N+4) \\ 0, & else \end{cases}$$

where L^* and R^* are the conjugates of L and R respectively. They are obtained by conjugation of the tensor and permutation of the indices. Specifically, using Tensortrack,

$$\begin{aligned} L^* &= tpermute\,(conj(L),[3,4,1,2]) \\ R^* &= tpermute\,(conj(R),[3,4,1,2]) \end{aligned} \tag{A.6}$$

Remark: In some implementations, elements on the diagonal (apart from in the upper left and lower right corner) should be avoided to avoid divergences. A less efficient implementation puts $\mathbb{1}$ on sites $(i,i+1)$ for the interaction between the first and last site.

A.3 Helix

The Hamiltonian of a helix can be written as

$$\begin{aligned} H_{helix} &= \sum_i B_i + H_{i,i+1} + H_{i,i+N} \\ &= \sum_i B_i + L_i R_{i+1} + L_i R_{i+N} \end{aligned} \tag{A.7}$$

with the same definitions for $H_{i,j}$ and B_i as before. For this Hamiltonian, a $(N+3) \times (N+3)$ matrix is needed. The elements are then

$$\left(M_i^{(N)}\right)_{(p,q)} = \begin{cases} \mathbb{1}, & (p,q) \in \{(1,1),(N+3,N+3),(i,i+1), i \in [2,N]\} \\ L_i, & (p,q) \in \{(1,2),(1,N+2)\} \\ R_i, & (p,q) \in \{(N+1,N+3),(N+2,N+3)\} \\ B_i, & (p,q) = (1,N+3) \\ 0, & else \end{cases} \tag{A.8}$$

A.4 Cylinder of the one-band model

The Hamiltonian of the cylinder describing the one-band model was given in (6.2), and is given here as a reminder

$$H = -t \sum_{\langle ii' \rangle \sigma} \left(d^\dagger_{i\sigma} d_{i'\sigma} + d^\dagger_{i'\sigma} d_{i\sigma} \right) - t' \sum_{\langle\langle ii' \rangle\rangle \sigma} \left(d^\dagger_{i\sigma} d_{i'\sigma} + d^\dagger_{i'\sigma} d_{i\sigma} \right) + U \sum_i n_{i\sigma} n_{i\bar{\sigma}} + V \sum_{\langle ii' \rangle \sigma\sigma'} n_{i\sigma} n_{i'\sigma'} \tag{A.9}$$

This equation is rewritten in (A.11), where $H^{(0)}$ denotes the on-site Hamiltonian, $H^{(1)}$ denotes the Hamiltonian acting between nearest neighbors, and $H^{(2)}$ denotes the Hamiltonian acting between next-to-nearest neighbors. Specifically,

$$\begin{aligned} H^{(0)} &= U \sum_i n_{i\sigma} n_{i\bar{\sigma}} \\ H^{(1)} &= -t \sum_{\langle ii' \rangle \sigma} \left(d^\dagger_{i\sigma} d_{i'\sigma} + d^\dagger_{i'\sigma} d_{i\sigma} \right) + V \sum_{\langle ii' \rangle \sigma\sigma'} n_{i\sigma} n_{i'\sigma'} \\ H^{(2)} &= -t' \sum_{\langle\langle ii' \rangle\rangle \sigma} \left(d^\dagger_{i\sigma} d_{i'\sigma} + d^\dagger_{i'\sigma} d_{i\sigma} \right) \end{aligned} \tag{A.10}$$

$$\begin{aligned} H_{cyl} = \sum_r \Bigg(& \sum_{i=r_0}^{r_0+N-1} H_i^{(0)} + \sum_{i=r_0}^{r_0+N-1} H^{(1)}_{i,i+N} + \sum_{i=r_0}^{r_0+N-2} H^{(1)}_{i,i+1} + H^{(1)}_{r_0+N-1,r_0} + \\ & \sum_{i=r_0}^{r_0+N-2} H^{(2)}_{i,i+N+1} + \sum_{i=r_0+1}^{r_0+N-1} H^{(2)}_{i,i+N-1} + H^{(2)}_{r_0,r_0+2N-1} + H^{(2)}_{r_0+N-1,r_0+N} \Bigg) \\ H_{cyl} = \sum_r \Bigg(& \sum_{i=r_0}^{r_0+N-1} H_i^{(0)} + \sum_{i=r_0}^{r_0+N-1} L_i^{(1)} R^{(1)}_{i+N} + \sum_{i=r_0}^{r_0+N-2} L_i^{(1)} R^{(1)}_{i+1} + L^{(1)}_{r_0+N-1} R^{(1)}_{r_0} + \\ & \sum_{i=r_0}^{r_0+N-2} L_i^{(2)} R^{(2)}_{i+N+1} + \sum_{i=r_0+1}^{r_0+N-1} L_i^{(2)} R^{(2)}_{i+N-1} L^{(2)}_{r_0} R^{(2)}_{r_0+2N-1} + L^{(2)}_{r_0+N-1} R^{(2)}_{r_0+N} \Bigg) \end{aligned} \tag{A.11}$$

The construction of the JordanMPOs from (A.11) is similar as in the previous examples and will, for brevity reasons, not be repeated.

A.5 Cylinder of the three-band model

The Hamiltonian of the cylinder describing the three-band model was given in (6.1) and is given here as a reminder.

$$
\begin{aligned}
H = &- \sum_{\langle ij \rangle \sigma} (-1)^{P_{ij}} t_{pd} \left(d^{\dagger}_{i\sigma} p_{j\sigma} + p^{\dagger}_{j\sigma} d_{i\sigma} \right) - \sum_{\langle jj' \rangle \sigma} (-1)^{P_{ij}} t_{pp} \left(p^{\dagger}_{j\sigma} p_{j\sigma} + p^{\dagger}_{j'\sigma} p_{j\sigma} \right) + \Delta_{dp} \sum_{i\sigma} n_{i\sigma} \\
&+ U_d \sum_i n_{i\uparrow} n_{i\downarrow} + U_p \sum_i n_{j\uparrow} n_{j\downarrow} + V_{pd} \sum_{\langle ij \rangle \sigma\sigma'} n_{i\sigma} n_{j\sigma'} + V_{dd} \sum_{\langle ii' \rangle \sigma\sigma'} n_{i\sigma} n_{i'\sigma'} + V_{pp} \sum_{\langle jj' \rangle \sigma\sigma'} n_{j\sigma} n_{j'\sigma'}
\end{aligned}
\tag{A.12}
$$

This equation is rewritten in (A.11). H^0_{Cu} and H^0_O denote the on-site Hamiltonians on the copper and oxygen atoms, respectively. $H^{(1+)}$ and $H^{(1-)}$ denote Hamiltonians acting between nearest-neighbor copper and oxygen atoms. $H^{(2+)}$ and $H^{(2-)}$ denote Hamiltonians acting between nearest-neighbor oxygen atoms. $H^{(3)}$ denotes the Hamiltonian acting between nearest-neighbor copper atoms. Specifically,

$$
\begin{aligned}
H^{(1+)} &= - \sum_{\langle ij \rangle \sigma} t_{pd} \left(d^{\dagger}_{i\sigma} p_{j\sigma} + p^{\dagger}_{j\sigma} d_{i\sigma} \right) + V_{pd} \sum_{\langle ij \rangle \sigma\sigma'} n_{i\sigma} n_{j\sigma'} \\
H^{(1-)} &= \sum_{\langle ij \rangle \sigma} t_{pd} \left(d^{\dagger}_{i\sigma} p_{j\sigma} + p^{\dagger}_{j\sigma} d_{i\sigma} \right) + V_{pd} \sum_{\langle ij \rangle \sigma\sigma'} n_{i\sigma} n_{j\sigma'} \\
H^{(2+)} &= - \sum_{\langle jj' \rangle \sigma} t_{pp} \left(p^{\dagger}_{j\sigma} p_{j\sigma} + p^{\dagger}_{j'\sigma} p_{j\sigma} \right) + V_{pp} \sum_{\langle jj' \rangle \sigma\sigma'} n_{j\sigma} n_{j'\sigma'} \\
H^{(2-)} &= \sum_{\langle jj' \rangle \sigma} t_{pp} \left(p^{\dagger}_{j\sigma} p_{j\sigma} + p^{\dagger}_{j'\sigma} p_{j\sigma} \right) + V_{pp} \sum_{\langle jj' \rangle \sigma\sigma'} n_{j\sigma} n_{j'\sigma'} \\
H^{(3)} &= V_{dd} \sum_{\langle ii' \rangle \sigma\sigma'} n_{i\sigma} n_{i'\sigma'} \\
H^{(0)}_{Cu} &= U_d \sum_i n_{i\uparrow} n_{i\downarrow} + \Delta_{dp} \sum_{i\sigma} n_{i\sigma} \\
H^{(0)}_{O} &= U_p \sum_i n_{j\uparrow} n_{j\downarrow}
\end{aligned}
\tag{A.13}
$$

$$
\begin{aligned}
H_{3-band} = \sum_r \Bigg(&\sum_{i=0}^{N-1} H^{(1+)}_{r_0+3i,r_0+3i+1} + \sum_{i=0}^{N-1} H^{(1+)}_{r_0+3i,r_0+3i+2} + \sum_{i=0}^{N-2} H^{(1-)}_{r_0+3i+2,r_0+3i+3} + H^{(1-)}_{r_0+3N-1,r_0} \\
&+ \sum_{i=0}^{N-1} H^{(1-)}_{r_0+3i+1,r_0+3i+3N} + \sum_{i=0}^{N-2} H^{(2+)}_{r_0+3i+2,r_0+3i+4} + H^{(2+)}_{r_0+3N-1,r_0+1} \\
&+ \sum_{i=0}^{N-1} H^{(2+)}_{r_0+3i+1,r_0+3i+3N+2} + \sum_{i=0}^{N-1} H^{(2-)}_{r_0+3i+1,r_0+3i+2} + \sum_{i=1}^{N-1} H^{(2-)}_{r_0+3i+1,r_0+3i-1} \\
&+ H^{(2-)}_{r_0+6N-1,r_0+1} + \sum_{i=0}^{N-1} H^{(3)}_{r_0+3i,r_0+3i+3N} + \sum_{i=0}^{N-2} H^{(3)}_{r_0+3i,r_0+3i+3} + H^{(3)}_{r_0+3N-3,r_0} \\
&+ \sum_{i=0}^{N-1} \left[H^{(0)}_{Cu,r_0+3i} + H^{(0)}_{O,r_0+3i+1} + H^{(0)}_{O,r_0+3i+2} \right] \Bigg)
\end{aligned}
\tag{A.14}
$$

$$
\begin{aligned}
H_{3-band} = \sum_{r} \Bigg(& \sum_{i=0}^{N-1} L^{(1+)}_{r_0+3i} R^{(1+)}_{r_0+3i+1} + \sum_{i=0}^{N-1} L^{(1+)}_{r_0+3i} R^{(1+)}_{r_0+3i+2} + \sum_{i=0}^{N-2} L^{(1-)}_{r_0+3i+2} R^{(1-)}_{r_0+3i+3} + L^{(1-)}_{r_0+3N-1} R^{(1-)}_{r_0} \\
& + \sum_{i=0}^{N-1} L^{(1-)}_{r_0+3i+1} R^{(1-)}_{r_0+3i+3N} + \sum_{i=0}^{N-2} L^{(2+)}_{r_0+3i+2} R^{(2+)}_{r_0+3i+4} + L^{(2+)}_{r_0+3N-1} R^{(2+)}_{r_0+1} \\
& + \sum_{i=0}^{N-1} L^{(2+)}_{r_0+3i+1} R^{(2+)}_{r_0+3i+3N+2} + \sum_{i=0}^{N-1} L^{(2-)}_{r_0+3i+1} R^{(2-)}_{r_0+3i+2} + \sum_{i=1}^{N-1} L^{(2-)}_{r_0+3i+1} R^{(2-)}_{r_0+3i-1} \\
& + L^{(2-)}_{r_0+6N-1} R^{(2-)}_{r_0+1} + \sum_{i=0}^{N-1} L^{(3)}_{r_0+3i} R^{(3)}_{r_0+3i+3N} + \sum_{i=0}^{N-2} L^{(3)}_{r_0+3i} R^{(3)}_{r_0+3i+3} + L^{(3)}_{r_0+3N-3} R^{(3)}_{r_0} \\
& + \sum_{i=0}^{N-1} \Big[H^{(0)}_{Cu,r_0+3i} + H^{(0)}_{O,r_0+3i+1} + H^{(0)}_{O,r_0+3i+2} \Big] \Bigg)
\end{aligned}
\tag{A.15}
$$

B

Details of VUMPS [25]

The set of injective MPS form a complex manifold [26]. Making smart use of the tangent space to this manifold, an algorithm resembling gradient descent can be devised. The combination of DMRG with the ideas of tangent spaces for MPS led to the development of another variational optimization algorithm, called Variational Uniform Matrix Product State (VUMPS) [18, 19].

Finding the ground state again amounts to finding the minimum of the energy functional, i.e.

$$E_{gs} = \min_{A} \frac{\langle \Psi(\bar{A}) | \, h \, | \Psi(A) \rangle}{\langle \Psi(\bar{A}) | \Psi(A) \rangle} = \min_{A} f(A, \bar{A}) \tag{B.1}$$

A vital ingredient in this minimization procedure will be the gradient, where the right-hand side of (B.1) is differentiated with respect to $\bar{A}$. Differentiation will just mean that a tensor is left out and its physical space is interpreted as an outgoing line, as given in figure B.1.

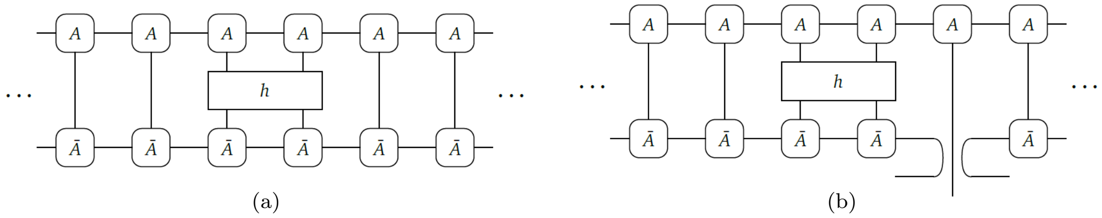

(a) (b)

Figure B.1: (a) E_{gs} and (b) $(\partial/\partial\bar{A}^i)E_{gs}$ for a normalised MPS [19]

The gradient g can be written as

$$\begin{aligned} g &= 2\frac{\partial}{\partial \bar{A}} f\left(A, \bar{A}\right) \\ g &= 2\frac{\partial}{\partial \bar{A}} \frac{\langle \Psi(\bar{A}) | \, h \, | \Psi(A) \rangle}{\langle \Psi(\bar{A}) | \Psi(A) \rangle} \\ &= \frac{2}{\langle \Psi(\bar{A}) | \Psi(A) \rangle} \frac{\partial}{\partial \bar{A}} \langle \Psi(\bar{A}) | \, h \, | \Psi(A) \rangle - 2\frac{\langle \Psi(\bar{A}) | \, h \, | \Psi(A) \rangle}{\langle \Psi(\bar{A}) | \Psi(A) \rangle^2} \frac{\partial}{\partial \bar{A}} \langle \Psi(\bar{A}) | \Psi(\bar{A}) \rangle \\ &= 2\frac{\frac{\partial}{\partial \bar{A}} \langle \Psi(\bar{A}) | \, h \, | \Psi(A) \rangle - E \frac{\partial}{\partial \bar{A}} \langle \Psi(\bar{A}) | \Psi(\bar{A}) \rangle}{\langle \Psi(\bar{A}) | \Psi(A) \rangle} \end{aligned} \tag{B.2}$$

where E is the current energy density.

$$E = \frac{\langle \Psi(\bar{A}) | \, h \, | \Psi(A) \rangle}{\langle \Psi(\bar{A}) | \Psi(A) \rangle} \tag{B.3}$$

---

[25] This discussion is mostly based on reference [19].

[26] More specifically, it forms a Kähler manifold [70]

By normalizing the MPS and by subtracting the expectation value from the Hamiltonian

$$h' = h - \left\langle \Psi(\bar{A}) \right| h \left| \Psi(A) \right\rangle \tag{B.4}$$

the expression for the gradient reduces to

$$g = 2 \frac{\partial}{\partial \bar{A}} \left\langle \Psi(\bar{A}) \right| h \left| \Psi(A) \right\rangle \tag{B.5}$$

This gradient can be calculated by taking the derivative with respect to $\bar{A}$ of the expression in figure B.1a. This is an infinite sum, where in each term one of the $\bar{A}$ is left out.

In optimizing the energy, the current MPS will be nudged in a certain direction, i.e.

$$A \to A + \epsilon B \tag{B.6}$$

which yields a certain nudge in the energy functional

$$\begin{aligned} f\left(A, \bar{A}\right) &\to f\left(A, \bar{A}\right) + 2\epsilon \frac{\partial}{\partial \bar{A}} f\left(A, \bar{A}\right) B + O(\epsilon^2) \\ &\to f\left(A, \bar{A}\right) + \epsilon g^\dagger B + O(\epsilon^2) \end{aligned} \tag{B.7}$$

It is now useful to interpret the set of uniform MPS with the same bond dimension as a manifold within the total Hilbert space of the system in which the energy will be minimized. This manifold is defined by the map from the tensors of a certain dimension A to the states in the physical Hilbert space $\left| \Psi(A) \right\rangle$. The sum of two MPS will not necessarily remain in this manifold. Therefore, the tangent space to every MPS will be defined, for which a basis is given by $\frac{\partial}{\partial A} \left| \Psi(A) \right\rangle$. A tangent tensor is then defined as

$$\left| \Phi(B; A) \right\rangle = B^i \frac{\partial}{\partial A^i} \left| \Psi(A) \right\rangle \tag{B.8}$$

where the Einstein-summation convention is used. Graphically, this means replacing every A^i with B^i.

g in (B.7) is a tensor, not a state in the Hilbert space. Since the nudge $A \to A + \epsilon B$ has the effect of

$$\left| \Psi(A + \epsilon B) \right\rangle \to \left| \Psi(A) \right\rangle + \epsilon \left| \Phi(B; A) \right\rangle \tag{B.9}$$

the resulting nudge in the energy functional (given by (B.7)) could be written as the overlap of this tangent vector $\left| \Phi(B; A) \right\rangle$ and a certain gradient vector $\left| \Phi(G; A) \right\rangle$.

$$f\left(A, \bar{A}\right) \to f\left(A, \bar{A}\right) + \epsilon \left\langle \Phi(G; A) \middle| \Phi(B; A) \right\rangle + O(\epsilon^2) \tag{B.10}$$

This tangent-space gradient can be obtained from g by means of the tangent-space projector, defined in [19]. In the language of the MPS manifold, this corresponds to the direction in which the energy is minimized, which can then be used in an optimization algorithm. In the mixed gauge, the vectorized version of this gradient can be written as

$$\vec{G} = \left| \Phi(G; A_L, A_R) \right\rangle \tag{B.11}$$

The gradient should be zero if the algorithm has converged. An error measure is thus given by

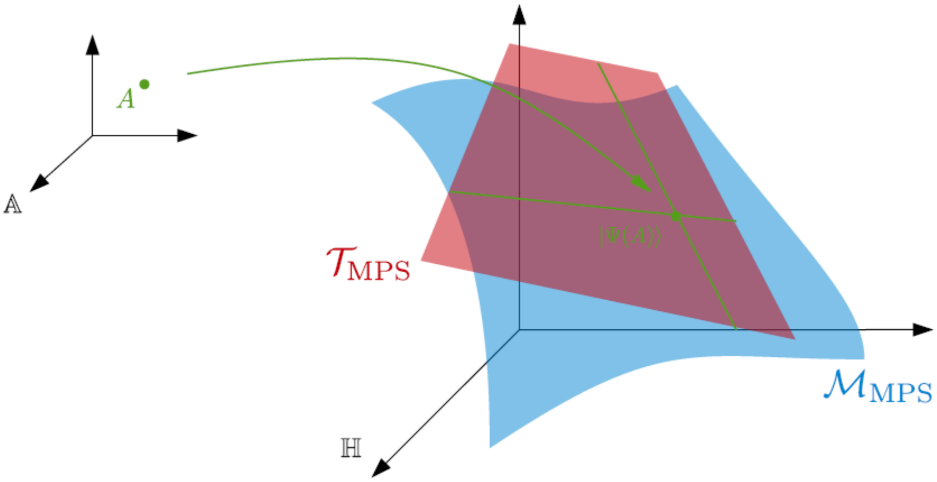

Figure B.2: MPS manifold and its tangent space [19]

$$\epsilon = (\vec{G}^{\dagger}\vec{G})^{1/2} = (\langle\Phi(G; A_L, A_R)|\Phi(G; A_L, A_R)\rangle)^{1/2} \tag{B.12}$$

Using the tangent-space projector, this yields

$$G = A'_C - A_L C' \tag{B.13}$$

where A'_C and C' are defined as

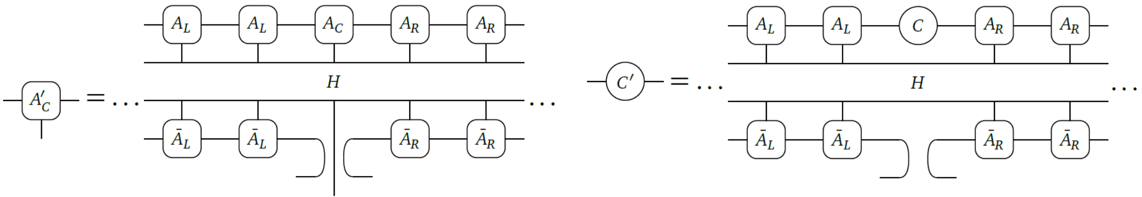

(a) $\mathrm{H}_{A_C}(A_C)$

(b) $\mathrm{H}_C(C)$

Figure B.3: Effective Hamiltonians of A_C and C used in the VUMPS update equations [19]

The equations from figure B.3 define effective Hamiltonians for A_C and C

$$\begin{aligned} A'_C &= H_{A_C}(A_C) \\ C' &= H_C(C) \end{aligned} \tag{B.14}$$

Together with the condition that the gradient should be zero in the minimum, these yield the VUMPS set of equations.

$$\begin{aligned} H_{A_C}(A_C) &\propto A_C \\ H_C(C) &\propto C \\ A_C &= A_L C = C A_R \end{aligned} \tag{B.15}$$

The VUMPS algorithm consists of first solving the two eigenvalue equations, which yield new values of A_C and C. The updates for A_L and A_R are calculated by minimizing the error in the third equation, i.e.

$$\begin{aligned} \epsilon_L &= \min \| A_C - A_L C \| \\ \epsilon_R &= \min \| A_C - C A_R \| \end{aligned} \tag{B.16}$$

These new values of A_L and A_R redefine the effective Hamiltonians H_{A_C} and H_C which are used in the next iteration step. If both epsilons are smaller than a certain predefined tolerance, the iteration procedure is said to have converged.

C Virtual spaces of the doped Hubbard model to create injective MPS

C.1 Using $U(1) \otimes U(1) \otimes f\mathbb{Z}_2$

The physical Hilbert space for the doped Hubbard model with filling $f = P/Q$, is, as mentioned in section 5.2

$$\begin{cases} |0\rangle & \sim (-P, 0, +1) \\ |\uparrow\rangle & \sim (Q-P, 1, -1) \\ |\downarrow\rangle & \sim (Q-P, -1, -1) \\ |\uparrow\downarrow\rangle & \sim (2Q-P, 0, +1) \end{cases} \in U(1) \otimes U(1) \otimes f\mathbb{Z}_2 \tag{C.1}$$

The virtual Hilbert space, in total, can be represented by

$$v = (Z_1, Z_2, \{\pm 1\}), \quad Z_1, Z_2 \in \mathbb{Z} \tag{C.2}$$

This will be decomposed in sectors v_k.

$$v_k = \begin{cases} (2QZ_1 - kP, 2Z_2, +), & Z_1, Z_2 \in \mathbb{Z} \\ (2QZ_1 + Q - kP, 2Z_2 + 1, -), & Z_1, Z_2 \in \mathbb{Z} \end{cases} \tag{C.3}$$

C.2 Using $U(1) \otimes SU(2) \otimes f\mathbb{Z}_2$

In this case, the physical Hilbert space for the doped Hubbard model with filling $f = P/Q$ is

$$\begin{cases} |0\rangle & \sim (-P, 1/2, +1) \\ |\uparrow\rangle & \sim (Q-P, 1/2, -1) \\ |\uparrow\downarrow\rangle & \sim (2Q-P, 1/2, +1) \end{cases} \in U(1) \otimes SU(2) \otimes f\mathbb{Z}_2 \tag{C.4}$$

The virtual Hilbert space, in total, is

$$v = (Z, N/2, \{\pm 1\}, \quad Z \in \mathbb{Z}, N \in \mathbb{N} \tag{C.5}$$

This will be decomposed in sectors v_k.

$$v_k = \begin{cases} (2QZ - kP, N, +), & Z \in \mathbb{Z}, N \in \mathbb{N} \\ (2QZ + Q - kP, N + \frac{1}{2}, -), & Z \in \mathbb{Z}, N \in \mathbb{N} \end{cases} \tag{C.6}$$

C.3 Not using $U(1)$ for the charge sector

The needed charges in the case where the $U(1)$ symmetry of the charge sector is dropped, can be obtained from sections C.1 and C.2 by just dropping the U(1) charges.

C.4 General remarks

For odd P, a $2Q$-site unit cell is needed, with virtual spaces v_k, $k \in [0, 2Q]$. For even P, a Q-site unit cell is needed, with virtual spaces v_k, $k \in [0, Q]$. This follows from the fact that $v_0 = v_Q$ only when P is even.

To implement this in the code, a finite set within each sector needs to be chosen when defining the spaces of an MPS. It is important that this choice allows for an MPS of full-rank, which translates in the conditions that the following two monomorphisms must exist

$$\begin{gathered} \mathcal{H}_{v_L} \otimes \mathcal{H}_p \hookrightarrow \mathcal{H}_{v_R} \\ \mathcal{H}_{v_L} \hookleftarrow \mathcal{H}_p^* \otimes \mathcal{H}_{v_R} \end{gathered} \tag{C.7}$$

where $\mathcal{H}_p$ and $\mathcal{H}_p^*$ are the physical Hilbert space and its dual. $\mathcal{H}_{v_L}$ and $\mathcal{H}_{v_R}$ are the left and right virtual Hilbert space of one particular tensor in the unit cell. The conditions need to be fulfilled for each site in the unit cell. The existence of a monomorphism $X \hookrightarrow Y$ means that each element in Y must be uniquely contained within X.

D Parameters for models of $HgBa_2CuO_4$

The used parameters for the one-band and three-band model of $HgBa_2CuO_4$ are given in tables D.1 and D.2 respectively. They were taken from reference [123].

Table D.1: Parameters of the one-band model for $HgBa_2CuO_4$ in accordance with (6.2). Parameters were implemented as given in this table. The original value of t, as given in the paper, is 0.461. This fixes the energy scale. In the code, all parameters were rescaled with t. Parameters taken from reference [123].

$HgBa_2CuO_4$	oneband
t (scale)	1
t'	-0.26
U	9.48
V	2.364

Table D.2: Parameters of the three-band model of $HgBa_2CuO_4$ in accordance with (6.1). The parameters that were implemented are the ones given in this table divided by t_{dp}. Parameters taken from reference [123].

$HgBa_2CuO_4$	threeband
t_{dp} (scale)	1.257
t_{pp}	0.751
Δ_{dp}	2.416
U_{dd}	8.84
U_{pp}	5.31
V_{dd}	0.8
V_{pp}	1.21
V_{dp}	1.99

E

Figures - correlation functions

This appendix shows the correlation functions corresponding to the results on the 2D Hubbard model, both for $N = 2$ and $N = 4$.

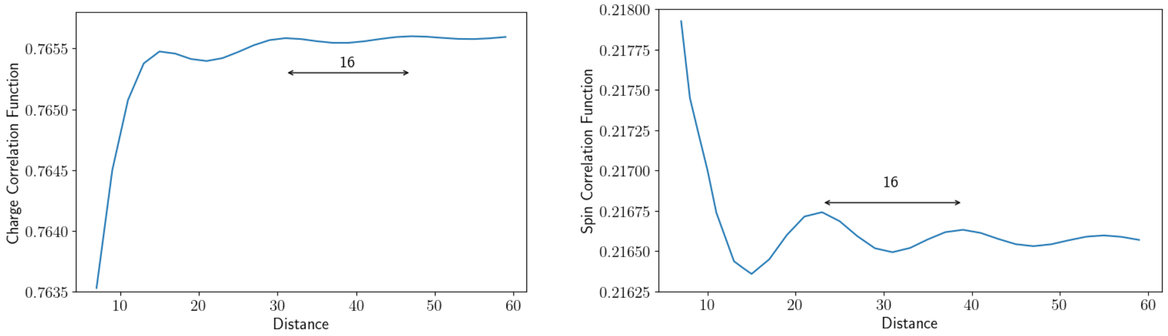

(a) Charge correlation function

(b) Spin correlation function

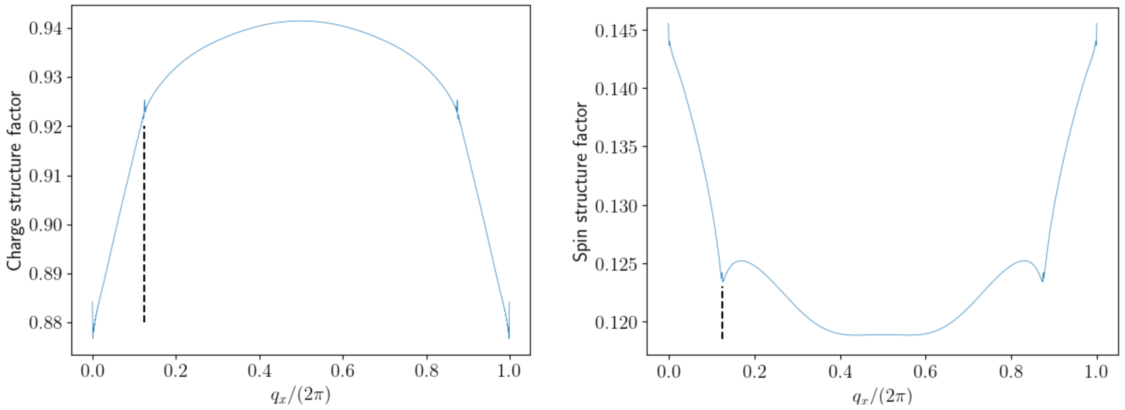

(c) Charge structure factor

(d) Spin structure factor

Figure E.1: Charge and spin correlation functions and structure factors for the 2D Hubbard model with $t = 1, U = 8$, and $\delta = 1/8$ on a cylinder with $N = 2$ and 8 rungs for $q_y = 0$. The dotted line corresponds to $q_x = \frac{2\pi}{8}$. $D = 600$. The fact that the period of the SDW is not double of the period of the CDW is due to the $SU(2)$ symmetry. Calculations using $U(1) \otimes U(1) \otimes f\mathbb{Z}_2$ confirmed $\lambda_{SDW} = 2\lambda_{CDW}$

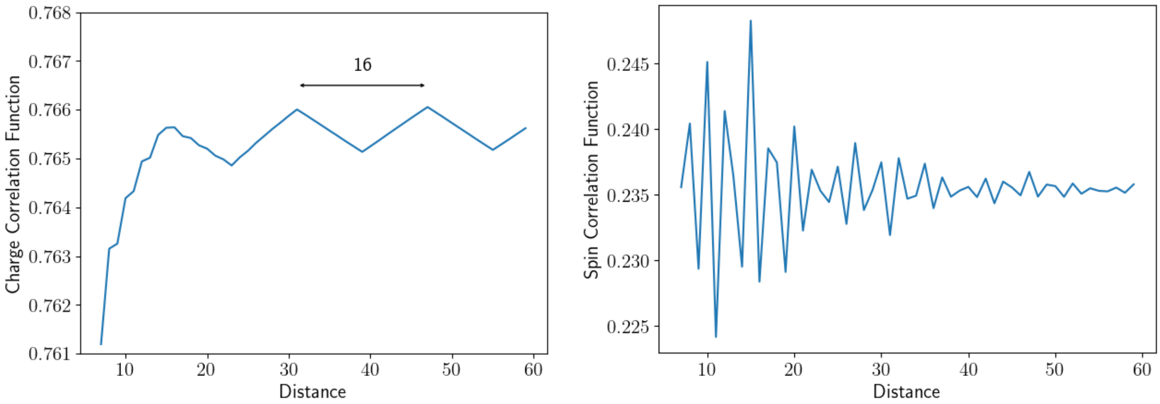

(a) Charge correlation function

(b) Spin correlation function

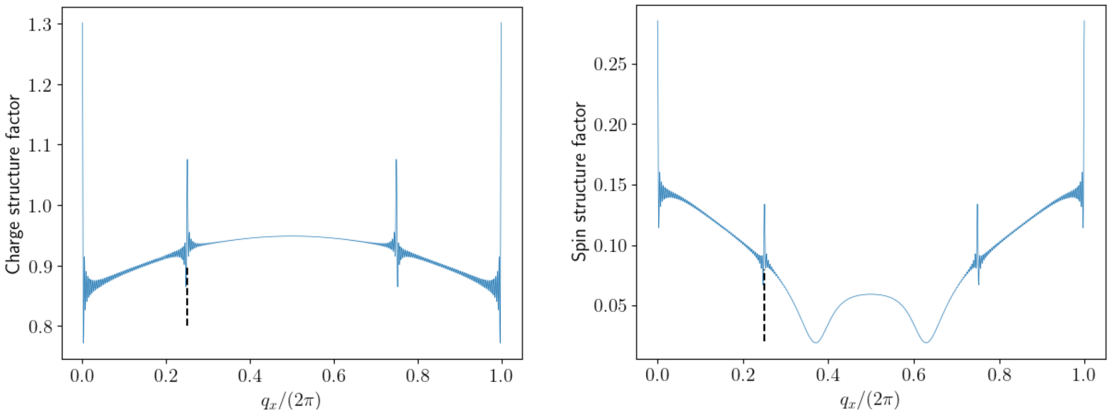

(c) Charge structure factor

(d) Spin structure factor

Figure E.2: Charge and spin correlation functions and structure factors for the 2D Hubbard model with $t = 1, U = 8$, and $\delta = 1/8$ on a cylinder with $N = 4$ and 8 rungs for $q_y = 0$. The dotted line corresponds to $q_x = \frac{2\pi}{4}$. $D = 767$.

F

Transfermatrix eigenvalues of the one-band model

Figures F.1 and F.2 show the eigenvalues of the transfer matrix of the one-band model of $HgBa_2CuO_4$. All cases exhibit filled stripes. The deviations from this behavior are listed in table F.1.

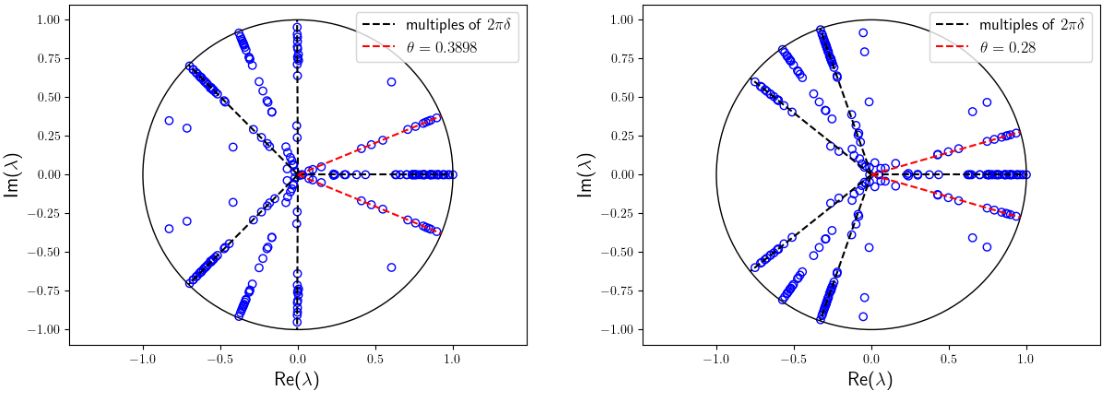

(a) $\mu = -6.5,\ \delta = 0.3746,\ D = 1523$

(b) $\mu = -7.5,\ f = 0.3036,\ D = 1760$

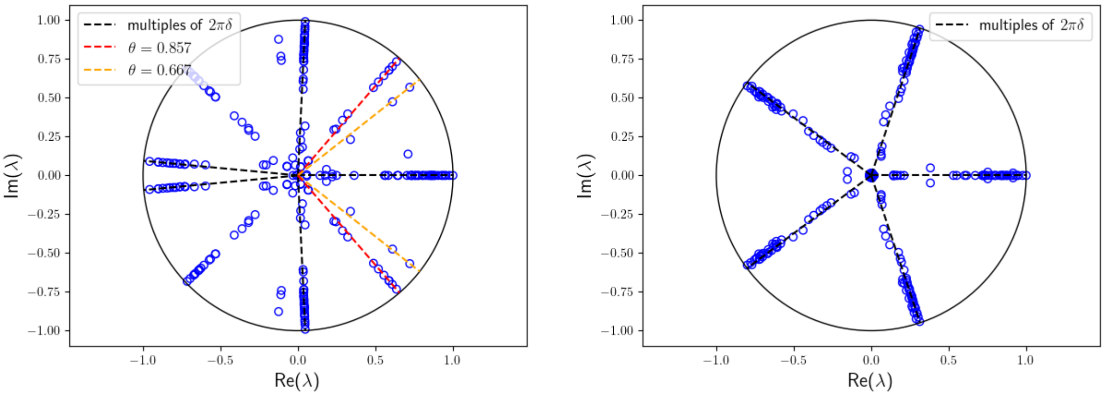

(c) $\mu = -8.5,\ f = 0.2425,\ D = 1721$

(d) $\mu = -9.2,\ f = 0.1990,\ D = 1460$

Figure F.1: Eigenvalues of the transfer matrix for different values of μ for the one-band model of $HgBa_2CuO_4$. The results that are expected for filled stripes are denoted by black dashed lines. (part 1)

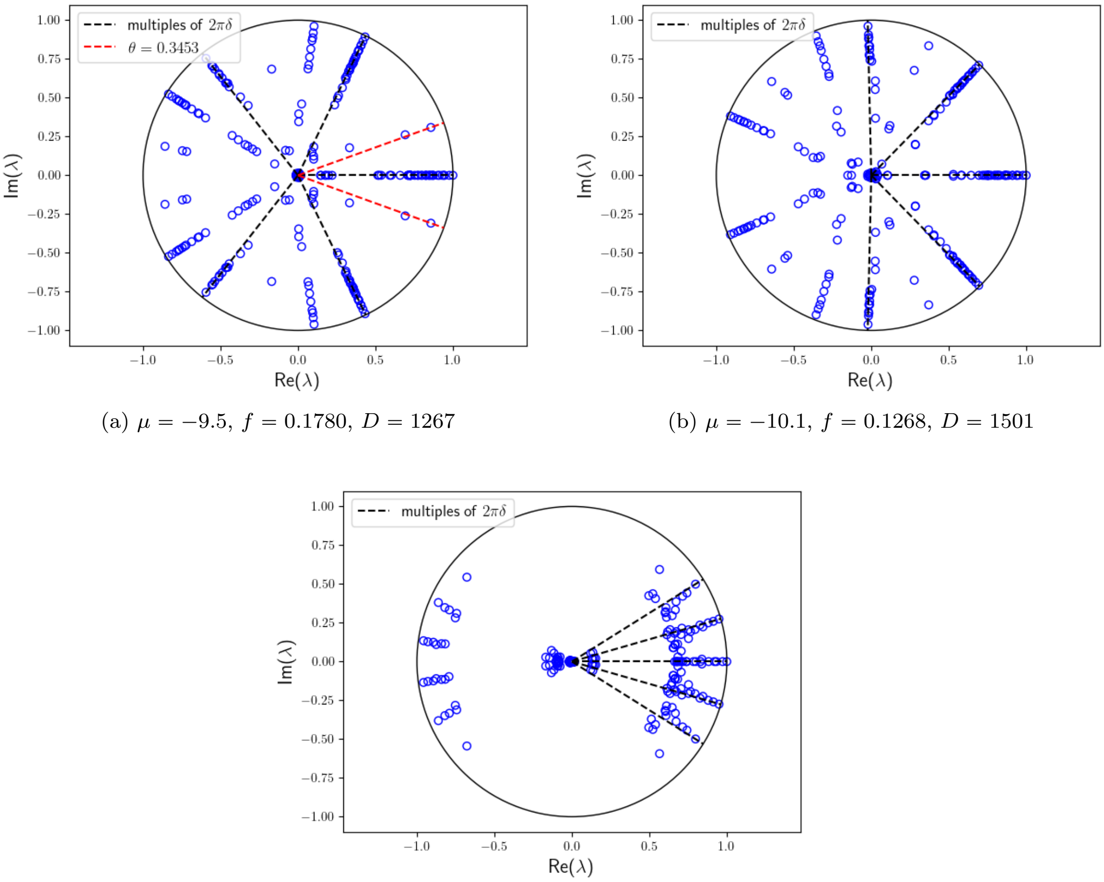

(a) $\mu = -9.5,\ f = 0.1780,\ D = 1267$

(b) $\mu = -10.1,\ f = 0.1268,\ D = 1501$

(c) $\mu = -10.607,\ f = 0.0445,\ D = 646$

Figure F.2: Eigenvalues of the transfer matrix for different values of μ for the one-band model of $HgBa_2CuO_4$. The results that are expected for filled stripes are denoted by black dashed lines. (part 2)

Table F.1: Angles not expected from filled stripes for the one-band model of $HgBa_2CuO_4$

μ	δ	θ	period of CDW $\lambda = \frac{2\pi}{\theta}$	FF
-6.5	0.3746	0.3898	16.12	6.04
-7.5	0.3036	0.28	22.44	6.81
-8.5	0.2425	0.667	9.42	2.28
-8.5	0.2425	0.857	7.33	1.78
-9.5	0.1780	0.3453	18.20	3.24